# **Life Prediction Model of Electronics Subjected to Thermo-Mechanical Environments**

by

Kazi Mahmud Mirza

A dissertation submitted to the Graduate Faculty of
Auburn University
in partial fulfillment of the
requirements for the Degree of
Doctor of Philosophy

Auburn, Alabama
December 10, 2016

Keywords: Life Prediction Model, Prognostics, Solder Joint Reliability,
Micro-Electronic Packaging

Copyright 2016 by Kazi Mahmud Mirza

Approved by

Pradeep Lall, Chair, Macfarlane Professor of Mechanical Engineering
Jeffrey C. Suhling, Quina Distinguished Professor of Mechanical Engineering
Roy W. Knight, Assistant Professor of Mechanical Engineering
Michael J. Bozack, Professor of Physics

Abstract

Microelectronic assemblies used in automotive, military and defense applications may be subjected to extreme high and extreme low temperature in addition to temperature cycling with intermittent prolonged period of storage. Field deployed electronics, unlike controlled laboratory testing, may experience a variety of sequential thermo-mechanical stresses during its lifetime. The field environment imposed on the electronic system may be influenced by ambient conditions and usage profile. Variation in the ambient temperature conditions, weather variations, usage location in addition to scheduled system usage or downtime may result in wide variance in the resulting field profile. Thermally induced stresses can be produced in fabrication stage also. In an electronic packaging assembly, one of the crucial parts affecting reliability the most is the solder joint, which actually bears most of the stress gradients formed inside packages due to CTE mismatch. Safety critical nature of the electronics systems necessitates that level-of-damage and reliability should be assessed prior to any future redeployment. The prognostic technique proposed in this thesis is based on Physics of Failure based damage indicators of second level interconnects. Both the test vehicle and thermal conditions have been thoughtfully selected to ensure relevancy to current packaging technologies and critical usage profiles. The impact of iso-thermal aging and effect of mean temperature of thermal cycling environment were investigated and the information derived from these investigations were used to develop the damage mapping and life prediction model. The damage mapping relationship deals

with finding a Time-Temperature combination required to reach a particular damage state and the predictive model shows how microstructural growth rate is related to fatigue life. The evolution of two different microstructural damage parameters were used in the process of developing the life prediction model.

Apart from microstructure based parameter, a new prognostic tool based on shear strain was presented, where shear strain evolution with number of thermal cycles undergone was investigated with a view to finally correlate with life degradation. A full-field optical technique like Digital Image Correlation was used to investigate the evolution of shear strain with number of thermal cycles, which is a completely new approach to assess the effect of thermal cycling duration on shear strain in real time. A quarter symmetry model of package was built in ANSYS and simulated using Anand's Visco-plastic Constitutive Model to check the validity of experimental finding and at the same time to calculate plastic work dissipated under a particular thermal cycling environment.

Finally popular life models like Coffin-Mansion and Darveaux's model were implemented with experimental data. A new model of Remaining Useful Life (RUL) prognostication was proposed based on microstructural damage indicators. Also a new approach to fatigue life calculation was presented by correlating microstructural parameter growth and plastic work dissipated.

Table of Contents

Abstract ... ii
List of Figures ... ix
List of Tables ... xvii
Chapter 1 Introduction ... 1
1.1 Electronic Packaging Overview ... 1
1.2 Packaging Design ... 2
1.3 Packaging Technology ... 3
1.4 Plastic Ball Grid Array Packages ... 6
1.5 Reliability ... 8
1.6 Soldering Alloy ... 10
1.7 Performance Characteristics of Solder Alloys ... 10
1.8 Sn-Ag-Cu (SAC) Series Alloys ... 13
1.9 SAC Phase Diagram ... 14
1.10 Mechanical Properties and Failure of Soldering Materials ... 17
1.11 Tensile Properties ... 19
1.13 Creep ... 20
1.14 Fatigue ... 23

1.15 Fatigue Life ..... 25
1.15.1 High Cycle Fatigue ..... 25
1.15.2 Low Cycle Fatigue ..... 26
1.16 Digital Image Correlation ..... 26
1.17 Prognostic Health Management System ..... 31
1.18 Thesis Layout ..... 33
Chapter 2 Literature Review ..... 35
2.1 Package Reliability ..... 35
2.2 Thermal Cycling reliability of SAC solders ..... 36
2.3 Isothermal Aging reliability of SAC solders ..... 38
2.4 Packaging Architecture ..... 42
2.5 Constitutive relations for Solder ..... 43
2.6 Stress-Strain ..... 44
2.7 Creep Model ..... 46
2.8 Anand's Viscoplastic Model ..... 47
2.9 Fatigue Life Prediction Models ..... 51
2.10 Digital Image Correlation ..... 53
2.11 Prognostic Health Management System ..... 54
Chapter 3 Damage Pre-Cursor Based Assessment of Impact of High Temperature Storage on Reliability of Lead-free Electronics ..... 56
3.1 Overview ..... 56

3.2 Test Vehicle ..... 57

3.3 Approach for Interrogation of Damage in Thermal Aging ..... 62

3.3.1 Damage Mapping Relationships for Phase Growth ..... 66

3.3.2 Damage Mapping Relationships for IMC Growth ..... 67

3.4 Leading Indicators for Thermal Aging ..... 68

3.4.1 Phase-Growth Damage Proxy ..... 68

3.4.2 Intermetallic Thickness Damage Proxy ..... 76

3.5 Damage Mapping ..... 81

3.6 Summary and Conclusions ..... 86

Chapter 4 Study of Effect of Mean Temperature of Thermal Cycle on SnAgCu Solder Joint Reliability ..... 88

4.1 Overview ..... 88

4.2 Test Vehicle ..... 89

4.3 Approach for Interrogation of Damage in Thermal Cycling ..... 91

4.3.1 Micro-structural Evolution of Damage ..... 91

4.3.2 Damage Mapping Relationships for Phase Growth ..... 94

4.3.3 Damage Mapping Relationships for IMC Growth ..... 96

4.3.4 Levenberg-Marquardt Algorithm ..... 97

4.4 Analysis of Results ..... 99

4.4.1 Phase-Growth Damage Proxy ..... 99

4.4.2 Inter-Metallic Thickness Growth Damage Proxy ..... 110

4.5 Damage Equivalency Relationships ... 118

4.6 Prognostication ... 121

4.7 Prognostics Performance Evaluation ... 127

4.7.1 Average Bias ... 128

4.7.3 Mean Squared Error (MSE) ... 129

4.7.4 Mean Absolute Percentage Error (MAPE) ... 129

4.7.5 α-λ accuracy ... 129

4.7.2 Sample Standard Deviation (SSD) ... 132

4.7.6 Relative Accuracy ... 132

4.7.7 Cumulative Relative Accuracy (CRA) ... 133

4.8 Conclusions ... 134

Chapter 5 DIC Based Investigation into The Effect of Mean Temperature of Thermal Cycle on The Strain State in SnAgCu Solder Joint ... 135

5.1 Overview ... 135

5.2 Test Vehicle ... 136

5.3 DIC Working Principle ... 139

5.4 Experimental Procedures ... 141

5.5 Experimental Results ... 144

5.6 Finite Element Analysis Results ... 152

5.7 Conclusions ... 165

Chapter 6 Determining the Effect of Aging on Thermal Cycling Reliability of Sn-Ag-Cu Interconnects Using Digital Image Correlation ... 166

6.1 Overview ... 166

6.2 Test Vehicle ... 167

6.3 Experimental Procedure ... 169

6.4 Experimental Results ... 171

6.5 Discussion ... 183

6.6 Finite Element Validation ... 186

6.8 Conclusion ... 189

Chapter 7 Life Prediction Model and Remaining Useful Life Prognostication ... 190
7.1 Overview ... 190

7.2 Coffin-Manson Model ... 190

7.2.1 Damage Mapping Using Coffin-Manson Relation ... 191

7.3 Darveaux Energy Based Model ... 197

7.4 Life Model based on Microstructural Growth Rate ... 199

7.5 Remaining Life Prognostic ... 205

7.5 Conclusion ... 210

Chapter 8 Summary ... 211
8.1 Damage Mapping Model ... 211

8.2 Life Prediction Model ... 211

8.3 Real time Investigation of Damage ... 212

8.4 Future Work ... 212

Reference ... 214

List of Figures


Figure 1-1: General Evolution of Electronic packaging Technology [4] .......................... 2

Figure 1-2: Three levels of packaging: the device is packaged into a component, the component is mounted on the board, and the board is installed into the subsystem chassis (MCM = multichip module, COB = chip-on-board)[5]. ........................... 3

Figure 1-3: Packaging Densities over Time [6] ................................................................ 5

Figure 1-4: Schematic of a typical PBGA package ........................................................ 7

Figure 1-5: A. Solder Mask Defined, and B. Non Solder Mask Defined [7] .................... 8

Figure 1-6: Typical 3-D Ternary Phase Diagram [20] .................................................... 15

Figure 1-7: Top View of Sn–Ag–Cu Ternary Phase Diagram [21] ................................ 16

Figure 1-8: Binary phase diagram (a) Sn–Ag and (b) Sn–Cu. [23] ................................ 17

Figure 1-9: Cyclic Stress Induced by CTE Mismatch [24] ............................................. 18

Figure 1-10: Solder Joints Subjected to Tensile Loading due to Substrate Flexing ......... 19

Figure 1-11: Typical Stress-Strain Curve of Pb-free Alloys [25] .................................... 20

Figure 1-12: Creep Curve under Constant Stress/Load and Temperature [26] ................ 20

Figure 1-13: Creation and propagation of dislocation [29] ............................................ 21

Figure 1-14: Macroscopic deformation of a cube produced by glide of (a) Edge dislocation and (b) Screw dislocation [30] ....................................................... 22

Figure 1-15: Climb of Edge dislocation and Cross Slip of Screw dislocation [31] .......... 22

Figure 1-16: Stages of Fatigue Failure [36-37] ............................................................... 25

Figure 1-17: Subset matching in DIC ............................................................................. 28

Figure 1-18: New location of pixel after deformation .................................................... 29

Figure 1-19: Approach for PHM for Thermo-mechanics, Shock and Vibration Environments [41] ........................................................................................ 32

Figure 2-1: Sn-3.0Ag-0.5Cu (wt.%) (SAC305) bulk microstructure before and after isothermal aging:(a) as assembled, unaged, and (b) after aging at 150$^{o}$ C for 1000 h [66] ................................................................................................................ 39

Figure 2-2: (a) Interface of SAC305 solder after soldering (b) Interface of solder after 500 hours of the aging (c) Interface of solder after 1000 hours of the aging [70] ....... 41

Figure 2-3: (a) Viscoplastic material behavior (a) Effect of strain rate on Stress-Strain (b) Stress Relaxation and (c) Creep ............................................................................ 48

Figure 3-1: Test Vehicle ....................................................................................................... 59

Figure 3-2: Stencil Printer ..................................................................................................... 60

Figure 3-3: Pick and Place Machine ...................................................................................... 61

Figure 3-4: Reflow oven ........................................................................................................ 61

Figure 3-5: EDS plot of Phase. .............................................................................................. 63

Figure 3-6: EDS plot of IMC. ................................................................................................ 63

Figure 3-7: Image Mapping ................................................................................................... 65

Figure 3-8: Image of IMC growth .......................................................................................... 66

Figure 3-9: SEM images of Phase Growth in (a) PBGA 256 and (b) CABGA 36 at different time intervals at 60°C (Magnification 750X) ........................................ 69

Figure 3-10: SEM images of Phase Growth in (a) PBGA 256 and (b) CABGA 36 at different time intervals at 75°C (Magnification 750X) ........................................ 70

Figure 3-11: SEM images of Phase Growth in (a) PBGA 256 and (b) CABGA 36 at different time intervals at 125°C (Magnification 750X) ...................................... 70

Figure 3-12: Normalized Phase Growth ($S_n$) versus Aging Time (t) for PBGA 256 ....... 71

Figure 3-13: Normalized Phase Growth ($S_n$) versus Aging Time (t) for CABGA 36 ...... 72

Figure 3-14: ln($a_0$) versus Aging temperature for PBGA 256 .......................................... 73

Figure 3-15: ln($a_0$) versus Aging temperature for CABGA 36 ........................................ 73

Figure 3-16: Plot of ln($b_0$) and Aging temperature for PBGA256 .................................... 74

Figure 3-17: Plot of $\ln(b_0)$ and Aging temperature for CABGA36 ..... 75

Figure 3-18: SEM images of IMC Growth in (a) PBGA 256 and (b) CABGA 36 at different time intervals at 60°C (Magnification 1000X) ..... 76

Figure 3-19: SEM images of IMC Growth in (a) PBGA 256 and (b) CABGA 36 at different time intervals at 75°C (Magnification 1000X) ..... 77

Figure 3-20: SEM images of IMC Growth in (a) PBGA 256 and (b) CABGA 36 at different time intervals at 125°C (Magnification 1000X) ..... 77

Figure 3-21: Relation between Normalized IMC Growth (Yn) and Aging Time (t) for PBGA 256 ..... 78

Figure 3-22: Relation between Normalized IMC Growth (Yn) and Aging Time (t) for CABGA 36 ..... 79

Figure 3-23: Plot of $\ln k_0$ and Aging temperature, T for PBGA 256 ..... 80

Figure 3-24: Plot of $\ln k_0$ and Aging temperature, T for CABGA 36 ..... 80

Figure 3-25: Iso-phase growth plots of Aging temperature (T) vs Aging time(t) ..... 82

Figure 3-26: Iso-IMC growth plots of Aging Time, ln(T) vs Aging Temperature ..... 83

Figure 4-1: Test vehicle ..... 90

Figure 4-2: Reflow profile ..... 91

Figure 4-3: Image Mapping ..... 93

Figure 4-4: IMC formation ..... 94

Figure 4-5: SEM images of Phase Growth in CABGA144 at different cycles at 750X magnification (a) for -50°C to 50°C (b) 0°C to 100°C and (c) 50°C to 150°C. 100

Figure 4-6: SEM images of Phase Growth in PBGA256 at different cycles at 750X magnification (a) for -50°C to 50°C (b) 0°C to 100°C and (c) 50°C to 150°C. . 100

Figure 4-7: SEM images of Phase Growth in PBGA676 at different cycles at 750X magnification (a) for -50°C to 50°C (b) 0°C to 100°C and (c) 50°C to 150°C. . 101

Figure 4-8: Relation between Normalized Phase Growth (lnSn) and Number of Cycles (lnN) for CABGA 144 ..... 102

Figure 4-9: Relation between Normalized Phase Growth (lnSn) and Number of Cycles (lnN) for PBGA 256 ..... 103

Figure 4-10: Relation between Normalized Phase Growth (lnSn) and Number of Cycles (lnN) for PBGA 676 ........ 103

Figure 4-11: Plot of $\ln a_0$ vs. inverse of mean temperature of cycling range (1/T) for phase growth ........ 104

Figure 4-12: Plot of phase growth accumulation rate (dlnSn/dlnN) vs. inverse of mean temperature of cycling range (1/T) ........ 105

Figure 4-13: Weibull Plot for CABGA 144 ........ 106

Figure 4-14: Weibull Plot for PBGA 256 ........ 106

Figure 4-15: Weibull Plot for PBGA 676 ........ 107

Figure 4-16: Plot of phase growth accumulation rate (dlnSn/dlnN) vs. Characteristic Life (Nf) ........ 108

Figure 4-17: Predictive model using Phase Growth as a damage proxy ........ 109

Figure 4-18: SEM images of IMC Growth in CABGA144 at different cycles at 1000X magnification) (a) for -50°C to 50°C (b) 0°C to 100°C and (c) 50°C to 150°C. 111

Figure 4-19: SEM images of IMC Growth in PBGA256 at different cycles at 1000X magnification) (a) for -50°C to 50°C (b) 0°C to 100°C and (c) 50°C to 150°C. 111

Figure 4-20: SEM images of IMC Growth in PBGA676 at different cycles at 1000X magnification) (a) for -50°C to 50°C (b) 0°C to 100°C and (c) 50°C to 150°C. 112

Figure 4-21: Relation between Normalized IMC Growth (lnYn) and Number of Cycles (lnN) for CABGA 144 ........ 112

Figure 4-22: Relation between Normalized IMC Growth (lnYn) and Number of Cycles (lnN) for PBGA 256 ........ 113

Figure 4-23: Relation between Normalized IMC Growth (lnYn) and Number of Cycles (lnN) for PBGA 676 ........ 113

Figure 4-24: Plot of $\ln k_0$ vs. inverse of mean temperature of cycling range (1/T) for IMC ........ 114

Figure 4-25: Plot of IMC accumulation rate ($d\ln Y_n/d\ln N$) vs. inverse of mean temperature of cycling range (1/T) ........ 115

Figure 4-26: Plot of IMC accumulation rate ($d\ln Y_n/d\ln N$) vs. Characteristic Life ($N_f$). 116

Figure 4-0-27: Predicting model using IMC as a damage proxy ........ 117

Figure 4-28: 3D plot of Error vs No. of Cycles and Normalized Phase Growth for CABGA 144 for temperature cycle $50^o$ - $150^o$ C ........................................ 122

Figure 4-29: 3D plot of Error vs No. of Cycles and Normalized Phase Growth for CABGA 144 for temperature cycle $0^o$ - $100^o$ C ........................................ 123

Figure 4-30: 3D plot of Error vs No. of Cycles and Normalized Phase Growth for CABGA 144 for temperature cycle $-50^o$ - $50^o$ C ........................................ 124

Figure 4-31: 3D plot of Error vs No. of Cycles and Normalized IMC Growth for CABGA 144 for temperature cycle $50^o$ - $150^o$ C ........................................ 125

Figure 4-32: 3D plot of Error vs No. of Cycles and Normalized IMC Growth for CABGA 144 for temperature cycle $0^o$ - $100^o$ C ........................................ 125

Figure 4-33: 3D plot of Error vs No. of Cycles and Normalized IMC Growth for CABGA 144 for temperature cycle $-50^o$ - $50^o$ C ........................................ 126

Figure 4-34: α-λ curve for Prognostication for CABGA144 at 50-150ºC (a) Using Phase growth as damage proxy and (b) Using IMC thickness as damage proxy .......... 130

Figure 4-35: α-λ curve for Prognostication for CABGA144 at 0-100ºC (a) Using Phase growth as damage proxy and (b) Using IMC thickness as damage proxy .......... 131

Figure 4-36: α-λ curve for Prognostication for CABGA144 at -50-50ºC (a) Using Phase growth as damage proxy and (b) Using IMC thickness as damage proxy .......... 131

Figure -1: Test vehicle ........................................ 137

Figure 5-2: X-Ray Image of Test Vehicle ........................................ 138

Figure 5-3: Reflow profile ........................................ 138

Figure 5-4: DIC working principle ........................................ 139

Figure 5-5: Experimental Setup ........................................ 142

Figure 5-6: Gold sputtered X–sectional image of sample ........................................ 143

Figure 5-7: Stages of image acquisition in thermal cycle ........................................ 143

Figure 5-8: Location where shear strain are measured ........................................ 144

Figure 5-9: Shear strain contours for CABGA 256 (SAC105) ........................................ 145

Figure 5-10: Shear strain contours for CABGA 144 (SAC105) ........................................ 146

Figure 5-11: Shear strain contours for CABGA 144 (SAC305) ........................................ 147

Figure 5-12: Shear strain contours for PBGA 256 (SAC305) ........................................ 148

Figure 5-13: Shear Strain Range vs Mean Temperature from Experiment .................... 149

Figure 5-14: Weibull plot for CABGA 144 (SAC 305) [112] ....................................... 151

Figure 5-15: Weibull plot for PBGA 144 (SAC 305) [112]........................................... 151

Figure 5-16: Quarter model of CABGA 144 ................................................................. 153

Figure 5-17: Quarter Model with boundary conditions ................................................. 153

Figure 5-18: Material used in model............................................................................... 154

Figure 5-19: Solder ball mesh scheme............................................................................ 155

Figure 5-20: Temperature profile used in simulation .................................................... 155

Figure 5-21: Temperature distribution during simulation for 50-150°C ........................ 156

Figure 5-22: Plastic shear strain distribution ................................................................. 157

Figure 5-23: Plastic work density distribution............................................................... 158

Figure 5-24: Location of maximum Plastic Shear Strain in critical solder joint. ........... 159

Figure 5-25: Location of maximum Plastic Work per volume in critical solder joint.... 159

Figure 5-26: Shear Strain vs Mean Temperature from Simulation................................ 161

Figure 5-27: Plastic work vs Mean Temperature from Simulation ............................... 162

Figure 5-28: Temperature Profile .................................................................................... 163

Figure 5-29: Plastic work density at different steps of thermal cycle for CABGA 256 (SAC105) ........................................................................................................ 163

Figure 5-30: Plastic work density at different steps of thermal cycle for CABGA 144 (SAC105) ........................................................................................................ 164

Figure 5-31: Plastic work density at different steps of thermal cycle for CABGA 144 (SAC305) ........................................................................................................ 164

Figure 5-32: Plastic work density at different steps of thermal cycle for PBGA 256 (SAC305) ........................................................................................................ 165

Figure 6-1: Test assembly.............................................................................................. 168

Figure 6-2: X-Ray Image of Packages .......... 168

Figure 6-3: SAC Reflow profile .......... 169

Figure 6-4: Stages of Image Acquisition in cycling .......... 170

Figure 6-5: Location where shear strain are measured .......... 171

Figure 6-6: Shear strain contour of CABGA 256 (SAC 105) at different cycle's count of 50-150$^{o}$C (a) without aging (b) with aging .......... 172

Figure 6-7: Shear strain contour of CABGA 256 (SAC 105) at different cycle's count of 0-100$^{o}$C (a) without aging (b) with aging .......... 172

Figure 6-8: Shear strain contour of CABGA 256 (SAC 105) at different cycle's count of -50-50$^{o}$C (a) without aging (b) with aging .......... 173

Figure 6-9: Effect of mean temperature and shear strain range evolution with number of cycles for CABGA 256 (SAC 105) .......... 173

Figure 6-10: Effect of prior aging on shear strain range for CABGA 256 (SAC 105)... 174

Figure 6-11: Shear strain contour of CABGA 144 (SAC 105) at different cycle's count of 50-150$^{o}$C (a) without aging (b) with aging .......... 174

Figure 6-12: Shear strain contour of CABGA 144 (SAC 105) at different cycle's count of 0-100$^{o}$C (a) without aging (b) with aging .......... 175

Figure 6-13: Shear strain contour of CABGA 144 (SAC 105) at different cycle's count of -50-50$^{o}$C (a) without aging (b) with aging .......... 175

Figure 6-14: Effect of mean temperature and shear strain range evolution with number of cycles for CABGA 144 (SAC 105) .......... 176

Figure 6-15: Effect of prior aging on shear strain range for CABGA 144 (SAC 105)... 176

Figure 6-16: Shear strain contour of CABGA 144 (SAC 305) at different cycle's count of 50-150$^{o}$C (a) without aging (b) with aging .......... 177

Figure 6-17: Shear strain contour of CABGA 144 (SAC 305) at different cycle's count of 0-100$^{o}$C (a) without aging (b) with aging .......... 177

Figure 6-18: Shear strain contour of CABGA 144 (SAC 305) at different cycle's count of -50-50$^{o}$C (a) without aging (b) with aging .......... 178

Figure 6-19: Effect of mean temperature and shear strain range evolution with number of cycles for CABGA 144 (SAC 305) .......... 178

Figure 6-20: Effect of prior aging on shear strain range for CABGA 144 (SAC 305)... 179

Figure 6-21: Shear strain contour of PBGA 256 (SAC 305) at different cycle’s count of 50-150$^{o}$C (a) without aging (b) with aging ........................................................ 179

Figure 6-22: Shear strain contour of PBGA 256 (SAC 305) at different cycle’s count of 0-100$^{o}$C (a) without aging (b) with aging ......................................................... 180

Figure 6-23: Shear strain contour of PBGA 256 (SAC 305) at different cycle’s count of -50-50$^{o}$C (a) without aging (b) with aging ......................................................... 180

Figure 6-24: Effect of mean temperature and shear strain range evolution with number of cycles for PBGA 256 (SAC 305) ...................................................................... 181

Figure 6-25: Effect of prior aging on shear strain range for PBGA 256 (SAC 305)...... 181

Figure 6-26: Effect of solder alloy composition and package geometry on shear strain range (without prior aging) ..................................................................... 182

Figure 6-27: Effect of solder alloy composition and package geometry on shear strain range (with prior aging) ........................................................................ 182

Figure 6-28: Shear stress-strain hysteresis loop of PBGA 256 (SAC305) for pristine condition ............................................................................................ 187

Figure 6-29: Shear stress-strain hysteresis loop of PBGA 256 (SAC305) after 2 months aging or after 1700 cycles in 50-150$^{o}$ C. ........................................................... 188

Figure 6-30: Shear stress-strain hysteresis loop of PBGA 256 (SAC305) after 4 months aging or after 2700 cycles in 50-150$^{o}$ C. ........................................................... 188

Figure 7-1: Characteristic Life (Nf) vs. Shear Strain Range ($\Delta e_{xy}$)............................... 192

Figure 7-2: Remaining Useful Life vs. Shear Strain Range plot .................................. 194

Figure 7-3: $N_i$ (Cycles to crack initiation) vs. Plastic Work Density ($\Delta$W).................... 198

Figure 7-4: Crack Growth Rate (da/dN) vs. Plastic Work Density ($\Delta$W) ...................... 199

Figure 7-5: Phase growth based life model.................................................................. 200

Figure 7-6: Plastic Work Density vs. Phase growth rate ............................................... 201

Figure 7-7: IMC growth based life model ..................................................................... 203

Figure 7-8: Plastic Work Density vs. IMC growth rate .................................................. 204

List of Tables

Table 1-1: Performance Characteristics of Solder Alloys ................................................11

Table 1-2: Pass-fail criteria used by NCMS [13]............................................................12

Table 2-1: Summary of Solder Joint Fatigue Models [89] ...............................................52

Table 3-1: Package features ...............................................................................................58

Table 3-2: Normalized Phase Growth Coefficients and Exponents for the PBGA 256 ....72

Table 3-3: Activation Energy of Phase Growth................................................................75

Table 3-4: Normalized IMC Growth Coefficients............................................................79

Table 3-5: Activation Energy for IMC Growth Coefficient .............................................81

Table 3-6: Validity of damage mapping model based on Phase Growth ..........................85

Table 3-7: Validity of damage mapping model based on IMC Growth ...........................86

Table 4-1: Package features ...............................................................................................90

Table 4-2: Normalized Phase Growth Coefficients and Exponents ................................104

Table 4-3: Activation energy of phase growth ................................................................105

Table 4-4: Characteristic life ...........................................................................................107

Table 4-5: Relation between Phase Growth Accumulation Rate and Characteristic life 108

Table 4-6: Comparison of experimental results and results from predictive model using Phase Growth as a damage proxy ..........................................................................110

Table 4-7: Normalized IMC Growth Coefficients and Exponents .................................114

Table 4-8: Activation energy for IMC growth ........ 115

Table 4-9: Relation between IMC Accumulation Rate and Characteristic life ........ 116

Table 4-10: Comparison of experimental results and results from predictive model using IMC Growth as a damage proxy ........ 118

Table 4-11: Damage mapping relationship for CABGA 144 ........ 119

Table 4-12: Damage Equivalency relationship for CABGA 144 ........ 119

Table 4-13: Damage mapping relationship for PBGA 256 ........ 119

Table 4-14: Damage Equivalency relationship for PBGA 256 ........ 120

Table 4-15: Damage mapping relationship for PBGA 676 ........ 120

Table 4-16: Damage Equivalency relationship for PBGA 676 ........ 120

Table 4-17: Comparison of results obtained from experiment and prognostication for 50$^{o}$ - 150$^{o}$ C ........ 126

Table 4-18: Comparison of results obtained from experiment and prognostication for 0$^{o}$ - 100$^{o}$ C ........ 127

Table 4-19: Comparison of results obtained from experiment and prognostication for -50$^{o}$ – 50$^{o}$ C ........ 127

Table 4-20: Comparison for Prognostics Metrics for Three Thermal Cycling Conditions. ........ 133

Table 5-1: Package Attributes ........ 136

Table 5-2: Summary of experimental results ........ 148

Table 5-3: Anand’s Constant [25] ........ 160

Table 6-1: Package attributes ........ 167

Table 6-2: Shear Strain range value for CABGA 256 (SAC 105) ........ 184

Table 6-3: Shear Strain range value for CABGA 144 (SAC 105) ........ 184

Table 6-4: Shear Strain range value for CABGA 144 (SAC 305) ........ 184

Table 6-5: Shear Strain range value for PBGA 256 (SAC 305) ........ 185

Table 6-6: Anand's constant for SAC 305 under aging condition of 125$^{o}$C [128]..........187

Table 6-7: Shear strain range values from simulation ....................................................189

Table 7-1: Life and shear strain for CABGA 144 (SAC305) and PBGA 256 (SAC305) ..........................................................................................................192

Table 7-2: Coffin-Manson constant value .......................................................................193

Table 7-3: Results from damage mapping model based on phase growth damage proxy ...............................................................................................................195

Table 7-4: Results from damage mapping model based on IMC growth damage proxy 196

Table 7-5: Characteristic life and Plastic work under different thermal conditions. .......197

Table 7-6: Required values for data fit ............................................................................201

Table 7-7: Results from life model based on Phase growth ............................................202

Table 7-8: Required values for data fit ............................................................................203

Table 7-9: Results from life model based on IMC growth .............................................204

Table 7-10: Results from RUL prognostic Model based on Phase Growth ....................206

Table 7-11: Results from RUL prognostic Model based on Phase Growth ...................207

Table 7-12: Results from RUL prognostic Model based on IMC Growth ......................208

Table 7-13: Results from RUL prognostic Model based on IMC Growth ......................209

# Chapter 1

# Introduction

## 1.1 Electronic Packaging Overview

Electronic packaging is an art of establishing interconnections between various levels of electronic devices, components, modules, and the system [1]. Electronic packaging can also be defined as an engineering and art of providing signal and power connections to the active components of an electronic circuit and protecting that circuit adequately from environments [2]. Electronic packaging serves multifold function of providing power and signal interconnection, heat dissipation, mechanical support, and a secured environment by preventing contamination, mechanical damage, and electromagnetic interference etc. But as ICs are becoming increasingly more complex as prophesized by Moore's Law [3], these functions are becoming increasingly difficult. Moore's Law states that the transistor density on an IC will double every 18 months. As an example, in 1971 Intel's 4004 chip had 2,250 transistors while in 2003 the Intel Itanium 2 Processor had 410 million transistors. With the increase in transistor density number of interconnections coming from the chip is also increasing. The International Technology Roadmap for Semiconductor (ITRS) 2007 Edition calls for a maximum interconnect count 600-2140 interconnects in 2007 to increase to 720-3367 interconnect by 2012 for cost performance packages. Figure 1-1 shows the trend of high volume package manufacturing technology [4].

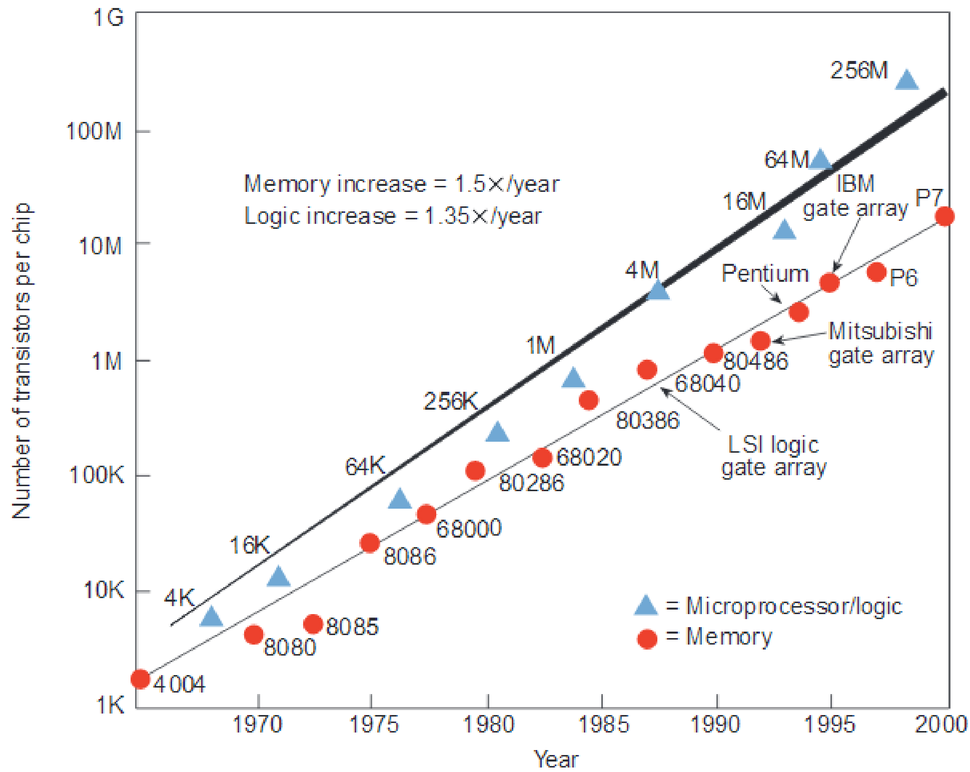


Figure 1-1: General Evolution of Electronic packaging density [4]

## 1.2 Packaging Design

In general an electronic packaging can be divided into three levels (Figure 1-2); device packaging, board packaging, and system packaging.

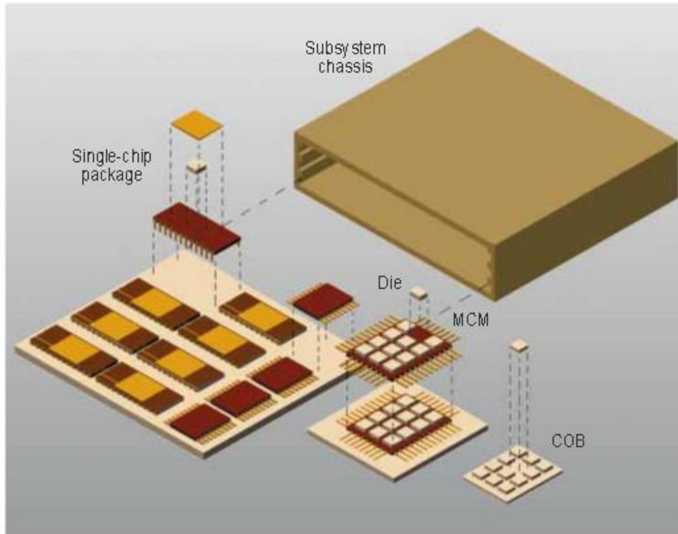


Figure 1-2: Three levels of packaging: the device is packaged into a component, the component is mounted on the board, and the board is installed into the subsystem chassis (MCM = multichip module, COB = chip-on-board)[5].

Each level of packaging provides similar functions but has a distinct purpose and design. Device packaging protects the integrated circuit from corrosion and dissipates heat, creating a component with an electrical interface and mechanical support for installation and testing. The printed wiring board or substrate provides support and interconnection of the device packages to create electronic sub-functions suitable for higher-level testing. Box-level packaging allows for electronic interconnection between the circuit substrates, and performs housing and interfacing (such as connectors or keyboards) to the outside world. [5]

### 1.3 Packaging Technology

Through-hole packaging was the most effective and popular technology at the early stage of microelectronics manufacturing. But with the advent VLSI (Very Large Scale Integration) technology and soaring demand of more and more functionality with limited

space, through-hole technology is at the edge of extinction now, and Surface Mount Technology (SMT) has been evolved as a replacement. Invention of sophisticated very high volume manufacturing facility also triggered this transition. Surface mount technology allows direst attachment of packages on the board through solder joints, thereby saves more surface area for additional components and reduce the electrical parasitic due to shorter interconnect length. Now different versions of interconnection geometries such as Pin Grid Array (PGA), Ball Grid Array (BGA), Column Grid Array (CGA) etc. have been used depending upon the types of final usage.  Figure 1-3 shows the evolution of packaging densities over time. In the late 1990s, industry introduced wafer level packaging, which resulted in many revolutionary advances such as chip-on-board (COB), tape-automated bonding (TAB), and multichip modules (MCMs). These technologies represent the next step in the evolution of packaging [6].

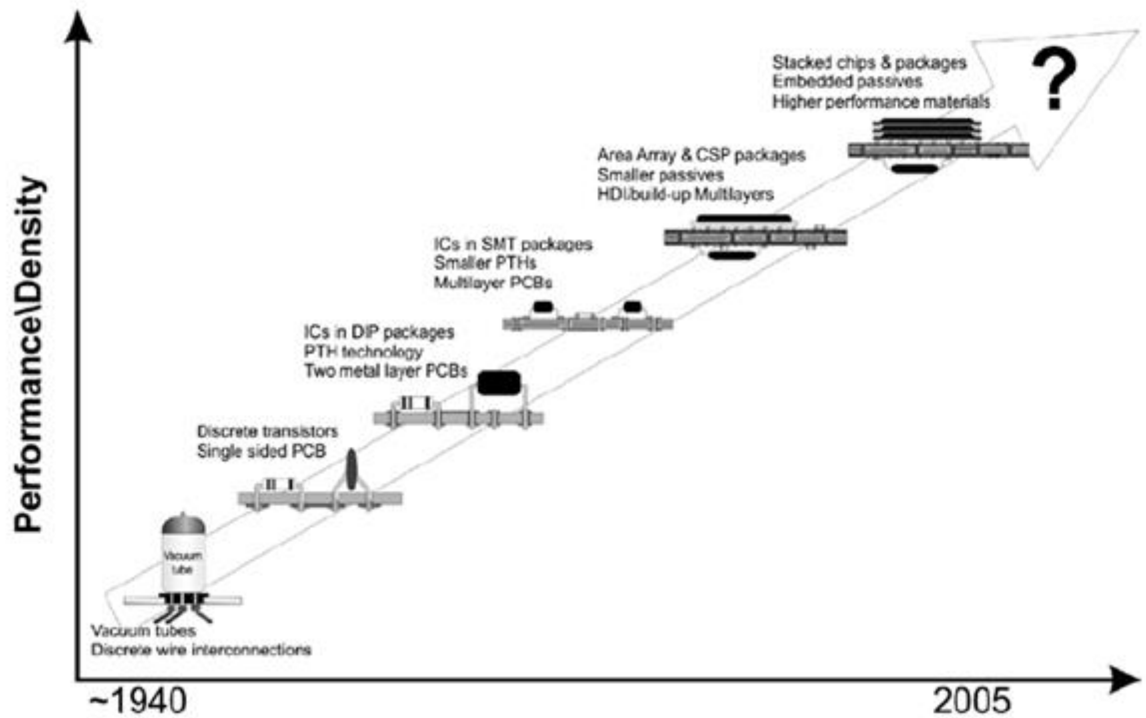


Figure 1-3: Packaging Densities over Time [6]

Ball Grid Array (BGA) and Chip Scale Package (CSP) being the most prevalent package types in portable hand held consumer electronics, meet most of the requirement of today's microelectronics industry. Using CSP technology, package size can be shrink down to silicon size ratio of 1.2, which helps more and more miniaturization of devices. BGAs have multifaceted advantages by having robust balls at higher pitches instead of fragile leads like QFP, along with elimination of co-planarity issues and truly amazing self-alignment capability during reflow even if they are misplaced by 50%. Due to this self-alignment capability, a BGA that is not properly placed will float back to its optimal position on the solder lands due to surface tension forces. BGA technology also helps obtaining higher I/O count for a given substrate area, reduction in size, weight and cost. Due to its simplified manufacturing process, it can extend to multichip modules like 3-D

Packaging. Another very important advantage of BGA is it allows heat to flow freely resulting in better heat dissipation.

### 1.4 Plastic Ball Grid Array Packages

BGAs are available in different types, from plastic overmolded BGA (also called PBGA) to flex tape BGAs (TBGA), high thermal metal top BGAs with low profile (HL-PBGA) and high themal BGA (H-PBGA). Plastic Ball Grid Array is a type of BGA with plastic molded body. Its size may range from 7 to 50mm with ball pitches of 1, 1.27 and1.5 mm. PBGA pin counts range from 16 to 2401. It is a laminate based substrate package where die is attached to the substrate made of two-metal layer copper clad Bismaleimide triazene (BT) laminate which has high glass transition temperature and is the most commonly used resin for PBGA . The inner connections are made either with wire bond or by the flip chip interconnection. The complete assembly is then over molded and the solder ball is formed to build the package. It is a low cost and low profile package. The lead coplanarity allowed by JEDEC standards is 0.006inch for smaller BGA's and 0.008inch for larger BGA's(1.27mm to 1.5mm pitches), because the larger PBGA packages are more susceptible to warpage than the smaller packages.

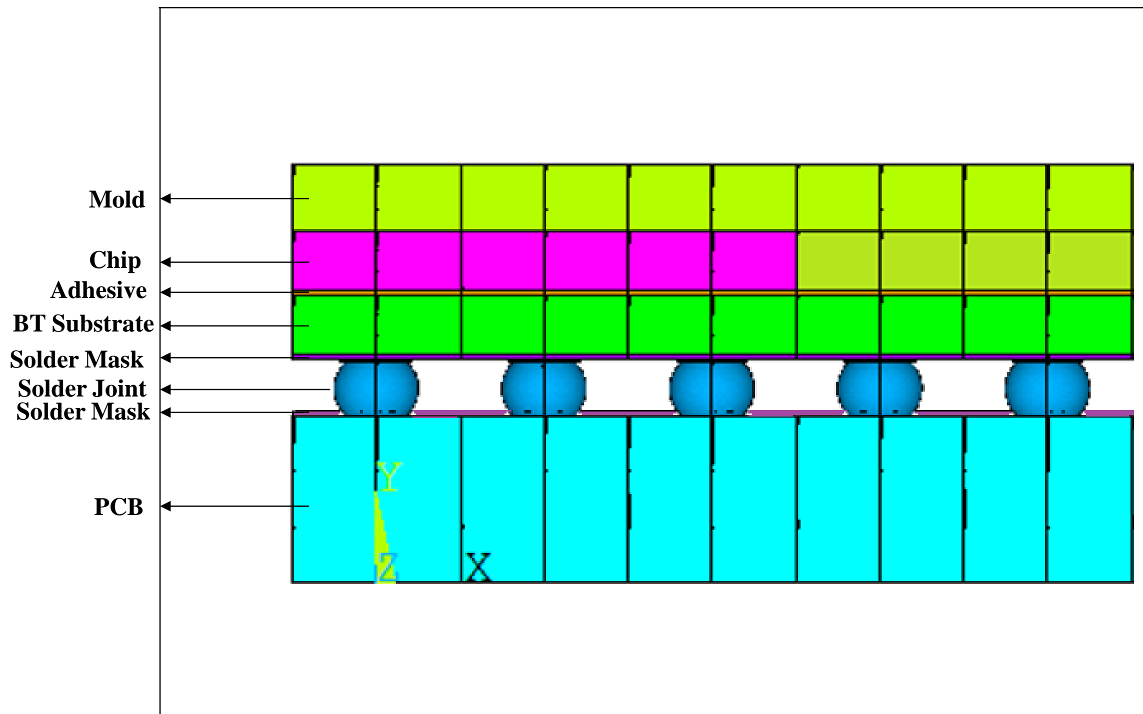


Figure 1-4: Schematic of a typical PBGA package

For the assembly of PBGA, general industry practice is to have stencil opening diameter equal to PCB pad diameter which provides better gasketting effect while doing stencil printing. Normally 0.1 to 0.2 mm thick stencils are commonly used, but it can be thicker for larger sized PBGASs. There are two types of pad configurations used for PBGAs, Solder mask defined (SMD) and non-solder mask defined (NSMD). Each design has its own advantages and drawbacks. But the biggest issue for SMD is the sharp edges formed in the solder balls where stress concentrations can occur. Examples of these two types of solder mask pads are in Figure 1-5.

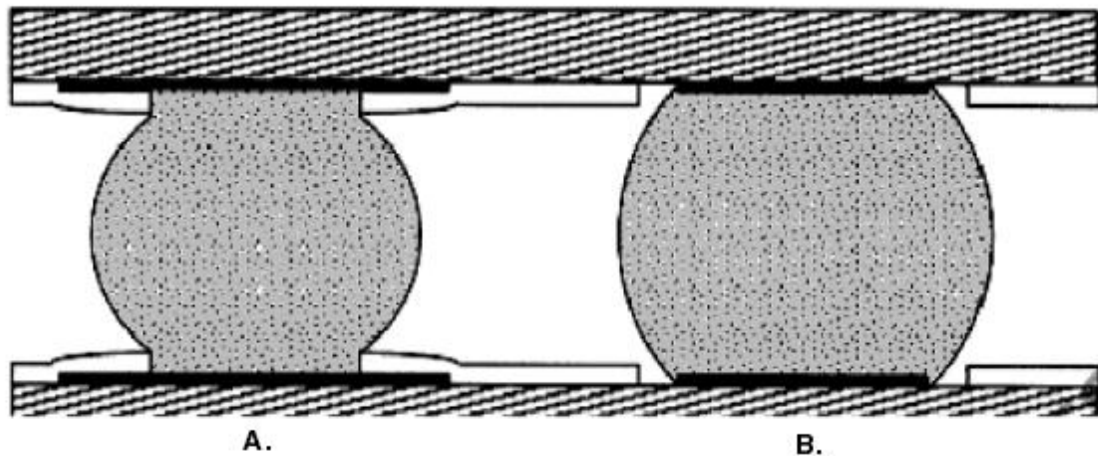


Figure 1-5: A. Solder Mask Defined, and B. Non Solder Mask Defined [7]

### 1.5 Reliability

Electronic Packages are delving more and more into extreme environment regime not only due to ambient temperature profile imposed, but also due to increased power density and more I/O's to satisfy increasing miniaturizing trends. A bunch of reliability issues arose due to the extreme environments, some of them are mentioned below.

1. Package materials can be exposed to high temperature or temperature fluctuation due to high power density devices or extreme ambient environments.
2. Thermally induced stresses which occur due to large mismatches in the coefficients of thermal expansion of the various materials in the package.
3. Stresses can also occur due to mechanical loading caused by the rest of the product containing the package or due to shock and vibration.
4. Packages may also be exposed to moisture and corrosive environments.

An electronic package is an assembly of different components like silicon die, copper pad, substrate, mold, solder joint etc. from materials ranging from metals to polymer or resin

sandwiched together. Each material widely varies in their physical and mechanical properties like Coefficient of Thermal Expansion (CTE), Young's Modulus (E), poison's ratio (ν), etc. Whenever a device starts operation or is exposed to surroundings, change in temperature induces thermal expansion mismatches among different components of packages, thereby creates cyclic shearing loads on the solder interconnects (BGA joints), eventually leading to fatigue failure. The major role player in this regard is the difference of CTE between silicon die (2.5ppm/ $^{o}$C) and substrate (20ppm/ $^{o}$C). The stiffer silicon die lowers the effective CTE in the substrate region, which increases the CTE mismatch between the printed circuit board and the substrate. This increased CTE mismatch causes more stress and deformation in the presence of thermal loads and this stress and deformation is in turn taken up by the solder ball, leading to a shortened fatigue life of the interconnect [8]. Cracking most often occurs in the neck of the solder ball and also at the lower side of the solder ball where the stress concentration is high. Apart from that, die fracture, severing of interconnections, wire bond failure, delamination of material interfaces, encapsulant cracking etc. are some of other types of common failure to be named. Extensive research has been going on to find the way to reduction of stress on solder joints to improve reliability, some of them are developing substrates with matching CTE thereby minimizing CTE difference in substrate and package, using underfill that strengthen solder ball during shearing and developing substrate with compliant top layers that can absorb some stress.

Solder Joint failure has emerged to be one of the predominant failure mode. Therefore, in this thesis thermo-mechanical reliability of solder joint has been studied.

## 1.6 Soldering Alloy

Anything with lead has inherent toxicity problems. It is hazardous both to personal safety and environment. Lead poisoning can occur when lead enters body through inhalation or ingestion, even with dermal contact. Even it can leach into drinking water if not disposed properly. To restrict its usage Restriction of Hazardous Substances (RoHS) directives was adopted by European Union in February 2003. Due to this, now industry has to move from Tin-Lead solder to lead free option although SnPb has been used more than thousand years for some of its advantages like low melting point, better wettability and malleability, availability and cost. In the course of extensive research to find the best substitute for SnPb, SAC which is a tin, silver, and copper alloy, emerged as better options until now. SAC alloys took the largest market share in industry due to their low melting temperatures and superior mechanical and solderability properties. Despite all its benefits and high market share, SAC alloys still are not a perfect Pb-free solder replacement due to some noticeable shortcomings like:

(1) SAC alloys have higher melting points than eutectic Sn–Pb

(2) SAC alloys are prone to excessive growth of intermetallic compounds at the interface between solder joints and copper pad, which can cause reliability problems [9, 10, 11];

(3) SAC alloys have higher material costs.

## 1.7 Performance Characteristics of Solder Alloys

Any alloy must pass through some stringent performance screening to be qualified to be used as solder alloy in industry (Table 1-1). First, it must have low melting temperature which can directly affect the other components of an electronic package and also the entire manufacturing process and cost involved. Second, it should meet the expected levels of

electrical and mechanical properties. Third, it should be able to adequately wet PCB lands. Also it should offer better reworkability and ease to inspection. Last, it must be economical and not significantly increase assembly cost. A summary of performance characteristics of solder alloys is listed in Table 1-1 [12]. Manufacturability describes to what extent a solder alloy suites current electronics packaging practices. Reliability is the dependability of solder joint under service condition. The thumb rule for selecting a potential Pb-free alternative soldering materials is to ensure that the properties of the alternative solders are superior or at least comparable to Sn-Pb solders.

Table 1-1: Performance Characteristics of Solder Alloys

| Manufacturability | Reliability |
|---|---|
| Melting/liquidus temperature | Electrical conductivity |
| Wettability (of copper) | Thermal conductivity |
| Cost | Coefficient of thermal expansion |
| Environmental friendliness | Shear properties |
| Availability and number of suppliers | Tensile properties |
| Manufacturability using current processes | Creep properties |
| Ability to be made in balls | Fatigue properties |
| Copper pick-up rate | Corrosion resistance |
| Recyclability | Oxidation resistance |
| Ability to be made into paste | Intermetallic compound formation |

In 1997 The National Center for Manufacturing Science (NCMS) developed a pass-fail criterion for deferent candidate alloys as shown in following table:

Table 1-2: Pass-fail criteria used by NCMS [13]

| Solder Property | Definition | Acceptable Levels |
| --- | --- | --- |
| Liquidus Temperature | Temperature at which solder alloy is completely molten. | <225ºC |
| Pasty Range | Temperature difference between solidus and liquidus temperatures; temperature range where the alloy is part solid and part liquid. | <30ºC |
| Wettability | A wetting balance test assesses the force resulting when a copper wire is immersed in and wetted by a molten solder bath. A large force indicates good wetting, as does a short time to attain a wetting force of zero and a short time to attain a value of two-thirds of the maximum wetting force. | $F_{max}>300\mu N$<br><br>$t_0<0.6s$ and $t_{2/3}<1$ s |
| Area of Coverage | Assesses the coverage of the solder on Cu after a typical dip test. | >85% coverage |
| Drossing | Assesses the amount of oxide formed in air on the surface of molten solder after a fixed time at the soldering temperature. | Qualitative scale |
| Thermo -mechanical Fatigue | Cycles-to-failure for a given percent failed of a test population based on a specific solder-joint and board configuration, compared to eutectic Sn-Pb. | Some percentage, usually>50% |

| Coefficient of Thermal Expansion (CTE) | | $<2.9 \times 10^{-5}/^{o}C$ |
|---|---|---|
| Creep | Stress required at room temperature to cause failure in 10,000 minutes. | >304MPa |
| Elongation | Total percent elongation of material under uniaxial tension at room temperature. | >>10% |

**1.8 Sn-Ag-Cu (SAC) Series Alloys**

In the long search of Pb free alternatives, scientists came out with a number of viable candidates such as Sn-Zn, Sn-Cu, Sn-Bs, Sn-In, Sn-Ag and various other systems. But until now there is no best choice which can better serve all applications. However, the Sn–Ag–Cu (SAC) series came out to be the most promising replacement. But in case of SAC also not a single composition works for all application. While one is good for thermal cycling, ends up poorly in drop and shock regime, and there are different versions of SAC alloys which have been experimented and adopted by electronics manufacturers for wide range of usages. NCMS and iNEMI led the early research endeavor on SAC alloys. Out of different compositions available the most popular versions are [14];

-Sn+3.9%Ag+0.6%Cu (iNEMI recommended)

-Sn+3.5%Ag+0.7%Cu

-Sn+3% Ag+0.5%Cu (JEITA recommended)

Due to ongoing research a large variety of SAC and non-SAC lead free versions emerged. Each version suites a specific usage profile. So the entire spectrum of composition can be grouped into some few distinct families as;

1. The near-eutectic tin-silver-copper alloys (SAC305, SAC387, and SAC405). These alloys perform well in thermal cycling, while showing comparable performance in drop and shock resistance. Other important qualities include shininess for automatic and reasonable reflow performance.
2. The second group is low silver alloys such as SAC105 and SAC0307. These alloys are well suited for drop and shock performance. The trade-off with less silver is decreased thermal cycling performance and also high melting point.
3. To improve the properties of the second family of alloys, additional metallic constituents are added in small amounts. This kinds of alloys constitute the third group. These are generally identified as SACX in industry.
4. Another group of alloys worth considering, but does not fit into above categories can be described as non-SAC alloys. Such as BiSnAg (Indalloy® 282) which has favorable properties for many applications. Its liquidus is 140°C, noticeable improvement if compared with SAC alloy having liquidus at approximately 220°C. It is especially suitable for temperature-sensitive applications or for attaching additional components after primary board assembly. However, BiSnAg alloys do not have acceptable drop shock performance for mobile products [15]

### 1.9 SAC Phase Diagram

Finding out the eutectic melting temperature of SAC alloys became researchers' main focus since the time it stands out to be the only viable alternative to Sn-Pb. Addition of Cu in SAC system helps lowering the melting temperature and improving wettability [16]. The melting point of near eutectic SAC alloys is 217 °C, lower than the melting temperature of

the binary eutectic 96.5Sn–3.5Ag at 221 °C. Miller et al. in 1994 [17] first discovered the eutectic composition of SAC series alloys using DTA. The eutectic point was 4.7 wt.% Ag and 1.7 wt.% Cu in the ternary system with a melting temperature of 217°C. In the year 2000, Loomans and Fine [18] came out with a refined version of this with 3.5 wt.% Ag and 0.9 wt.% using thermal analysis of monovariant Sn-Cu and Sn-Ag binary eutectics. Then Moon, et al. [19] confirmed that by using thermal analysis, simulated DTA curves and thermodynamic calculations. The final version of melting point of the ternary system is 217.2 ± 0.2 °C with 2σ standard deviation. The resulting 3-D ternary phase diagram of SAC system is illustrated in Figure 1-6.

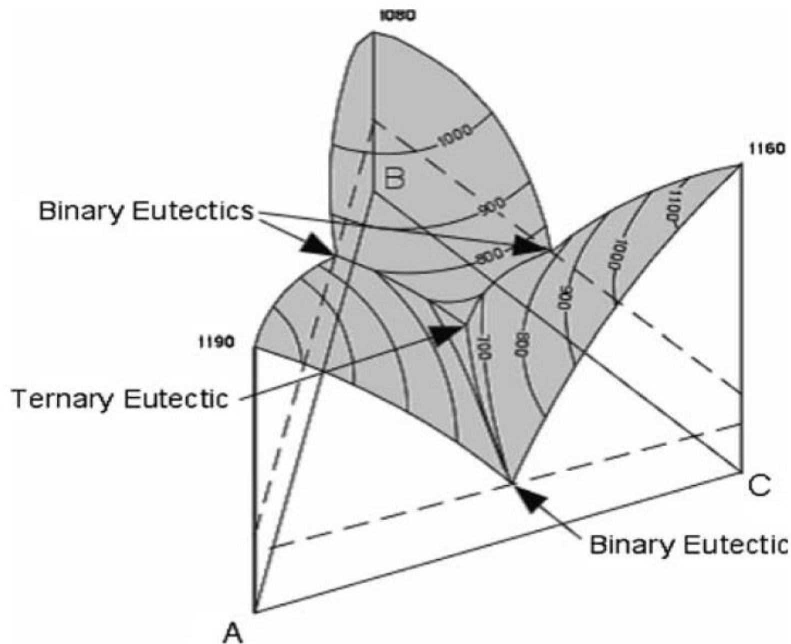


Figure 1-6: Typical 3-D Ternary Phase Diagram [20]

The contours on the top surface in Figure 1-6 (shaded area) represent isothermal lines and the lowest point where all the isothermal lines converge, is the eutectic point of the ternary system. The eutectic reaction can be written as:

$L \rightarrow Ag_3Sn + Cu_6Sn_5 + Sn$ (Matrix)

The entire ternary phase diagram is a fusion of three binary phase diagrams of Sn-Ag, Sn-Cu and Ag-Cu. Figure 1-7 shows the top view of the ternary phase diagram where the red boundary region represents the near eutectic region or the % amount of Ag and Cu needed to form near eutectic composition.

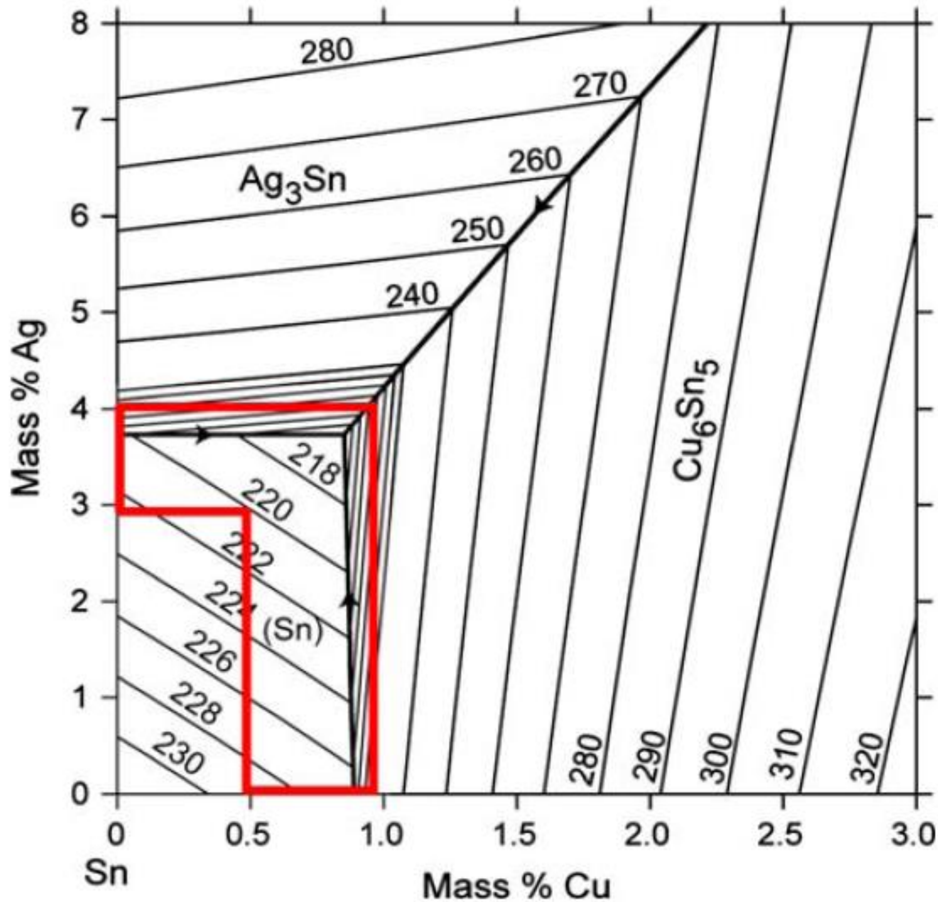


Figure 1-7: Top View of Sn–Ag–Cu Ternary Phase Diagram [21]

In SAC alloys, the formation of intermetallic compounds between the primary elements Sn and Ag, and Cu affect all the properties of the alloys [22]. There are three possible intermetallic compounds that may be formed: $Ag_3Sn$ forms due to the reaction between Sn and Ag as shown in Figure 1-8 (a) and $Cu_6Sn_5$ forms due to the Sn and Cu reaction as shown in Figure 1-8 (b), but $Cu_3Sn$ will not form at the eutectic point unless the Cu content is high enough for the formation of $Cu_3Sn$ at higher temperatures. So according to Ma et. al. $Cu_3Sn$ is not present in bulk specimens. [22]

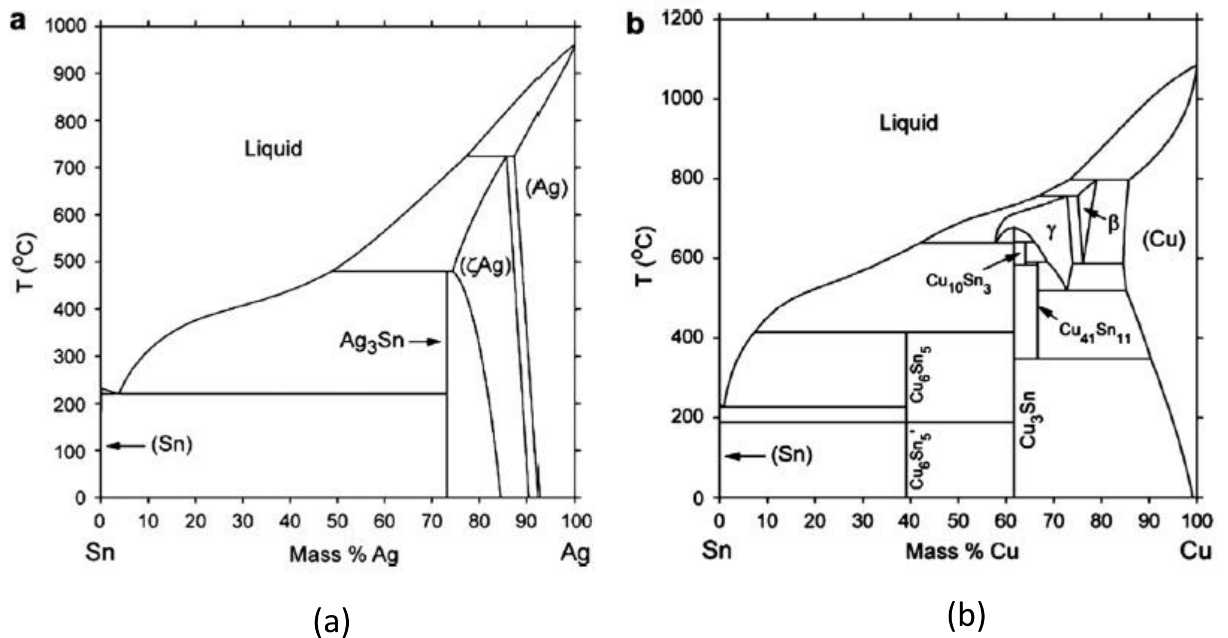


Figure 1-8: Binary phase diagram (a) Sn–Ag and (b) Sn–Cu. [23]

### 1.10 Mechanical Properties and Failure of Soldering Materials

Reliability of solder joints are heavily influenced by electrical, thermal and mechanical properties of the joint. The relevant solder properties are crucial to the reliability issue in electronics packaging. Failures on solder joints can be classified into three, electrical, mechanical, or corrosion induced. But the fatigue and/or fracture induced failure is the most dominant one, which leads to unexpected device or service shut down without

showing any prior symptom. This kind of failure, usually known as thermo-mechanical failure is the result of inherent mismatch of CTE (coefficient of thermal expansion) among the various components like metals, polymers, composites etc. Heat, generated every time an electronic product is powered on make the entire assembly to contract or expand un-uniformly and finally develop thermal stress. Whenever an electronic assembly is subjected to temperature change, the solder joint is subjected to shearing to compensate for the CTE mismatch mainly between substrate and die, as shown in Figure 1-9.

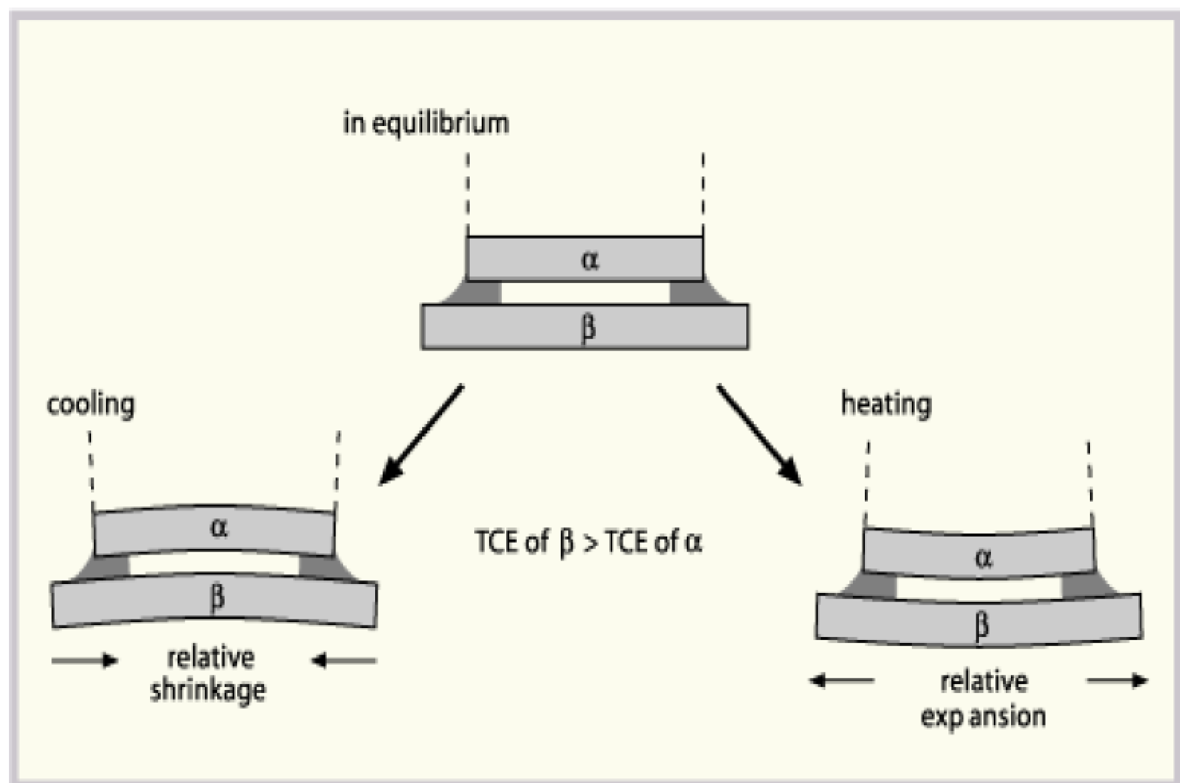


Figure 1-9: Cyclic Stress Induced by CTE Mismatch [24]

The governing factors influencing reliability the most have been identified as the CTE mismatch, the range of temperature variation, solder joint distribution and geometry, and the solder alloy elastic-plastic and creep constitutive relationships.

### 1.11 Tensile Properties

Whenever an electronic package is on, its solder joints are subjected to shear deformation. This shear always accompanies tensile loading as shown in Figure 1-10 as a result of substrate or PCB flexing.

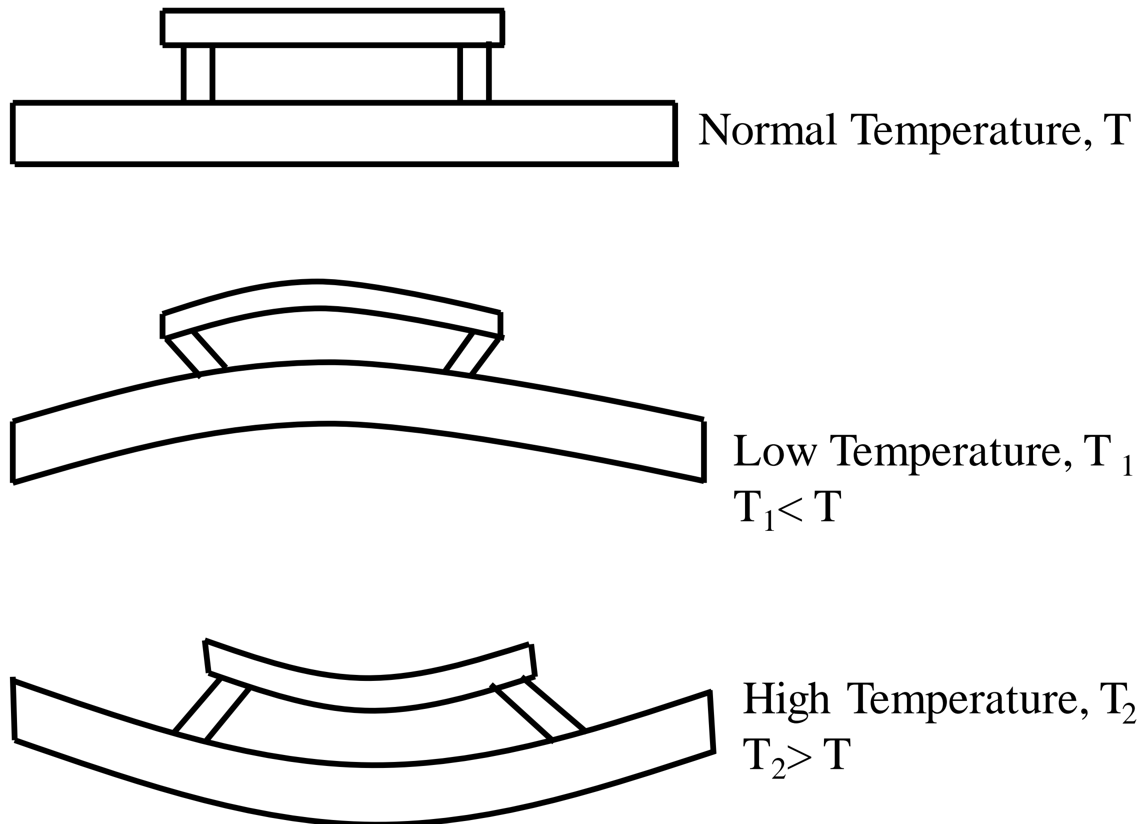


Figure 1-10: Solder Joints Subjected to Tensile Loading due to Substrate Flexing

Therefore, the information about various tensile properties of solder joint like yield strength, ultimate tensile strength and elastic modulus are very important in determining the extent of tensile deformation a solder joint can sustain prior to failure. A typical engineering stress-strain curve of Pb-free solders is shown in Figure 1-11 along with all important mechanical properties of solder materials.

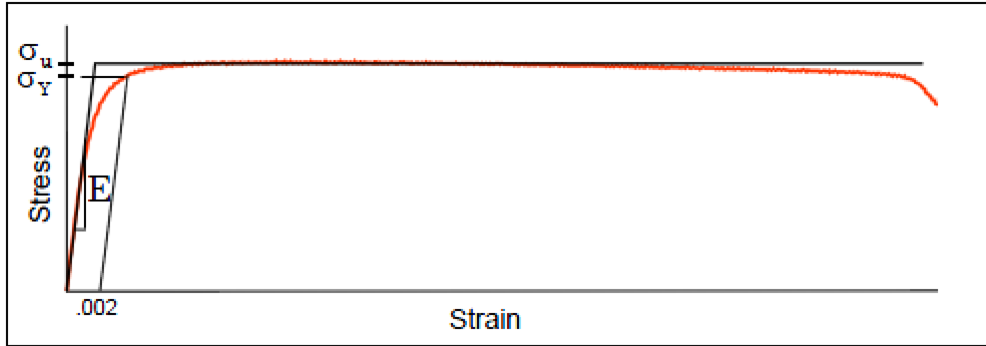


Figure 1-11: Typical Stress-Strain Curve of Pb-free Alloys [25]

### 1.13 Creep

Creep is time dependent deformation when a material is subjected to stress for a prolonged period of time, but theoretically it can occur at any temperature above absolute zero. But Creep failure becomes a significant factor at a particular temperature called as Homologous temperature defined as 0.5 of melting temperature. As common solders are low temperature alloys, development of creep becomes significant even at subzero temperature. Temperature and amount of load are dominant factors in creep. For most materials, creep develops in three stages, primary, secondary and tertiary creep. A typical creep curve for solder is shown in Figure 1-12.

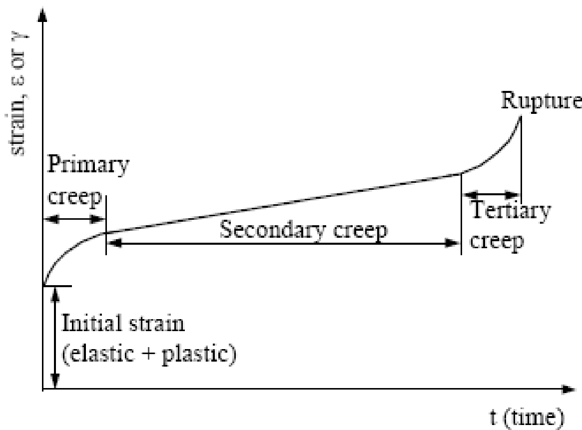


Figure 1-12: Creep Curve under Constant Stress/Load and Temperature [26]

The creep response begins with an initial instantaneous strain, which consists of elastic or time-independent plastic deformation as soon as the constant load is applied [27, 28]. The creep deformations then occur which typically are divided into three regions or stages as discussed below:

Stage I (Primary Creep): In this stage, the creep strain rate (dε/dt) decreases rapidly over time due to strain hardening, Strain Hardening (happen at low temperature or less than $0.4T_m$) is the strengthening of a metal by plastic deformation. Before Strain or work hardening, the lattice of the material exhibits a regular, nearly defect-free pattern. As the material is strained more and more it becomes increasingly saturated with new dislocations (Dislocations are areas where the atoms are out of position in the crystal structure), which prevent new dislocations from nucleating (a resistance to dislocation-formation develops). This is called work hardening, which manifests itself as a resistance to plastic deformation and results in decreasing creep strain rate (dε/dt).

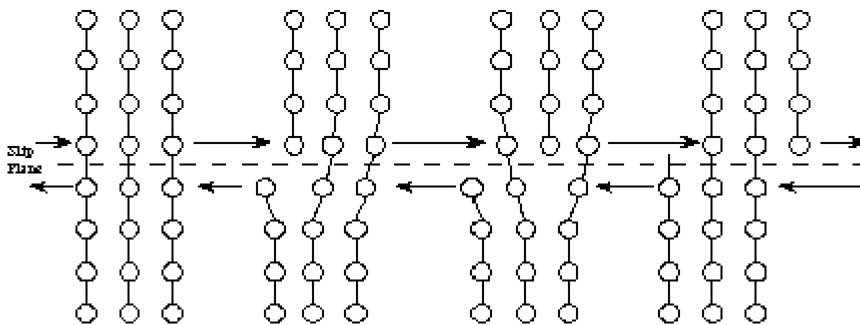

Figure 1-13: Creation and propagation of dislocation [29]

Stage II (Secondary Creep or Steady-State Creep): In this stage, the creep strain rate is relatively stable (linear part of the curve) as strain hardening and recovery softening reach a dynamic balance. At higher temperatures, the stress – strain curve becomes flat which

means the strain hardening rate is close to zero. In hardening, flow stress increases due to dislocation storage, whereas in softening flow stress decreases due to dislocation annihilation resulting from cross slip and/or climb of dislocations.

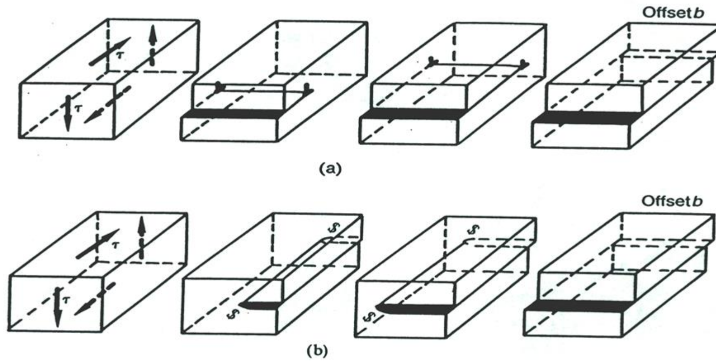


Figure 1-14: Macroscopic deformation of a cube produced by glide of (a) Edge dislocation and (b) Screw dislocation [30]

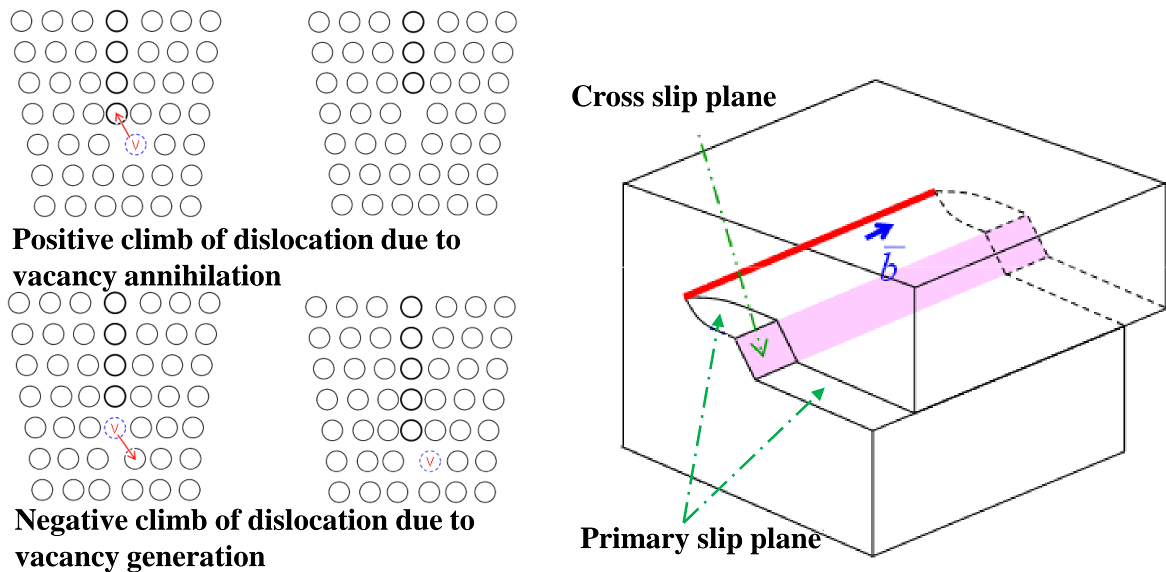


Figure 1-15: Climb of Edge dislocation and Cross Slip of Screw dislocation [31]

Stage III (Tertiary Creep): Tertiary creep is characterized by an accelerated creep rate, which may be caused by various weakening metallurgical instabilities such as localized

necking, corrosion, inter-crystalline fracture, formation of microvoids etc. [32]. Eventually, at the end of this stage, rupture occurs. As most of the solder alloy have low melting temperature, they are subjected to creep even at normal operating conditions due to high homologous conditions (> 0.5Tm). Therefore, stress level is very influential factor in dictating creep deformation mechanism. At low stress levels, creep takes place by lattice diffusion and grain-boundary diffusion. Diffusion creep occurs through diffusion of atoms within a grain. As the stress rises creep phenomena is dictated by dislocation which is a motion of dislocation through gliding in slip plane. Additionally, grain boundary gliding also contributes to all these stages mentioned above [33].

## 1.14 Fatigue

Solder joints in electronic assemblies are often subjected to cyclic loadings due to temperature fluctuation or on-off cycles. This thermal fatigue is the most detrimental effect a manufacturer has to consider to project its operational life span. Fatigue failure usually occurs at stress levels lower than the material's yield stress. Fatigue is responsible for a large percentage of failures of engineering materials. Fatigue failure is expedited by localized stress concentrations. As the thermal cycling is going on, micro-cracks will initiate at the spots of high stress concentration. This newly generated crack tips themselves act as stress raisers and make situation more suitable for crack propagation. This continuing process reduces cross sectional area more and more to such a point where it can no longer support the applied load, culminating in a sudden and catastrophic failure. The fatigue damage is cumulative, and the materials will not recover after load removal. This kind of failure is brittle like and involves very little plastic deformation. There are three stages for a fatigue failure to fully develop and occur [32].

Stage 1: (Crack nucleation): Once initiated, fatigue crack propagates along high shear stress planes (45 degrees).

Stage 2: When stress intensity increases due to crack growth or higher applied stress, slips starts to develop in different planes close to crack tip, but in this stage crack propagates at 90 degrees to applied load while it is 45 degrees at stage 1. This stage has two steps:

Step I: Slow propagation along crystal planes with high resolved shear stress and it has flat fracture surface.

Step II: Faster propagation perpendicular to applied stress. Crack grows by repetitive blunting

And sharpening process at crack tip. It shows rough fracture surface [34].

Stage 3: At stage three crack growth become unstable. Here crack growth is controlled by static modes of failure [35].

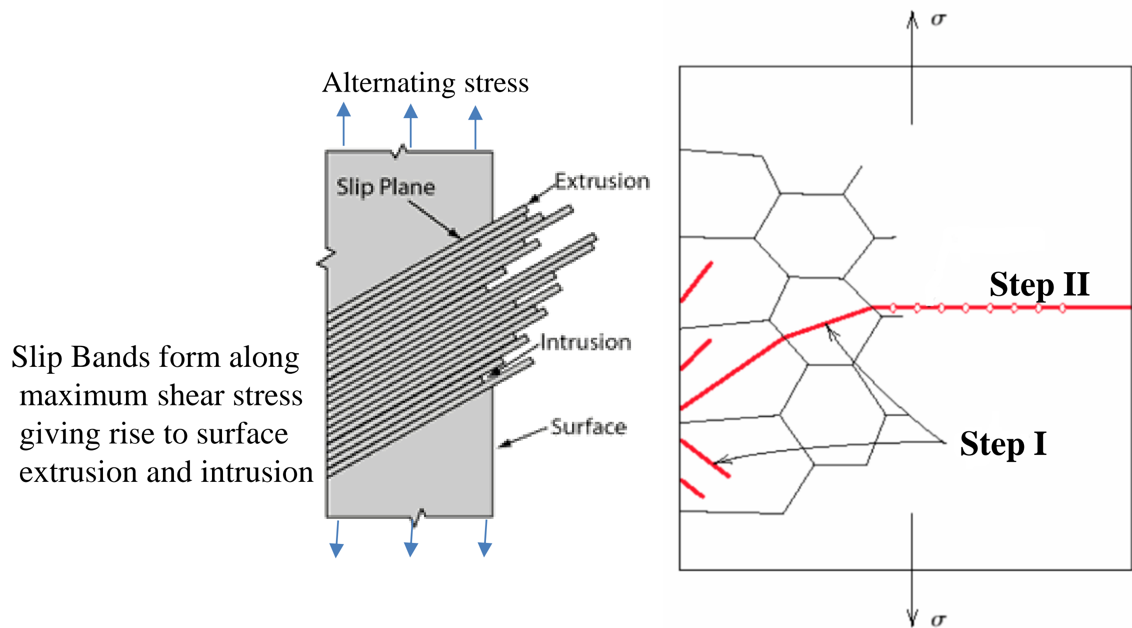


Figure 1-16: Stages of Fatigue Failure [36-37]

### 1.15 Fatigue Life

The American Society for Testing Materials (ASTM) defines fatigue life by $N_f$, the number of cycles to fail at specified stress level. Solder joint geometry, pad geometry, thermal load amplitude and its history, solder microstructure, surface finish etc. have profound effect on fatigue life. The fatigue life formulae used can be divided into two domains namely, high cycle fatigue and low cycle fatigue depending upon the stress level.

#### 1.15.1 High Cycle Fatigue

In this case stress does not exceed yield stress limit and occurs at relatively large cycle numbers ($N > 10^5$). Deformation incurred is primarily elastic and fatigue strength is described by stress-based parameters. Vibration loading can be described as high cycle fatigue. Miner's rule or the Palmgren-Miner linear damage law [38] is one of the most

widely used cumulative damage theories which attempts to determine the proportion of life consumed by stress reversal at each magnitude and form a linear combination of their aggregate:

$$\sum_{i=1}^{k} \frac{n_i}{N_i} = C \qquad \text{Eq. 1.1}$$

where k is the number of stress levels in the loading spectrum; $\sigma_i$ is the ith stress level; $n_i$ is the number of cycles applied at $\sigma_i$; Ni is the fatigue life at $\sigma_i$; and C is usually assumed to be 1 for design purposes and is experimentally found to be somewhere between 0.7 and 2.2.

### 1.15.2 Low Cycle Fatigue

Characterized by small cycle numbers ($N < 10^3$) and caused by high stress. Since the stress is high, plastic deformation occurs. Thermally induced fatigue is of this type and strain-based parameters are normally used to predict fatigue life. The most widely accepted theory for low cycle fatigue is the Coffin-Manson relation [39].

$$\frac{\Delta\varepsilon_p}{2} = \varepsilon_f' \left(2N_f\right)^C \qquad \text{Eq. 1.2}$$

$\Delta\varepsilon_p$ is the plastic strain amplitude; $\varepsilon_f'$ is an empirical constant known as the fatigue ductility coefficient; $N_f$ is the fatigue life or number of reversals to failure, and C is an empirical constant known as the fatigue ductility exponent.

## 1.16 Digital Image Correlation

Digital image correlation (DIC) is a digital image and numerical computing based optical metrology which gives full field displacements and strain by comparing the digital images of specimen surface before and after deformation. It was first developed by a group of researchers at university of South Carolina in 1980s. It has been widely used to quantify

the deformations and associated strains and to locate the most vulnerable sites of electronic packages because of its number of advantages, such as, it needs less surface preparation as compared to Moiré method, it does not need any coherent light source like laser, and it offers a wide range of measurement sensitivity and resolution depending upon the resolution of image capturing device. Also it is a contactless method covering a wide range of loading conditions and geometries and does not need isolated environment for application like interferometric method. In case of displacement measurement, it can go upto 0.01-pixel accuracy (i.e. 1 µm with 1 Mpixel camera) and 100 µstrain (0.01%) in case of strain. It can even go up to nanoscale accuracy if coupled with optical microscopy, scanning electron microscopy etc. DIC is a pattern tracking method based on subset of pixels which applies a mathematical correlation algorithm to obtain kinematic information from digital images acquired during deformation. The correlation works by matching small square subsets of the non-deformed image to locations in the deformed image. There are three very important components of DIC algorithm, namely, matching, interpolation and shape function. At first, a square subset centered at point $P(x_0,y_0)$ from the reference image is chosen, then its corresponding location in deformed image is tracked. To evaluate the degree of similarity Zero Normalized Sum of Squared Difference (ZNSSD) is used. The location of deformed subset is detected at the place which have the lowest value of ZNSSD.

$$C_{ZNSSD} = \sum \left( \frac{f_i - \bar{f}}{\sqrt{\sum (f_i - \bar{f})^2}} - \frac{g_i - \bar{g}}{\sqrt{\sum (g_i - \bar{g})^2}} \right) \quad \text{Eq. 1.3}$$

Where '*f*' is the reference image intensity and '*g*' is deformed image intensity. ZNSSD is used to correct for illumination change and offset and also it is the most noise proof algorithm.

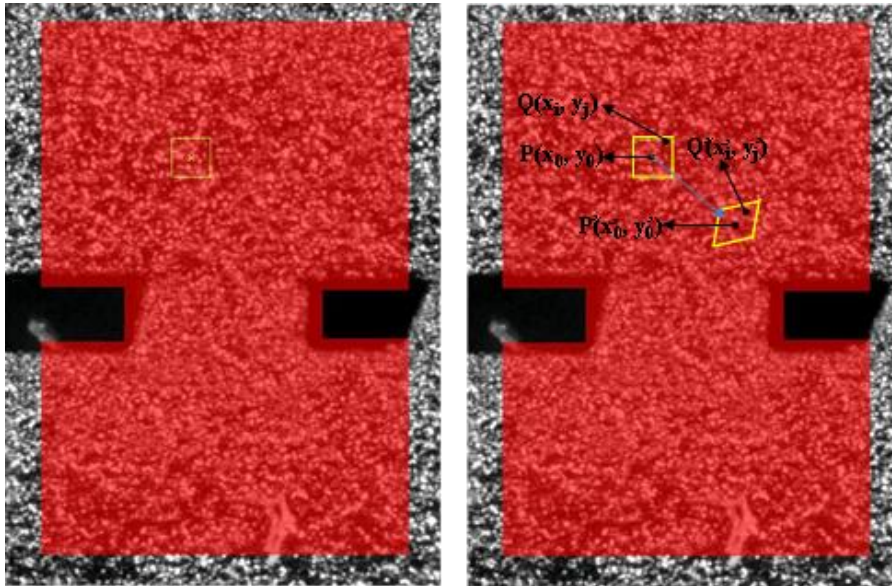


**AOI: Area of interest (shaded by red)**
**Subset: Marked by yellow, $P(x_0,y_0)$: Subset center**

Figure 1-17: Subset matching in DIC

Now a point of interest in the deformed subset may locate between pixels i.e. in subpixel locations. So the intensity at these subpixel locations should be provided prior to calculate the similarity criterion using ZNSSD equation.

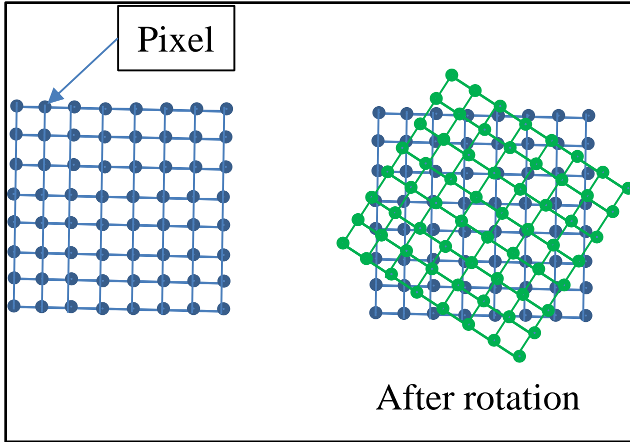


Figure 1-18: New location of pixel after deformation

Various sub-pixel interpolation schemes is used such as, cubic polynomial, cubic B spline, quintic B spline interpolation etc. A cubic B spline curve is constructed by using different cubic polynomial curve between each two data points, in other words it is made of number of cubic polynomials glued together. The shape of the interpolating curve closely follows a given sequence of points which are called control points. The reason for choosing cubic polynomial is that it is the lowest degree polynomial which supports inflection point and also it always show smooth rather than wildly fluctuating shape shown by other higher order polynomials. Cubic B-spline curves is actually a blend of several cubic functions where three continuity conditions are assumed at the junction of a pair of cubic curve which are: (a) Positional Continuity ($C^0$) i.e. the functional value at the end point of segment 'i' is the same as the starting point of segment 'i + 1', (b) Tangential Continuity ($C^1$): i.e. no abrupt change in slope occurs at the transition between segment 'i' and segment 'i + 1', and (c) Curvature Continuity ($C^2$): i.e. no change in curvature at the transition between segment 'i' and segment 'i + 1'. Each segment can be written in the following form;

$$y_i(x_i) = a_i(x - x_i)^3 + b_i(x - x_i)^2 + c_i(x - x_i) + d_i \qquad \text{Eq. 1.4}$$

Now if there are m number of segments, we have 4m unknowns. Now applying the above three continuity conditions and assuming the curvature of the beginning and ending portion

of the total curve to be zero (Natural spline) and then solving for $a_i$, $b_i$, $c_i$ and $d_i$, following recursive formula can be written;

$$\sigma_{i-1} + 4\sigma_i + \sigma_{i+1} = \frac{6(y_{i+1} - 2y_i + y_{i-1})}{h^2}$$
$$\text{where } h = x_{i+1} - x_i, i = 1,2.........m-1 \qquad \text{Eq. 1.5}$$

Where $\sigma_i$ is the 2nd derivative at $x_i$ and $a_i$, $b_i$, $c_i$ and $d_i$ can be written as an expression of $\sigma_i$. We can write this recursive formula in the form of a system of linear equations as following;

$$\begin{bmatrix} 4 & 1 & & & \\ 1 & 4 & 1 & & \\ & 1 & 4 & 1 & \\ & & & & \\ & & & 1 & 4 \end{bmatrix} \begin{Bmatrix} \sigma_1 \\ \sigma_2 \\ \\ \\ \sigma_{m-1} \end{Bmatrix} = \frac{6}{h^2} \begin{Bmatrix} y_2 - 2y_1 + y_0 \\ y3 - 2y_2 + y_1 \\ \\ \\ y_m - 2y_{m-1} + y_{m-2} \end{Bmatrix} \qquad \text{Eq. 1.6}$$

Now due to deformation the subset size and shape which is originally a square in reference image may change in deformed image. Thus a neighboring point $Q(x_i, y_j)$ around the subset center $P(x_0, y_0)$ in Figure 1-17 can be mapped into $Q'(x_{i'}, y_j')$ by using appropriate shape or mapping function. Normally first order mapping function is used which allows translation, rotation, shear, normal strains and their combinations. This transformation from un-deformed to deformed using the first order mapping function is known as Affine Transformation, which can be written as;

$$\begin{Bmatrix} x' \\ y' \\ t \end{Bmatrix} = \begin{bmatrix} a & b & t_x \\ c & d & t_y \\ 0 & 0 & 1 \end{bmatrix} \begin{Bmatrix} x \\ y \\ t \end{Bmatrix} \qquad \text{Eq. 1.7}$$

where $(x',y',t)^T$ is deformed space and $(x,y,t)^T$ is undefromed space

In the above equation, 't' is point and it is included to incorporate change in origin. Depending upon the value of a, b, c and d all kinds of transformation like translation, scaling, shear, refection, rotation and their combination can be mapped.

### 1.17 Prognostic Health Management System

Prognostics Health Management (PHM) is the interrogation of system state and the assessment of product survivability in deployed systems using non-destructive assessment of underlying damage. Here, health is defined as the extent of degradation or deviation from an expected normal condition.[40] The goal of proactive fault monitoring is to protect the end user from unexpected failure and downtime and provide advanced alert of impending failure in due time to help corrective measures to be taken prior to failure. Over the past decade, extensive research has been conducted in PHM with a view to providing advance warnings of failure, enabling forecasted maintenance, improving system qualification, extending system life, and diagnosing intermittent failures. PHM has been implemented to detect and interpret the parameters indicating:

- Performance degradation, such as deviation of operating parameters from their expected values
- Physical degradation, such as increases in electrical resistance or threshold voltage, crack development, corrosion, interfacial delamination, or

- Changes in a life-cycle profile, such as usage duration and frequency, ambient temperature and humidity, vibration, and shock [40]

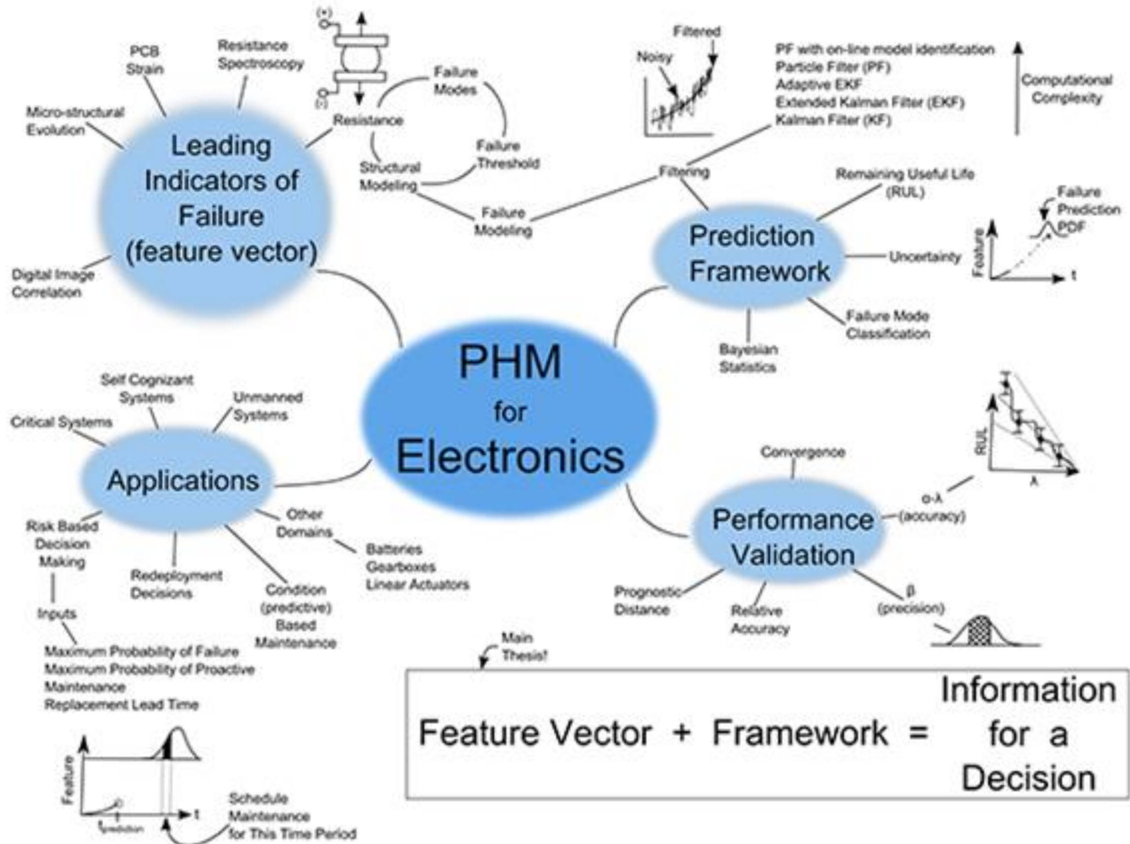


Figure 1-19: Approach for PHM for Thermo-mechanics, Shock and Vibration Environments [41]

PHM techniques depend on the observation of precursor variables. It enables self-cognizant systems capable of assessing their own real-time performance under actual usage conditions and adaptively trigger risk-mitigation actions to virtually eliminate unplanned failures [41]. Detecting fault in the system and computing residual life at any given point is the core function of any PHM technique. Typical fault detection involves interrogation

of system state for physics of failure based damage proxies or leading indicators of failures which provide information about the current damage state or impending failure. These damage proxies are then used in PHM model development which are directly and indirectly related to the overall life of the system.

### 1.18 Thesis Layout

This dissertation is sequentially divided into the following chapters:

Chapter 1: Introduction to Micro-electronics packaging fundamentals, its reliability related issues like solder alloys, mechanical properties, reliability models and experimental techniques used to extract reliability metrics.

Chapter 2: Discussion on existing literature on topics discussed in Chapter 1.

Chapter 3: Discussion on quantifying the effect of iso-thermal aging on reliability through microstructural investigation, and development of a damage mapping model to probe time-temperature combination pertinent to a particular damage state.

Chapter 4: Discussion on quantifying the effect of mean temperature of thermal cycling on reliability through microstructural investigation, and development of a combined life prediction model based on microstructural damage accrual rate.

Chapter 5: Discussion on implementation of Digital Image Correlation which is more a real-time method as compared to microstructural investigation, to see the effect of mean temperature of thermal cycling on reliability. Evolution of shear strain field with mean temperature was investigated, and the overall trend was then validated by building and simulating a non-linear finite element model of a package.

Chapter 6: This chapter shows further implementation of Digital Image Correlation in investigating evolution of shear strain field with number of thermal cycles undergone, and also the effect of aging on fatigue reliability at the same time.

Chapter 7: Here constants of conventional life models like Coffin-Mansion formula and Darveaux's Energy based model were determined using strain data and finite element model outcome. A newer model based on microstructure damage state was proposed and all the model outcome then compared with experimental life results derived through accelerated life testing.

Chapter 8: This chapter summarizes all the findings of this study and proposes some additional works to be done in future studies.

# Chapter 2

# Literature Review

## 2.1 Package Reliability

In the early 1950s, reliability problems came to focus as industries and researchers confronted the unreliability issue of some US Airforce components. Electronics industries started booming in the late 1950s, and along with it came manifold of reliability problems. To delve deeper and to knock the root of these problems the idea of 'Physics of Failure' emerged in the early 1960s [42]. The major reliability issue with BGA package is the thermal mismatch arising from large difference in CTE between chip and printed circuit board (PCB) which induces shear in solder ball. According to Syed [43], packages designed with perimeter arrays, thicker BT substrates, and an increased pad size can impart more reliability to withstand under the hood environment, because in case of perimeter array the impact of the die is lessened and thicker BT substrate helps abate the CTE mismatch between the die and the PCB. Reliability is also greatly influenced by die size [44]. Ghaffarian showed that the smaller die has positive impact on package life. Furthermore, larger pitched ball grid arrays tend to outperform the fine pitch ball grid arrays. Bradley [45] showed that HASL finish improves reliability if compared to immersion nickel based finishes. Oxidation of the nickel through gold layer cause poor solderability resulting into bad connection between the solder ball and copper pad. Suhling [46] showed the superiority of HASL pad finish over Palladium based pad finishes in thermal testing on BGA's. Mawer [47] showed that better reliability can be achieved with NSMD or non-solder mask defined copper pads. Research was also done on the effect of underfill on

package reliability. Elkaday [48] showed that the underfill improves the life of the packages by investigating the impact of underfill on thermal performance of smaller perimeter array packages. According to Pyland [49] low CTE and higher Young's modulus underfill improves reliability of a super BGA. Chiang [50] reported that a better reliability of package can be achieved by $2^{nd}$ reflow process as ball stand-off height can be increased by $2^{nd}$ reflow. Approximately 2X increase in characteristic life is reported by him under thermal cycling due to significant reduction in equivalent plastic strain, energy density and Von Mises stress in solder joint. According to Charles [51], increase in fatigue life can be attained by fabricating solder joints with large fillets and lower stand-off height. Large fillet helps reduce stress concentration and lower standoff height increases net cross-sectional area and prevents early stress buildup.

## 2.2 Thermal Cycling Reliability of SAC Solders

Thermal Cycling Reliability and the failure mechanism of solder joints under thermal cycling test have attracted the most attention from researchers. Matin [52] and Mattila [53] found that thermal fatigue cracks always occur inside the bulk solder of the joint close to the interfaces regions. The propagation of the thermal fatigue cracks, and therefore the reliability of the solder joint, relies on the mechanical and microstructure properties of the bulk solder [54]. The thermal strain and mechanical strain combined at elevated temperature during thermal fatigue process induces recrystallization in the highly strained region of the bulk solder finally leading to the development of the cracks in the recrystallized regions [54-55]. Because the recrystallization behavior of Sn grains in Sn–Ag–Cu solders is dominated by thermal strain [56-59], better thermal reliability can be obtained in Sn–xAg–Cu solders by keeping thermal strain smaller. One way to suppress

thermal strain in Sn–xAg–Cu solders can be an existence of larger number of fine $Ag_3Sn$ IMC dispersoids in the bulk solder since their presence helps improve the yield strength and elastic modulus of the bulk solder [56, 60-61], which in effect suppresses the plastic deformation significantly. One of the most detailed studies on thermal fatigue failure rate of Sn–xAg–Cu solder joints was conducted by Terashima et al. [56]. He found that increasing Ag content increases the fatigue resistance of SAC solder. Thus, the number and dispersion morphology of the $Ag_3Sn$ IMC particles strongly affects the mechanical properties of the SAC solder. Recrystallization being a dominating phenomenon in thermal cycling is actually a transformation of Sn macro-grains in grains of smaller size in highly stressed zones. Crack is initiated at the interface of these recrystallized tin grains, and then propagates [62]. Matin [52] has found that the fatigue damage within solder initiates at grain boundaries (the intrinsic thermal fatigue contribution) and also takes the form of persistent slip bands (the mechanical fatigue contribution). He also found by correlating the observed damage and the calculated stress fields that three crucial factors exist: intrinsic thermal mismatches caused by Sn anisotropy, thermal mismatch between Cu and solder, and the mechanical constraints posed by the Cu on the soldered joint. So the location and severeness of fatigue damage is determined by the combined effect of these three factors. Xu [63] performed -40$^{o}$C to125$^{o}$C thermal cycling test on his test subject. He showed significant change in grain size during the thermal cycling test indicative of dynamic recrystallization. During thermal cycling, thermal stress is induced by CTE mismatch in every temperature cycle and causes solder deformation. During the temperature ramp up from -40$^{o}$C to125$^{o}$C (for SAC, Tm is 217$^{o}$ C or 490K, 125 C=398K=0.8Tm), dynamic recrystallization occurred, new grains formed and the stress is released. Then, the next

temperature cycle came and new deformation started before the enlargement of the grains from previous deformation. Arfaei [64] observed similarities in the failure mechanisms of a variety (BGA, CSP, QFN) of Pb free SAC solder joints which were subjected to variety of thermal cycling regimes. Solder fatigue was observed in all of the samples, with evidence of crack propagation along grain boundaries of recrystallized regions of the sample.

### 2.3 Isothermal Aging reliability of SAC solders

It is known that the microstructure changes dramatically during thermal aging [65]. During aging, two metallurgical processes take place in solder joints: (a) coarsening of the eutectic structure in the bulk solder (b) Kirkendall voiding in $Cu_3Sn$ layer. Figure 2-1 shows, the pristine microstructure of a Sn-3.0Ag-0.5Cu (wt.%) solder alloy with distinctive region of β-Sn dendrites, which appears as a rounded grain microstructure, and eutectic zones decorating the β-Sn grains, which are a mixture of small $Ag_3Sn$ and $Cu_6Sn_5$ IMC precipitates. Once a thermal aging process is applied, the eutectic zones begin to evolve to accumulate larger IMC precipitates. [66]

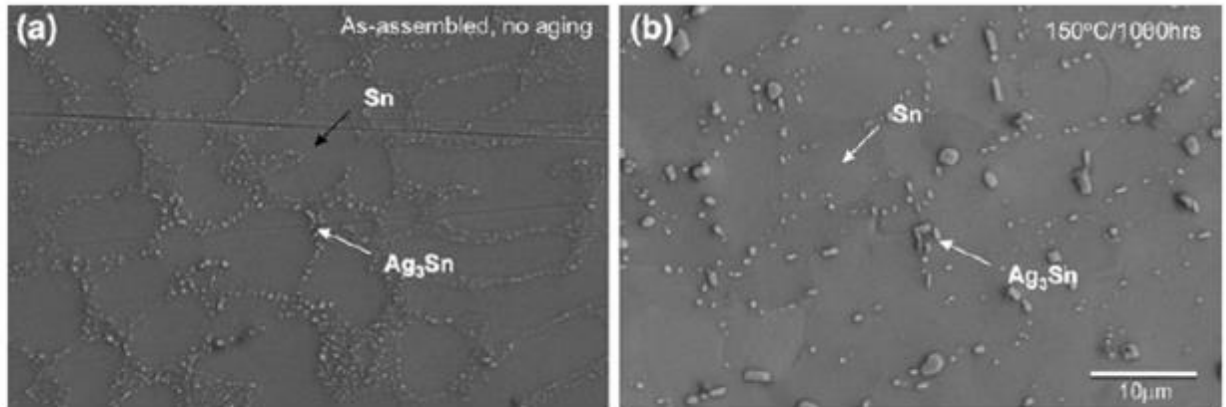


Figure 2-1: Sn-3.0Ag-0.5Cu (wt.%) (SAC305) bulk microstructure before and after isothermal aging:(a) as assembled, unaged, and (b) after aging at 150$^o$ C for 1000 h [66]

Li et al [67-68] studied microstructure of flip-chip packaging with SAC387 solder joints being aged at different temperatures. According to him, the facet-like morphology of interfacial IMC $(Cu,Ni)_6Sn_5$ remained unchanged during aging, but its thickness increased considerably by a volume diffusion mechanism. Existence of $Ag_3Sn$ IMCs were found to be either plate-like or lamella-like phases or small particles around the β-Sn dendrites in the bulk solder and then these plate and lamella $Ag_3Sn$ phases broke up into small parts and then coarsened into pebble-like phases. Another important feature of aging microstructure is the formation of Kirkendall voids at the solder/Cu interface which has been reported for many years. Firstly, the inter-diffusion of Cu and Sn and secondly the asymmetry of diffusion of these two materials lead to void in solder joints. There are two steps for this process. (1) Cu atoms leave the Cu pad and diffuse towards the solder, which generates vacancies near the Sn layer. (2) These vacancies then coalesce into voids with time and higher temperature. Chiu et al. [69] reported tests of ball grid arrays (BGAs) with Sn-Ag-Cu solder balls with Cu pad being thermally aged at 100 $^o$C, 125 $^o$C, 150 $^o$C, and

175 $^{o}C$ for 3, 10, 20, 40 and 80 days. They found extensive Kirkendall voids at the interface of solder joint to Cu substrate. The voiding process was activated even at 100$^{o}C$, and after 10 days of aging at 125$^{o}C$ the drop performance degraded 80%. Higher temperature will generate more voids during the same aging time. In case of thermal storage, the most prominent effect is interfacial IMC formation. Most of the investigations for predicting the IMC layer growth in solid joints either is based on the one-dimensional Fick's law or assumes a power law. For the solid-solid interaction, the kinetics of IMC growth often follow Fick's law,

$$d = d_0 + (Dt)^{0.5} \qquad \text{Eq. 2.1}$$

Where d is the thickness of IMC layer at aging time t; $d_0$ is the initial IMC thickness after reflow; D is the diffusion coefficient of a specific IMC atom species at a certain aging temperature and t is the isothermal aging time. The diffusion coefficient D is given by an Arrhenius expression:

$$D = D_0 \exp\left(\frac{-Q}{K_B T}\right) \qquad \text{Eq. 2.2}$$

Where $D_0$ is the diffusion constant of a specific IMC atom species (at initial temperature); Q is the activation energy for the growth of a specific IMC layer; $K_B$ is the Boltzman constant; and T is the absolute temperature. The growth kinetics of the IMCs was analyzed and revealed to follow diffusion principles. It was found that $Cu_6Sn_5$ was formed at the solder and Cu interface during reflow, but the most important influence on the layer thickness was attributed to isothermal aging. As shown in Figure 2-2, with the increase of

the aging time, the size of the interfacial $Cu_6Sn_5$ increased and its morphology was changed from scallop-like to needle-like and then to rod-like. [70]

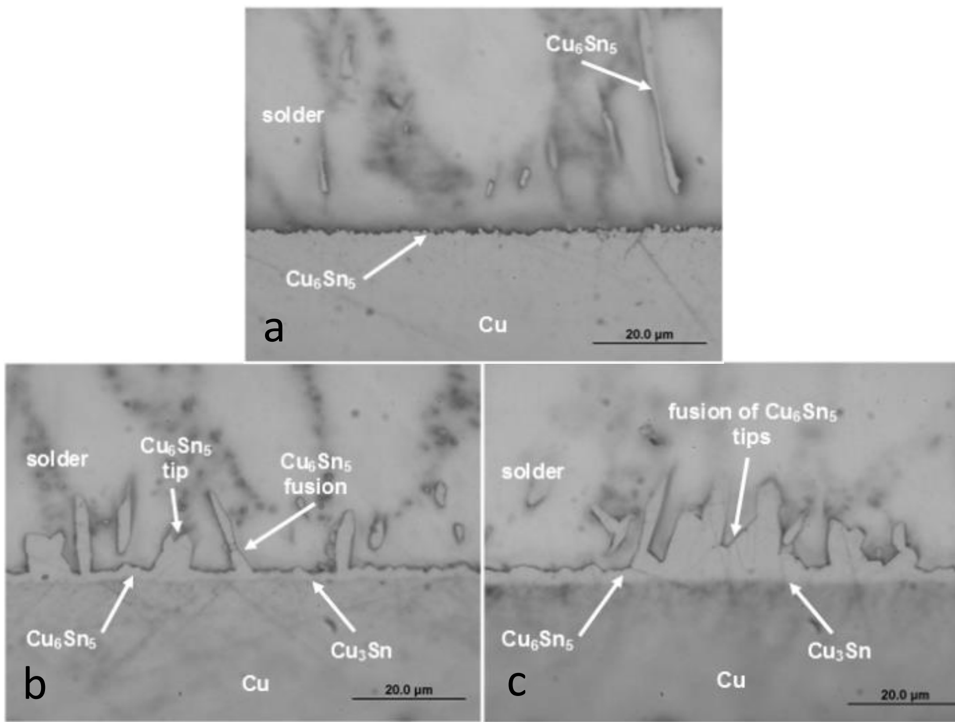


Figure 2-2: (a) Interface of SAC305 solder after soldering (b) Interface of solder after 500 hours of the aging (c) Interface of solder after 1000 hours of the aging [70]

The chemical composition of interfacial IMCs and their effect on reliability also can be greatly influenced by surface finish type. One of the most commonly used surface finishes on the package side is electrolytic Ni/Au plated over Cu. Electrolytic Ni/Au involves quick dissolution of Au during ball attachment and reflow process and is associated with Ni dissolution and diffuse into the solder material, which causes a difference in the initial microstructure, with needle-shaped IMCs at the interface. Actually Ni layer prevents rapid reaction between the solder and the Cu layer, which is under the Ni layer and the gold prevents the oxidation of the underlying nickel layer, thereby enhancing solderability.

Packages with electrolytic Ni/Au as a substrate finish as compared to OSP show IMC growth by consumption of Cu and/or Ni, which reside in the solder ball. On the other hand, when there is no Ni at the package-side interface, a continuous flow of Cu from the board and package sides is observed. Ni/Au surface finish shows better reliability which is expected due to the existence of Ni in the solder joints in the bulk solder region near the package-side interface, which increases the initial hardness and provides more crack propagation resistance. [71]

### 2.4 Packaging Architecture

Darveaux et al. [72-73] and Syed [74] in their effort to characterize the impact of design and material choice on solder joint fatigue life for fine pitch BGAs, identified some influential factors like die size, package size, ball count, pitch, mold compound and substrate material, test board thickness, pad configuration and pad size, different testing profile effects etc. These findings can be summarized as;

- The row of joints near the die edge failed first under most of the test conditions.

- Fatigue life went up-to 6X as die size was reduced,

- For a given die size, fatigue life showed 2X increase for larger packages with more solder balls.

- Mold compounds with higher filler content showed reduced fatigue life by up to 2X due to higher stiffness and lower thermal expansion coefficient.

- Tape based packages showed almost similar degree of board level reliability to laminate based packages if optimized.

- As compared to 1.6 mm thick boards, 0.9 mm thick test boards showed 20% longer fatigue life due to lower assembly stiffness.

- For CSP applications, NSMD test board pads outperformed SMD pads by up-to 3.1X life improvement.

- In case of thermal test profile, faster ramps and larger range will result in higher stresses and more creep in the solder.

In an attempt to study under-the-hood reliability of smaller PBGA packages (15 and 17 mm) Suhling et al. [46] reported that increased BT substrate thickness and NSMD pad can enhance the reliability, and underfill by strengthening solder joints can make smaller components to meet the typical automotive thermal cycling requirements. Ghaffarian [75] found that a failure shift from solder joint to package may occur more often for miniaturized CSP packages. He also found that increasing the maximum cycling temperature has more damaging effect than decreasing the minimum temperature, and also fatigue rather than creep, is considered to be main damage mechanism below one-half of the absolute melting temperature while studying accelerated thermal cycling test methods used in current industry to characterize the interconnect reliability of BGA and CSP assemblies.

## 2.5 Constitutive relations for Solder

In electronic packages, thermal mismatch induced stresses can result in extensive plastic deformation at solder joints, which is responsible for the low cycle thermal fatigue failure of solder materials. An expression for the strain was proposed by Yang, et al. [76]:

$$\varepsilon_t = \varepsilon_e + \varepsilon_p + \varepsilon_c$$

$$\varepsilon_t = \frac{\sigma}{E} + C_1\sigma^m + \gamma_T\left(1 - \exp(-B\dot{\varepsilon}_s t)\right) + C_2 \dot{\varepsilon}_s t \qquad \text{Eq. 2.3}$$

where σ is the stress; ε is the strain; E is the modulus of elasticity; m is the reciprocal of the strain-hardening exponent; $C_1$ is the reciprocal of the strength coefficient; $\dot{\varepsilon}_s$ is the steady-state creep-rate which is a function of the applied stress; $\gamma_T$ is the amplitude of primary creep strain; and B and $C_2$ are material (deformation mechanism) constants for the creep response. The four terms on right-hand-side of the above equation (Eq. 2.3) are the elastic, plastic, time dependent primary creep, and steady-state creep strain components respectively. This relation is also commonly known as the classical elastic-plastic-creep constitutive equation which has been extensively investigated for electronic solders. It serves as the basis for constitutive modeling of the material behavior of solder alloys.

## 2.6 Stress-Strain

Tensile strength decreases significantly with decreasing strain rate and increasing test temperature as indicated by the two equations below [77, 78];

$$\sigma = C\dot{\varepsilon}^m \qquad \text{Eq. 2.4}$$

$$\sigma = -\alpha T + \beta \qquad \text{Eq. 2.5}$$

Nose, et al. [79] performed a parametric study of tensile strength in Sn-Pb solders as a function of chemical composition, strain rate and temperature. The tensile strength was described as:

$$\sigma = A_0 + m\log_{10}\dot{\varepsilon} + n\log_{10}T \quad \text{Eq. 2.6}$$

Where σ is the tensile strength; $\varepsilon^{\cdot}$ is the strain rate; T is the test temperature (°K); and $A_0$, m, and n are all functions of the weight percent ratio of Sn in the alloys. They found that both elastic modulus and yield strength increase with increasing Sn content. Pang, et al. [80] developed a modified Ramberg-Osgood model to describe the temperature and strain rate dependent stress-strain curves for SAC387. The Ramberg-Osgood model for elastic-plastic behavior can be expressed as:

$$\varepsilon = \frac{\sigma}{E} + \alpha\left(\frac{\sigma}{\sigma_0}\right) \quad \text{Eq. 2.7}$$

The modified temperature and strain rate dependent Ramberg-Osgood Model can be described as:

$$\varepsilon\left(T,\dot{\varepsilon}\right) = \frac{\sigma}{E} + \alpha\left[\frac{\sigma\left(T,\dot{\varepsilon}\right)}{\sigma_0}\right]^{n\left(T,\dot{\varepsilon}\right)} \quad \text{Eq. 2.9}$$

Where the hardening exponent n and stress coefficient σ are temperature and strain rate dependent:

$$\sigma\left(T,\dot{\varepsilon}\right) = \sigma_0 + \alpha T^* + b\dot{\varepsilon}^* \quad \text{Eq. 2.10}$$

$$n\left(T,\dot{\varepsilon}\right) = n_0 + cT^* + d\dot{\varepsilon}^* \quad \text{Eq. 2.11}$$

Where $T^* = \frac{T - T_r}{T_m - T_r}$ and $\dot{\varepsilon}^* = \ln\left(\frac{\dot{\varepsilon}}{\dot{\varepsilon}_r}\right)$

In these relations, a and c are temperature coefficients; c and d are strain rate coefficients; $T_r$ and $\dot{\varepsilon}_r$ are reference temperature and reference strain rate respectively; $T_m$ is the melting temperature of SAC387 (217 °C); and $n_0$ and $\sigma_0$ are the hardening exponent and stress coefficient at the reference temperature and strain rate.

## 2.7 Creep Model

Two constitutive creep models became the most popular, namely, the Harper and Dorn power law model (Harper and Dorn 1957) and Garofalo hyperbolic sine model [81]. These relationships can be expressed as:

$$\dot{\varepsilon} = A\sigma^n \exp\left(\frac{-Q}{RT}\right) \qquad \text{Eq. 2.12}$$

$$\dot{\varepsilon} = C\left[\sinh(\alpha\sigma)\right]^n \exp\left(\frac{-Q}{RT}\right) \qquad \text{Eq. 2.13}$$

In these expressions, $\dot{\varepsilon}$ is the secondary creep strain rate; $\sigma$ is the applied stress; $\alpha$ is a temperature independent parameter; R is the universal gas constant; T is temperature in Kelvin; A and C are material dependent constants; n is the stress exponent; and Q is the activation energy. These models only take steady-state creep into consideration, and do not include aging effects or other phenomena. That is why it is a matter of debate that whether the Dorn and Garofalo laws can be reasonably applicable to actual solder joints. Ma and Suhling [22] have evaluated the creep parameters in the two models for various Pb-containing and Pb-free solder alloys and found large discrepancies in the creep data for

solder alloys of the same chemical composition. This can be explained by variation in specimen design, testing method and storage time and temperature before the creep test. The more important thing to note is that the creep behavior of bulk solder significantly differs from real solder joint due to the effects of microstructure evolution, intermetallic compound formation, and constraint due to different methods of assembly.

### 2.8 Anand's Viscoplastic Model

Almost all the solder alloys popular in industries have low melting point, such as 183$^{o}$C for SnPb, 217$^{o}$C for SAC 305, 228$^{o}$C for SAC105 etc. This feature of solder alloy renders the solder joint to operate at high homologous temperature even at sub-zero environment and creep becomes very significant. There are some constitutive models available ranging from elasto-plastic model which divides total strain into three different components namely elastic strain, time independent plastic strain and time dependent creep strain to modified Ramberg-Osgood Model in which the hardening constant and stress coefficient are modified to be temperature and strain rate dependent. Power Law Creep constitutive equation as described in previous section is also frequently used. But the time independent and time dependent inelastic strains are very difficult to separate realistically as both of these two strain arise from similar mechanism due to dislocation. Therefore, a unified plastic/creep constitutive relation is highly desirable which can combine creep and plastic strain components under a unified state variable, which was first proposed by the Anand Viscoplastic model, initially proposed by Anand et al [82] and subsequently developed by Brown, et al. [83] for the rate-dependent deformation of metals at high temperatures. Since then this model has been applied extensively to describe the viscoplastic behavior of solder alloy. Viscoplastic materials are those which show rate dependent inelastic behavior or in

other words these kinds of materials undergo time dependent plastic deformation. The main difference between rate-independent plastic and viscoplastic material models is that the latter exhibit not only permanent deformations after the application of loads but continue to undergo a creep flow as a function of time under the influence of the applied load.

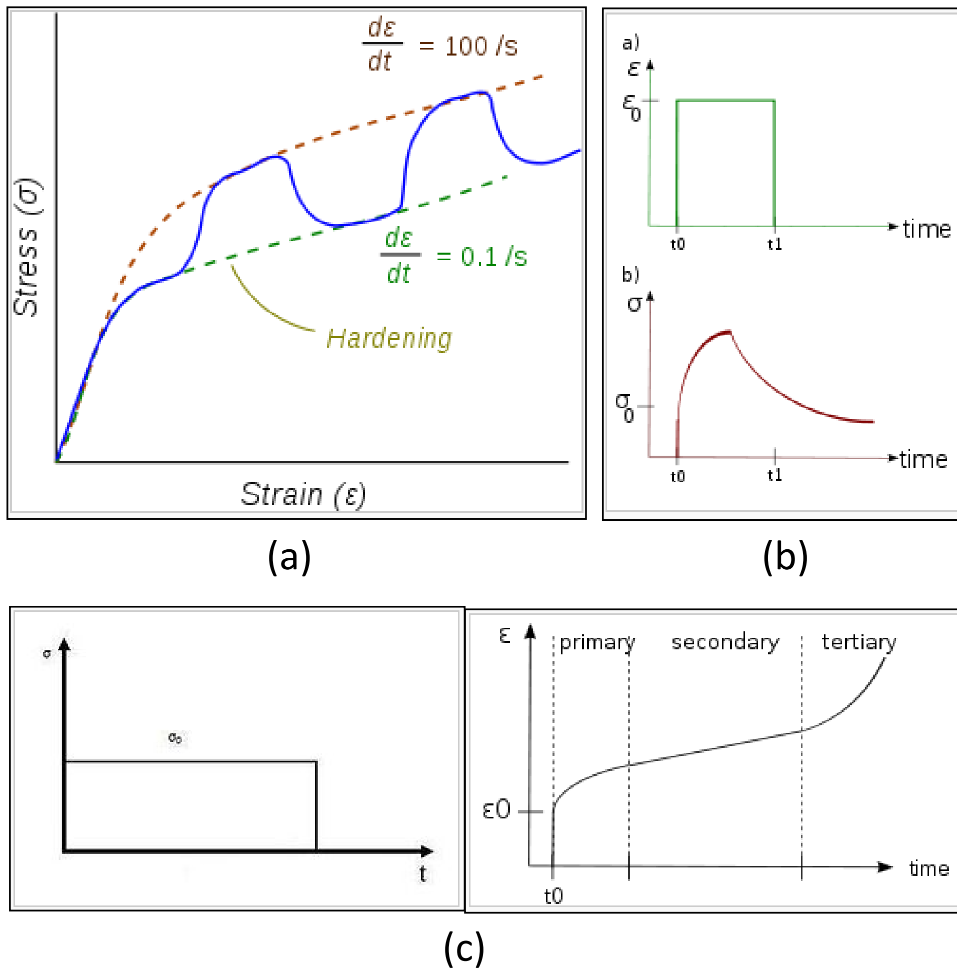


Figure 2-3: (a) Viscoplastic material behavior (a) Effect of strain rate on Stress-Strain (b) Stress Relaxation and (c) Creep

The parameters in the unified constitutive model can be determined in a direct method by combining both rate-dependent and rate independent plastic strains into viscoplastic strain and plastic flow terms. This model has two distinctive features. Firstly, this model needs no explicit yield condition and no loading/unloading criterion. Plastic strain is assumed to

take place at all nonzero stress values. Secondly, this model employs a single scalar as an internal variable to represent isotropic resistance to plastic flow offered by the internal state of material. The internal variable is denoted by s, which is isotropic resistance to macroscopic plastic flow developed due to strengthening mechanisms like dislocation density, solid solution strengthening, grain size effects etc. This deformation resistance 's' is proportional to equivalent stress 'σ'.

$$\sigma = c.s; c < 1 \qquad \text{Eq. 2.14}$$

Where c is a material parameter and a constant which can be defined as;

$$c = \frac{1}{\xi}\sinh^{-1}\left\{\left[\frac{\dot{\varepsilon}_p}{A} e^{\frac{Q}{RT}}\right]^m\right\} \qquad \text{Eq. 2.15}$$

Where $\dot{\varepsilon}_p$ is the inelastic (plastic) strain rate, T is the absolute temperature, ξ is the multiplier of stress, A is the pre-exponential factor, Q is the activation energy, R is the universal gas constant, and m is the strain rate sensitivity. The following equation is called flow equation which accommodate the strain rate dependence on stress.

$$\dot{\varepsilon}_p = Ae^{-\frac{Q}{RT}}\left[\sinh\left(\xi\frac{\sigma}{s}\right)\right]^{\frac{1}{m}} \qquad \text{Eq. 2.16}$$

In the above equation temperature dependence is incorporated by Arrhenius term and the stress and state dependence is introduced by simple modification of hyperbolic sine form proposed by Garofalo to model steady state plastic flow or secondary creep.

The evolution equation for the internal state variable 's' can be written as,

$$\dot{s} = g(\sigma, s, T)\,\dot{\varepsilon}$$

$$\dot{s} = \left\{ h_0 \left[ 1 - \frac{s}{s^*} \right]^a .\text{sign}\left( 1 - \frac{s}{s^*} \right) \right\} \dot{\varepsilon}_p \; ; a > 1 \qquad \text{Eq. 2.17}$$

Where

$$s^* = \hat{s} \left\{ \left[ \frac{\dot{\varepsilon}_p}{A} e^{\frac{Q}{RT}} \right]^n \right\} \qquad \text{Eq. 2.18}$$

$h_0$ is the hardening/softening constant, a is the strain rate sensitivity of hardening /softening. s* is the saturation value of s and ŝ is a coefficient and n is the strain rate sensitivity for the saturation value of deformation resistance. After integrating we get,

$$s = \hat{s} \left[ \frac{\dot{\varepsilon}_p}{A} e^{\frac{Q}{RT}} \right]^n - \left[ \begin{array}{c} \left( \hat{s} \left[ \frac{\dot{\varepsilon}_p}{A} e^{\frac{Q}{RT}} \right]^n - s_0 \right)^{(1-a)} + \\ (a-1) \left\{ h_0 \left( \hat{s} \left[ \frac{\dot{\varepsilon}_p}{A} e^{\frac{Q}{RT}} \right]^n \right)^{-a} \right\} \varepsilon_p \end{array} \right]^{\frac{1}{1-a}} \qquad \text{Eq. 2.19}$$

Where $s_0$ is the initial value of s at time t = 0.

Rodgers et al. [84] has shown the validity of Anand model in simulating SAC alloy by showing the close match between the results derived from experiment and ANSYS. Amagai [85] reported the value of eight of the nine Anand constants necessary for FEM simulation. Chang et al. [86] presented Anand constants for SAC 305 and Chen et al. [87] presented Anand constants for Sn3.5Ag lead free solder alloy. Nie, et al. [88] have

investigated the limitations of the Anand model. He explained that since the Anand model does only account for secondary creep, it can only be expected to perform well under the conditions of high strain rate loading such as shock and drop testing, in which creep is not able to play a significant role. Also, the Anand model may not be effective in predicting the noticeable strain hardening observed in compression tests.

### 2.9 Fatigue Life Prediction Models

Different researchers proposed different Fatigue-life prediction models and the application of these models vastly vary based upon the assumptions i.e. the way the physical and metallurgical aspects of the alloy are taken onto account. There are two approaches to model fatigue: high cycle fatigue (HCF) and low cycle fatigue (LCF). In HCF, stress reversals are considered to be within the elastic regime and does not exceed the yield point, but for LCF, plastic deformation and creep becomes the dominating feature. Lee, et al. [89] have conducted a thorough review of solder fatigue models. They identified 14 models in the literature, which were developed based upon various assumptions, including the manner in which the physical and metallurgical aspects of fatigue are taken into account. According to the fundamental damage mechanisms, these models can be classified into such categories as stress-based, plastic strain-based, creep strain-based, energy-based, and damage-based. The characteristics of the 14 identified fatigue models are presented in Table 2-1.

Table 2-1: Summary of Solder Joint Fatigue Models [89]

| Fatigue Model | Model Class | Parameters | Coverage | Applicability |
|---|---|---|---|---|
| Coffin-Manson | Plastic strain | Plastic strain | Low cycle fatigue | All |
| Total Strain | Plastic + elastic strain | Strain range | High and low Cycle Fatigue | All |
| Solomon | Plastic shear strain | Plastic shear strain | Low cycle fatigue | All |
| Engelmaier | Total shear strain | Total shear strain | Low cycle fatigue | Leaded & leadless, TSOP |
| Miner | Superposition | Plastic failure & creep failure | Plastic shear and matrix creep | PQFP, FCOB |
| Knecht & Fox | Matrix creep | Matrix creep Shear Strain | Matrix creep only | All |
| Syed | Accumulation of creep strain energy | gbs energy and mc energy | Implies all coverage | PBGA, SMD, NSMD |
| Dasgupta | Total strain energy | Energy | Joint geometry accounted for | LLCC, TSOP |
| Liang | Stress/strain energy density based | Energy | Constants from isothermal low cycle fatigue tests | BGA and leadless joints |
| Heinrich | Energy density based | Energy | Hysteresis curve | BGA |
| Darveaux | Energy density based | energy | Hysteresis curve | PBGA, leadless |
| Pan | Strain energy density | Strain energy density and plastic | Hysteresis curve | LCCC |

| | | | | |
|---|---|---|---|---|
| | | energy density | | |
| Stolkarts | Damage accumulation | Damage | Hysteresis curve & damage evolution | All |
| Norris & Landzberg | Temperature and frequency | Temperature frequency | Test condition vs. use conditions | All |

It is evident from the above table how shear strain plays the central role in developing a major chunk of most popular fatigue models, and it is obvious as shear strain contributes the most in defining solder joint deformation and failure mechanism during thermal cycling. Previously, strain gages were used to measure strain, but due to exponential trend of interconnect miniaturization optical techniques like Moire and Digital Image Correlation (DIC) became the handiest tool to capture in-situ displacement and strain.

## 2.10 Digital Image Correlation

Park et. al. [90] determined thermal deformation of solder ball by DIC technique and then correlated with Sn grains, grain boundaries and larger intermetallic precipitates to study the role of different grain orientations and larger primary intermetallics in the failure mechanism. Nguyen et. al. [91] used DIC to characterize the mechanical properties of actual SAC105, SAC305, and SAC405 solder joints. Sun et. al. [92] used DIC to measure thermal deformation of Solder ball as a test case to address the effect of the influences of the computer vision system, specimen surface condition, out-of plane deformation and rigid body translation and rotation to evaluate the noise effects on measure accuracy. Zhang et al. [93] used DIC to measure thermal deformation of Solder ball to illustrate how stress and strain distribution in electronic packages are influenced by location of solder balls.

Pendse et. al. [94] used DIC to derive solder strain data to determine solder joint fatigue life.

## 2.11 Prognostic Health Management System

Built- In-Self Test (BIST) circuit, which includes onboard hardware and software diagnostic, has been used for error detection and fault location [95]. BIST is a reactive failure detection process which generates failure data and these can be correlated to show exactly when the failure occurred. It eliminates interaction with external automated test equipment (ATE) and provides more robust "at-speed" test facility of the circuitry. But very seriously lacking any estimates of system level reliability or the remaining useful life of the system. Several researches [96-98] revealed that BIST can be prone to false alarms and can result in unnecessary costly replacement, re-qualification, delayed shipping, and loss of system availability. Fuses within circuits protects components form excessive current and voltage transients. Thermostats is such an example which shut down the system whenever critical temperature threshold reached. Canaries can be used as prognostic cells devices which are located with the actual circuitry experience similar stresses as the actual component. Although they have similar operational environments and similar damage mechanism like actual components, these prognostic canaries are designed to fail faster to facilitate advanced warning and ultimately this failure of the canary devices can be used to estimate the time to failure of actual product. Canary components created on printed circuit board has been used for prognostication by failing before the actual component [99]. But fuses and canaries can provide limited insight into the remaining use life of the system. PHM approach presented here is based on pre-failure-space of the electronic-system without existence of any macro-indicators such as cracks or delamination. It enables the

estimation of prior damage by interrogation of the system state. An electronic component operating in harsh environment is subjected to both temperature variations as well aging for during use-life. A mathematical approach has been proposed in this thesis to model damage state, time and temperature to facilitate life prediction across different temperature profiles and package geometries. Previously, Lall et. al. [100-112] have developed leading indicators of failure like phase growth rate of solder interconnects, growth of intermetallics compound between solder and copper pad, normal stress at chip interface, and interfacial shear stresses which have been experimentally identified as indicators to failure. This methodology does not need any knowledge of prior stress histories and enables interrogation of system state using the identified damage pre-cursors and can be implemented prior to appearance of any macro-indicators of damage. This prognostics approach can be extended from single environment to multiple environments condition by quantifying the physical degradation contributed from each of these environments.

# Chapter 3

# Damage Pre-Cursor Based Assessment of Impact of High Temperature Storage on Reliability of Lead-free Electronics

## 3.1 Overview

Electronic systems may be subjected to prolonged and intermittent periods of storage prior to deployment or usage. Prior studies have shown that leadfree solder interconnects show measurable degradation in the mechanical properties even after brief exposures to high temperature. In this paper, a method has been developed for the determining equivalent storage time to produce identical damage at a different temperature. Field deployed electronics, unlike controlled laboratory testing, may experience a variety of sequential thermo-mechanical stresses during its lifetime. The field environment imposed on the electronic system may be influenced by ambient conditions and usage profile. Variation in the ambient temperature conditions, weather variations, usage location in addition to scheduled system usage or downtime may result in wide variance in the resulting field profile. There is need for tools and techniques to quantify damage in deployed systems in absence of macro-indicators of damage without knowledge of prior stress history. Previously, leading indicators of damage have been used to quantify the accrued thermo-mechanical damage under steady-state and cyclic temperature exposure in leadfree solders. [100-106]. Equivalence of accrued damage under multiple thermal aging environments is new. The presented framework is targeted towards high reliability applications such as avionic and missile systems which may have long period of storage prior to field usage. In this paper, a framework has been developed to investigate the system state and estimate

the remaining useful life of solder ball subjected to a variety of isothermal aging conditions including 60°C, 75°C and 125°C for periods of time between 1-week and 4-week. Data on damage precursors has been collected and analyzed to derive physics based damage mapping relationships for aging. Mathematical relationships have been derived for the damage mapping to various thermal storage environments to facilitate determining appropriate time-temperature combination to reach a particular level of damage state. Activation energy for the leading indicators of failure is also computed. Specific damage proxies examined include the phase-growth indicator and the intermetallic thickness. The viability of the approach has been demonstrated for leadfree test assemblies subjected to multiple thermal aging at 60° C, 75°C and 125°C. Damage mapping relationships are derived from data based on the two separate leading indicators.

### 3.2 Test Vehicle

In this study, CABGA36 and CABGA 256 packages soldered to glass-epoxy laminate board assemblies were used. The CABGA36 package is 6mm x 6mm in size, with 36 I/O, at 0.8 mm Pitch. The CABGA256 package is 16mm x 16mm in size, with 256 I/O at 0.8mm Pitch. Package interconnects were made of Sn3Ag0.5Cu solder in both cases.

Table 3-1: Package features

| | CABGA 36 | PBGA 256 |
|---|---|---|
| Solder | Sn3Ag0.5Cu | Sn3Ag0.5Cu |
| Package Size (mm) | 6x6 | 16x16 |
| I/O Count | 36 | 256 |
| I/O Pitch (mm) | 0.8 | 1 |
| Ball Diameter (mm) | 0.48 | 0.48 |
| Mold thickness (mm) | 1.5 | 1.5 |
| PCB Thickness | 1.55 | 1.55 |
| Pad (board) | NSMD | NSMD |
| Pad (package) | SMD | SMD |
| Board Finish | ImSn | ImSn |
| Package side substrate | Electrolytic NiAu | Electrolytic NiAu |

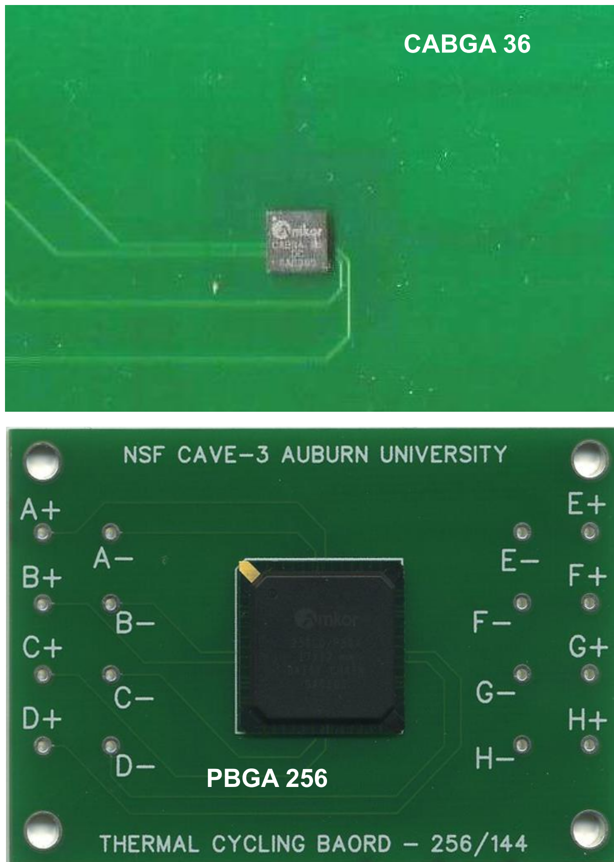


Figure 3-1: Test Vehicle

The ball height after reflow is 0.3 mm for CABGA36 and 0.32 for PBGA256. The printed circuit board thickness was 1.55 mm in both cases. Package attributes are shown in

Table 3-1. The printed circuit board was a double-sided FR4-06 material. The printed circuit board pads were Non-solder mask defined (NSMD) with immersion Tin finish.

Figure 3-1 shows the CABGA 36 and CABGA 256 package respectively. All test vehicles were subjected to isothermal aging at 60°C, 75°C and 125°C for various lengths of time. The test board is a JEDEC form-factor test board with corner holes. Each test package has four daisy chain patterns corresponding to the four quadrants. Packages were assembled at in-house surface mount facility of CAVE3.

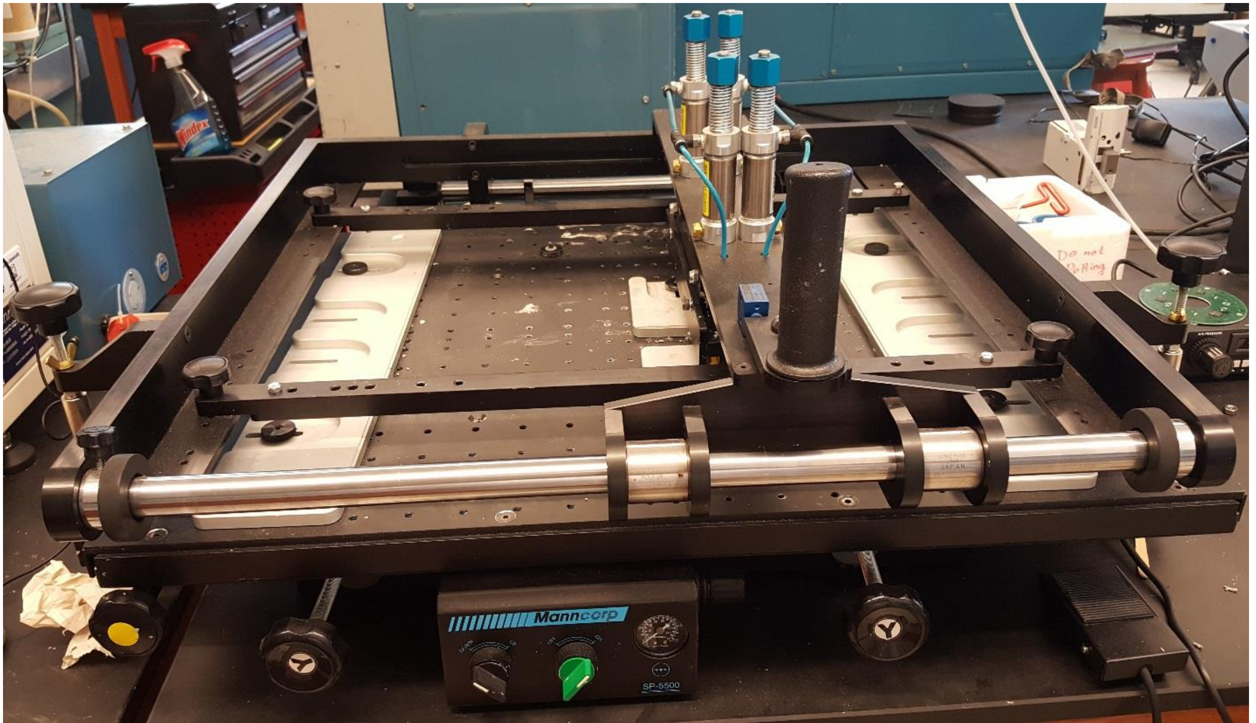


Figure 3-2: Stencil Printer

Figure 3-3: Pick and Place Machine

Figure 3-4: Reflow oven

### 3.3 Approach for Interrogation of Damage in Thermal Aging

In operational environments electronic systems may be stored after manufacture for a finite period prior to deployment. During the storage period, the systems may be exposed to a finite time-period of thermal aging at extreme low or extreme high temperatures in addition to thermal cycling. Once deployed, the systems may be exposed to further thermal aging along with intermittent thermo-mechanical cycling due to power on-off cycles or ambient temperature excursions. Extended exposure to elevated temperature aging may reduce thermo-mechanical reliability in cyclic environments. In this paper, a damage mapping method has been presented based on the underlying failure physics to relate the damage accrued under steady-state thermal aging with a particular combination of temperature and storage time. To achieve this goal, micro-structural evolution of damage has been measured first. In this step, board assemblies have been subjected to single stresses of thermal aging. Samples have been withdrawn periodically and cross-sectioned. Damage proxies studied include the phase-growth parameter, rate of change of phase growth parameter per cycle and the intermetallic thickness. In this thesis, $Ag_3Sn$ and $Cu_6Sn_5$ have been termed as Phase and IMC respectively. EDS was done to ascertain the constituents of these two damage proxies we used as shown in Figure 3-5 and Figure 3-6.

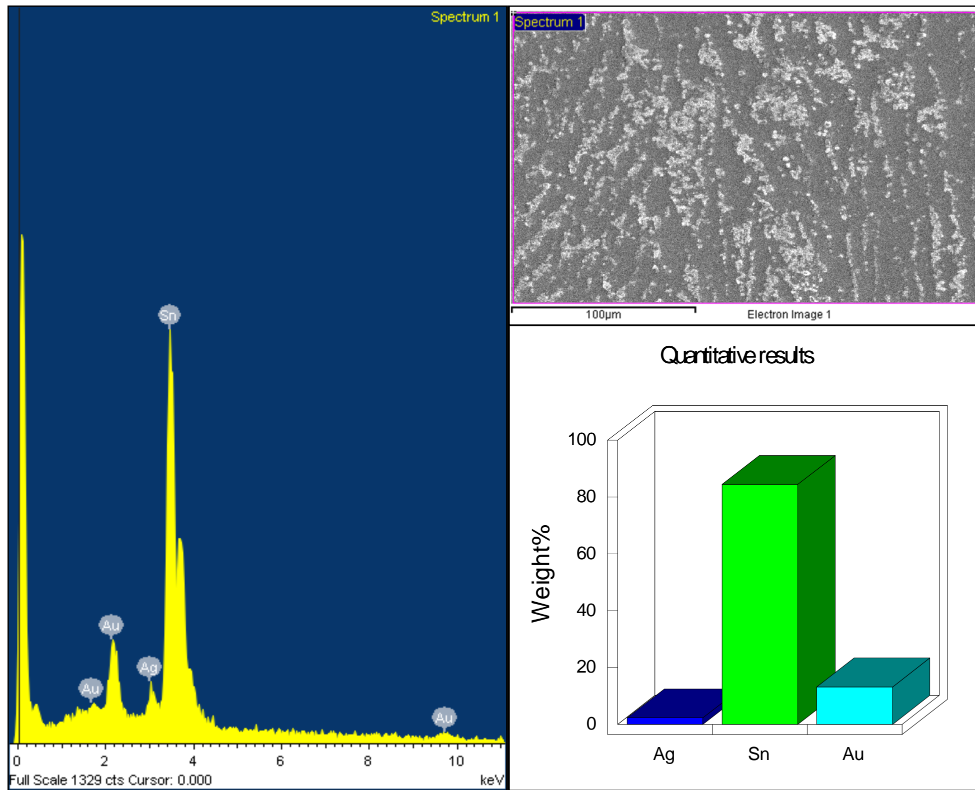


Figure 3-5: EDS plot of Phase.

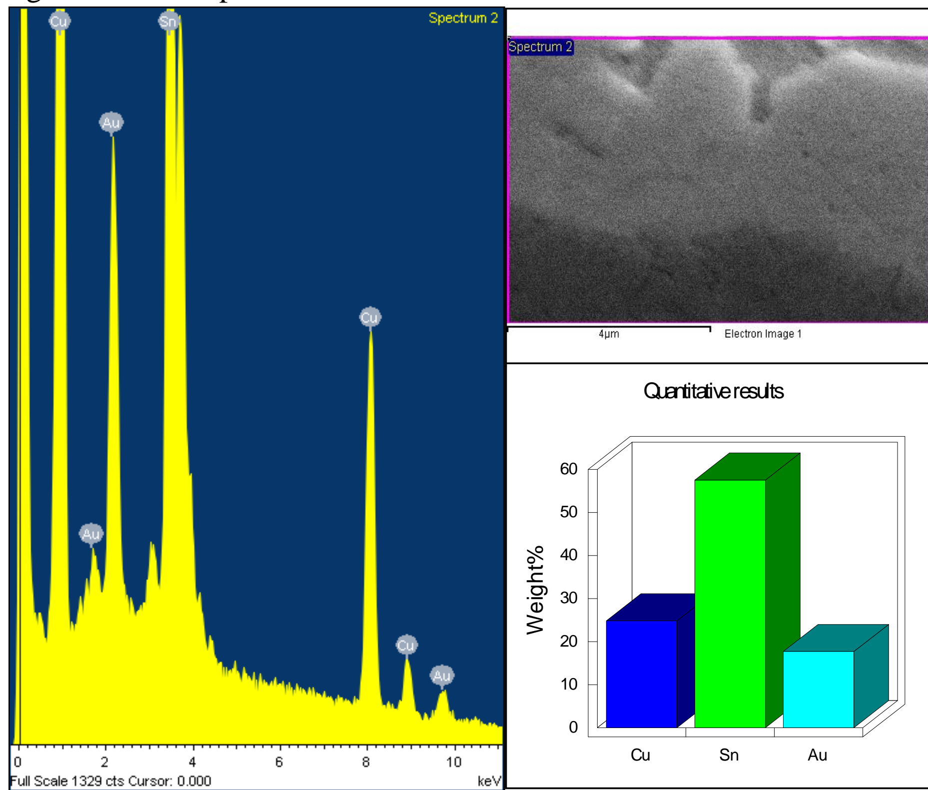


Figure 3-6: EDS plot of IMC.

The phase-growth parameter is represented by symbol 'S' in Eq 3.1. Previously, it has been shown that the rate of change in phase growth parameter [d(lnS)/d(lnN)] is valid damage proxy for prognostication of thermo-mechanical damage in solder interconnects and assessment of residual life [100-109]. The damage proxy [d(lnS)/d(lnN)] is related to the micro structural evolution of damage by the following equation:

$$s = g^4 - g_0{}^4 = at^b \exp(\frac{-E_A}{K_B T}) \qquad \text{Eq. 3.1}$$

where, g is the average grain size at time of prognostication, $g_0$ is the average grain size of solder after reflow, t is the period of aging, S is the phase growth parameter, parameters a and b are the coefficient and exponent respectively. It is anticipated that, longer period of aging at higher temperature will result in higher accrued thermo-mechanical damage in a shorter time. Test samples have been withdrawn and cross-sectioned at periodic intervals. Images of polished samples were taken under SEM at 750x magnification. . Growth rate of $Cu_6Sn_5$ and $Ag_3Sn$ phases was observed. Phase size is measured using image analysis software NI-MAQ. The quantitative measure of $Ag_3Sn$ phase size was determined from a 480pixel x 360pixel rectangular region selected from the SEM images. Figure 3-7 shows the mapping of image.

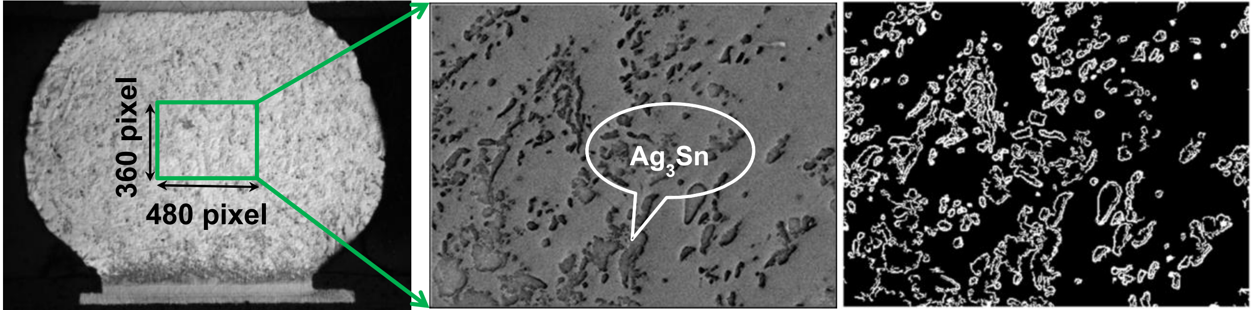


Figure 3-7: Image Mapping

Growth of Inter-Metallic thickness during thermal aging has been studied as another leading indicator of failure in bulk solder. From past studies it has been established that growth of intermetallic thickness is used as a damage precursor for computation of remaining useful life [100-109]. The interfacial intermetallic layers are formed between solder and copper, and some precipitates appear near the interface of the IMCs/solder as shown in Figure 3-8. Trend analysis of intermetallic thickness growth indicates that IMC thickness changes with the square root of aging time,

$$y(t) = y_0 + kt^n \exp\left(\frac{-E_A}{K_B T}\right) \quad \text{Eq. 3.2}$$

where y(t) is IMC growth thickness during aging, $y_0$ is the initial thickness of intermetallic compounds, k is the coefficient standing for the square root of the diffusivity at aging temperature, t is aging time, $E_A$ is the activation energy, $K_B$ is Boltzmann's Constant ($8.617 \times 10^{-5}$ ev/K) and $T_A$ is aging temperature in Kelvin. The exponent value, n = ½ has been used in the above equation, which reveals a diffusion-controlled mechanism during aging. A similar kind of relation can be derived for thermal cycling also.

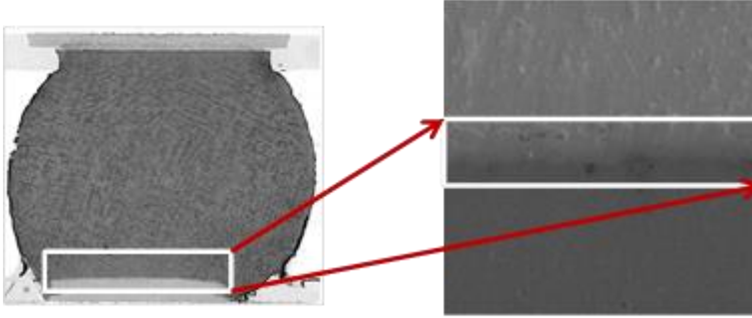

Figure 3-8: Image of IMC growth

### 3.3.1 Damage Mapping Relationships for Phase Growth

In terms of phase growth, the relation between phase growth and aging time can be represented as;

$$\left(\frac{g_p}{g_0}\right)^4 - 1 = S_n = a_0 t^{b_0} = a_1 \exp\left(\frac{-E_A}{K_B T}\right)\left[t^{b_1 \exp\left(\frac{-E_B}{K_B T}\right)}\right] \qquad \text{Eq. 3.3}$$

Where $S_n$ is the normalized phase growth parameter, '$a_1$' is the coefficient for phase growth, '$b_1$' is the phase-growth exponent, $E_A$ is the activation energy, $K_B$ is the Boltzmann Constant, T is the temperature in Kelvin. The normalized phase growth expression has been rearranged as follows:

$$S_n = a_0 t^{b_0} \qquad \text{Eq. 3.4}$$

$$\ln S_n = \ln a_0 + b_0 \ln t \qquad \text{Eq. 3.5}$$

Where,

$$a_0 = a_1 \exp(\frac{-E_A}{K_B T})$$

$$b_0 = b_1 \exp(\frac{-E_B}{K_B T})$$

Eq. 3.6

Using Eq. 3.6 Activation energy was calculated. By using Eq. 3.3 and Eq. 3.6, the relation between aging temperature (T) and aging time (t) for a particular level of damage state in terms of phase growth can be developed as shown below,

$$\ln t = \frac{\ln S_n - \ln a_1 + \left(\frac{E_A}{K_B T}\right)}{b_1 \exp\left(\frac{-E_B}{K_B T}\right)}$$

Eq. 3.7

3.3.2 Damage Mapping Relationships for IMC Growth

The intermetallic thickness based proxy has been related to aging temperature and aging time using the following normalized IMC thickness equation,

$$\frac{y_p}{y_0} - 1 = Y_n = k_0 t^{0.5} = k_1 t^{0.5} \exp(\frac{-E_A}{K_B T})$$

Eq. 3.10

$$Y_n = k_0 \sqrt{t} \text{ where } k_0 = k_1 \exp(\frac{-E_A}{K_B T})$$

Eq. 3.11

Using Eq. 3.11, activation energy of IMC growth was calculated. Slightly rearranging Eq. 3.10, a damage mapping relation for IMC can be derived as shown below,

$$t = \left( \frac{Y_n}{k_1 \exp\left( \frac{-E_A}{K_B T} \right)} \right)^2 \qquad \text{Eq. 3.12}$$

**3.4 Leading Indicators for Thermal Aging**

A set of packages was subjected to aging at 60°C, 75°C and 125°C and were withdrawn after a periodic time-interval of 1- week or 168-hours increments. The samples were cross sectioned, polished. The same joint was examined in each cross-section. Phase growth and intermetallic growth was studied using images taken by SEM at each time interval.

3.4.1 Phase-Growth Damage Proxy

The image analysis software has been used to measure the average phase size. Eq. 3.3 represents the evolution of phase growth in thermal aging based on experimental data. The test data has been used to derive the parameters for normalized phase growth equation. Micrographs of phase structure are shown in Figure 3-9, Figure 3-10 and Figure 3-11 for CABGA 36 and CABGA 256 packages at 60°C, 75°C and 125°C respectively at a time-interval of 168 hours.

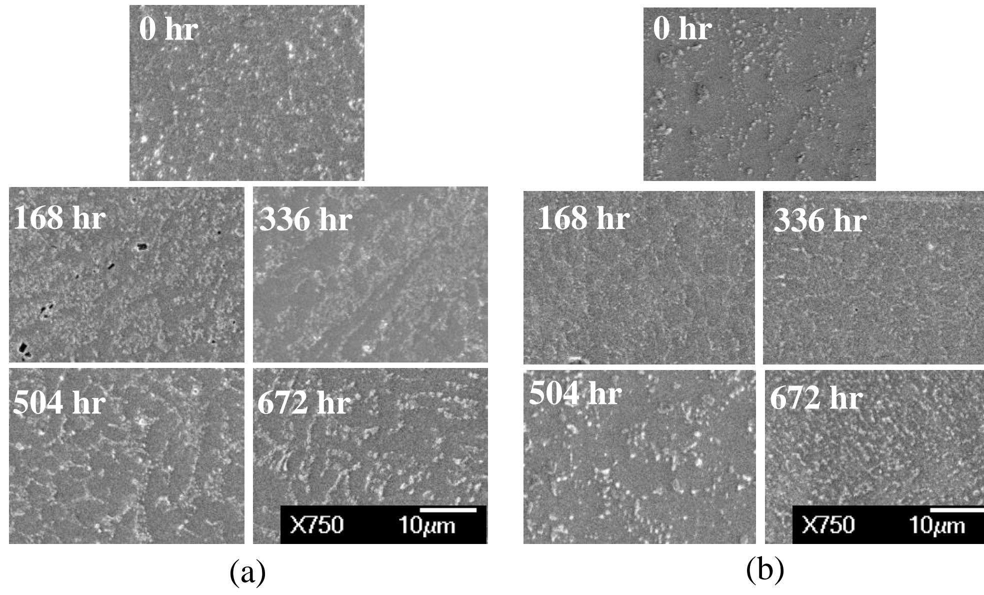


Figure 3-9: SEM images of Phase Growth in (a) PBGA 256 and (b) CABGA 36 at different time intervals at 60°C (Magnification 750X)

The phase coarsening in the microstructure is clearly visible by comparison of 672 hour microstructure with 0-hour microstructure.

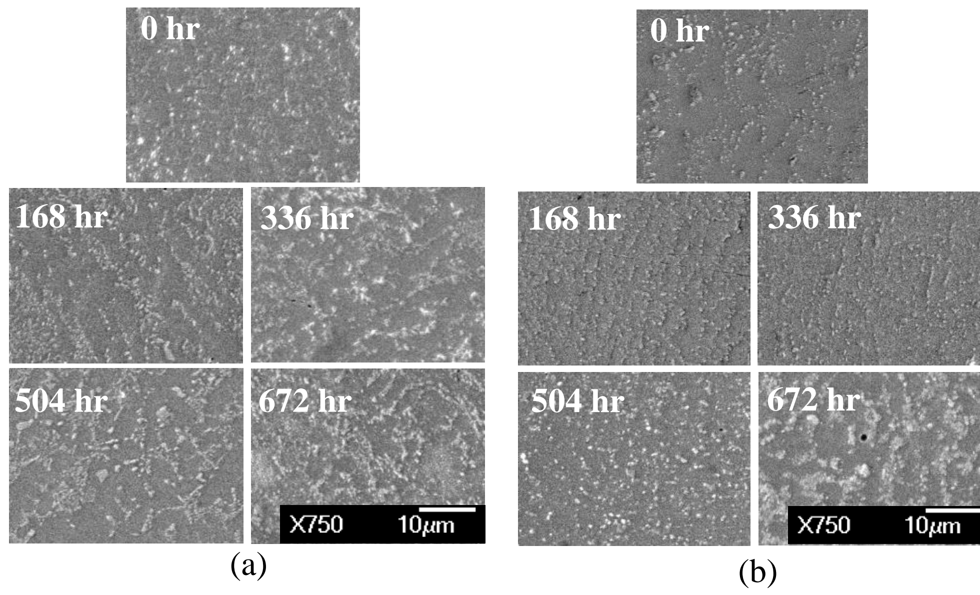


Figure 3-10: SEM images of Phase Growth in (a) PBGA 256 and (b) CABGA 36 at different time intervals at 75°C (Magnification 750X)

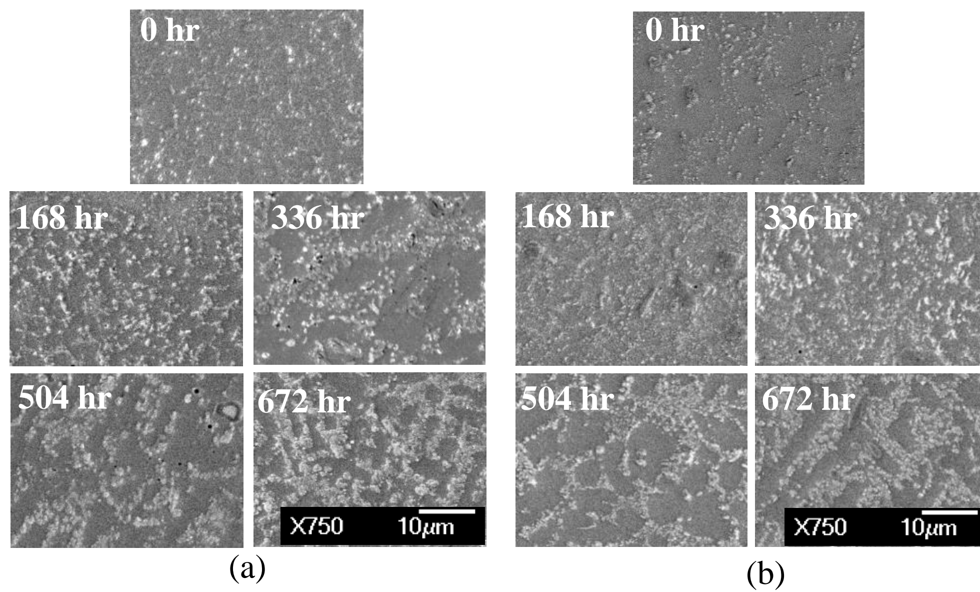


Figure 3-11: SEM images of Phase Growth in (a) PBGA 256 and (b) CABGA 36 at different time intervals at 125°C (Magnification 750X)

Figure 3-12 and Figure 3-13 show the plots of normalized phase growth at different isothermal aging temperature and at various time intervals for PBGA 256 and CABGA 36 respectively. The graphs for the higher temperature have higher normalized phase growth values. The increase in normalized phase growth parameter correlates well with the underlying physics, since higher temperatures will produce more phase growth in an identical period of time. The equation parameters of Eq. 3.3 have been derived based on statistical fit of the experimental data.

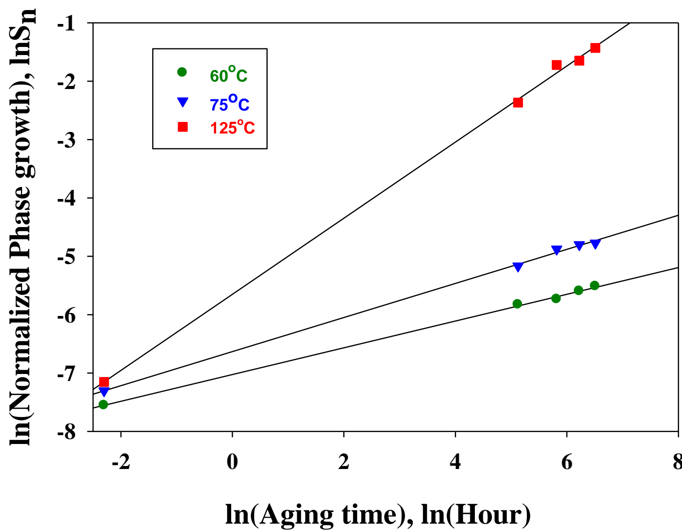


Figure 3-12: Normalized Phase Growth ($S_n$) versus Aging Time (t) for PBGA 256

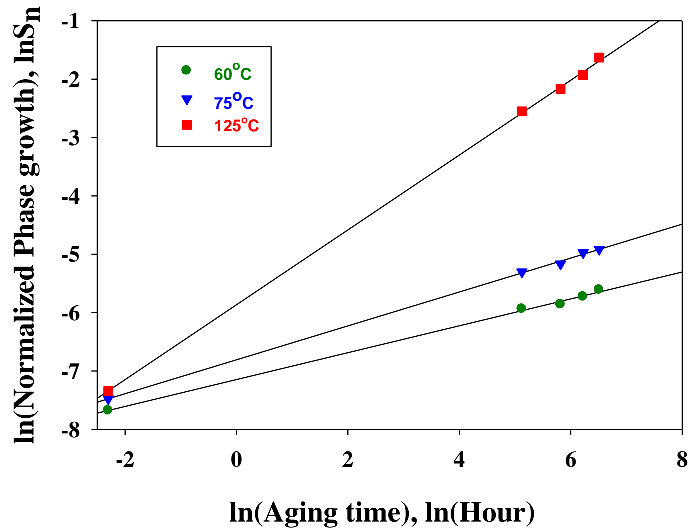


Figure 3-13: Normalized Phase Growth ($S_n$) versus Aging Time (t) for CABGA 36

Table 3-2 shows the values for the phase growth coefficient and the phase growth exponent for the CABGA 36 and the CABGA 256 packages. Values indicate that the phase growth coefficient increases with aging temperature.

Table 3-2: Normalized Phase Growth Coefficients and Exponents for the PBGA 256

| Temperature | $\ln S_n = \ln a_0 + b_0 \ln t$ | | | |
|---|---|---|---|---|
| | PBGA256 | | CABGA36 | |
| | $a_0$ | $b_0$ | $a_0$ | $b_0$ |
| 60°C | 8.9E-4 | 0.24 | 7.95E-4 | 0.23 |
| 75°C | 1.34E-3 | 0.29 | 1.1E-3 | 0.29 |
| 125°C | 3.5E-3 | 0.65 | 2.8E-3 | 0.64 |

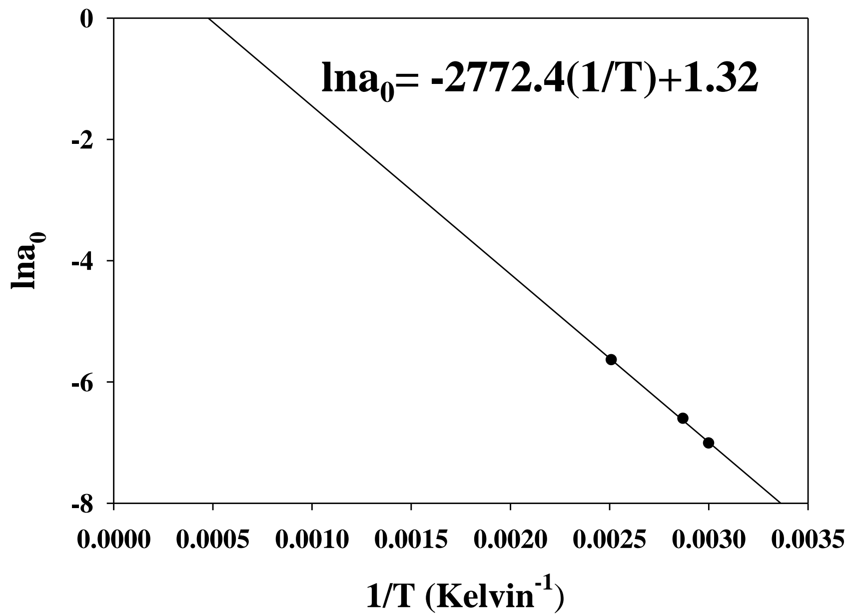


Figure 3-14: $\ln(a_0)$ versus Aging temperature for PBGA 256

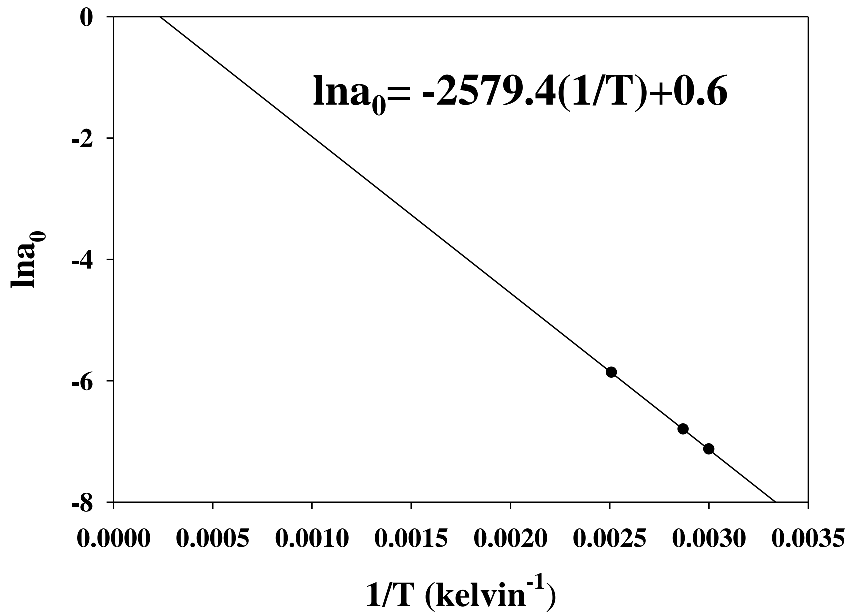


Figure 3-15: $\ln(a_0)$ versus Aging temperature for CABGA 36

The coefficient term changes with temperature of exposure because of the underlying agglomeration of phases proceeds at a faster pace at a higher temperature. The activation

energy of the coefficient term has been computed by fitting the data to Equation 3.6. Figure 3-14 and Figure 3-15 show the relationship between ln($a_0$) and (1/T), where T is the absolute temperature. Slope of the fit of ln(a0) versus (1/T) is $E_A/K_B$, where $E_A$ is the activation energy; $K_B$ is Boltzmann's Constant (8.617x10- 5 ev/K). The Activation energy of phase growth is calculated as 0.22eV for CABGA 36 and 0.24eV for PBGA 256.

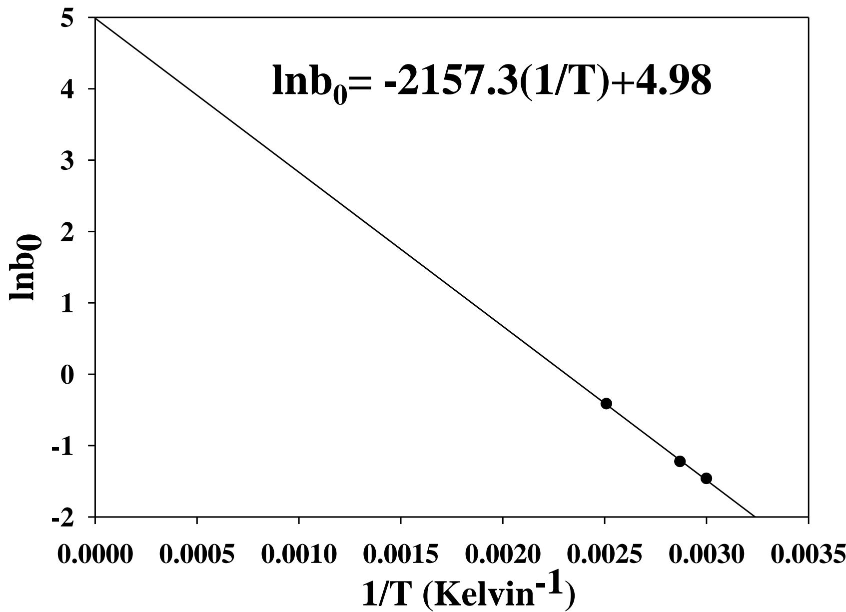


Figure 3-16: Plot of ln($b_0$) and Aging temperature for PBGA256

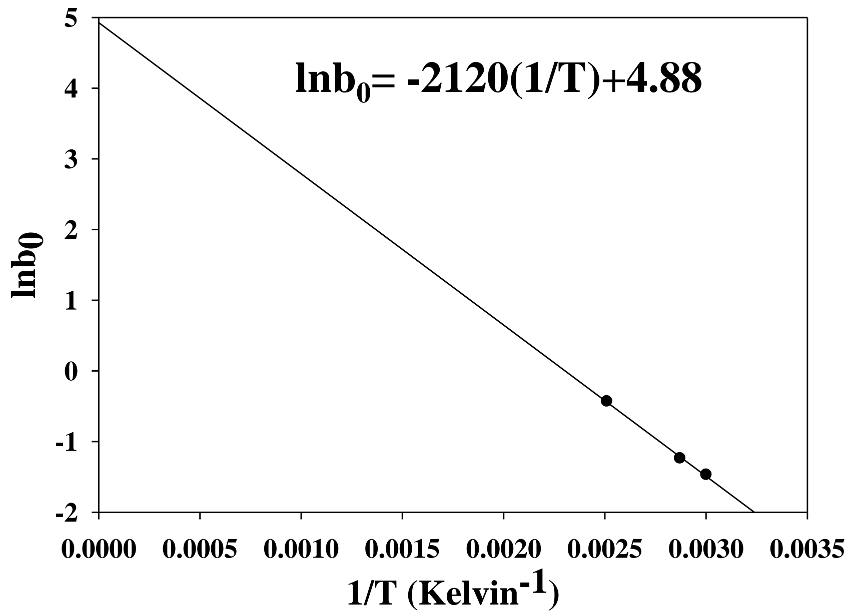


Figure 3-17: Plot of $\ln(b_0)$ and Aging temperature for CABGA36

The exponent term ($b_0$) also changes with temperature of exposure. The activation energy of the exponent term has been computed by fitting the data to Equation 3.6. Slope of this fit is $E_B/K_B$, where $E_B$ is the activation energy based on exponent; $K_B$ is Boltzmann's Constant (8.617x10-5 ev/K). The Activation energy based on phase growth exponent is calculated as 0.18eV for CABGA 36 and 0.19eV for PBGA 256.

Table 3-3: Activation Energy of Phase Growth

| | $E_A$ (ev) | $E_B$ (ev) |
|---|---|---|
| CABGA 36 | 0.22 | 0.18 |
| PBGA 256 | 0.24 | 0.19 |

3.4.2 Intermetallic Thickness Damage Proxy

The image analysis software has been used to measure the average intermetallic thickness. Eq. 3.10 represents the evolution of intermetallic growth in thermal aging based on experimental data. The equation parameters have been derived based on experimental measurements of the intermetallic growth from cross-sections. Micrographs of IMC for 60°C are shown in Figure 3-18, for 75°C in Figure 3-19 and for 125°C in Figure 3-20 for both CABGA 36 and CABGA 256 packages at a time-interval of 168 hours. The increase in thickness in the microstructure is clearly visible by comparison of 672 hour microstructure with 0-hour microstructure.

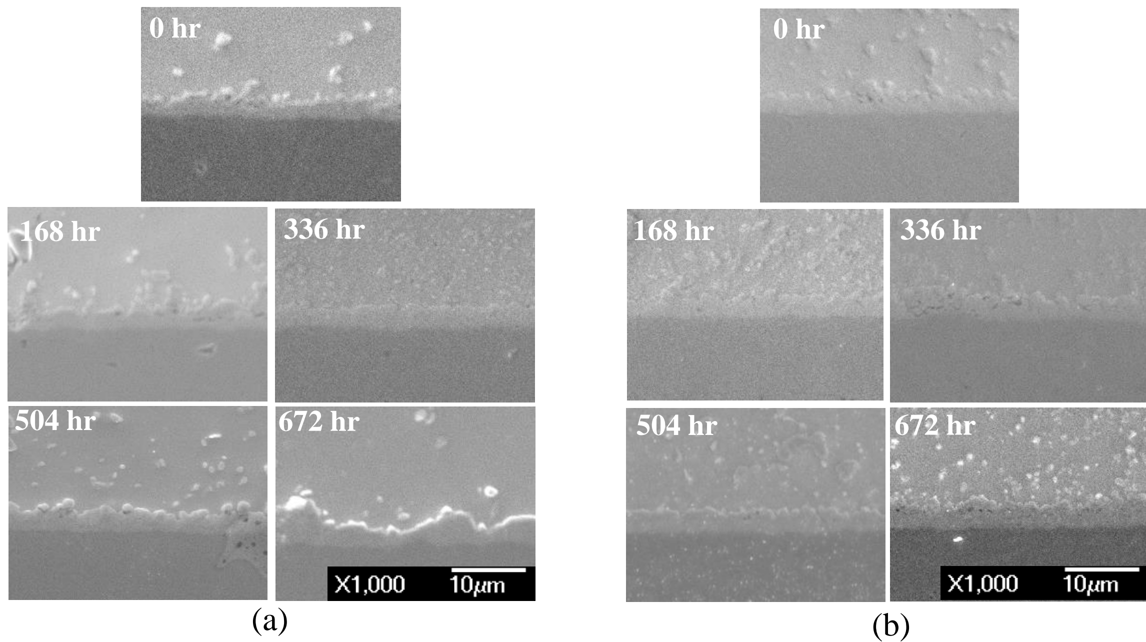


Figure 3-18: SEM images of IMC Growth in (a) PBGA 256 and (b) CABGA 36 at different time intervals at 60°C (Magnification 1000X)

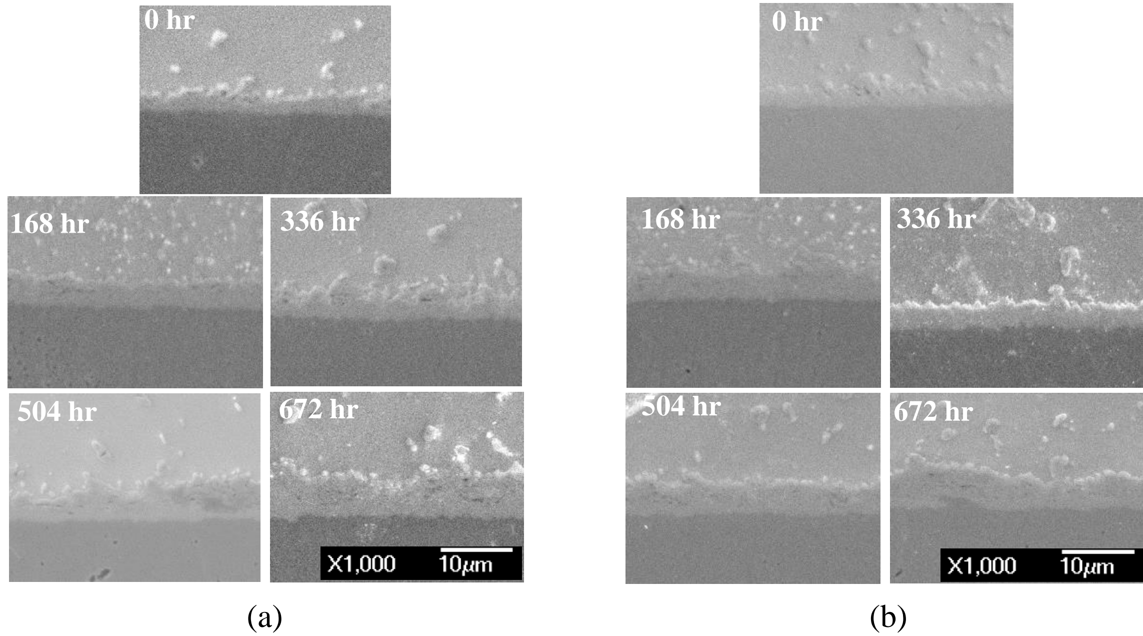


Figure 3-19: SEM images of IMC Growth in (a) PBGA 256 and (b) CABGA 36 at different time intervals at 75°C (Magnification 1000X)

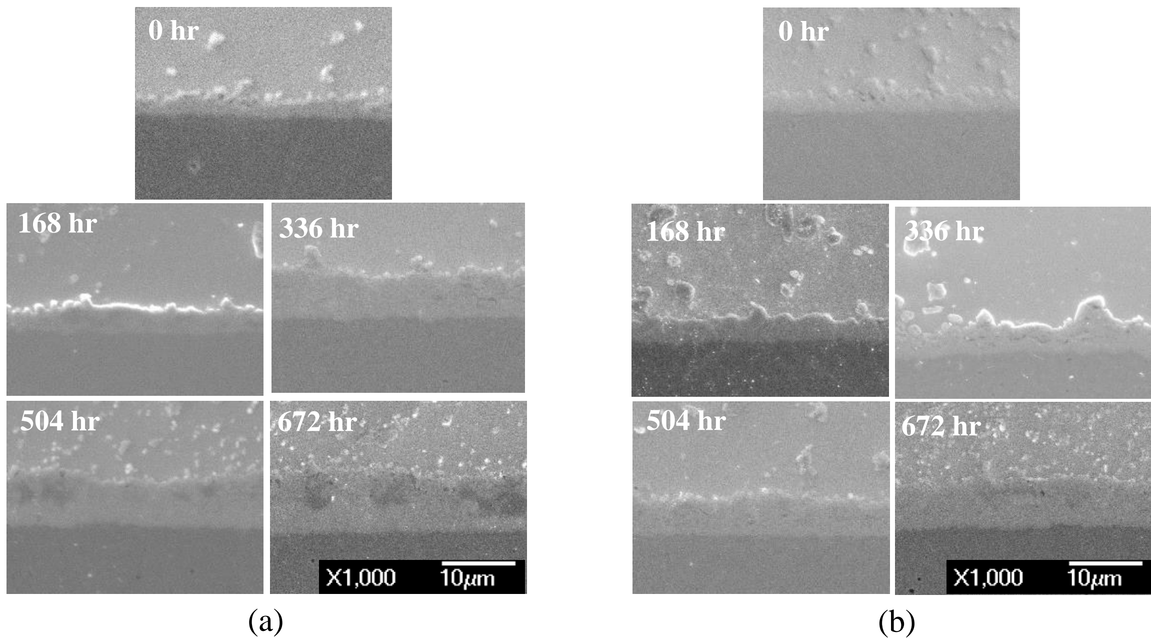


Figure 3-20: SEM images of IMC Growth in (a) PBGA 256 and (b) CABGA 36 at different time intervals at 125°C (Magnification 1000X)

Figure 3-21 and Figure 3-22 show the plots of normalized intermetallic growth at different isothermal aging temperature and at various time intervals for PBGA 256 and CABGA 36 respectively. The graphs for the higher temperature have higher normalized intermetallic growth values. The increase in normalized intermetallic thickness parameter correlates with the underlying physics, since the higher temperatures will produce more intermetallic thickness due to higher diffusion rates in an identical period of time. Eq. 3.11 for IMC growth under thermal aging has been fit to experimental data. The equation parameters have been derived based on statistical fit of the experimental data.

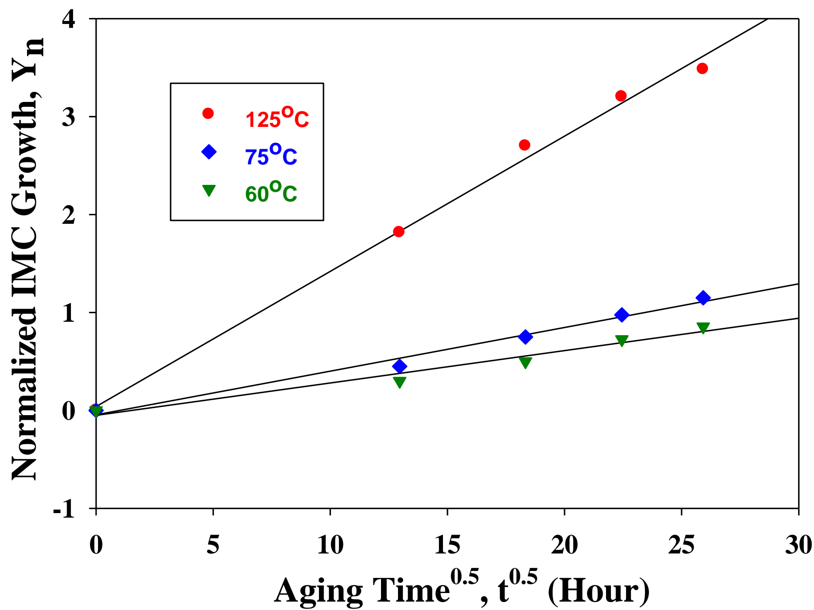


Figure 3-21: Relation between Normalized IMC Growth (Yn) and Aging Time (t) for PBGA 256

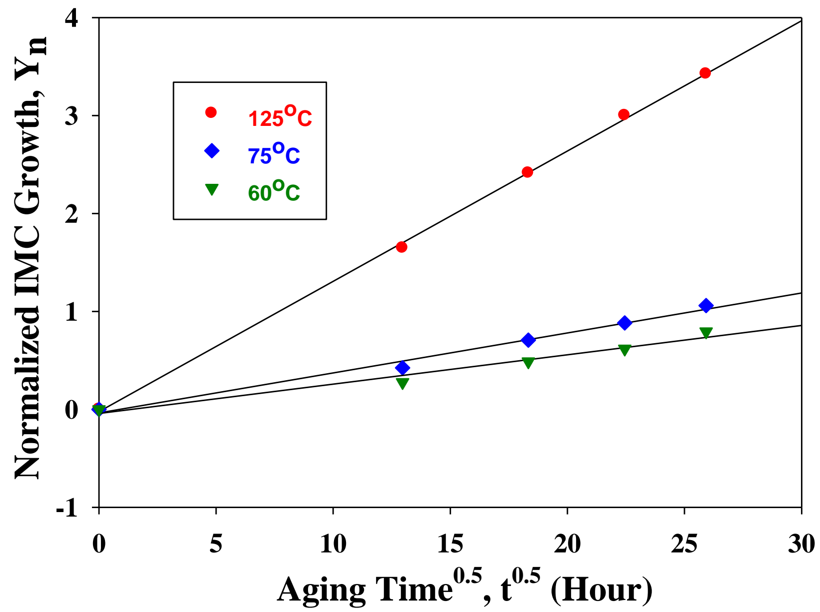


Figure 3-22: Relation between Normalized IMC Growth (Yn) and Aging Time (t) for CABGA 36

Table 3-4: Normalized IMC Growth Coefficients

| | $Y_n = k_1 \exp\left(\frac{-E_A}{K_B T}\right) t^{0.5} = k_0 t^{0.5}$ | |
|---|---|---|
| Temp. | $k_0$(CABGA 36) | $k_0$(PBGA 256 ) |
| 60°C | 0.028 | 0.03 |
| 75°C | 0.039 | 0.042 |
| 125°C | 0.13 | 0.14 |

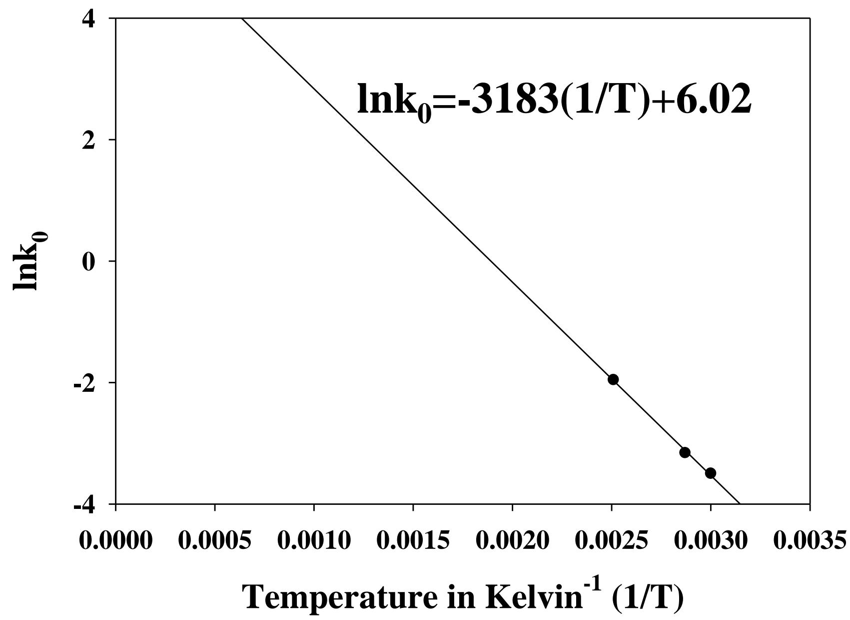


Figure 3-23: Plot of $lnk_0$ and Aging temperature, T for PBGA 256

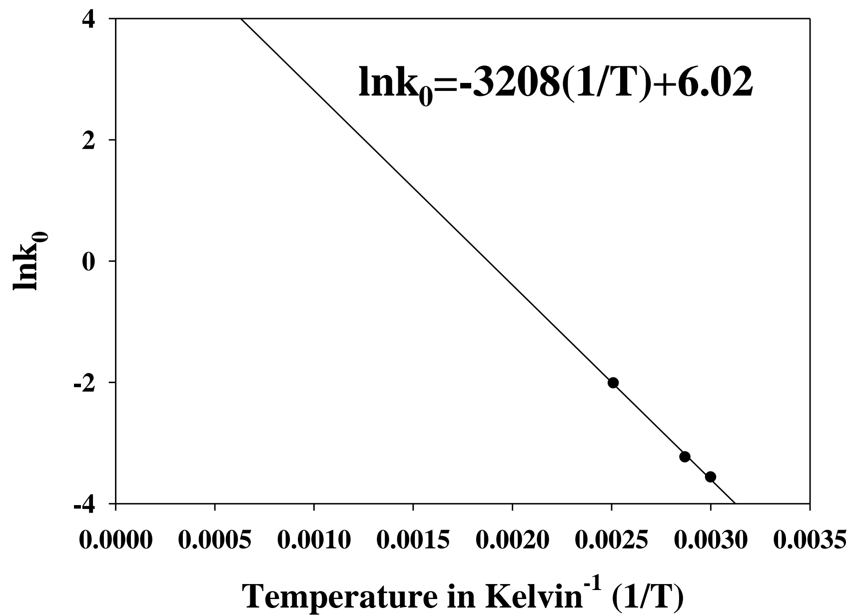


Figure 3-24: Plot of $lnk_0$ and Aging temperature, T for CABGA 36

The activation energy has been computed by fitting the experimental data according to Eq. 3.11. Figure 3-23 and Figure 3-24 show the relationship between $\ln k_0$ and (1/T), where T is the absolute temperature.

Table 3-5: Activation Energy for IMC Growth Coefficient

| | $E_A$ (ev) |
|---|---|
| CABGA 36 | 0.28 |
| PBGA 256 | 0.27 |

Slope of this fit is $E_A/K_B$, where $E_A$ is the activation energy; $K_B$ is Boltzmann's Constant (8.617x10-5 ev/K). The Activation energy of IMC growth is calculated as 0.28eV for both CABGA 36 and PBGA 256.

### 3.5 Damage Mapping

In this section, a method for damage mapping has been developed using the data gathered on the test vehicles. Temperature and time combinations required to achieve a specified value of normalized phase growth have been calculated. The damage accrued can thus be sustained in a shorter time at a high temperature or in a longer time at a lower temperature. Now re-visiting Eq 3.7,

$$\ln t = \frac{\ln S_n - \ln a_1 + \dfrac{E_A}{K_B T}}{b_1 \exp\left(\dfrac{-E_B}{K_B T}\right)} \qquad \text{Eq. 3.7}$$

This equation shows relation between aging time (t) and aging temperature (T) for a particular value of damage state ($S_n$) i.e. normalized phase growth value.

Figure 3-25 shows the relation between aging temperatures and required aging time in hours for a particular value of damage state in terms of phase growth for both the CABGA 36 and CABGA 256 packages.

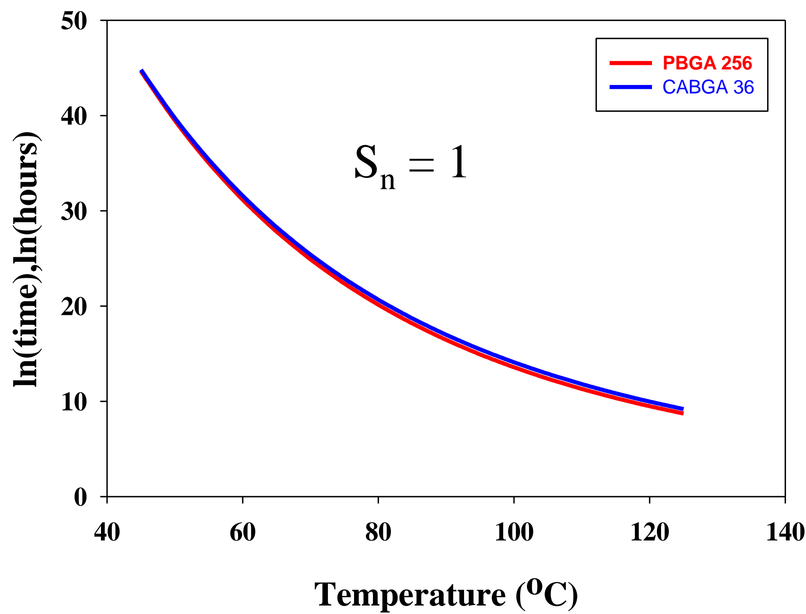


Figure 3-25: Iso-phase growth plots of Aging temperature (T) vs Aging time(t)

Now revisiting Eq 3.12,

$$t = \left( \frac{Y_n}{k_1 \exp\left( \frac{-E_A}{K_B T} \right)} \right)^2 \qquad \text{Eq. 3.12}$$

This equation shows relation between aging time (t) and aging temperature (T)for a particular value of damage state ($Y_n$)i.e. normalized IMC growth value. Figure 3-26 plots this relation i.e. the temperature and time combinations required to achieve a specified value of normalized IMC thickness.

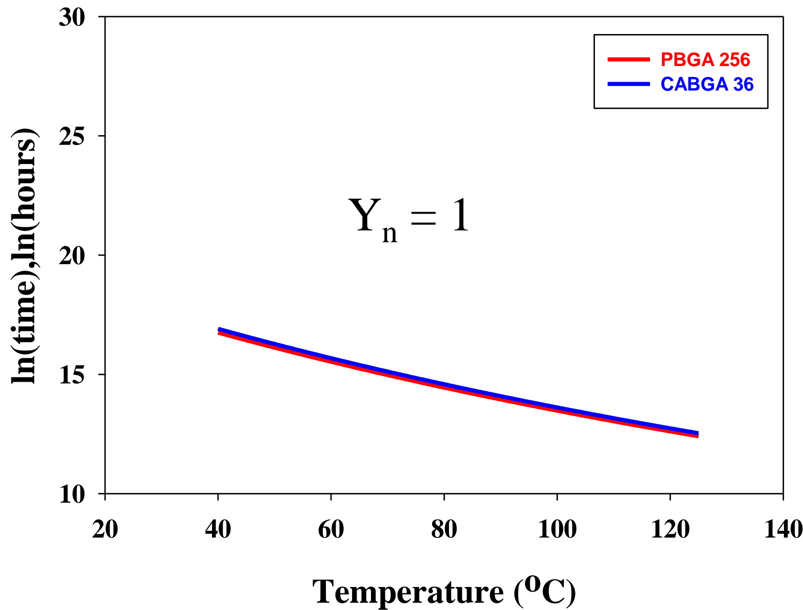


Figure 3-26: Iso-IMC growth plots of Aging Time, ln(T) vs Aging Temperature

Figure 3-25 and Figure 3-26 revealed that CABGA 36 and PBGA 256 showed almost similar performance in terms of reliability. Although PBGA 256 has larger chip size than CABGA 36, its effect on shear strain was compensated by larger ball stand-off height in PBGA 256. Figure 3-25 and Figure 3-26 also bears an implication of using a unified damage mapping model as damage mapping plots for both packages almost merged for both of the damage proxy used. The following tables show the validity of the unified damage mapping model. Here a single model was used to calculate the aging time required

to reach a particular level of damage at a particular aging temperature and then compared with experimental value. Average error was calculated and it was found to be within tolerable limit.

Table 3-6: Validity of damage mapping model based on Phase Growth

| | PBGA 256 | | | | CABGA 36 | | | |
|---|---|---|---|---|---|---|---|---|
| | $lnS_n$ | Time (Data fit) hr. | Time (Exp.) hr. | Error (%) | $lnS_n$ | Time (Data fit) hr. | Time (Exp.) hr. | Error (%) |
| 60°C | -5.83 | 186.91 | 168 | 11.25 | -5.94 | 209.63 | 168 | 24.78 |
| | -5.74 | 281.75 | 336 | 16.15 | -5.86 | 290.94 | 336 | 13.41 |
| | -5.60 | 526.94 | 504 | 4.55 | -5.73 | 525.20 | 504 | 4.21 |
| | -5.51 | 758.59 | 672 | 12.89 | -5.61 | 884.35 | 672 | 31.60 |
| 75°C | -5.17 | 145.21 | 168 | 13.57 | -5.30 | 158.70 | 168 | 5.53 |
| | -4.88 | 384.27 | 336 | 14.37 | -5.17 | 250.09 | 336 | 25.57 |
| | -4.80 | 498.20 | 504 | 1.15 | -4.97 | 480.76 | 504 | 4.61 |
| | -4.78 | 540.94 | 672 | 19.50 | -4.92 | 582.79 | 672 | 13.28 |
| 125°C | -2.37 | 157.93 | 168 | 5.99 | -2.55 | 180.87 | 168 | 7.66 |
| | -1.72 | 426.49 | 336 | 26.93 | -2.17 | 329.70 | 336 | 1.88 |
| | -1.65 | 478.49 | 504 | 5.06 | -1.93 | 480.52 | 504 | 4.66 |
| | -1.43 | 670.26 | 672 | 0.26 | -1.63 | 764.15 | 672 | 13.71 |
| | Average Error | | | 11% | Average Error | | | 12.7% |

Table 3-7: Validity of damage mapping model based on IMC Growth

| | PBGA 256 | | | | CABGA 36 | | | |
|---|---|---|---|---|---|---|---|---|
| | $\ln Y_n$ | Time (Data fit) hr. | Time (Exp.) hr. | Error (%) | $\ln Y_n$ | Time (Data fit) hr. | Time (Exp.) hr. | Error (%) |
| 60°C | 0.3 | 106.61 | 168 | 36.54 | 0.276 | 105.34 | 168 | 37.3 |
| | 0.50 | 296.14 | 336 | 11.86 | 0.488 | 328.51 | 336 | 2.23 |
| | 0.73 | 622.63 | 504 | 23.54 | 0.618 | 525.73 | 504 | 4.31 |
| | 0.86 | 865.93 | 672 | 28.86 | 0.794 | 869.07 | 672 | 29.33 |
| 75°C | 0.45 | 105.22 | 168 | 37.37 | 0.424 | 107.73 | 168 | 35.87 |
| | 0.75 | 292.29 | 336 | 13.01 | 0.706 | 299.26 | 336 | 10.93 |
| | 0.98 | 493.97 | 504 | 1.99 | 0.882 | 467.60 | 504 | 7.22 |
| | 1.15 | 687.20 | 672 | 2.26 | 1.06 | 673.34 | 672 | 0.20 |
| 125°C | 1.82 | 171.94 | 168 | 2.35 | 1.65 | 160.71 | 168 | 4.34 |
| | 2.70 | 380.50 | 336 | 13.24 | 2.41 | 344.58 | 336 | 2.55 |
| | 3.20 | 534.47 | 504 | 6.05 | 3.00 | 533.17 | 504 | 5.79 |
| | 3.48 | 632.09 | 672 | 5.94 | 3.42 | 694.33 | 672 | 3.32 |
| | Average Error | | | 15.24% | Average Error | | | 12% |

### 3.6 Summary and Conclusions

A damage mapping method has been developed based on the underlying physics-based leading indicators to relate aging time and temperature needed to reach a particular level of damage under accelerated steady-state thermal storage. The method has been developed with two different packages including the CABGA36 and the PBGA256 packages.

Analysis results indicate convergence of damage mapping relationships for the two package architecture examined for the failure mechanisms of solder joint failure. Also activation energy of formation of both of the damage proxies were calculated and found to be within acceptable range, which also supports the validity of the damage proxies used.

# Chapter 4

# Study of Effect of Mean Temperature of Thermal Cycle on SnAgCu Solder Joint Reliability

## 4.1 Overview

Electronics in a variety of applications such as automotive underhood on-engine, on-transmission, high-performance computing, military, and defense applications may be subjected to prolonged exposure to high temperature in addition to wide cyclic temperature extremes. Further, the mean temperature of the thermal excursion may vary based on application. Prior, studies have revealed that leadfree material properties degrade with prolonged exposure to high temperature. Furthermore, prior exposure to high temperature aging has been shown to reduce life by as much as 50% during thermal cycling. The effects are most pronounced in the widely used SnAgCu based alloys including SAC105, SAC205, SAC305 and SAC405 solders. Thus, prior data suggests that the cyclic life for leadfree assemblies cannot be considered without considering mean cyclic temperature. However, the current, closed form life prediction models for leadfree second-level interconnects do not provide any method for quick-assessment of effect of mean temperature on the expected life under thermal cycling. In this paper, a new model has been developed for the assessment of the effect of the thermal cycle's mean temperature on the cyclic life of a leadfree assembly. Three ball-grid arrays including CABGA 144, PBGA 256 and PBGA 676 have been subjected to three thermal cycling conditions including -50°C to +50°C, 0°C to 100°C, 50°C to 150°C. The temperature difference of all the thermal cycling profiles has been kept the same while the mean temperature has been varied.

Microstructural indicators including phase growth in solder interconnects, intermetallic thickness has been measured. In addition, a separate population of the parts has been cycled to failure under each of the three conditions. Predictive model has been developed for mapping the cyclic damage for leadfree electronics subjected to mean cyclic temperatures. Model predictions have been correlated with experimental Weibull failure distributions in order to quantify the model accuracy and precision. The ability to assess the effect of mean cyclic temperature on the thermal fatigue reliability will allow reliability assessment of leadfree electronics using prior accelerated test data for any mean temperature and thermal cycle magnitude.

## 4.2 Test Vehicle

In this study, three different leadfree assemblies with CABGA 144, PBGA-676 and PBGA-256 packages have been used. The packages are full-array configuration and Sn3Ag0.5Cu solder interconnects. The ball diameter for the 144 I/O, 256 I/O and 676 I/O BGA is 0.3, 0.32 and 0.48 mm respectively. Package attributes are shown in Table 4-1. The printed circuit board was a double-sided FR4-06 material. The printed circuit board pads were non-solder mask defined (NSMD) with immersion tin finish. Figure 4-1 shows the packages. All test vehicles were subjected to thermal cycling environments ranging from TC1: -50°C to 50°C, TC2: 0°C to 100°C and TC3: 50°C to 150°C for various numbers of cycles. The test board is a JEDEC form-factor test board with corner holes. Each test package has four daisy chain patterns corresponding to the four quadrants. Board assemblies were assembled at in-house surface mount facility of CAVE3. The reflow profile used for assembly is shown in Figure 4-2

Table 4-1: Package features

| | Board A | Board B | Board C |
|---|---|---|---|
| Solder | Sn3Ag0.5Cu | Sn3Ag0.5Cu | Sn3Ag0.5Cu |
| Body Size (mm) | 27 mm | 17 mm | 13mm |
| Package Type | Plastic BGA | Plastic BGA | CABGA |
| I/O Count | 676 | 256 | 144 |
| I/O Pitch (mm) | 1 | 1 | 1 |
| Ball Height (mm) | 0.48 | 0.32 | 0.3 |
| Matrix | 26 x 26 | 16 x 16 | 12 x 12 |
| Pad (board) | NSMD | NSMD | NSMD |
| Pad (package) | SMD | SMD | SMD |
| Board Finish | ImSn | ImSn | ImSn |

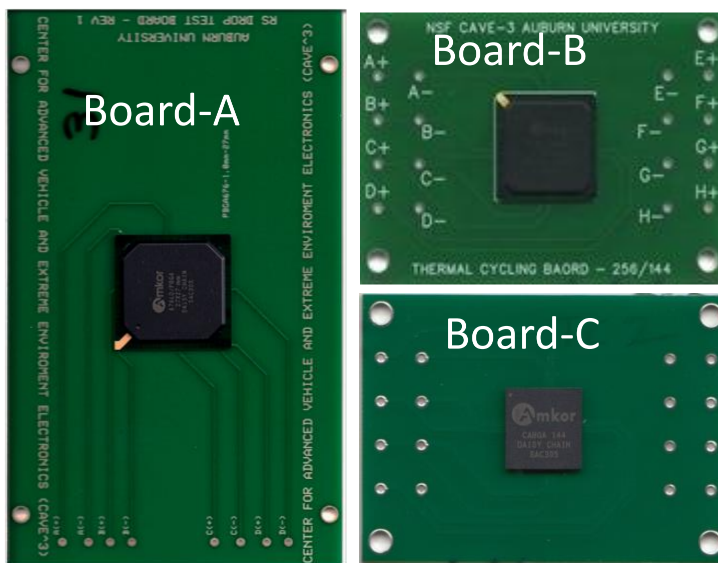


Figure 4-1: Test vehicle

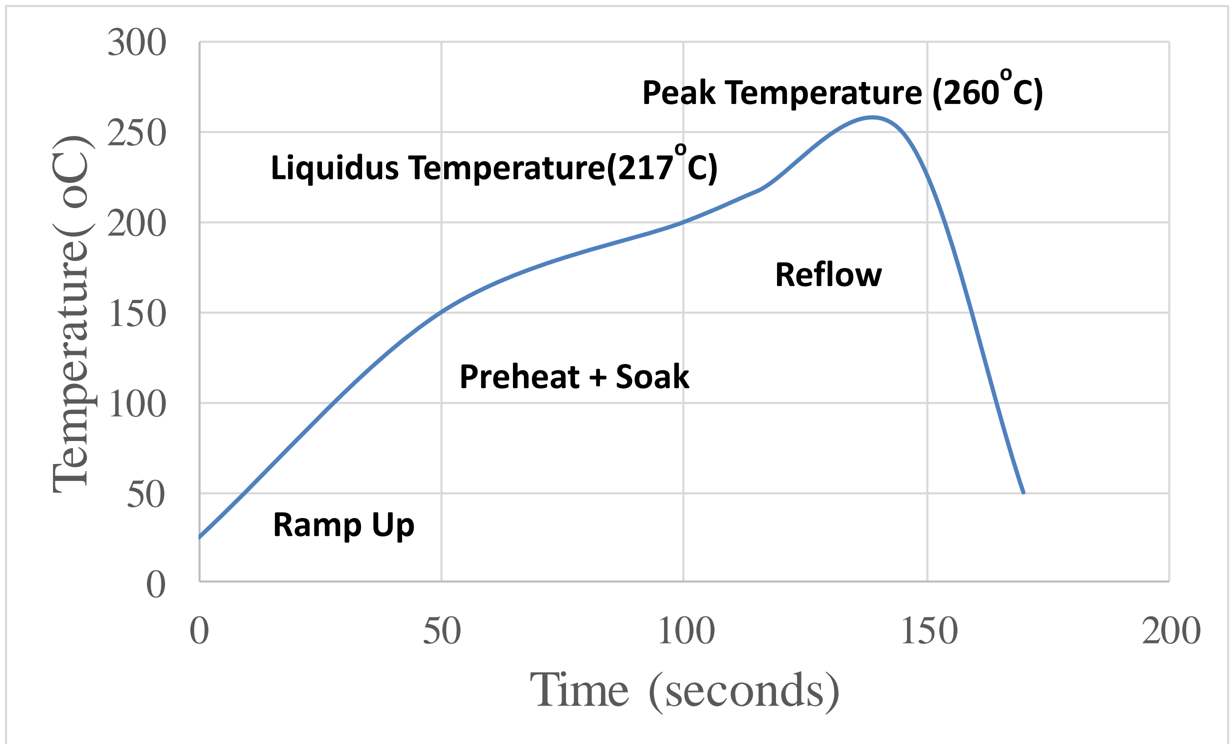


Figure 4-2: Reflow profile

### 4.3 Approach for Interrogation of Damage in Thermal Cycling

Packages in operational environments may be exposed to various ranges of thermal cycling due to power on-off cycles or ambient temperature excursions. This makes mapping of accelerated test data to operational environments very challenging. In this paper, a damage mapping method has been presented based on the underlying failure physics to relate the damage accrual rate amongst different thermal cycling test conditions having same ΔT but varying mean temperature. The approach has been developed in three steps.

#### 4.3.1 Micro-structural Evolution of Damage

In this step, three sets of board assemblies have been subjected to single stresses of thermal cycling. Samples have been withdrawn periodically and cross-sectioned. Damage proxies studied include the phase-growth parameter and the intermetallic thickness parameter. The

phase-growth parameter is represented by symbol ‘S’ in Eq. 4.1. Previously, it has been shown that the rate of change in phase growth parameter [d(lnS)/d(lnN)] is a valid damage proxy for prognostication of thermo-mechanical damage in solder interconnects and assessment of residual life [100-109]. The damage proxy [d(lnS)/d(lnN)] is related to the micro structural evolution of damage by the following equation:

$$S = g^4 - g_0{}^4 = aN^b \qquad \text{Eq. 4.1}$$

$$\ln S = \ln(g^4 - g_0{}^4) = \ln a + b \ln N$$

$$\frac{d\ln S}{d\ln N} = b = \text{Phase growth accumulation rate}$$

where, g is the average grain size at time of prognostication, $g_0$ is the average grain size of solder after reflow, N is the number of cycle, S is the phase growth parameter, parameters a and b are the coefficient and exponent respectively. It is anticipated that, higher number of cycles at higher mean temperature will result in higher accrued thermo-mechanical damage and result in a higher slope of the phase growth parameter versus number of cycles. Test samples have been withdrawn and cross-sectioned at periodic intervals. Images of polished samples were taken under SEM at 750x magnification. . Growth rate of $Ag_3Sn$ phases was observed. Phase size is measured using image analysis software NI-MAQ. The quantitative measure of $Ag_3Sn$ phase size was determined from a 480µm x 360µm rectangular region selected from the SEM images. Figure 4-3 shows the mapping of image.

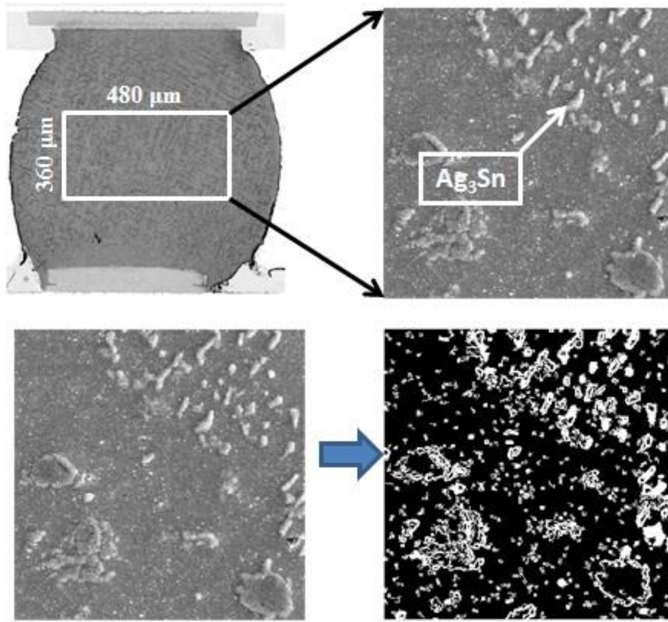


Figure 4-3: Image Mapping

Growth of Inter-Metallic thickness during thermal cycling has been studied as another leading indicator of failure in bulk solder. From past studies it has been established that growth of intermetallic thickness is used as a damage precursor for computation of remaining useful life [100-109]. The interfacial intermetallic layers are formed between solder and copper, and some precipitates appear near the interface of the IMCs/solder as shown in Figure 4-4. These intermetallic layers have been identified to consist of $Cu_3Sn$ and $Cu_6Sn_5$ phases. Eq. 4.2 shows how IMC thickness is related with number of cycles.

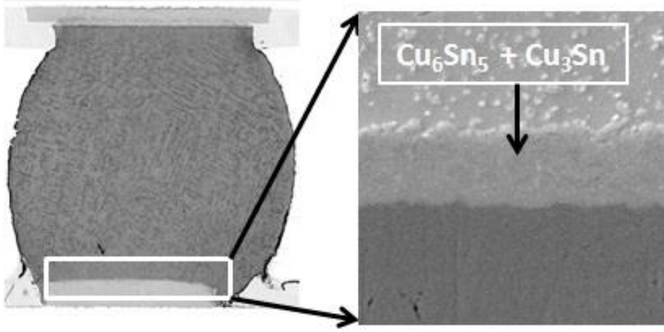


Figure 4-4: IMC formation

$$y(t) = y_0 + kN^n \exp\left(\frac{-E_A}{K_B T}\right) \qquad \text{Eq. 4.2}$$

where y(t) is IMC growth thickness during cycling, $y_0$ is the initial thickness of intermetallic compounds, k is the coefficient of IMC growth, N is number of cycles, $E_A$ is the activation energy, $K_B$ is Boltzmann's Constant (8.617 x $10^{-5}$ ev/K) and T is mean temperature of cycling range in Kelvin .

4.3.2 Damage Mapping Relationships for Phase Growth

The relation between phase growth and number of cycles has been normalized with respect to the initial phase size, as follows,

$$S_n = \left(\frac{g_p}{g_0}\right)^4 - 1 = a_0 N^{b_0} \qquad \text{Eq. 4.3}$$

$$S_n = a_1 \exp\left(\frac{-E_A}{K_B T}\right)\left[N^{b_1 \exp\left(\frac{-E_B}{K_B T}\right)}\right]$$

Where $S_n$ is the normalized phase growth parameter, '$a_1$' is the coefficient for phase growth, '$b_1$' is the phase-growth exponent, $E_A$ and $E_B$ is the activation energy based on phase growth coefficient and exponent respectively, $K_B$ is the Boltzmann Constant, T is the mean temperature of cycling range in Kelvin. The normalized phase growth expression from Eq. 4.3 has been rearranged as follows:

$$S_n = a_0 N^{b_0}$$
$$\ln S_n = \ln a_0 + b_0 \ln N \qquad \text{Eq. 4.4}$$

$$a_0 = a_1 \exp\left(\frac{-E_A}{K_B T}\right) \qquad \text{Eq. 4.5}$$

$$b_0 = b_1 \exp\left(\frac{-E_B}{K_B T}\right) \qquad \text{Eq. 4.6}$$

Here $a_0$ is the temperature dependent phase growth coefficient and $b_0$ is temperature dependent phase growth exponent. Taking a natural logarithm of Eq. 4.5 and Eq. 4.6, the relationship has been reduced to that of a straight line,

$$\ln a_0 = \ln a_1 - \left(\frac{E_A}{K_B T}\right) \qquad \text{Eq. 4.7}$$

$$\ln b_0 = \ln b_1 - \left(\frac{E_B}{K_B T}\right) \qquad \text{Eq. 4.8}$$

By plotting experimental values of normalized phase growth ($S_n$) with respect to number of cycles (N) the values of coefficient and exponent in Eq. 4.4 have been computed. The intercept ($\ln a_0$) and slope ($b_0$) have been plotted with respect to mean temperature to calculate the Activation energy of phase growth based on coefficient ($E_A$) and Activation energy of phase growth based on exponent ($E_B$) respectively.

### 4.3.3 Damage Mapping Relationships for IMC Growth

The intermetallic thickness based damage proxy has been related to mean temperature of cycling range and number of cycles using the following normalized IMC thickness equation,

$$Y_n = \frac{y_p}{y_0} - 1 = k_0 N^{b_0}$$

$$\ln Y_n = \ln k_0 + b_0 \ln N \qquad \text{Eq. 4.9}$$

Where

$$k_0 = k_1 \exp\left(\frac{-E_A}{K_B T}\right) \qquad \text{Eq. 4.10}$$

$$\ln b_0 = \ln b_1 - \left(\frac{E_B}{K_B T}\right) \qquad \text{Eq. 4.11}$$

Here $k_0$ is the temperature dependent IMC growth coefficient and $b_0$ is temperature dependent IMC growth exponent. The experimental values of normalized IMC thickness ($Y_n$) have been plotted with respect to number of cycles (N) to compute the coefficient and

exponent for Eq. 4.9. The intercept ($\ln k_0$) and slope ($b_0$) of Eq. 4.9 have been plotted with respect to mean temperature to calculate the Activation energy of IMC growth for coefficient ($E_A$) and Activation energy of IMC growth for exponent ($E_B$) respectively.

### 4.3.4 Levenberg-Marquardt Algorithm

The relationship between the phase growth parameter and time is nonlinear because it contains terms with fourth power. Inverse solution for interrogation of system-state which requires solution for N or t is challenging for damage evolution in such non-linear systems of equations. Levenberg-Marquardt (LM) algorithm, an iterative technique that computes the minimum of a non-linear function in multidimensional variable space, has been used for identifying the solution in the prognostication neighborhood [113-114]. Let $f$ be a assumed functional relation between a measurement vector referred to as prior damage and the damage parameter vector, p, referred to as predictor variables. The measurement vector is the current values of the leading-indicator of failure and the parameter vector includes the prior system state, and accumulated damage and the damage evolution parameters. An initial parameter estimate $p_0$ and a measured vector x are provided and it is desired to find the parameter vector p, that best satisfies the functional relation $f$ i.e. minimizes the squared distance or squared-error, $\varepsilon^T\varepsilon$ with $\varepsilon = x - f(p)$ . Assume that $g(p) = \varepsilon$ is the error. The minimizer parameter vector, p, and the least square error function has been represented as,

$$F(p) = \frac{1}{2}\sum_{i=1}^{m}\left(g_i(p)\right)^2 = \frac{1}{2}g\left(p\right)^T g\left(p\right) \quad \text{Eq. 4.12}$$

$$F'(p) = J(p)^T g(p) \quad \text{Eq. 4.13}$$

$$F''(p) = J(p)^T J(p) + \sum_{i=1}^{m} g_i(x) g_i''(x) \qquad \text{Eq. 4.14}$$

Where F(p) represents the objective function for the squared error term $\varepsilon^T\varepsilon$ , J(p) is the Jacobian, and F´(p) is the gradient, and F´´(p) is the Hessian. The variation of an F-value starting at "p" and with direction "h" is expressed as a Taylor expansion, as follows:

$$F(p + \alpha h) = F(p) + \alpha h^T F'(p) + O(\alpha^2) \qquad \text{Eq. 4.15}$$

Where α is the step-length from point "p" in the descent direction, "h". Mathematically, "h" is the descent direction of F(p) if $h^T F'(p) < 0$ . If no such "h" exists, then F´(p)=0, showing that in this case the function is stationary. Since the condition for the stationary value of the objective function is that the gradient is zero, i.e. f´(p+h) = L´(h) = 0. The descent direction is computed from the equation,

$$(J^T J) h_{gn} = -J^T g \qquad \text{Eq. 4.16}$$

In each step, Newton method uses α = 1, and $p = p + \alpha h_{gn}$, where subscript '$g_n$' indicates gauss-newton. The value of α is found by line search principle described above. Levenberg-Marquardt algorithm is a hybrid method which utilizes both steepest descent principle as well as the Gauss-Newton method. When the current solution is far from the correct one, the algorithm behaves like a steepest descent method: slow, but guaranteed to converge. When the current solution is close to the correct solution, it becomes a Gauss-Newton method. The LM method actually solves a slight variation of Eq. 4.16, known as the augmented normal equations.

$$(J^T J + \mu I) h = -J^T g \qquad \text{Eq. 4.17}$$

The term μ is called as the damping parameter, μ >0 ensures that coefficient matrix is positive definite, and this ensures that h is a descent direction. When the value of μ is very small, then the step size for LM and Gauss-Newton are identical. Algorithm has been modified to take the equations of phase growth and inter-metallic growth under both isothermal aging and cycling loads to calculate the unknowns.

## 4.4 Analysis of Results

Board assemblies A, B and C were subjected to cycling at -50°C to 50°C, 0°C to 100°C and 50°C to 150°C and were withdrawn after a periodic time-interval of 250 cycles. The samples were cross sectioned, potted and polished. The same joint was examined in each cross-section. Phase growth and intermetallic growth was studied using images taken by SEM at each periodic interval.

### 4.4.1 Phase-Growth Damage Proxy

The image analysis software has been used to measure the average phase size. Eq. 4.3 represents the evolution of phase growth in thermal cycling based on experimental data. The test data has been used to derive the parameters for normalized phase growth of Eq. 4.3. Micrographs of phase structure are shown in Figure 4-5, Figure 4-6 and Figure 4-7 for CABGA 144, PBGA 256 and PBGA 676 respectively.

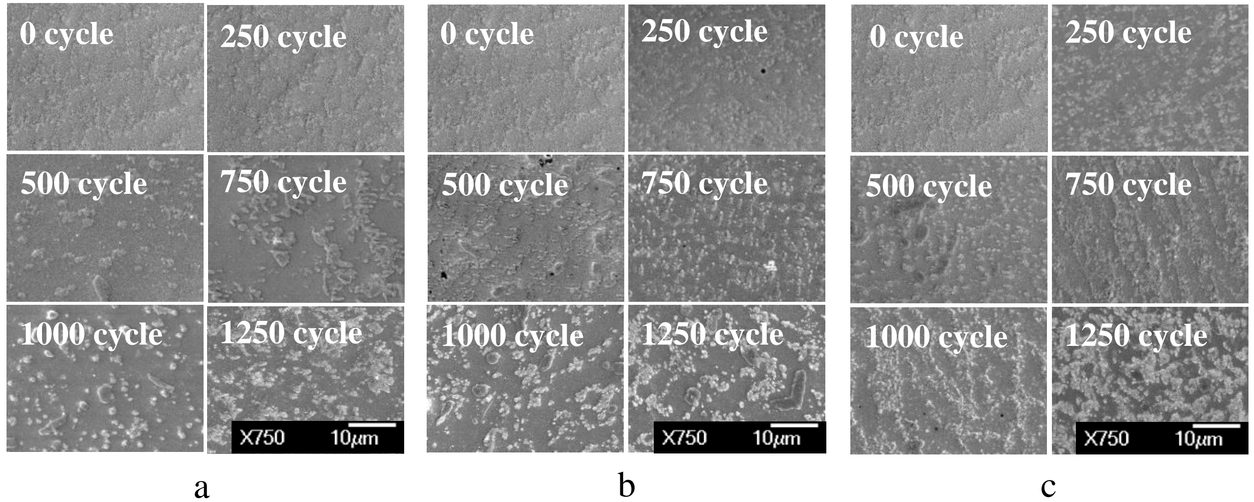


Figure 4-5: SEM images of Phase Growth in CABGA144 at different cycles at 750X magnification (a) for -50°C to 50°C (b) 0°C to 100°C and (c) 50°C to 150°C.

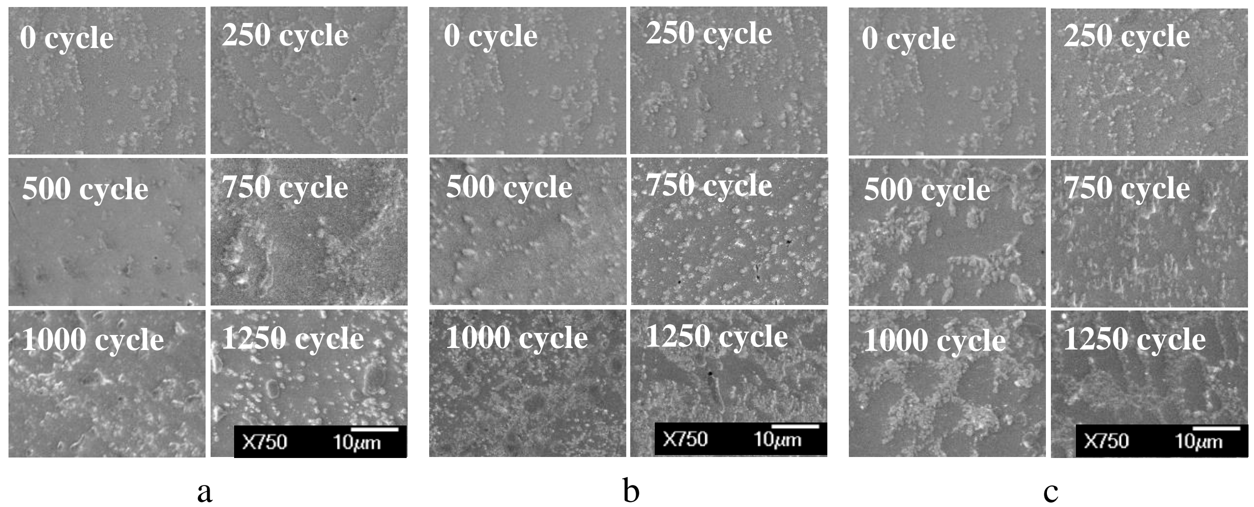


Figure 4-6: SEM images of Phase Growth in PBGA256 at different cycles at 750X magnification (a) for -50°C to 50°C (b) 0°C to 100°C and (c) 50°C to 150°C.

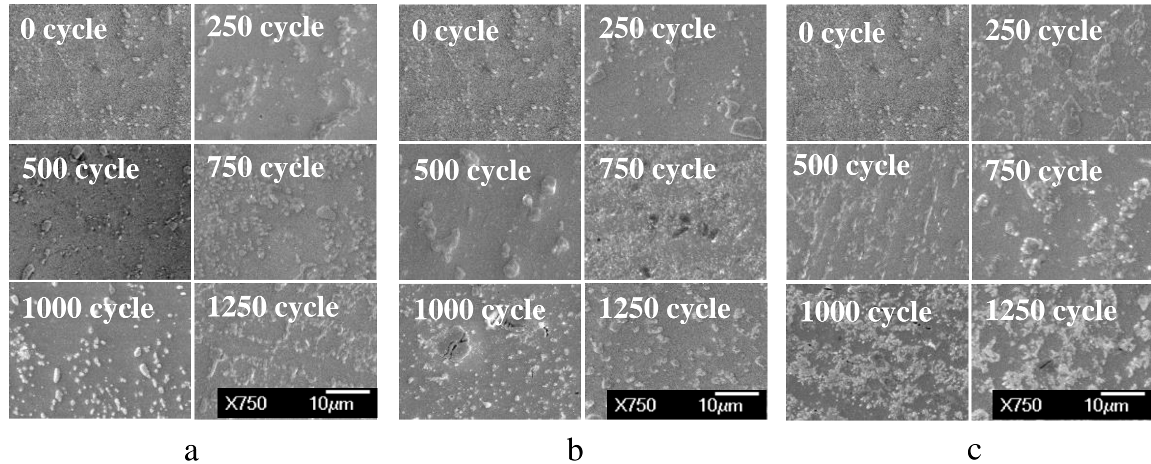


Figure 4-7: SEM images of Phase Growth in PBGA676 at different cycles at 750X magnification (a) for -50°C to 50°C (b) 0°C to 100°C and (c) 50°C to 150°C.

Figure 4-8, Figure 4-9 and Figure 4-10 show the plot of normalized phase growth parameter ($S_n$) with number of cycles (N) in log-log scale for CABGA144, PBGA 256 and PBGA 676 respectively, which clearly reveals that phase growth is higher in solder joint with higher strain level with higher value of phase growth accumulation rate ($dlnS_n/dlnN$). As CABGA 144 package has larger die size than PBGA 256, the solder ball under die shadow region will undergo more strain in CABGA 144 as compared to PBGA 256. But this is not the case in case of PBGA 676. PBGA 676 has larger die size than PBGA 256 but still its phase growth accumulation is less than PBGA 256, which can be explained by beneficial effect of joint height. PBGA 676 has much larger stand-off height than both CABGA 144 and PBGA 256 as revealed by

Table 4-1, and DNP formula says that shear strain is inversely proportional to joint height, and also relatively higher number of I/O count of PBGA 676 may be one of the cause of this interesting finding as same level of thermal load is now applied on much larger number of solder joints. Both the coefficient and exponent term change with mean temperature of cycling range because the underlying agglomeration of phases proceeds at a faster pace at

a higher temperature. Table 4-2 shows the value of phase growth coefficient ($a_0$) and phase growth exponent or phase growth accumulation rate ($b_0$) for CABGA144, PBGA 256 and PBGA 676. This table clearly shows that both phase growth coefficient ($a_0$) and phase growth exponent or phase growth accumulation rate ($b_0$) are increasing with mean temperature.

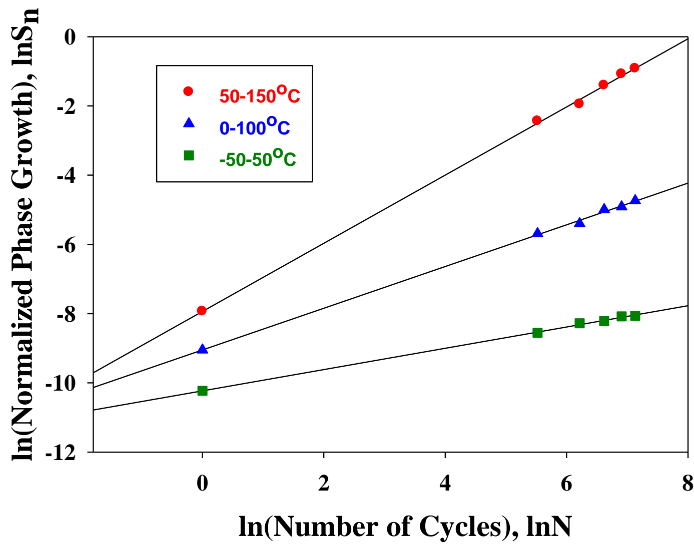


Figure 4-8: Relation between Normalized Phase Growth (lnSn) and Number of Cycles (lnN) for CABGA 144

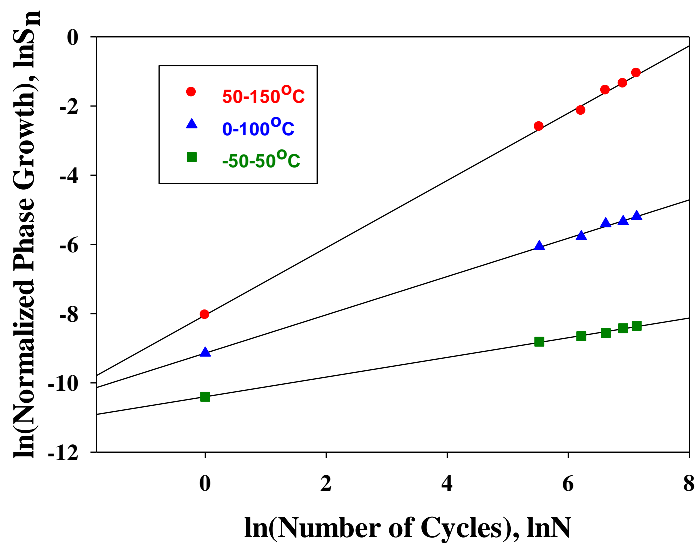


Figure 4-9: Relation between Normalized Phase Growth (lnSn) and Number of Cycles (lnN) for PBGA 256

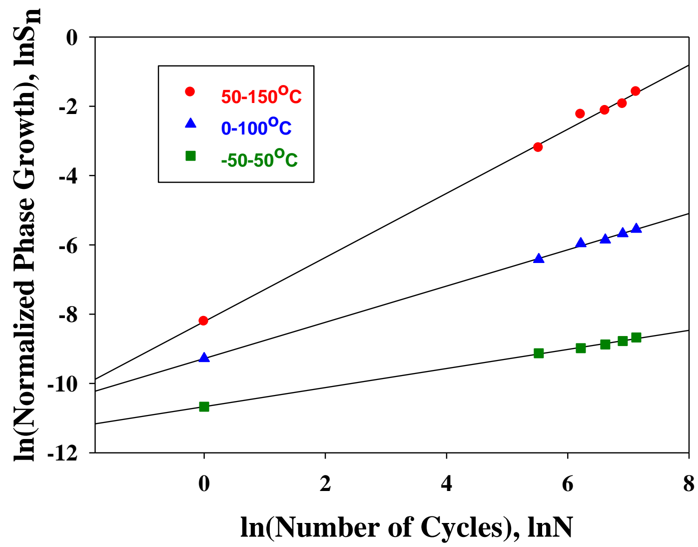


Figure 4-10: Relation between Normalized Phase Growth (lnSn) and Number of Cycles (lnN) for PBGA 676

Table 4-2: Normalized Phase Growth Coefficients and Exponents

| Temp. | $S_n = a_0 N^{b_0}$ <br> $\ln S_n = \ln a_0 + b_0 \ln N$ | | | | | |
|---|---|---|---|---|---|---|
| | CABGA 144 | | PBGA256 | | PBGA676 | |
| | $a_0$ | $b_0$ | $a_0$ | $b_0$ | $a_0$ | $b_0$ |
| $50^o$-$150^o$ C (Tm = 373K) | 3.6E-4 | 0.984 | 3.2E-4 | 0.96 | 3E-4 | 0.924 |
| $0^o$-$100^o$ C (Tm = 323K) | 1.17E-4 | 0.6 | 1.07E-4 | 0.55 | 9.3E-5 | 0.52 |
| $-50^o$-$50^o$ C (Tm = 273K) | 3.6E-5 | 0.31 | 3.04E-5 | 0.28 | 2.3E-5 | 0.28 |

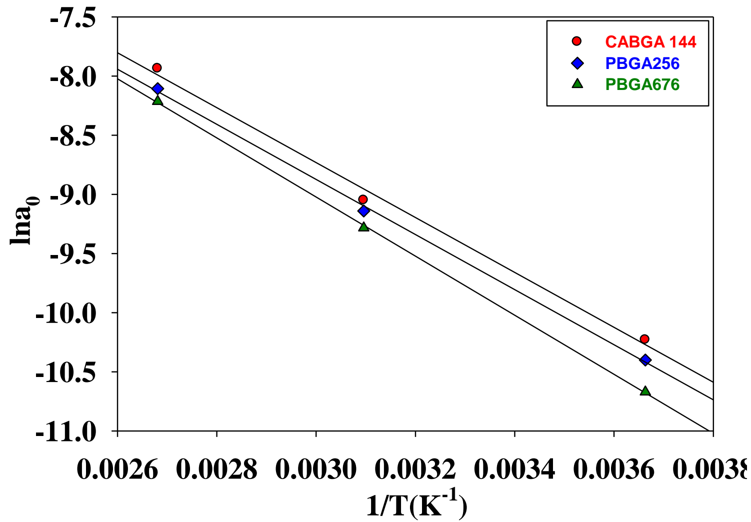


Figure 4-11: Plot of $\ln a_0$ vs. inverse of mean temperature of cycling range (1/T) for phase growth

The activation energy has been computed by fitting the data to Eq. 4.7. Figure 4-11 shows the relationship between $\ln(a_0)$ and (1/T), where T is the mean temperature in Kelvin scale.

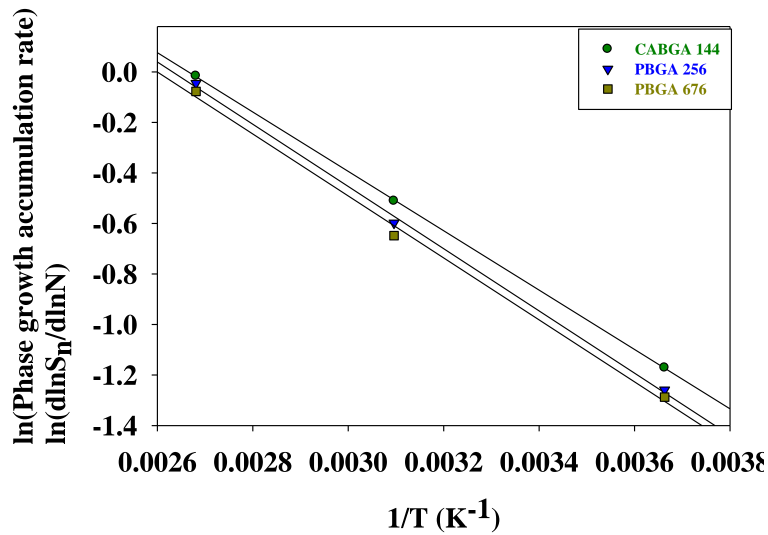


Figure 4-12: Plot of phase growth accumulation rate (dlnSn/dlnN) vs. inverse of mean temperature of cycling range (1/T)

The activation energy of the exponent term has been computed by fitting the data in Eq. 4.8. Figure 4-12 shows the relationship between $\ln(b_0)$ and (1/T), where T is the mean temperature in Kelvin scale.

Table 4-3: Activation energy of phase growth

| | $E_A$ (Activation energy based on growth coefficient) | $E_B$ (Activation energy based on growth exponent) |
|---|---|---|
| CABGA 144 | 0.2 ev | 0.1 ev |
| PBGA 256 | 0.2 ev | 0.11 ev |
| PBGA 676 | 0.22 ev | 0.11 ev |

Table 4-3 shows the Activation Energy calculated based on both Phase growth Coefficient and Phase growth Exponent. A separate set of Board A, B and C packages are subjected to

cyclic environment and their characteristic life (63.2%) were calculated by plotting percent failed with respect to Cycle to Failure which is called Weibull plot. Figure 4-13, Figure 4-14 and Figure 4-15 show the Weibull Plot for CABGA 144, PBGA 256 and PBGA 676 respectively.

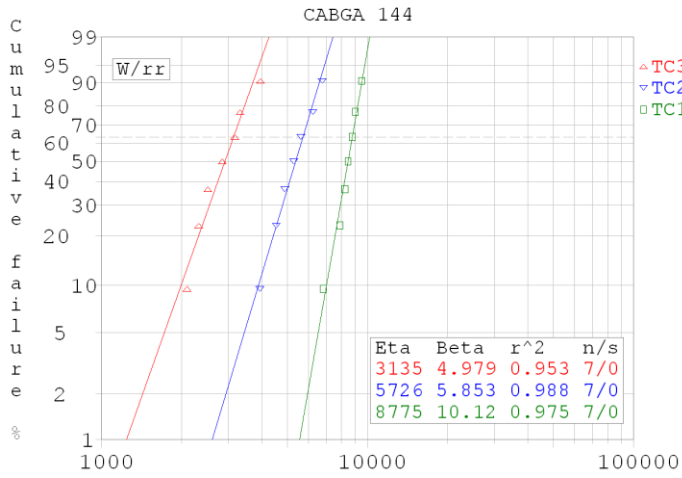


Figure 4-13: Weibull Plot for CABGA 144

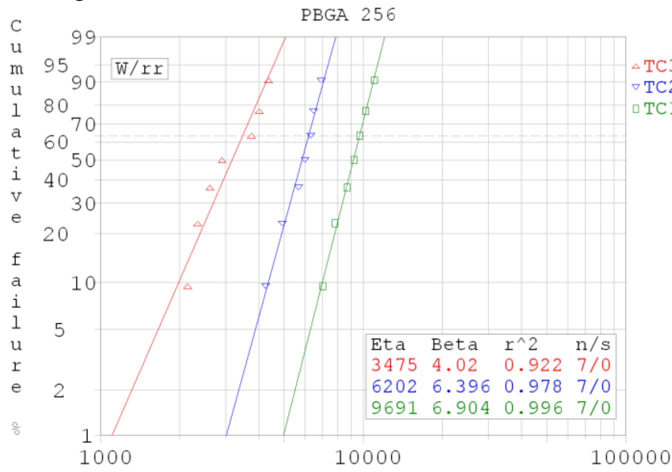


Figure 4-14: Weibull Plot for PBGA 256

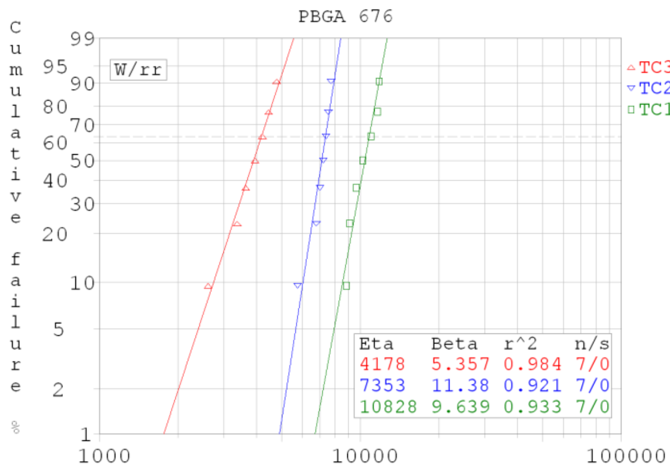


Figure 4-15: Weibull Plot for PBGA 676

Table 4-4 contains the Characteristic life of all the test vehicles we used for three different cyclic environments.

Table 4-4: Characteristic life

| | CABGA 144 | PBGA 256 | PBGA 676 |
|---|---|---|---|
| $50^o$-$150^o$ C | 3135 | 3475 | 4178 |
| $0^o$-$100^o$ C | 5726 | 6202 | 7353 |
| -$50^o$-$50^o$ C | 8775 | 9691 | 10828 |

The Phase Growth Accumulation Rate ($dlnS_n/dlnN$) vs. Characteristic life has been plotted in Figure 4-16 to get a relation between solder joint accrued damage (considering Phase Growth Accumulation Rate as a proxy to solder joint accrued damage) and Characteristic life ($N_f$).

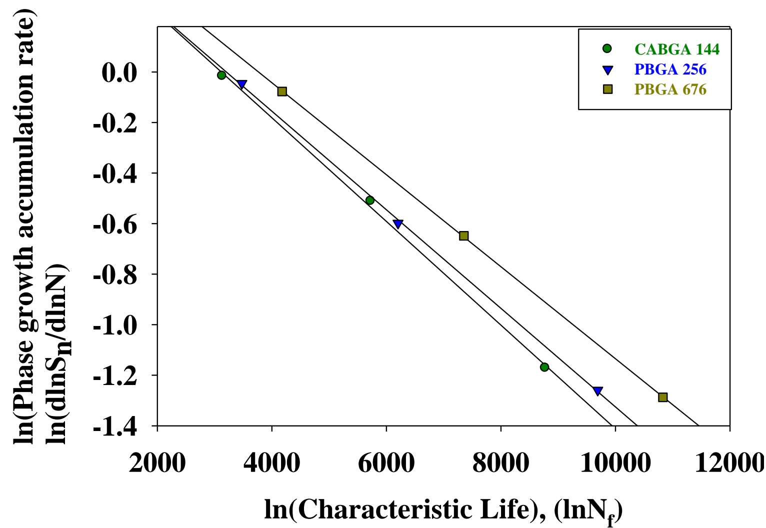


Figure 4-16: Plot of phase growth accumulation rate (dlnSn/dlnN) vs. Characteristic Life (Nf)

The relation between Characteristic Life and Phase growth Accumulation Rate as derived from the data fit are shown in Table 4-5.

Table 4-5: Relation between Phase Growth Accumulation Rate and Characteristic life

| | |
|---|---|
| CABGA 144 | $N_f = 3300\ (dlnS_n/dlnN)^{-0.91}$ |
| PBGA 256 | $N_f = 3500(dlnS_n/dlnN)^{-0.85}$ |
| PBGA 676 | $N_f = 4100(dlnS_n/dlnN)^{-0.8}$ |

In Figure 4-17, all data from CABGA 144, PBGA 256 and PBGA 676 were fitted in one single plot to develop a combined predictive model.

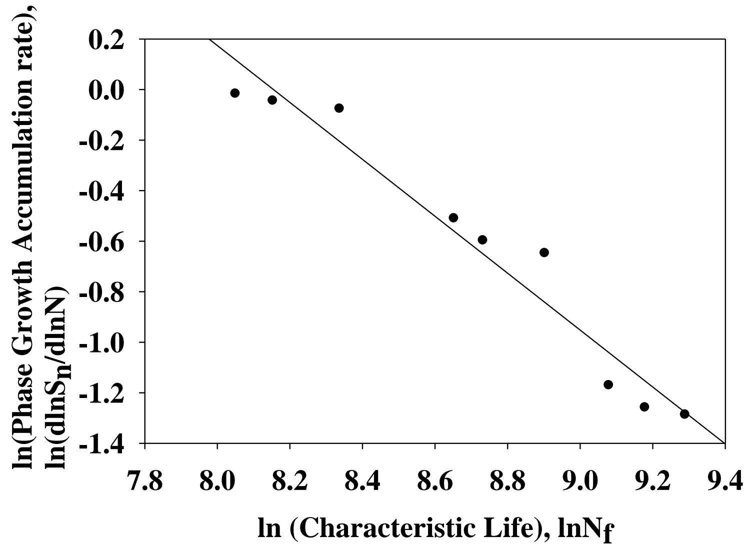


Figure 4-17: Predictive model using Phase Growth as a damage proxy

The equation we derived from the data fit shown in Figure 4-17 is as follows;

$$N_f = 3500\left(\frac{dlnS_n}{dlnN}\right)^{-0.89} \qquad \text{Eq. 4.18}$$

The Characteristic Life for all three test vehicles was calculated using Eq. 4.18 and then compared with our experimental findings as shown in Table 4-6 to show the validity of the predictive model derived.

Table 4-6: Comparison of experimental results and results from predictive model using Phase Growth as a damage proxy

| | CABGA 144 | | | PBGA 256 | | | PBGA 676 | | |
|---|---|---|---|---|---|---|---|---|---|
| | Exp. | Predict. | Error (%) | Exp. | Predict. | Error (%) | Exp. | Predict. | Error (%) |
| $50^o$-$150^oC$ | 3135 | 3532.69 | 12.69 | 3475 | 3600 | 3.6 | 4178 | 3725.13 | 10.84 |
| $0^o$-$100^oC$ | 5726 | 5476.24 | 4.36 | 6202 | 5916.11 | 4.61 | 7353 | 6186.54 | 15.86 |
| $-50^o$-$50^oC$ | 8775 | 9843.17 | 12.17 | 9691 | 10639.35 | 9.79 | 10828 | 10912.74 | 0.78 |

### 4.4.2 Inter-Metallic Thickness Growth Damage Proxy

Eq. 4.9 represents the evolution of IMC thickness growth in thermal cycling based on experimental data. The test data has been used to derive the parameters for normalized IMC growth of Eq. 4.9. Micrographs of IMC thickness are shown in Figure 4-18 for CABGA 144, in Figure 4-19 for PBGA 256, and in Figure 4-20 for PBGA 676. Figure 4-21, Figure 4-22 and Figure 4-23 show the plot of normalized IMC growth parameter ($Y_n$) with number of cycles (N) in log-log scale for CABGA144, PBGA 256 and PBGA 676 respectively, which clearly reveals that IMC growth also follow the same trend like phase growth. Both the coefficient and exponent term change with mean temperature of cycling range because the underlying agglomeration of IMC proceeds at a faster pace at a higher temperature. Table 4-7 shows the value of IMC growth coefficient ($k_0$) and IMC growth exponent or IMC accumulation rate ($b_0$) for all the test samples. Again this table clearly shows that

both IMC growth coefficient ($k_0$) and IMC growth exponent or IMC accumulation rate ($b_0$) are increasing with mean temperature.

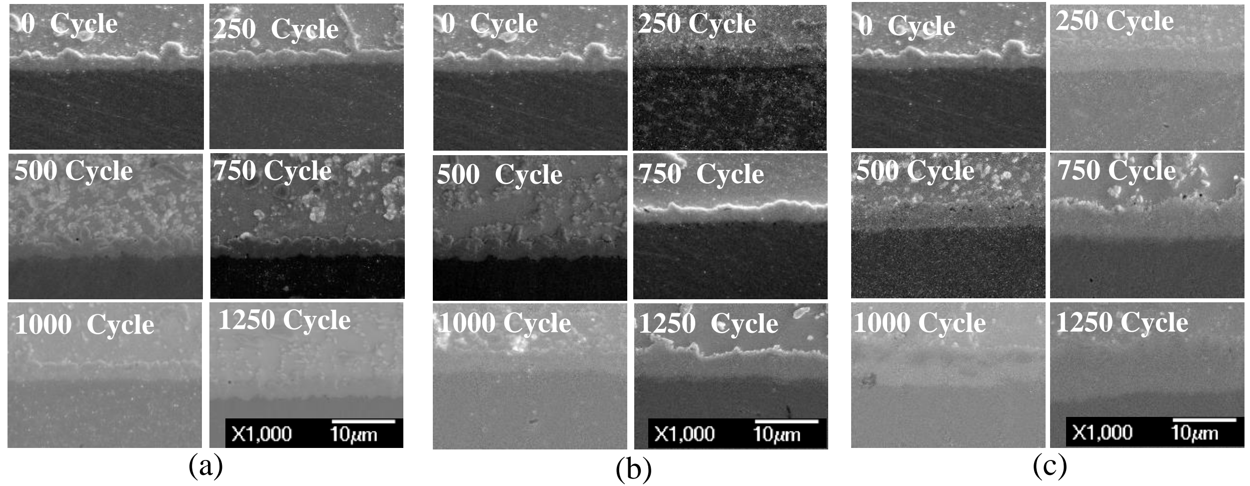


Figure 4-18: SEM images of IMC Growth in CABGA144 at different cycles at 1000X magnification) (a) for -50°C to 50°C (b) 0°C to 100°C and (c) 50°C to 150°C.

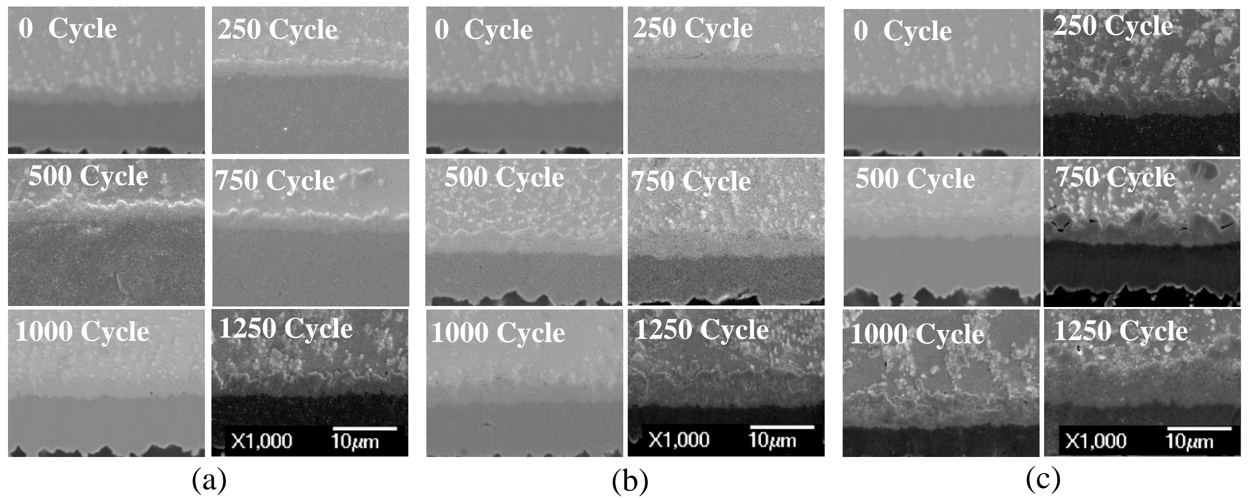


Figure 4-19: SEM images of IMC Growth in PBGA256 at different cycles at 1000X magnification) (a) for -50°C to 50°C (b) 0°C to 100°C and (c) 50°C to 150°C.

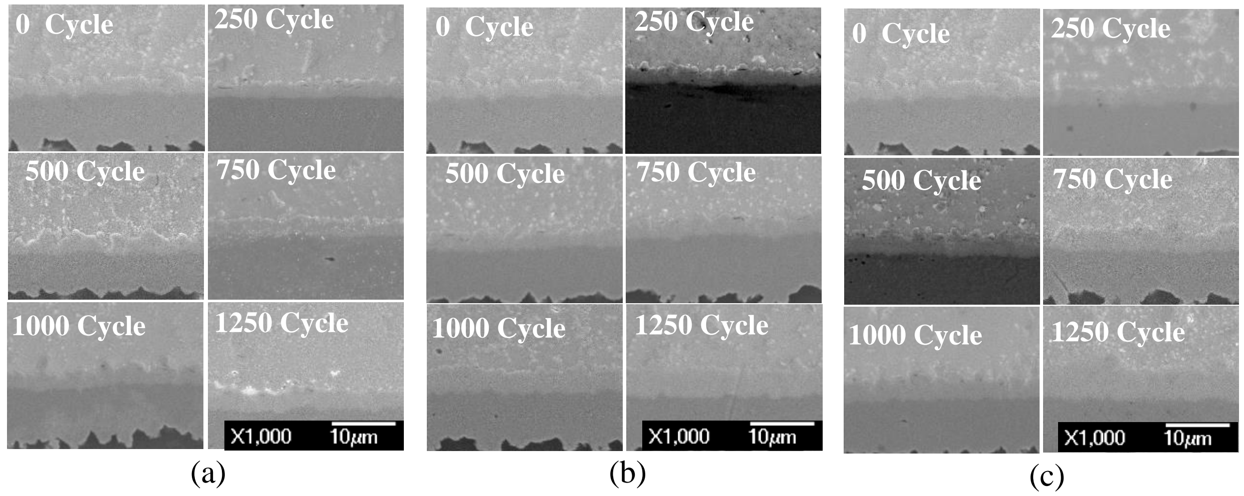


Figure 4-20: SEM images of IMC Growth in PBGA676 at different cycles at 1000X magnification) (a) for -50°C to 50°C (b) 0°C to 100°C and (c) 50°C to 150°C.

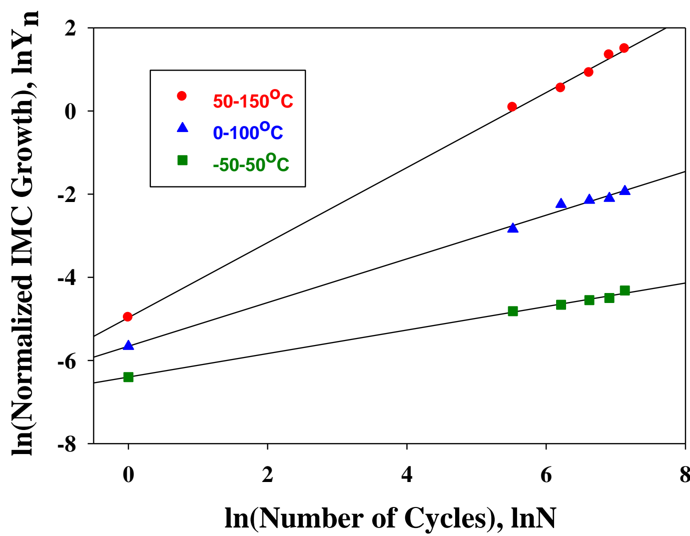


Figure 4-21: Relation between Normalized IMC Growth (lnYn) and Number of Cycles (lnN) for CABGA 144

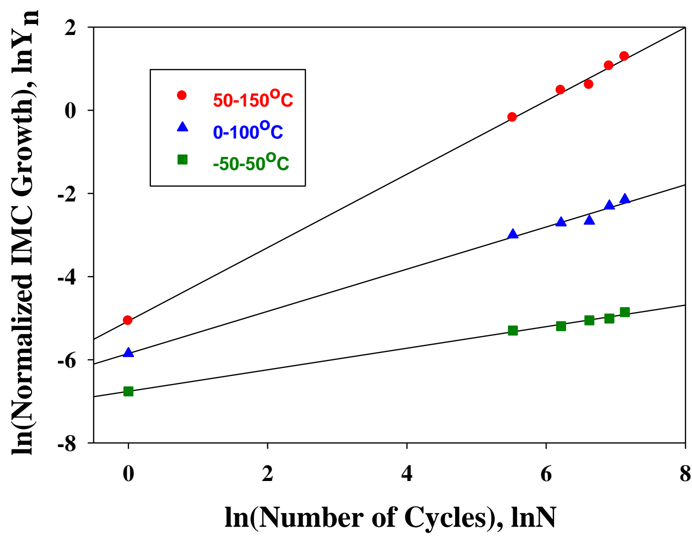


Figure 4-22: Relation between Normalized IMC Growth (lnYn) and Number of Cycles (lnN) for PBGA 256

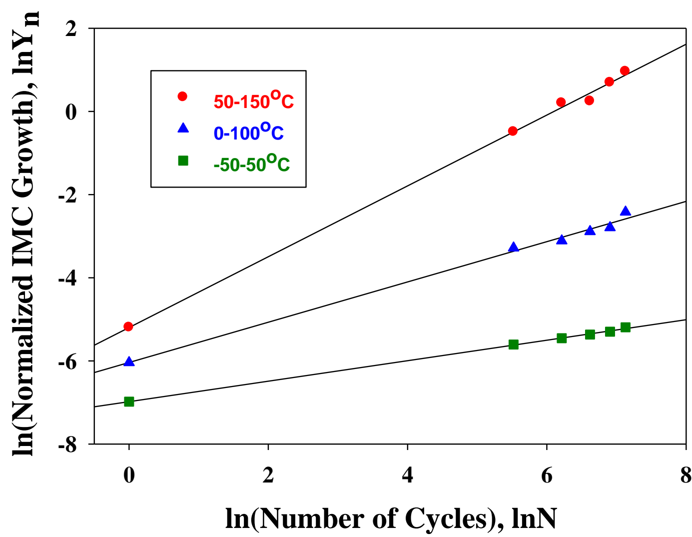


Figure 4-23: Relation between Normalized IMC Growth (lnYn) and Number of Cycles (lnN) for PBGA 676.

Table 4-7: Normalized IMC Growth Coefficients and Exponents

| Temp. | $Y_n = k_0 N^{b_0}$<br>$\ln Y_n = \ln k_0 + b_0 \ln N$ | | | | | |
|---|---|---|---|---|---|---|
| | CABGA 144 | | PBGA256 | | PBGA676 | |
| | $k_0$ | $b_0$ ($d\ln Y_n/d\ln N$) | $k_0$ | $b_0$ ($d\ln Y_n/d\ln N$) | $k_0$ | $b_0$ ($d\ln Y_n/d\ln N$) |
| 50°-150° C (Tm = 373K) | 0.0069 | 0.91 | 0.0063 | 0.88 | 0.0055 | 0.855 |
| 0°-100° C (Tm = 323K) | 0.0035 | 0.52 | 0.0029 | 0.5 | 0.0024 | 0.48 |
| -50°-50° C (Tm = 273K) | 0.0017 | 0.28 | 0.0012 | 0.26 | 0.00093 | 0.245 |

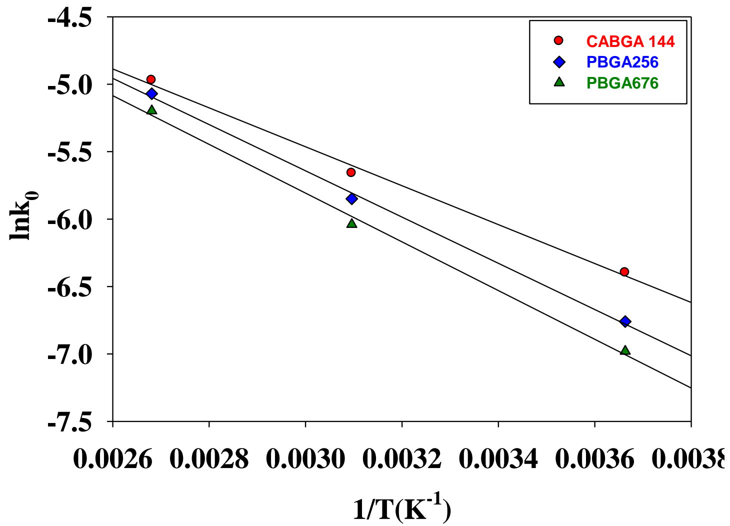


Figure 4-24: Plot of $\ln k_0$ vs. inverse of mean temperature of cycling range (1/T) for IMC

The activation energy of IMC thickness growth based on coefficient has been computed by fitting the data to Eq. 4.10. Figure 4-24 shows the relationship between $\ln(k_0)$ and (1/T), where T is the mean temperature in Kelvin scale.

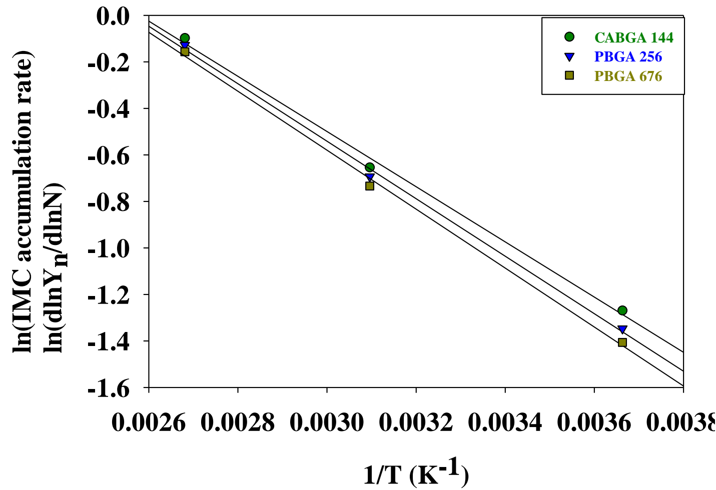


Figure 4-25: Plot of IMC accumulation rate ($dlnY_n/dlnN$) vs. inverse of mean temperature of cycling range (1/T)

The activation energy based on exponent term has been computed by fitting the data in Eq. 4.11. Figure 4-25 shows the relationship between $\ln(b_0)$ and (1/T), where T is the mean temperature in Kelvin scale.

Table 4-8: Activation energy for IMC growth

| | Activation Energy ($E_A$) based on coefficient | Activation Energy ($E_B$) based on exponent |
|---|---|---|
| CABGA 144 | 0.124 ev | 0.1 ev |
| PBGA 256 | 0.15 ev | 0.11 ev |
| PBGA 676 | 0.16 ev | 0.11 ev |

Table 4-8 show the Activation Energy based on IMC growth Coefficient and IMC growth exponent respectively.

The IMC Accumulation Rate ($dlnY_n/dlnN$) vs Characteristic life (Table 4-4) has been plotted in Figure 4-26 to get a relation between solder joint accrued damage (considering

IMC Accumulation Rate as a proxy to solder joint accrued damage) and Characteristic life ($N_f$).

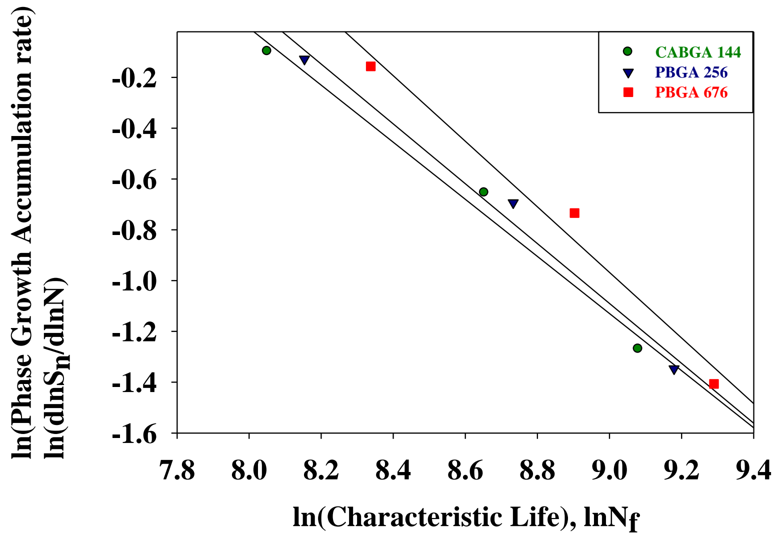


Figure 4-26: Plot of IMC accumulation rate ($dlnY_n/dlnN$) vs. Characteristic Life ($N_f$)

The relation between Characteristic Life and IMC Accumulation Rate as derived from the data fit is shown in Table 4-9.

Table 4-9: Relation between IMC Accumulation Rate and Characteristic life

| | |
|---|---|
| CABGA 144 | $N_f = 2975(dlnY_n/dlnN)^{-0.89}$ |
| PBGA 256 | $N_f = 3197.1\ (dlnY_n/dlnN)^{-0.85}$ |
| PBGA 676 | $N_f = 3824\ (dlnY_n/dlnN)^{-0.77}$ |

In Figure 4-27, all data from CABGA 144, PBGA 256 and PBGA 676 were fitted in one single plot to develop a combined predictive model.

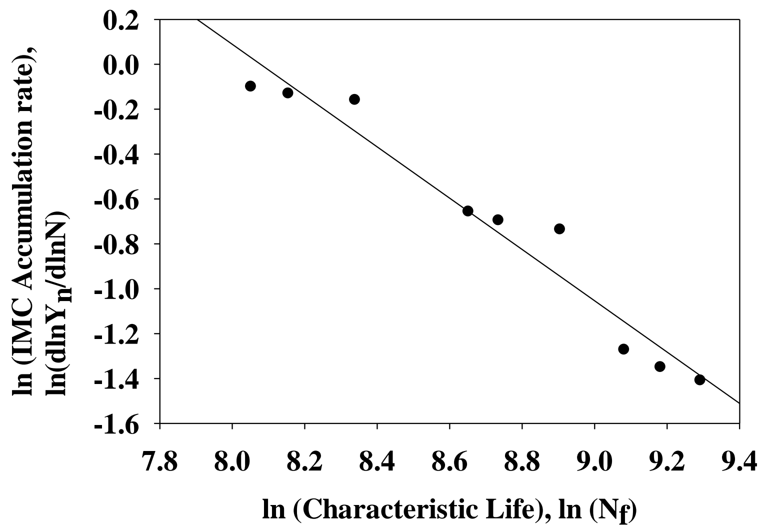


Figure 4-27: Predicting model using IMC as a damage proxy

The equation we derived from the data fit shown in Figure 4-27 is as follows;

$$N_f = 3232.46\left(\frac{\mathrm{dlnY}}{\mathrm{dlnN}}\right)^{-0.875} \qquad \text{Eq. 4.19}$$

The Characteristic Life for all three test vehicles was calculated using Eq. 4.19 and then compared with our experimental findings as shown in Table 4-10 to show the validity of the predictive model derived.

Table 4-10: Comparison of experimental results and results from predictive model using IMC Growth as a damage proxy

| | CABGA 144 | | | PBGA 256 | | | PBGA 676 | | |
|---|---|---|---|---|---|---|---|---|---|
| | Exp. | Predict. | Error (%) | Exp. | Predict. | Error (%) | Exp. | Predict. | Error (%) |
| $50^o$-$150^oC$ | 3135 | 3512 | -12.02 | 3475 | 3606 | -3.77 | 4178 | 3698 | 11.49 |
| $0^o$-$100^oC$ | 5726 | 5713 | 0.23 | 6202 | 5913 | 4.67 | 7353 | 6127 | 16.67 |
| $-50^o$-$50^oC$ | 8775 | 9787 | -11.52 | 9691 | 10475 | -8.08 | 10828 | 11033 | -1.89 |

**4.5 Damage Equivalency Relationships**

Damage accrued from the two different thermal cycling environments has been equivalenced based on two damage proxies including normalized intermetallic thickness and normalized phase growth to get Damage Equivalency Relationships shown in Table 4-12,

Table 4-14 and Table 4-16. Table 4-11, Table 4-13 and Table 4-15 show the damage mapping relationship for CABGA 144, PBGA 256 and PBGA 676 respectively obtained by plotting Normalized Phase Growth or Normalized IMC Growth parameter with respect to number of cycles. Then these Damage mapping relations for any two test conditions are

equivalenced to get Damage Equivalency relationship which actually shows the relationship between number of cycles or time required under any two test conditions to reach a particular damage state.

Table 4-11: Damage mapping relationship for CABGA 144

| | Phase Growth | IMC |
|---|---|---|
| 50$^o$-150$^o$ C (TC3) | $S_{nTC3}= 0.00036N_{TC3}^{0.98}$ | $Y_{nTC3}= 0.0069N_{TC3}^{0.907}$ |
| 0$^o$-100$^o$ C (TC2) | $S_{nTC2}= 0.000117N_{TC2}^{0.6}$ | $Y_{nTC2}= 0.0035N_{TC2}^{0.52}$ |
| -50$^o$-50$^o$ C (TC1) | $S_{nTC1}= 0.000036N_{TC1}^{0.31}$ | $Y_{nTC1}= 0.0017N_{TC1}^{0.28}$ |

Table 4-12: Damage Equivalency relationship for CABGA 144

| Phase Growth | IMC |
|---|---|
| $N_{TC3}=0.32N_{TC2}^{0.61}$ | $N_{TC3}=0.47N_{TC2}^{0.573}$ |
| $N_{TC2}=0.14N_{TC1}^{0.517}$ | $N_{TC2}=0.25N_{TC1}^{0.54}$ |

Table 4-13: Damage mapping relationship for PBGA 256

| | Phase Growth | IMC |
|---|---|---|
| 50$^o$-150$^o$ C (TC3) | $S_{nTC3}= 0.000322N_{TC3}^{0.96}$ | $Y_{nTC3}= 0.0063N_{TC3}^{0.88}$ |
| 0$^o$-100$^o$ C (TC2) | $S_{nTC2}= 0.000107N_{TC2}^{0.55}$ | $Y_{nTC2}= 0.0029N_{TC2}^{0.5}$ |
| -50$^o$-50$^o$ C (TC1) | $S_{nTC1}=$ | $Y_{nTC1}=$ |

|  | $0.00003N_{TC1}^{0.284}$ | $0.0012N_{TC1}^{0.26}$ |
|---|---|---|

Table 4-14: Damage Equivalency relationship for PBGA 256

| Phase Growth | IMC |
|---|---|
| $N_{TC3}=0.32N_{TC2}^{0.57}$ | $N_{TC3}=0.41N_{TC2}^{0.57}$ |
| $N_{TC2}=0.1N_{TC1}^{0.516}$ | $N_{TC2}=0.17N_{TC1}^{0.52}$ |

Table 4-15: Damage mapping relationship for PBGA 676

|  | Phase Growth | IMC |
|---|---|---|
| $50^o$-$150^o$ C (TC3) | $S_{nTC3}=0.0003N_{TC3}^{0.924}$ | $Y_{nTC3}=0.0055N_{TC3}^{0.855}$ |
| $0^o$-$100^o$ C (TC2) | $S_{nTC2}=0.000093N_{TC2}^{0.52}$ | $Y_{nTC2}=0.0024N_{TC2}^{0.48}$ |
| $-50^o$-$50^o$ C (TC1) | $S_{nTC1}=0.000023N_{TC1}^{0.276}$ | $Y_{nTC1}=0.00093N_{TC1}^{0.245}$ |

Table 4-16: Damage Equivalency relationship for PBGA 676

| Phase Growth | IMC |
|---|---|
| $N_{TC3}=0.284N_{TC2}^{0.55}$ | $N_{TC3}=0.38N_{TC2}^{0.56}$ |
| $N_{TC2}=0.07N_{TC1}^{0.528}$ | $N_{TC2}=0.14N_{TC1}^{0.51}$ |

In this paper both Phase growth and IMC growth are considered as damage proxy. Therefore, the damage equivalency relationship obtained using both these damage proxies should be same. Table 4-12, Table 4-14 and Table 4-16 reveal the convergence of the

damage equivalency relationships from two separate damage proxies which supports the validity of the correlation.

### 4.6 Prognostication

The prognostic model predicts the life consumed or the number of cycles 'N' the system has been subjected to in a thermal cycling environment based on the real time grain size measurement 'g'. So this algorithm tries to find the solution to the system of equation shown in Eq. 4.20 through number of iterations and stops when error value reaches a particular threshold and final solution corresponds to this minimum error. The non-linear normalized phase growth equation has to be solved for the 4 unknowns viz. N, a, b and $g_0$. To solve for four unknowns, four equations are needed. To obtain these systems of equations we used grain size measurements at four cycle count as shown in Eq. 4.20.

$$\begin{aligned}
\left[\left(\frac{g_N}{g_0}\right)^4 - 1\right] &= a(N)^b \\
\left[\left(\frac{g_{N+\Delta N}}{g_0}\right)^4 - 1\right] &= a(N+\Delta N)^b \\
\left[\left(\frac{g_{N+2\Delta N}}{g_0}\right)^4 - 1\right] &= a(N+2\Delta N)^b \\
\left[\left(\frac{g_{N+3\Delta N}}{g_0}\right)^4 - 1\right] &= a(N+3\Delta N)^b
\end{aligned} \qquad \text{Eq. 4.20}$$

Levenberg-Marquardt algorithm iteratively minimizes the error in the solution space and selects the final solution corresponding to the minimum error. For prognostication using IMC growth as a damage proxy, Eq. 4.21 is used which is obtained after simplifying Eq.

4.9. In this equation $y_0$ (Initial IMC Growth), k (IMC Growth Coefficient), b (IMC Growth Exponent) and N (Number of Cycles) are four unknowns; therefore, four equations are needed to solve this as shown in Eq. 4.22.

$$y_p = y_0 + kN^b \qquad \text{Eq. 4.21}$$

$$\begin{aligned} y_p &= y_0 + kN^b \\ y_{p+\Delta N} &= y_0 + k(N+\Delta N)^b \\ y_{p+2\Delta N} &= y_0 + k(N+2\Delta N)^b \\ y_{p+3\Delta N} &= y_0 + k(N+3\Delta N)^b \end{aligned} \qquad \text{Eq. 4.22}$$

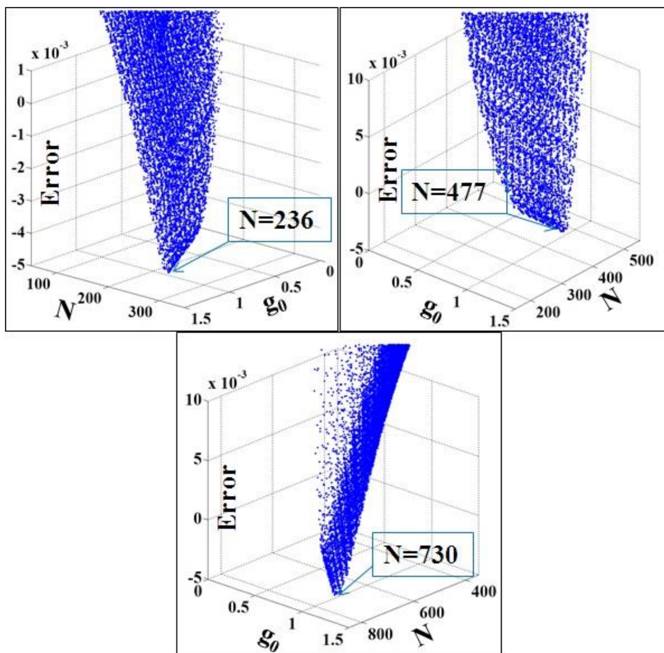


Figure 4-28: 3D plot of Error vs No. of Cycles and Normalized Phase Growth for CABGA 144 for temperature cycle $50^o$ - $150^o$ C

In Figure 4-28, Figure 4-29 and Figure 4-30, 3D plot of Error vs No. of Cycles and Normalized Phase Growth by using LM Algorithm are shown for CABGA 144 for temperature cycling range of 50° - 150°, 0° - 100°, and -50° - 50° respectively.

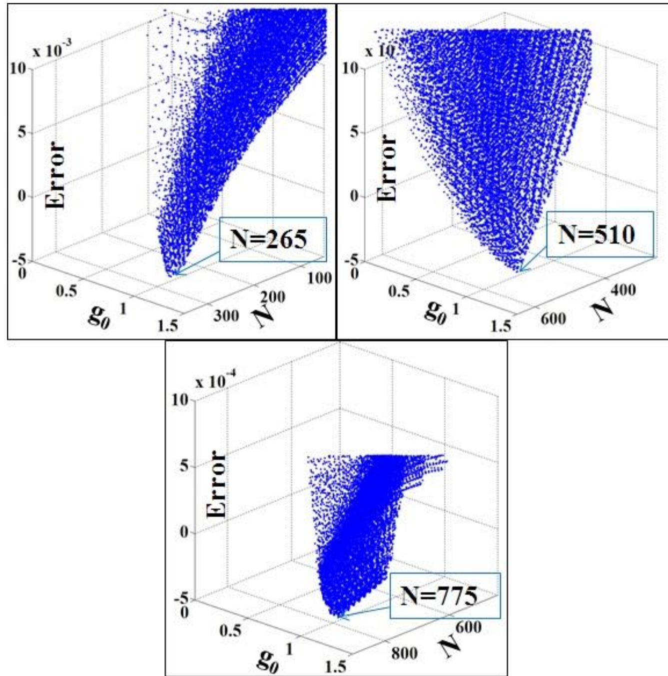


Figure 4-29: 3D plot of Error vs No. of Cycles and Normalized Phase Growth for CABGA 144 for temperature cycle 0° - 100° C

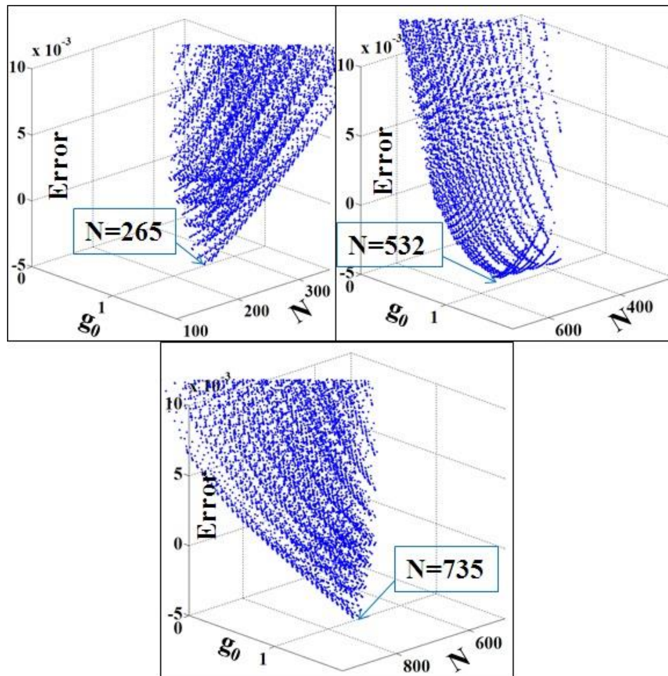


Figure 4-30: 3D plot of Error vs No. of Cycles and Normalized Phase Growth for CABGA 144 for temperature cycle -50º - 50º C

In Figure 4-31, Figure 4-32 and Figure 4-33, 3D plot of Error vs No. of Cycles and Normalized IMC Growth by using LM Algorithm are shown for CABGA 144 for temperature cycling range of 50º - 150º, 0º - 100º, and -50º - 50º respectively.

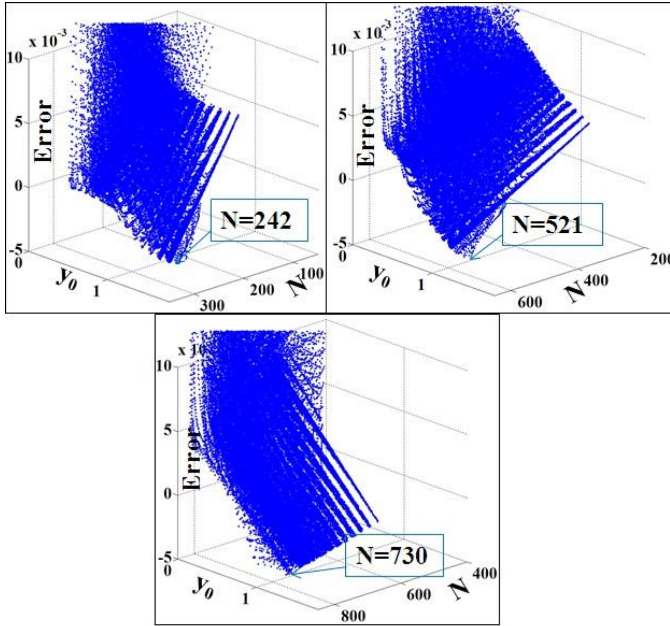


Figure 4-31: 3D plot of Error vs No. of Cycles and Normalized IMC Growth for CABGA 144 for temperature cycle 50º - 150º C

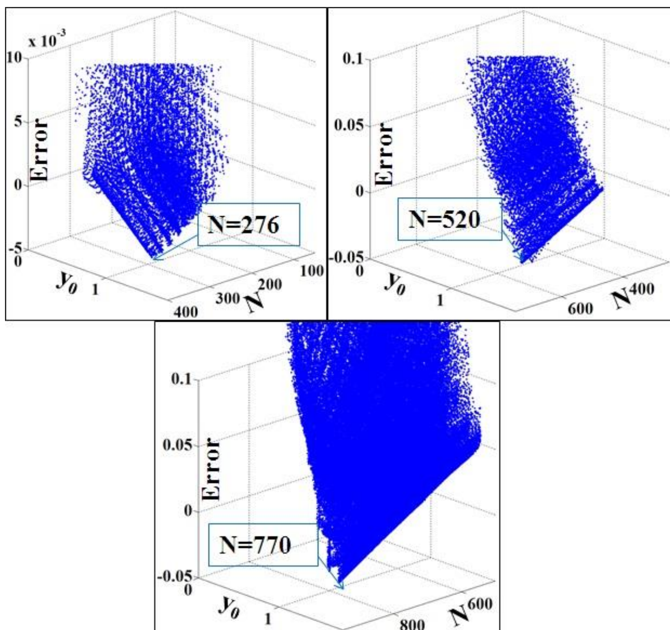


Figure 4-32: 3D plot of Error vs No. of Cycles and Normalized IMC Growth for CABGA 144 for temperature cycle 0º - 100º C

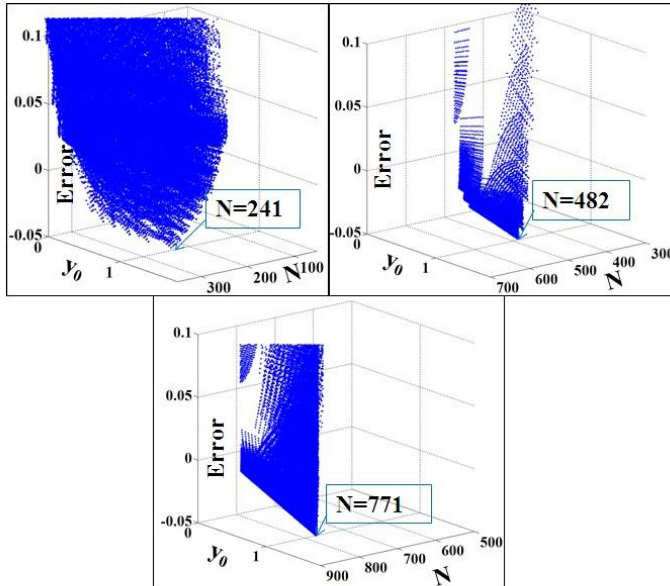


Figure 4-33: 3D plot of Error vs No. of Cycles and Normalized IMC Growth for CABGA 144 for temperature cycle -50$^o$ - 50$^o$ C

Table 4-17, Table 4-18 and Table 4-19 show the comparison of results obtained from experiment and prognostication. The convergence of both the results validates our experimental approach.

Table 4-17: Comparison of results obtained from experiment and prognostication for 50$^o$ - 150$^o$ C

| 50$^o$ - 150$^o$ C | | | |
|---|---|---|---|
| Phase Growth | | IMC growth | |
| N (Exp.) | N(Prog.) | N (Exp.) | N(Prog.) |
| 250 | 236 | 250 | 242 |
| 500 | 477 | 500 | 521 |
| 750 | 730 | 750 | 730 |

Table 4-18: Comparison of results obtained from experiment and prognostication for $0^o$ - $100^o$ C

| $0^o$ - $100^o$ C | | | |
|---|---|---|---|
| Phase Growth | | IMC growth | |
| N (Exp.) | N(Prog.) | N (Exp.) | N(Prog.) |
| 250 | 265 | 250 | 276 |
| 500 | 510 | 500 | 520 |
| 750 | 775 | 750 | 770 |

Table 4-19: Comparison of results obtained from experiment and prognostication for $-50^o$ – $50^o$ C

| $-50^o$ - $50^o$ C | | | |
|---|---|---|---|
| Phase Growth | | IMC growth | |
| N (Exp.) | N(Prog.) | N (Exp.) | N(Prog.) |
| 250 | 265 | 250 | 241 |
| 500 | 532 | 500 | 482 |
| 750 | 735 | 750 | 771 |

**4.7 Prognostics Performance Evaluation**

Prognostics is an emerging concept in condition based monitoring system, desired to predict remaining useful life to avoid catastrophic failures. Using concept of prognostics and physics of failure, we can predict remaining useful life based on evolution of proxies that will indicate probable future failure. Successful prognostics model should not only predict remaining useful life accurately but also it should have the precision in predictions and high confidence bound. The model should be passed through stringent evaluation criterion on using different parameters so that it can be implemented into critical applications where accuracy of prediction matters most. Currently there are no set of

standard parameters defined for evaluation of developed prognostics model [115]. In this thesis, two separate prognostication models based on two leading indicators of failure viz. phase-growth and inter-metallic compound growth of second level solder interconnects have been proposed and implemented for the life prediction of electronics. The sole purpose of evaluating various performance metrics was to relatively compare the two models and see which leading indicator of failure accurately predicts life. For this, seven different performance metrics viz. accuracy, precision, Mean Squared Error (MSE), and Mean Absolute Percentage Error (MAPE), α-λ accuracy, relative accuracy (RA) and cumulative relative accuracy (CRA) have been computed. These parameters have been being used by past researchers [115-116] also to compare performance of different prognostics metrics.

4.7.1 Average Bias

This method averages prediction errors made at all subsequent time steps after $\ell^{th}$ unit under test (UTT). This method is then extended to establish overall bias over all UTT. In this form variability in prediction and presence of outliers is neglected [115]. Average bias $B_l$ can be calculated by,

$$B_l = \frac{1}{\ell} * \sum_{i=P}^{EOP} \{\Delta^l(i)\} \qquad \text{Eq. 4.24}$$

Where,

$\ell = EOP - P + 1$

$\ell$ is cardinality of the set of all time indices at which predictions are made, EOP is End of Prediction is earliest time index, i, after prediction crosses failure threshold, and P is time

index at which first prediction was made by prognostic model. $\Delta^l(i)$ is the error between predicted and true RUL at time index i for UTT l [115].

### 4.7.3 Mean Squared Error (MSE)

In simple average bias calculation, over prediction and under prediction cancel out each other. So it might not reflect actual accuracy and precision of model. To avoid this, average of the square of prediction error for multiple UTT is calculated, which is known as MSE. Derivative of MSE is root mean square error (RMSE) [115].

$$MSE = \frac{1}{\ell}\sum_{i=1}^{\ell}(\Delta^l(i))^2 \qquad \text{Eq. 4.26}$$

### 4.7.4 Mean Absolute Percentage Error (MAPE)

MAPE is unit free accuracy measure only for ration scaled data []117. MAPE weights errors with RUL and averages the absolute percentage error in the multiple predictions [115].

$$MAPE(i) = \frac{1}{\ell}\sum_{i=1}^{\ell}\frac{100\Delta^l(i)}{r_*^l(i)} \qquad \text{Eq. 4.27}$$

Where, $r_*^l(i)$ in true RUL at time $t_1$ given that data is available up to $\ell^{th}$ UTT.

### 4.7.5 α-λ accuracy

It is essential to know whether the model predictions are within the specified limit of error bound at given time. Time instances are defined as percentage of remaining useful life after first prediction was made [115]. The α-λ curve has been plotted for both the damage proxies

at all three different temperature cycling conditions as shown in Figure 4.34, Figure 4.35 and Figure 4.36 for CABGA 144 package. It is a normalized plot of Remaining Useful Life (RUL) Vs Life which is compared against the ground truth and the error bounds. In this case the ground truth is the experimental data obtained from accelerated testing shown by blue line in the plots and ± 10% error bounds are imposed shown by red and green lines. It should be noted that the selection of error bounds is application specific and typically tighter bounds are imposed as the criticality of the system increases.

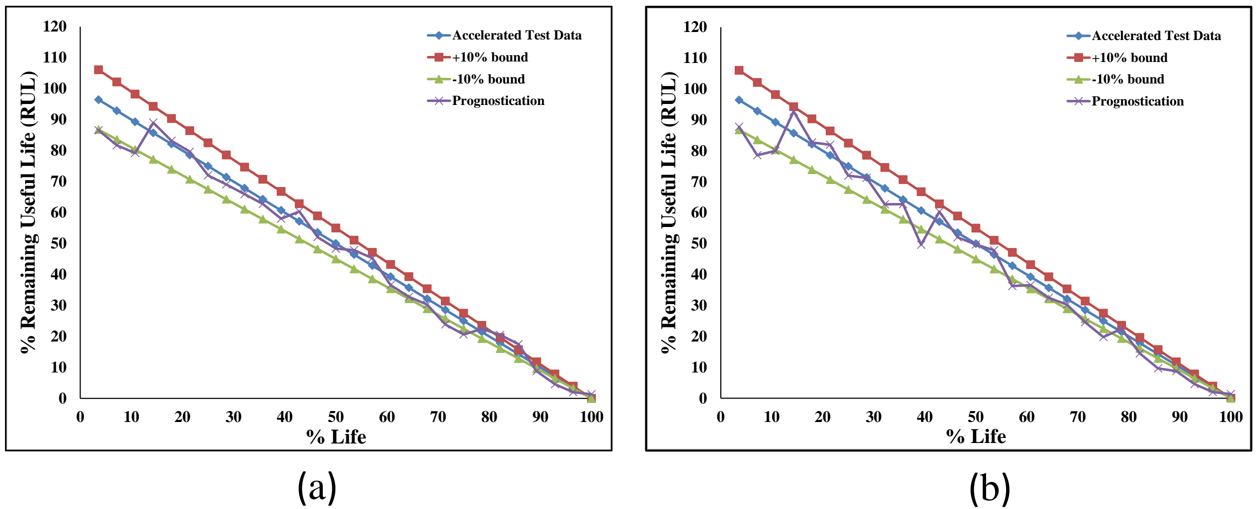


Figure 4-34: α-λ curve for Prognostication for CABGA144 at 50-150°C (a) Using Phase growth as damage proxy and (b) Using IMC thickness as damage proxy

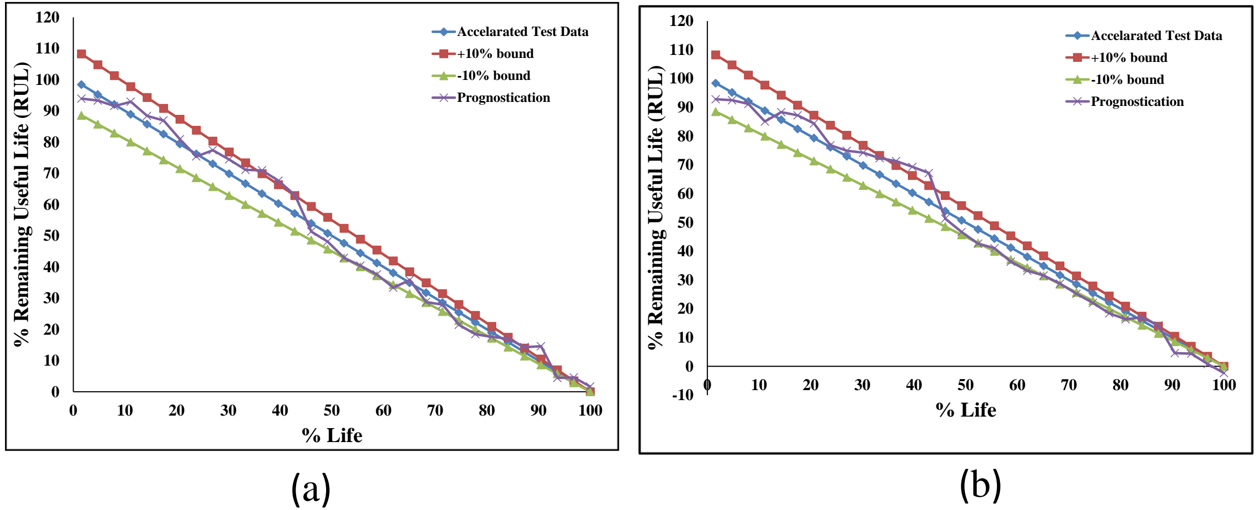


Figure 4-35: α-λ curve for Prognostication for CABGA144 at 0-100ºC (a) Using Phase growth as damage proxy and (b) Using IMC thickness as damage proxy

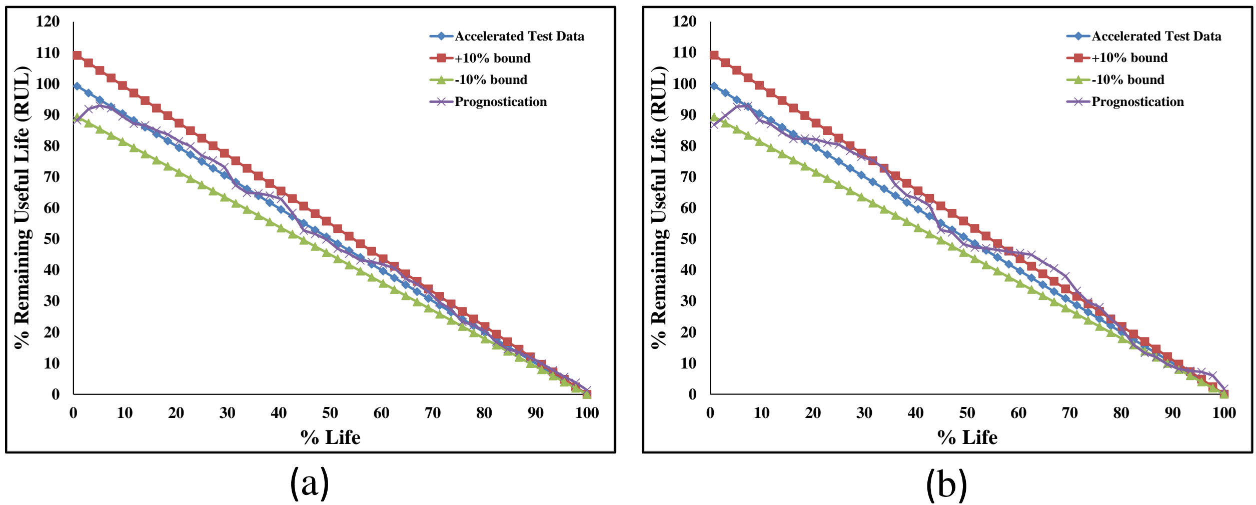


Figure 4-36: α-λ curve for Prognostication for CABGA144 at -50-50ºC (a) Using Phase growth as damage proxy and (b) Using IMC thickness as damage proxy

The main idea to plot α-λ curves for the two models was not to find the prognostic horizon point but to compare the relative performance of the models visually. It is clear from the plots that in case of IMC, overshooting outside the error bounds are more than that of Phase growth damage proxy although still relatively it remains close to the blue line. It helps

conclude that the prognostication model developed using phase-growth parameter as the leading indicator of failure performs better than the prognostication model developed using IMC for the current field conditions.

### 4.7.2 Sample Standard Deviation (SSD)

Precision in predictions is as important as accuracy. SSD calculates variability in prediction by measured spread of error with respect to sample mean of the error. This metric is restricted to assumption of normal distribution of errors [115].

$$S(i) = \sqrt{\frac{\sum_{l=1}^{n} [\Delta^{l}(i) - M]^{2}}{n-1}} \qquad \text{Eq. 4.25}$$

Where, M is sample mean of error.

### 4.7.6 Relative Accuracy

Relative accuracy for prediction is similar to α-λ curve, but here we measure accuracy level. The time instant is described as a fraction of actual remaining useful life from the first prediction point.

$$RA_{\lambda} = 1 - \frac{r_{*}(t_{\lambda}) - r^{l}(t_{\lambda})}{r_{*}(t_{\lambda})} \qquad \text{Eq. 4.28}$$

Where $\mathbf{t_{\lambda} = P + \lambda(EOL - P)}$ and $r^{l}(i)$ is the RUL estimation for the $l^{th}$ UTT at time $T_i$ as determined from measurements [115].

4.7.7 Cumulative Relative Accuracy (CRA)

CRA aggregates the accuracy levels calculated at multiple time intervals. CRA is normalized weighted sum of relative prediction accuracies at specific instances [115].

$$CRA = \frac{1}{\ell} \sum_{i=1}^{\ell} w(r^l) RA_{\lambda} \quad \text{Eq. 4.29}$$

Where, w is a weight factor as a function of RUL at all the time indices. In most cases it is desirable to weight the relative accuracies higher when closer to end of life.

Table 4-20: Comparison for Prognostics Metrics for Three Thermal Cycling Conditions.

| | Prognostic Parameter | 50-150°C | | 0-100°C | | -50-50°C | |
|---|---|---|---|---|---|---|---|
| | | PG | IMC | PG | IMC | PG | IMC |
| 1 | Average Bias | 0.53 | 0.98 | -0.14 | 0.15 | -0.25 | -0.94 |
| 2 | SSD | 53.16 | 66.72 | 109.69 | 138.15 | 106 | 219.26 |
| 3 | MSE | 3473.8 | 6688.4 | 13719.2 | 19297.13 | 12579.15 | 66382.65 |
| 4 | MAPE | 10.07 | 12.54 | 10.31 | 12.42 | 5.69 | 12.73 |
| 5 | RA (λ=0.5) | 0.967 | 0.99 | 0.95 | 0.92 | 0.98 | 0.95 |
| 6 | CRA | 0.019 | 0.018 | 0.0089 | 0.0087 | 0.00642 | 0.0059 |

Table 4-20 shows comparison of prognostics models based upon parameters discussed earlier. Algorithm maintains higher relative accuracy at λ=0.5 (i.e. after consuming 50% life) for all three temperature ranges. Higher RA is always desirable. Both leading indicators based prognostic algorithms show comparable performance.

## 4.8 Conclusions

Using three different packages, effect of mean temperature of temperature cycling on package reliability was investigated. A damage mapping method has been developed based on the underlying physics-based leading indicators to relate the damage accrual rate to life consumed under three different temperature cyclic environments. A Predictive Model has also been developed using the failure data of all three packages analyzed. Convergence of both Damage Mapping relationships and Predictive Model using two damage proxies and convergence of Prognosticated Values and Experimental Values of damage indicators established the validity of our approach.

# Chapter 5

# DIC Based Investigation into The Effect of Mean Temperature of Thermal Cycle on The Strain State in SnAgCu Solder Joint

## 5.1 Overview

Field deployed electronics, unlike controlled laboratory testing, may experience a variety of sequential thermo-mechanical stresses during its lifetime. The field environment imposed on the electronic system may be influenced by ambient conditions and usage profile. Variation in the ambient temperature conditions, weather variations, usage location in addition to scheduled system usage or downtime may result in wide variance in the resulting field profile. Thermally induced stresses can also be produced in fabrication stage also. The CTE mismatch between the chip, substrate and printed circuit board (PCB) produces this thermally induced mechanical stresses. In an electronic packaging assembly, the crucial part affecting reliability the most is the solder ball which actually bears most of the stress gradients formed inside packages due to CTE mismatch. Thus safety critical nature of the electronics systems necessitates that level-of-damage and reliability be assessed prior to any future redeployment. To satisfy this need extensive research based on in-situ thermal deformation measurement mostly using Digital Image Correlation (DIC) and Moiré Interferometry was done, not necessarily aimed at investigating the effect of different thermal loading condition. In this study two different test vehicles, BGA 144 and 256 with two different solder alloys namely as SAC 305 and SAC 105 were used in this study under three different test conditions 50-150ºC, 0-100ºC and -50-50ºC. The temperature cycling range is carefully chosen to have same ΔT but different mean

temperature to reveal the effect of mean temperature on package reliability. DIC was done on pristine packages under three different temperature conditions with different set of package size to show how strain amplitude varies with mean temperature.

## 5.2 Test Vehicle

In this study, two different leadfree assemblies CABGA 144 and PBGA-256 with two different SAC alloys namely SAC105 and SAC305 have been used. The packages are full-array configuration and the ball diameter for the 144 I/O and 256 I/O is 0.3 and 0.32 mm respectively. Package attributes are shown in Figure 5-3.

Table 5-1. The printed circuit board was a double-sided FR4-06 material. The printed circuit board pads were solder mask defined (SMD) with immersion silver finish. Figure 5-1 shows the packages. All test vehicles were subjected to thermal cycling environments ranging from TC1: -50°C to 50°C, TC2: 0°C to 100°C and TC3: 50°C to 150°C. The test board is a JEDEC form-factor test board with corner holes. Each test package has four daisy chain patterns corresponding to the four quadrants. Board assemblies were assembled at in-house surface mount facility of CAVE3. The reflow profile used for assembly is shown in Figure 5-3.

Table 5-1: Package Attributes

| | Board A | Board B | Board C | Board D |
|---|---|---|---|---|
| Solder | Sn3Ag0.5Cu | Sn3Ag0.5Cu | Sn1Ag0.5Cu | Sn1Ag0.5Cu |
| Body Size (mm) | 17mm | 13 mm | 17mm | 13 mm |
| Package Type | PBGA | CABGA | CABGA | CABGA |

| I/O Count | 256 | 144 | 256 | 144 |
|---|---|---|---|---|
| I/O Pitch (mm) | 1 | 1 | 1 | 1 |
| Ball Diameter (mm) | 0.32 | 0.3 | 0.32 | 0.3 |
| Matrix | 16 x 16 | 12 x 12 | 16 x 16 | 12 x 12 |
| Pad (board) | NSMD | NSMD | NSMD | NSMD |
| Pad (package) | SMD | SMD | SMD | SMD |
| Board Finish | ImSn | ImSn | ImSn | ImSn |

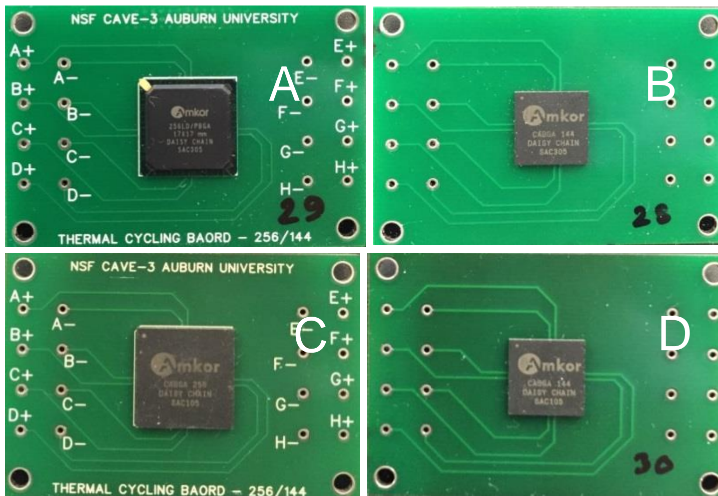


Figure 5-1: Test vehicle

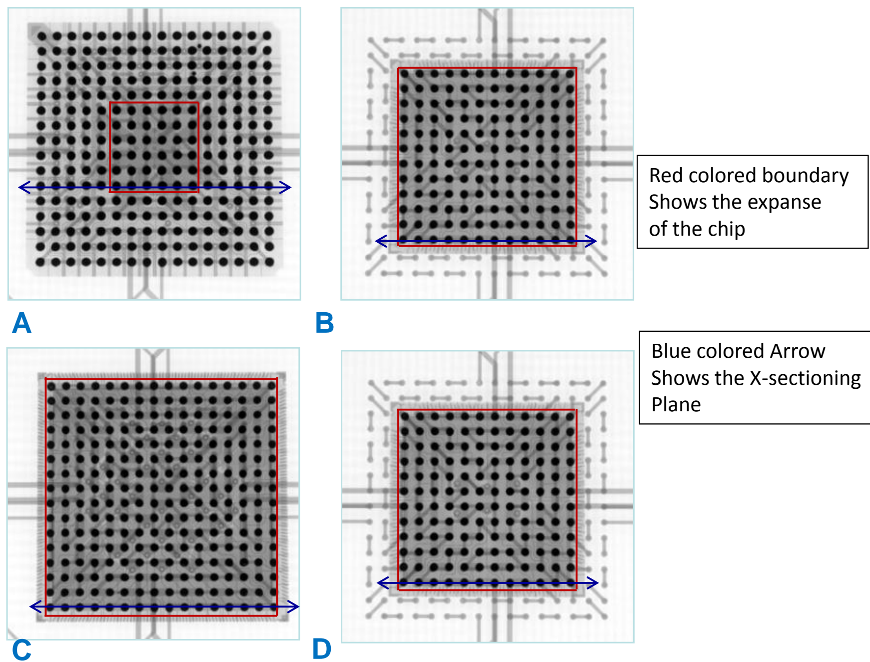


Figure 5-2: X-Ray Image of Test Vehicle

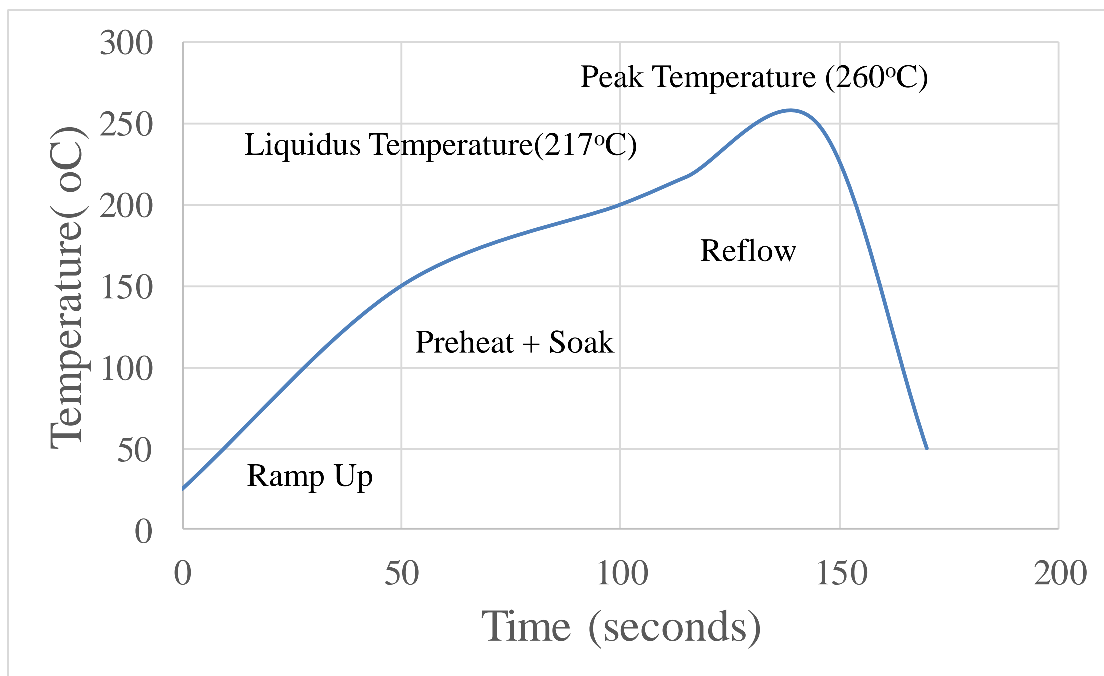


Figure 5-3: Reflow profile

## 5.3 DIC Working Principle

The basic principle of DIC is the tracking (or matching) of the same image points located in the two digital images of the test specimen surface recorded before and after deformation [118]. The test specimen surface must be covered with a random speckle pattern in the DIC technique, which serves as a carrier of deformation information [119-121].

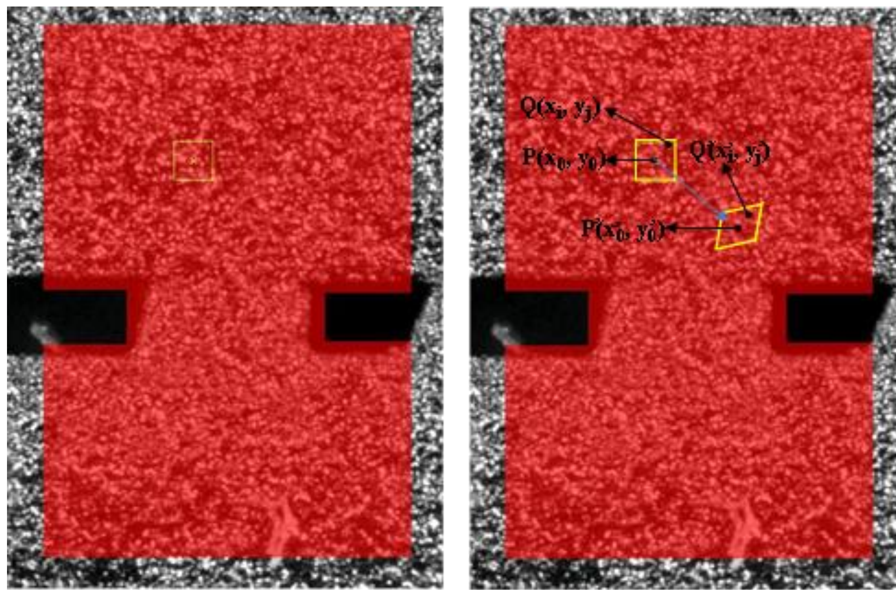


AOI: Area of interest (shaded by red)
Subset: Marked by yellow, $P(x_0,y_0)$: Subset center

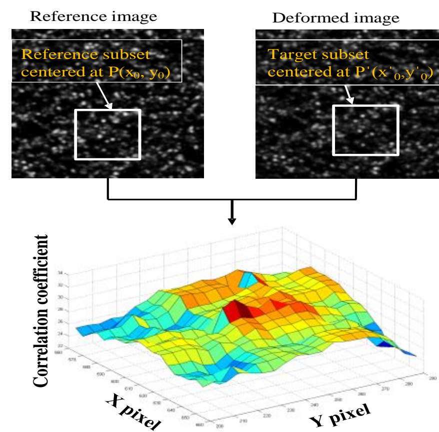


Figure 5-4: DIC working principle

As can be seen from Figure 5-4, in order to compute the displacements of a point of interest $P(x_0, y_0)$, a square reference subset of NXN pixels centered at the point of interest P from the reference image is chosen and used to track its corresponding location in the deformed image. To accurately track the position of the reference subset in the deformed image, a criterion must be established to evaluate the similarity or difference between the selected reference subset and the target subset. By sliding the reference subset in the searching area of the deformed image and computing the correlation coefficient at each location, a correlation coefficient map is obtained as schematically illustrated in Figure 5-4. Subsequently, the matching procedure is completed through searching for the peak value of the distribution of correlation coefficient using certain optimization algorithm. Once the correlation coefficient extreme is detected, the position of the deformed subset can be determined. The differences of the positions of the reference subset center and the target subset center yield the in-plane displacement vector at the point P. [122]

The correlation coefficient is computed between the reference subset and target subset. For a square subset containing n (=NXN) discrete pixels, let $f(x_i, y_i)$ and $g(x'_i, y'_i)$ denote the gray values of the ith pixel of the reference subset and the target subset, respectively. For avoid complexity, both $f(x_i, y_i)$ and $g(x'_i, y'_i)$ are substituted by $f_i$ and $g_i$ beyond this point. The most widely used formula to find degree of correlation is Normalized Correlation Coefficient (NCC) [122]

$$C_{NCC} = \frac{\sum f_i g_i}{\sqrt{\sum f_i^2 \sum g_i^2}} \qquad \text{Eq 5.1}$$

The VIC 2D software which we used implements Normalized Sum of Squared Difference (NSSD) as a correlation criterion which is same intuitively but has difference in

implementation scheme. While our goal is to maximize in case of NCC, it changes to minimization in case of NSSD that is to minimize the difference between the reference and deformed image.

$$C_{NSSD} = \Sigma\left(\frac{f_i}{\sqrt{\Sigma f_i^2}} - \frac{g_i}{\sqrt{\Sigma g_i^2}}\right) \qquad \text{Eq 5.2}$$

**5.4 Experimental Procedures**

As the ball under die shadow is the most crucial spot to investigate, all the packages were sectioned and polished until the half section of the first row of balls under die shadow showed up. Very fine polishing paper was used to get as smooth surface as possible. Then the polished surface was first black painted and then given a very thin layer of gold sputtering to facilitate DIC. Then these speckled samples were thermally cycled in an environmental chamber. A Nikon ED camera with reverse stack lens was used to get magnified image of desired solder ball at different stage of thermal cycling. Board assemblies A, B, C and D were subjected to cycling at -50°C to 50°C, 0°C to 100°C and 50°C to 150°C . For the in-plane (2D) DIC measurement, the speckled cross-sectioned surface of the solder joints was projected onto the camera through the glass window. The sample surface was magnified by 50mm reverse stack lens mounted over 200mm primary lens. Image resolution is 1920X1080 pixels. 1 mm actual physical length is represented by 390 pixels in magnified image rendering 1 pixel approximately equal to 0.00256mm.

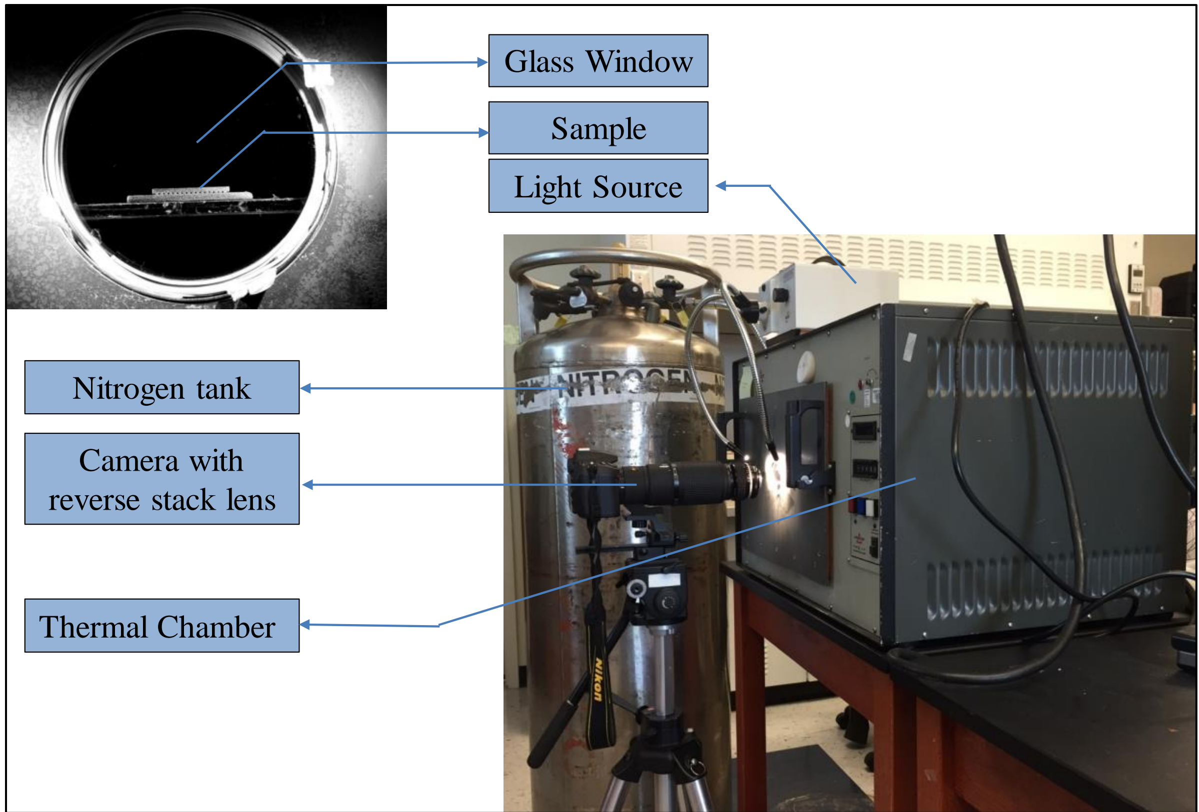


Figure 5-5: Experimental Setup

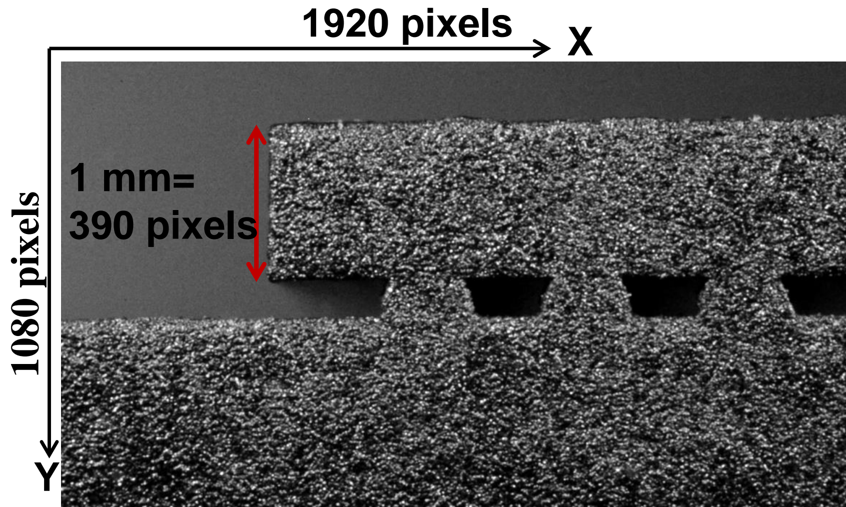


Figure 5-6: Gold sputtered X–sectional image of sample

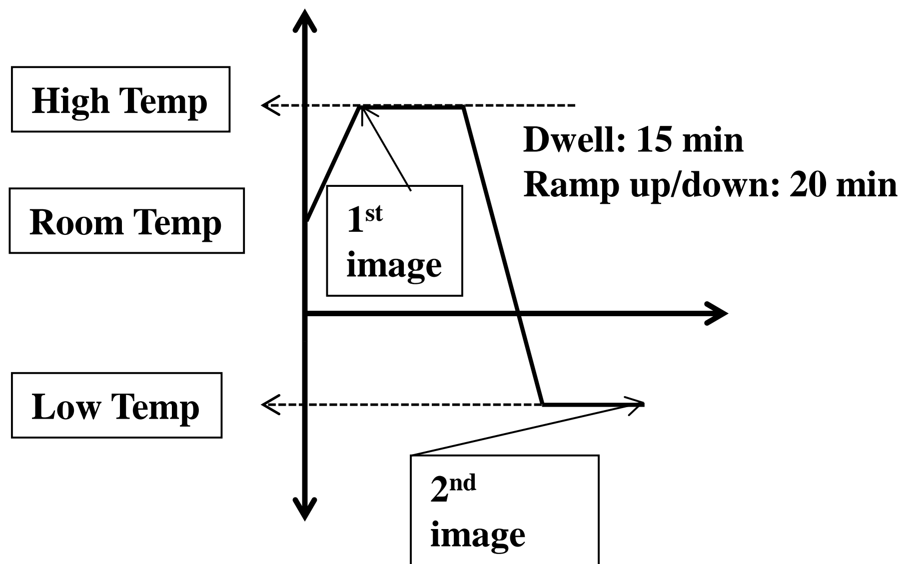


Figure 5-7: Stages of image acquisition in thermal cycle

In this experiment, images were taken at stage 1 and 2 as shown in Figure 5-7. Then DIC was done using image 1 as a reference and image 2 as deformed image. DIC analysis was done by VIC 2D software.

### 5.5 Experimental Results

As we are only interested with solder ball, in all the following contour plots we only investigate shear strains at the interface of component and solder ball and interface of PCB and solder ball. These two interfaces are the most crucial spots revealed by previous researches due to global mismatch of coefficient of thermal expansion.

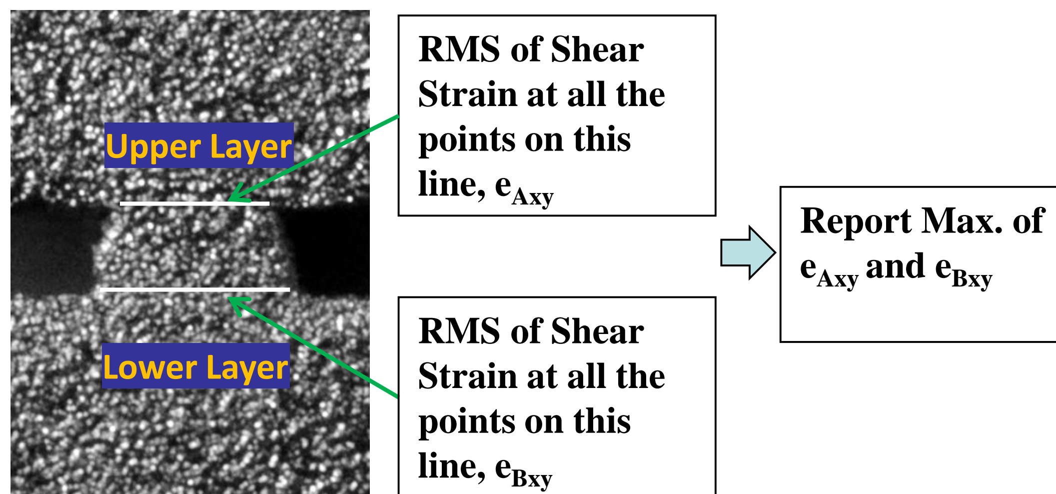


Figure 5-8: Location where shear strain are measured

Root mean square of shear strain values at each pixel situated on the lines denoted by upper and lower layer was calculated to investigate where the maximum shear strain occurs. Only the maximum shear strain value was reported. The following figures show the contour plots of shear strain distribution on a solder joint under die shadow region. Figure 5-9, Figure 5-10, Figure 5-11 and Figure 5-12 show the shear strain contour for CABGA 256 (SAC 105), CABGA 144 (SAC 105), CABGA 144 (SAC 305) and PBGA 256 (SAC 305) respectively.

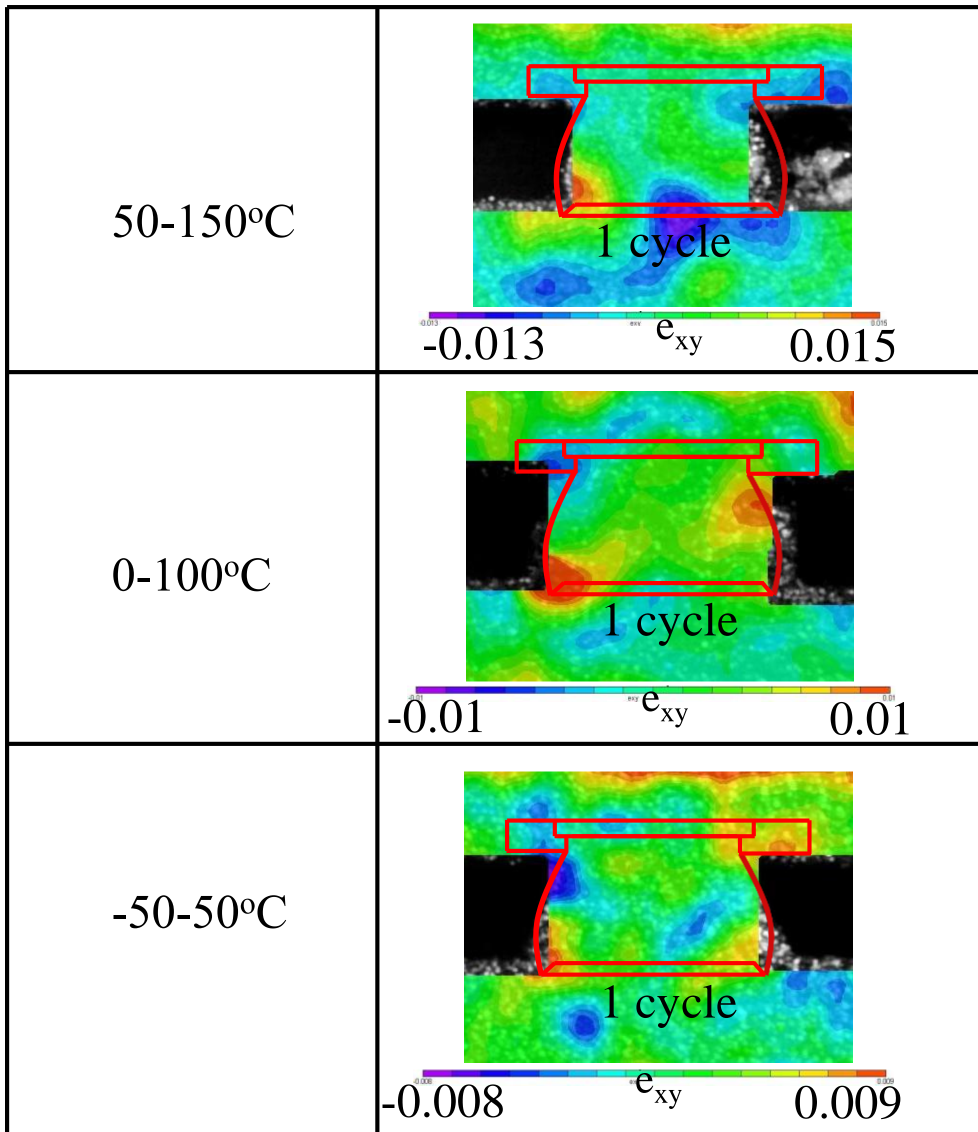


Figure 5-9: Shear strain contours for CABGA 256 (SAC105)

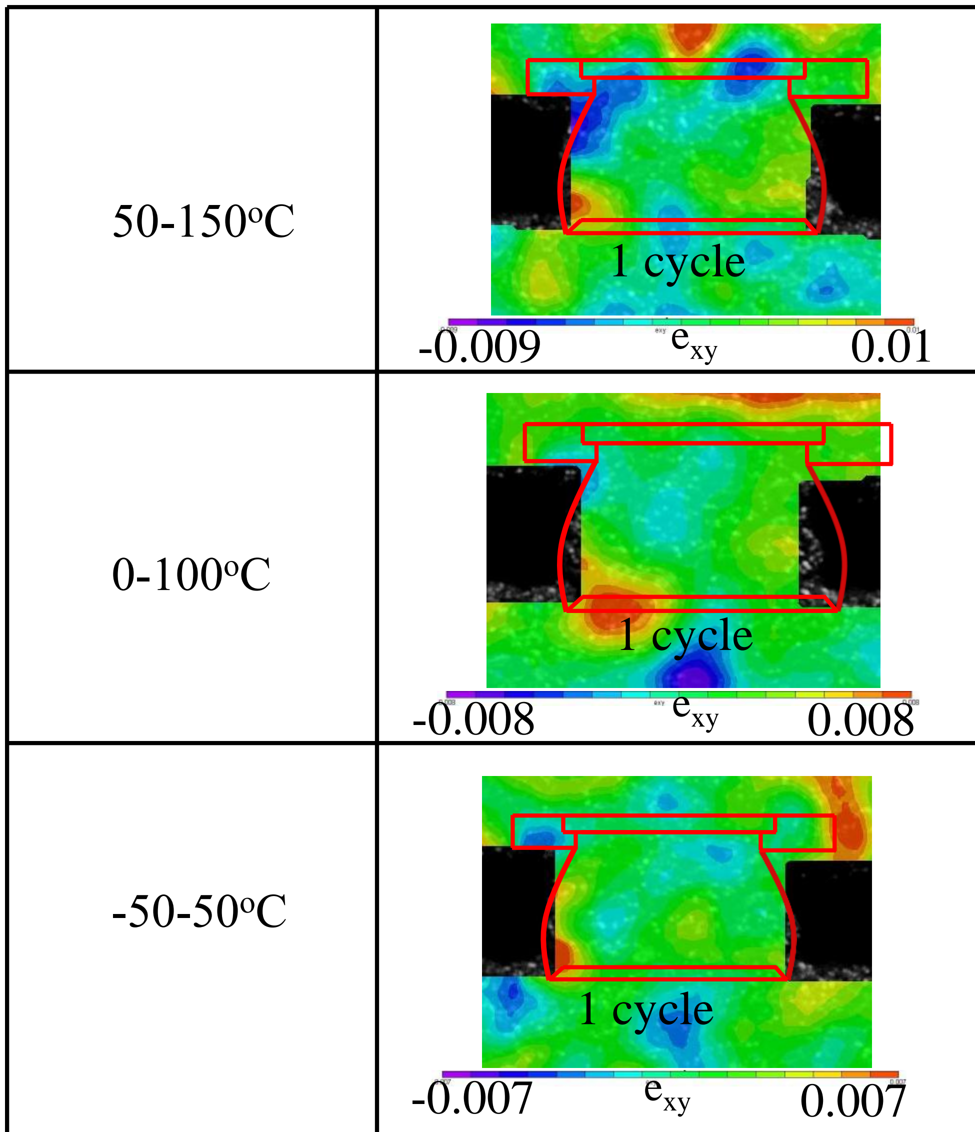


Figure 5-10: Shear strain contours for CABGA 144 (SAC105)

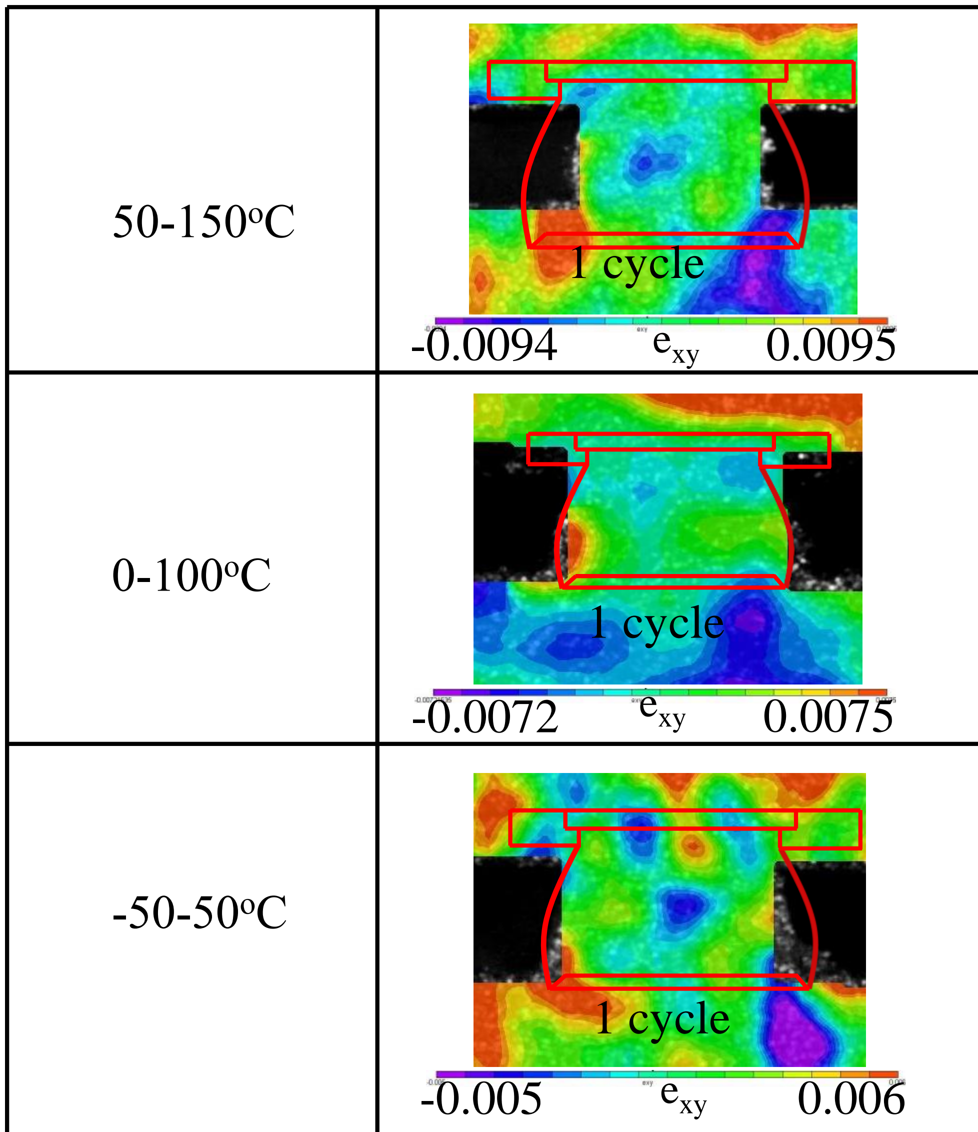


Figure 5-11: Shear strain contours for CABGA 144 (SAC305)

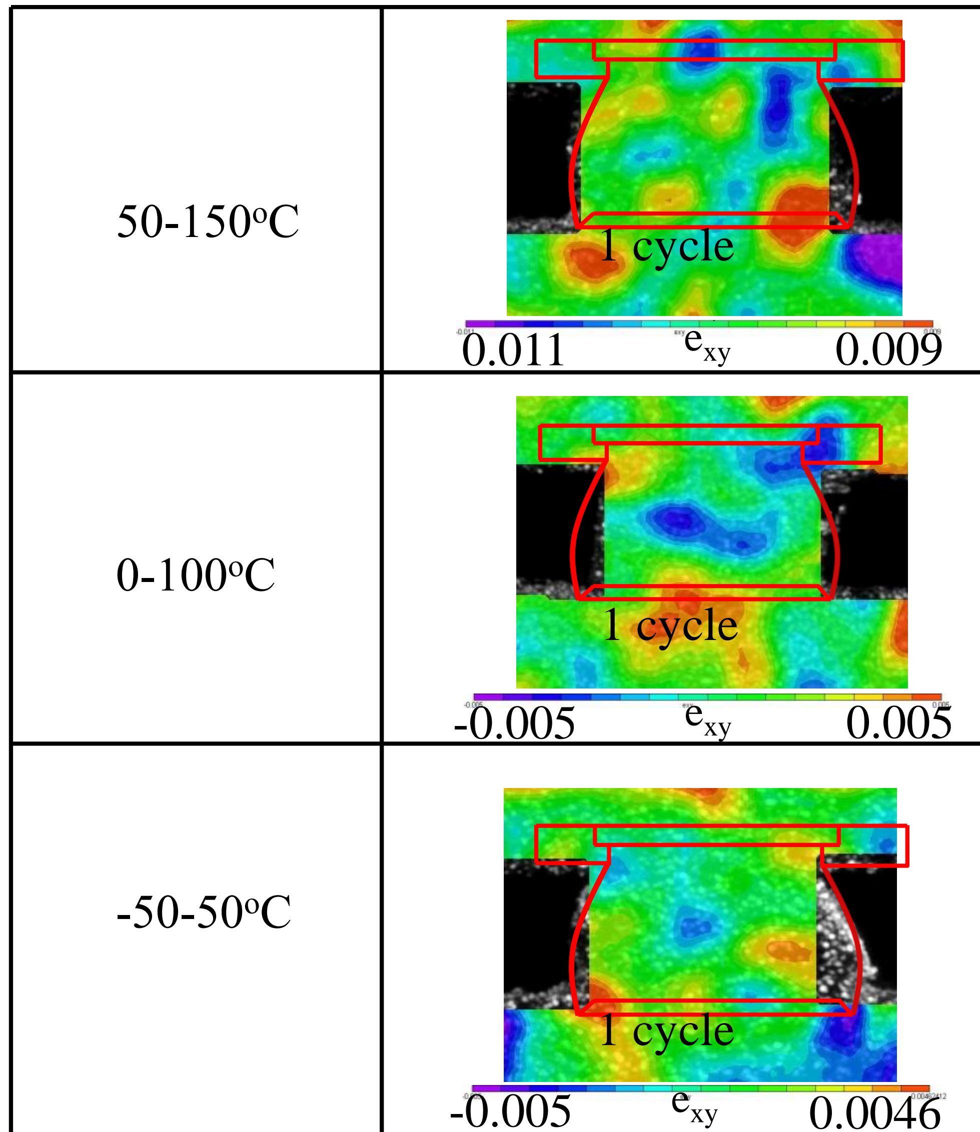


Figure 5-12: Shear strain contours for PBGA 256 (SAC305)

Table 5-2: Summary of experimental results

| | Shear Strain Range ($\Delta e_{xy}$) | | | |
|---|---|---|---|---|
| | CABGA 256 (SAC 105) | CABGA 144 (SAC 105) | CABGA 144 (SAC 305) | PBGA 256 (SAC 305) |
| 50-150°C | 0.005 | 0.0042 | 0.0039 | 0.0037 |
| 0-100°C | 0.004 | 0.0033 | 0.0028 | 0.0025 |
| -50-50°C | 0.0033 | 0.0027 | 0.0021 | 0.00198 |

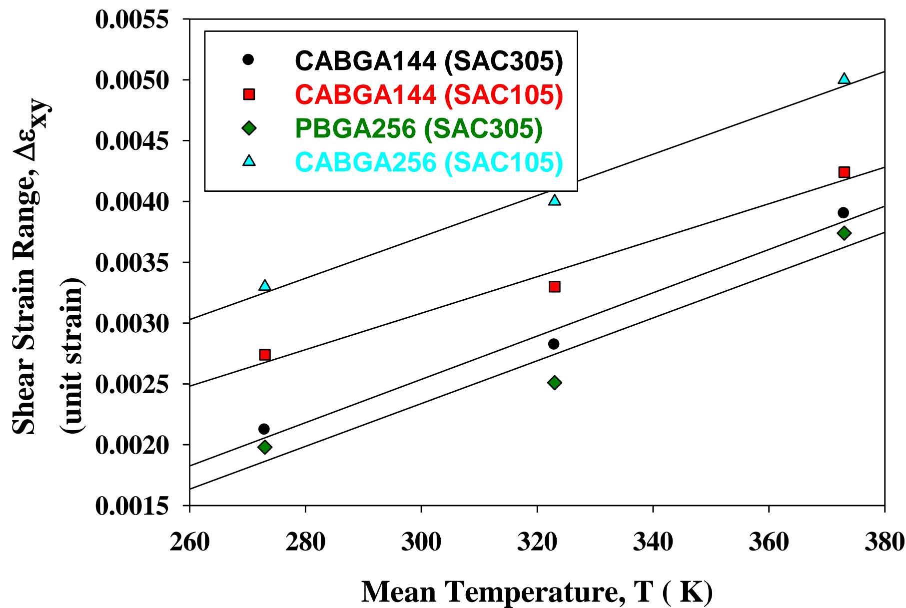


Figure 5-13: Shear Strain Range vs Mean Temperature from Experiment

It is obvious from Table 5-2 and Figure 5-13 that shear strain increases with mean temperature of thermal cycling. Thermal cycling at higher mean temperature means aging at higher temperature and creep increases with high level of thermal loading. This can explain higher magnitude of shear strain at higher mean temperature although temperature difference is the same for all three temperature conditions. SAC105 tends to be more ductile than SAC305 as we see for same level of thermal loading condition and same package architecture SAC105 solder ball undergoes higher level of displacement and shear strain which supports the notion that SAC105 is more vulnerable in thermal fatigue than its counterpart SAC305. One of the most detailed studies on thermal fatigue failure rate of Sn–xAg–Cu solder joints was conducted by Terashima et. al.[56] who found that increasing Ag content increases the fatigue resistance of SAC solder. Higher Ag containing alloys contains higher number of $Ag_3Sn$ dispersoid on bulk Sn matrix which in turn inhibit

coarsening of alloys rendering it to be more fatigue resistant. Furthermore, higher Ag containing solder alloys have smaller Sn grain structure. This means that during temperature cycling there will less chance of stress buildup at the grain boundaries. Also, since the starting grain sizes are smaller, overall impact of grain coarsening will be small. Both of these would also result in improved temperature cycling performance [123]. Another interesting finding supported by this experiment is shear strain dependency on package geometry. Shear strain shows decreasing tendency with decreasing die or chip size. This is a valid consequence as the larger the die size the more the die shadow solder ball will undergo shear strain according to DNP formula (Distance from neutral point).In case of SAC 305 PBGA 256 has smaller die size than CABGA 144 and in case of SAC 105 CABGA 256 has larger die size than CABGA 144 as revealed by Figure 5-2. The following Weibull plot also strengthen our experimental findings in which 50-150$^{o}$C, 0-100$^{o}$C and -50-50$^{o}$C are denoted by TC3, TC2 and TC1 respectively.

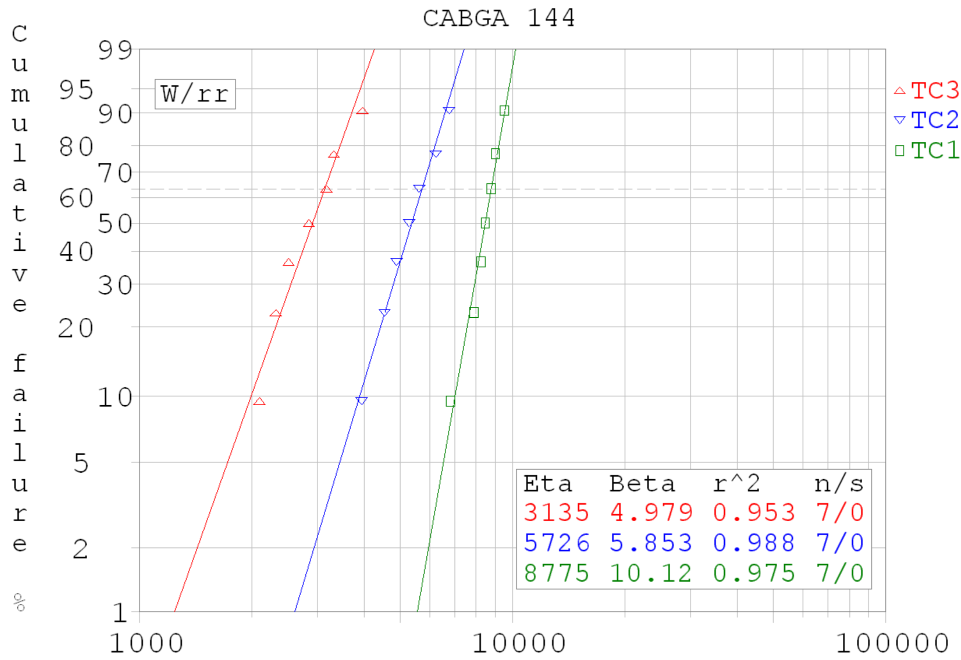


Figure 5-14: Weibull plot for CABGA 144 (SAC 305) [112]

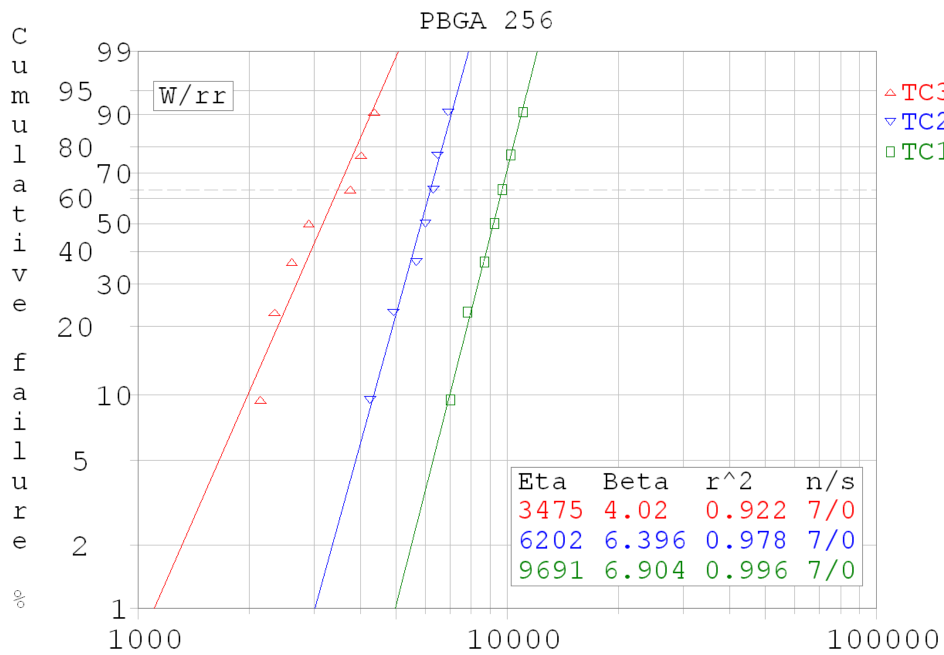


Figure 5-15: Weibull plot for PBGA 144 (SAC 305) [112]

### 5.6 Finite Element Analysis Results

Three-dimensional non-linear finite element modeling was used to calculate the strain energy density accumulation in solder joints. The solder material was modeled as a viscoplastic solid, the printed circuit boards as orthotropic linear elastic solids, and the rest of the materials as linear elastic solids. The quarter symmetry model was used with mapped finite element mesh. Solder ball materials were meshed with VISCO 107 materials and all other package materials are meshed with SOLID 185 elements. The quarter model has symmetry boundary condition along the symmetry line i.e. zero X displacement in X faces and zero Z displacement in Z faces of the full package and the bottom corner most node is given zero Y displacement to resist rigid body movement.

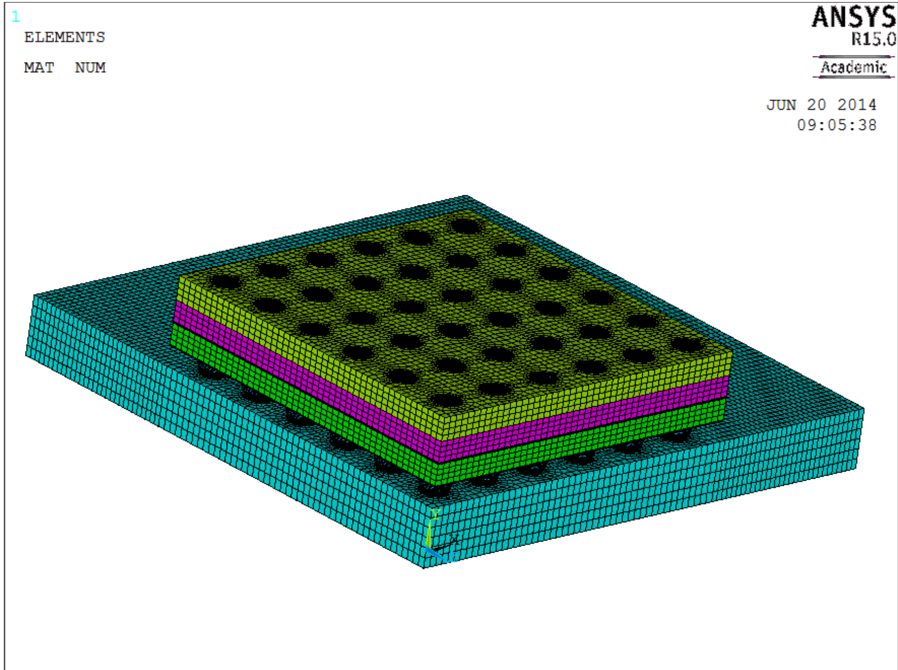


Figure 5-16: Quarter model of CABGA 144

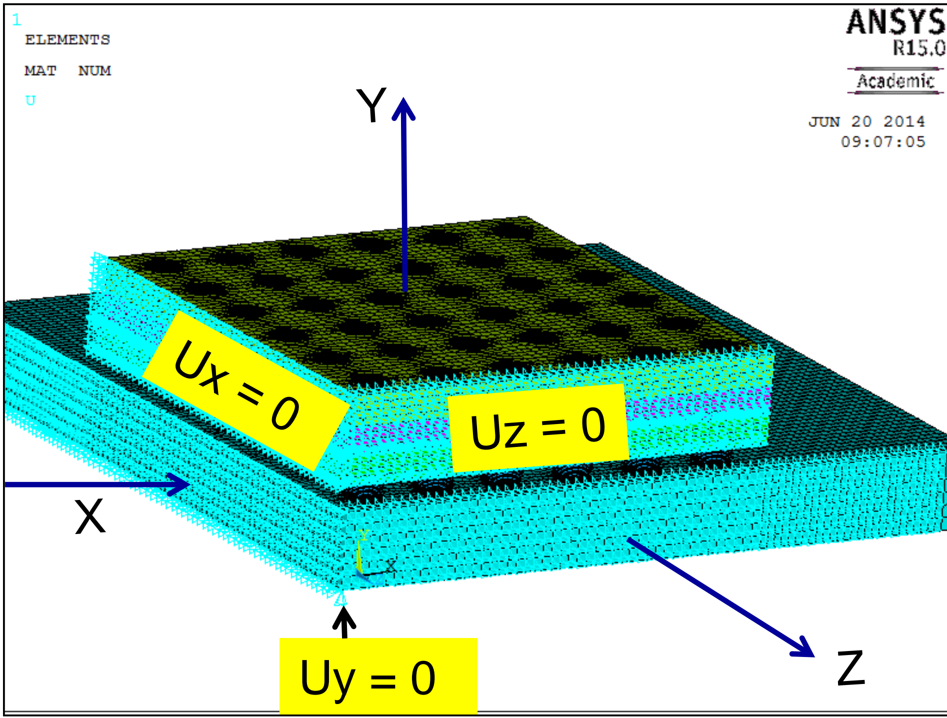


Figure 5-17: Quarter Model with boundary conditions

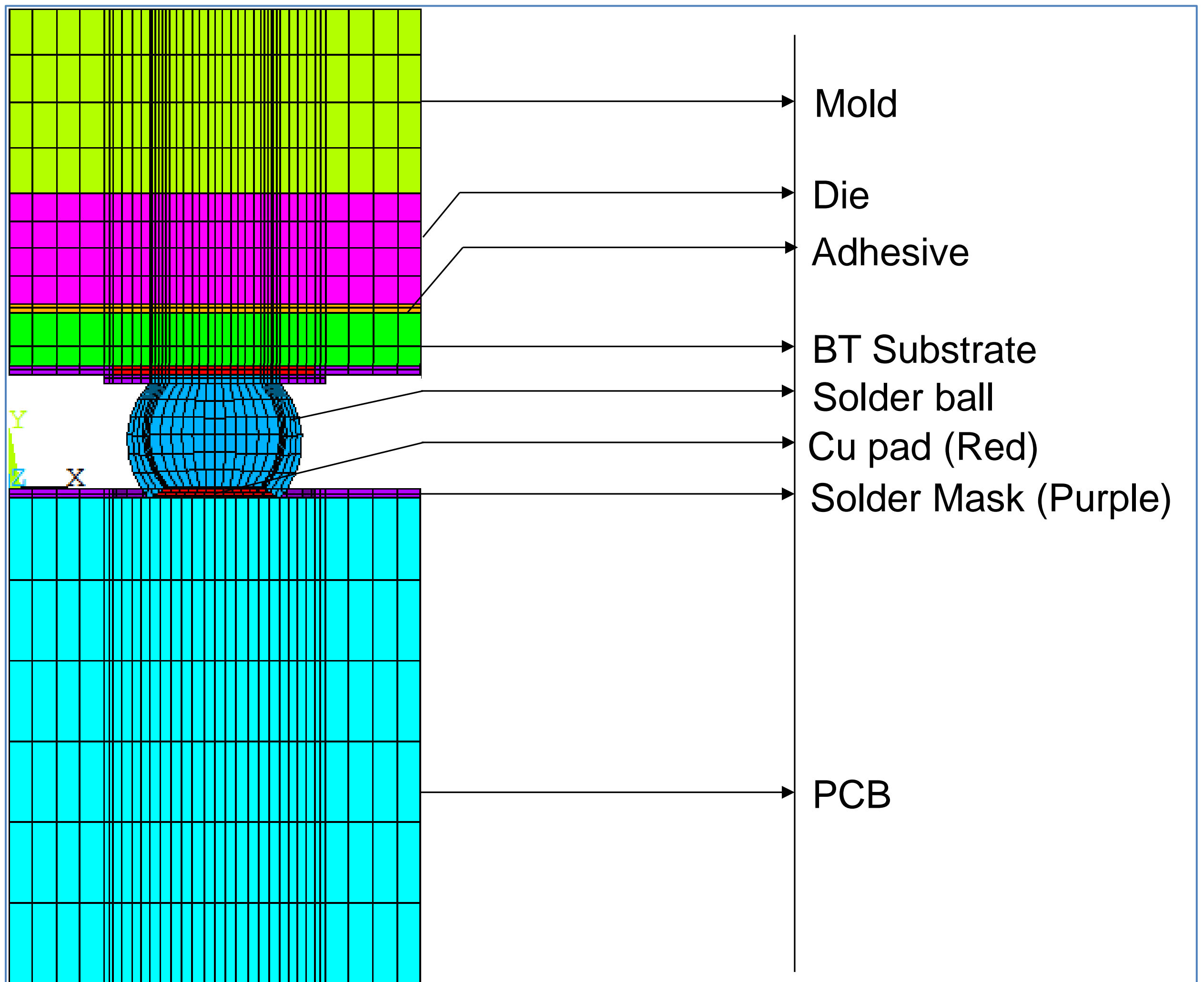


Figure 5-18: Material used in model

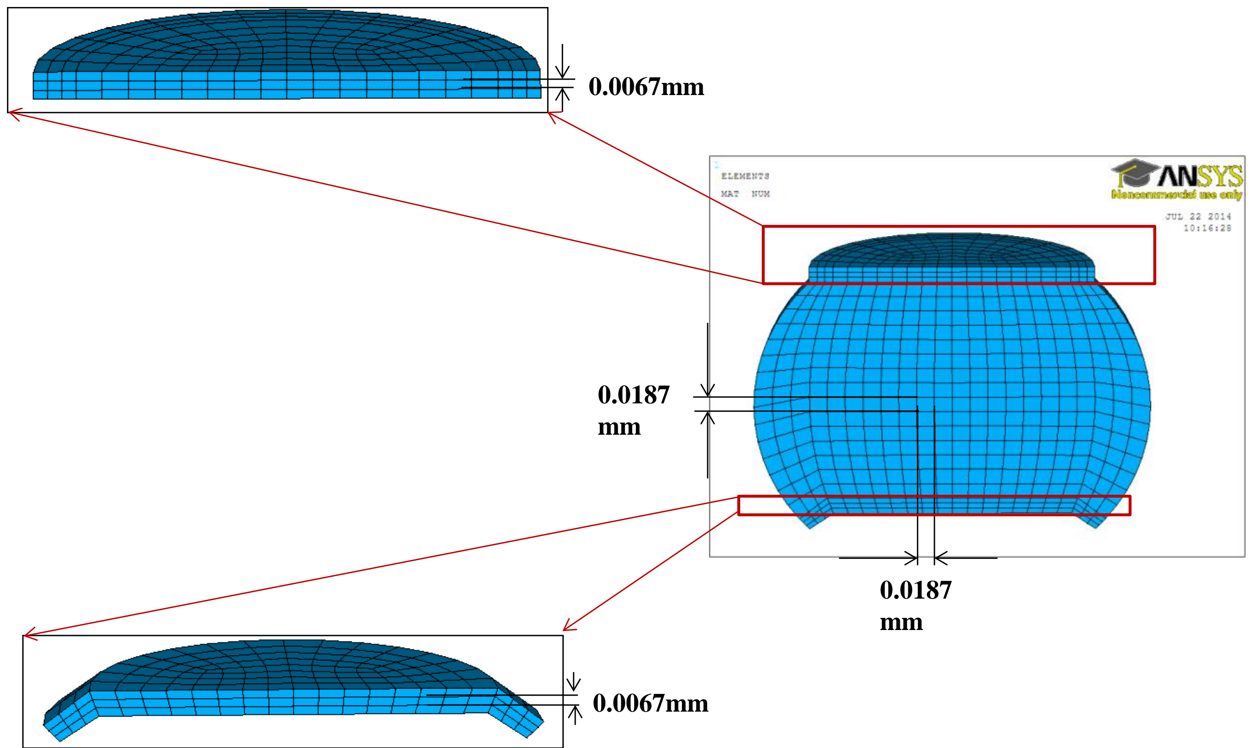


Figure 5-19: Solder ball mesh scheme

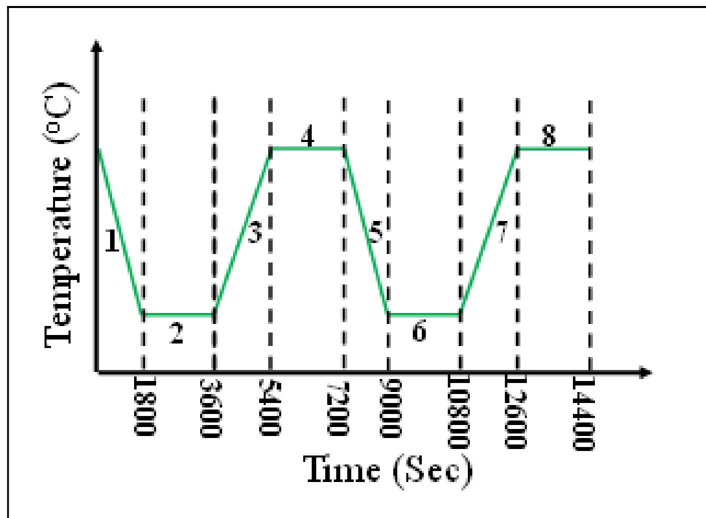


Figure 5-20: Temperature profile used in simulation

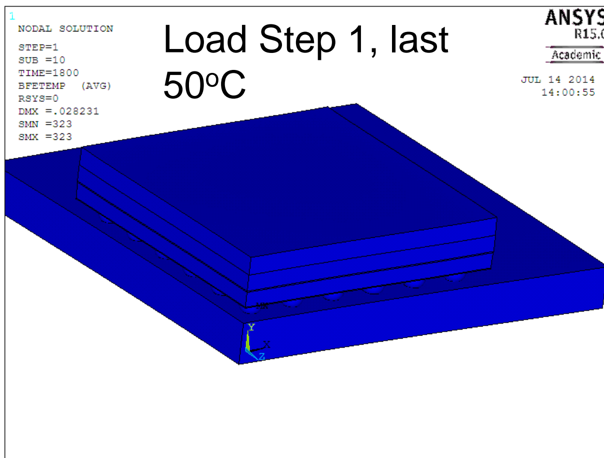


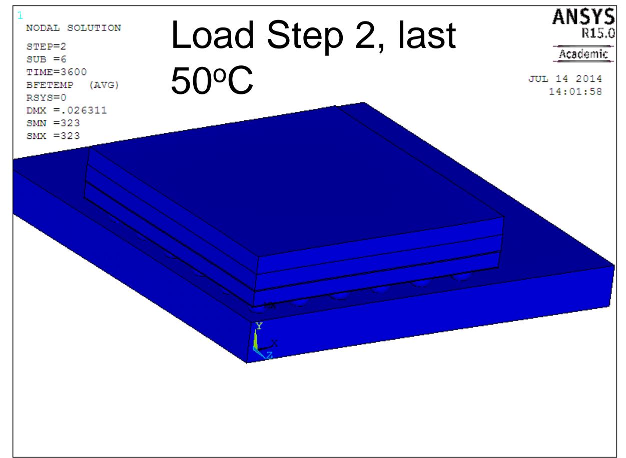


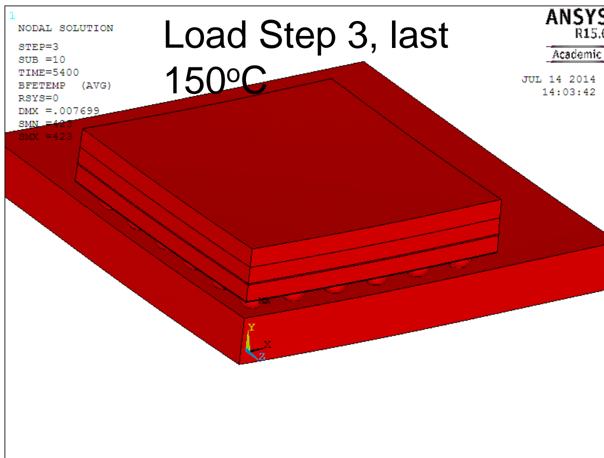


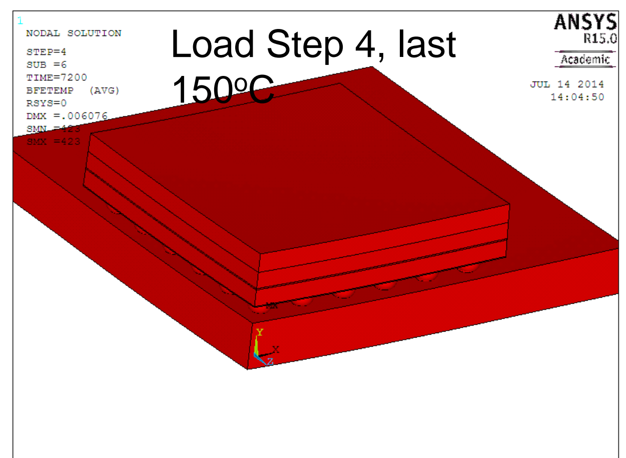


Figure 5-21: Temperature distribution during simulation for 50-150ºC

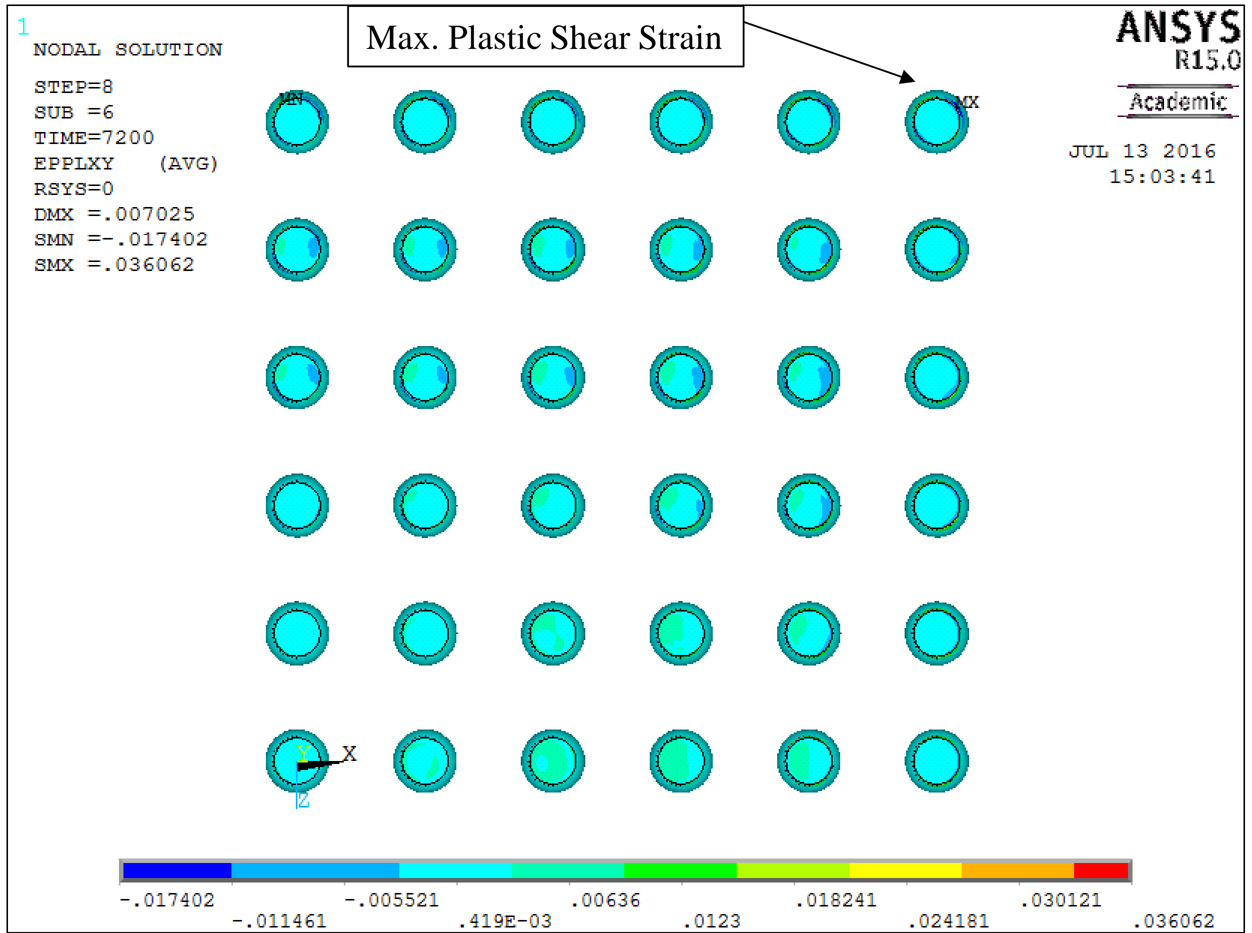


Figure 5-22: Plastic shear strain distribution

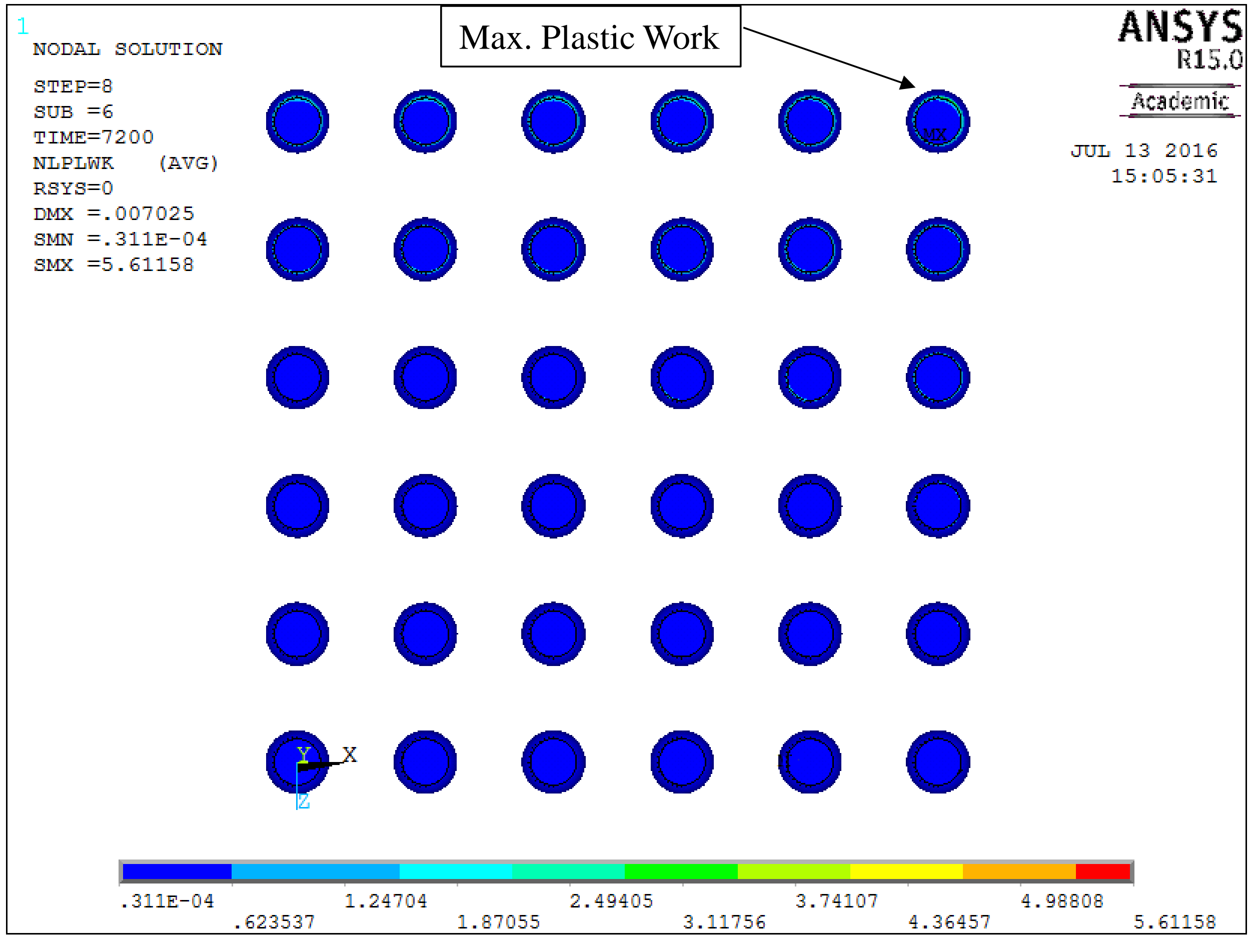


Figure 5-23: Plastic work density distribution

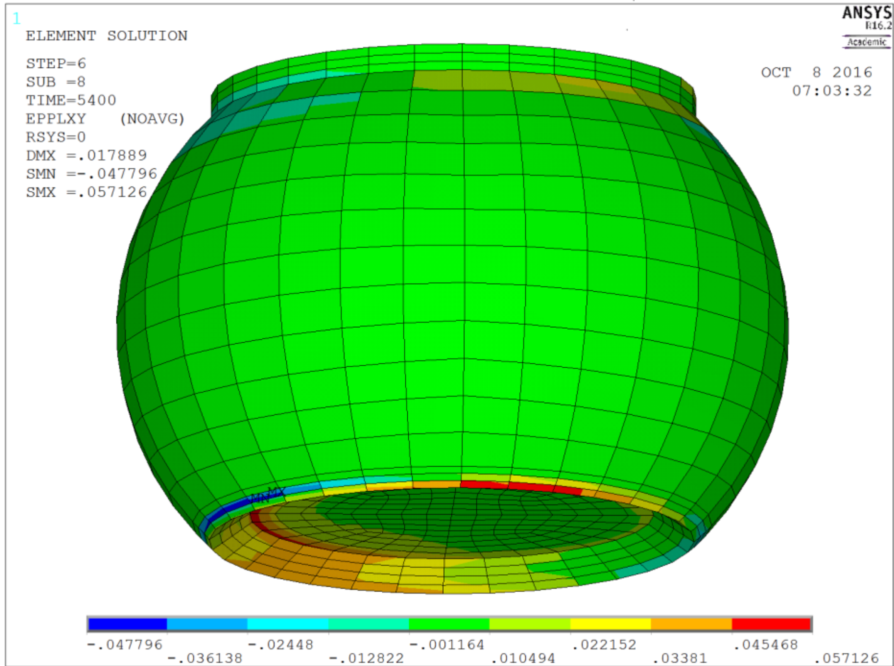


Figure 5-24: Location of maximum Plastic Shear Strain in critical solder joint.

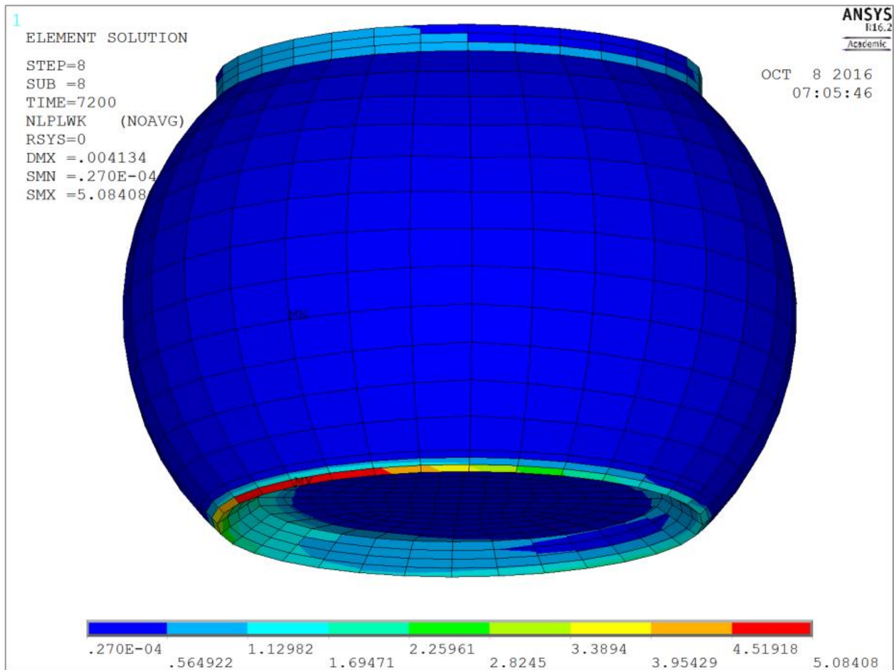


Figure 5-25: Location of maximum Plastic Work per volume in critical solder joint.

Table 5-3: Anand's Constant [25]

| | Unit | SAC305 | SAC105 |
|---|---|---|---|
| $S_0$ | MPa | 21 | 7.5 |
| Q/R | 1/K | 9320 | 8850 |
| A | $Sec^{-1}$ | 3501 | 6900 |
| $\xi$ | | 4 | 4 |
| m | | 0.25 | 0.215 |
| $h_0$ | MPa | 180000 | 137500 |
| $\hat{s}$ | MPa | 30.2 | 25.1 |
| n | | 0.01 | 0.0062 |
| a | | 1.78 | 1.96 |

As shown in Figure 5-19, the top and bottom most layer of solder ball is very finely meshed to capture stress concentration. Previous researches confirmed that solder joint is prone to crack nucleation and propagation either at component side or PCB side due to higher stress concentration. This concentration of stress results from abrupt change in geometry, existence of sharp edge of solder mask at substrate side (in case of SMD design), less area offered for ball attachment with Cu pad etc. Also the formation of Kirkendal void due to asymmetric diffusion nature of Cu and Sn near these regions aggravates the situations more. Volume average technique was used to calculate plastic work density.

$$\Delta W_{ave} = \frac{\Sigma \Delta W V}{\Sigma V} \quad \text{Eq. 5.3}$$

Where $\Delta W_{ave}$ is average visco-plastic strain energy density per cycle (Joule/mm$^3$), $\Delta W$ is visco-plastic strain energy density per cycle for each element, and V volume of each element (mm$^3$). Figure 5-24 and Figure 5-25 reveal that maximum shear strain, hence maximum plastic work occurs at either bottom or top layer which also supports our experimental findings. In our experiment most of the cases maximum shear strain occurred at bottom layer except some few cases.

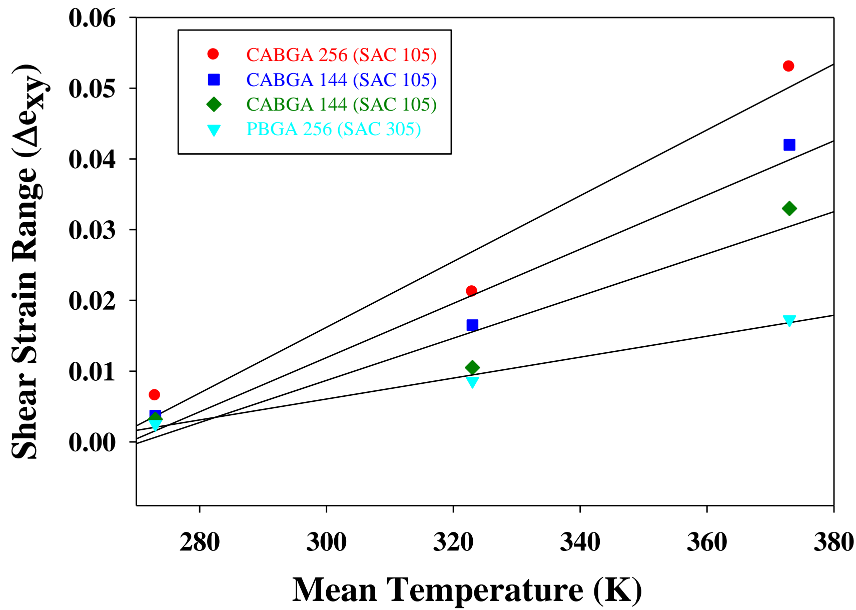


Figure 5-26: Shear Strain vs Mean Temperature from Simulation

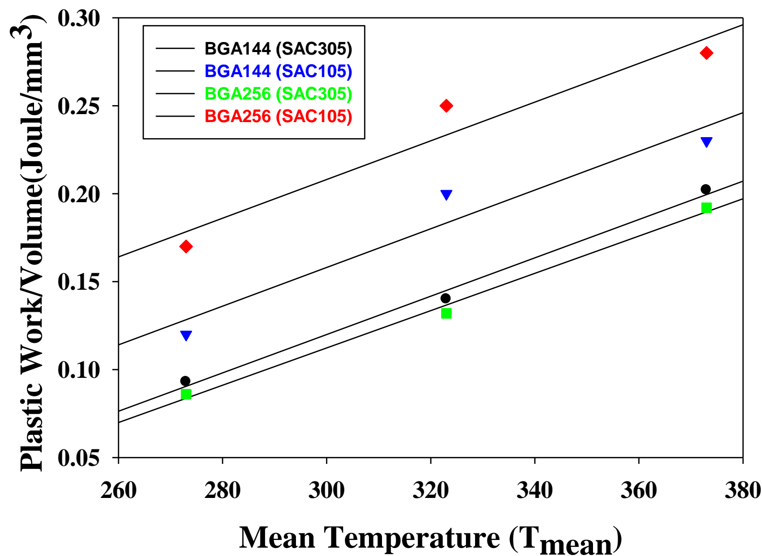


Figure 5-27: Plastic work vs Mean Temperature from Simulation

Figure 5-26 and Figure 5-27 also supports our experimental findings revealing increasing level of shear strain and plastic work with increasing mean temperature, although the shear strain value obtained from simulation is higher than the experimental one. This difference can be attributed to the difference in mechanical properties like Young's Modulus, Modulus of Rigidity, coefficient of thermal expansion etc. between bulk solder test sample (which were used to derive those above mentioned properties experimentally) and real solder joint. Real solder joints always show higher Young's modulus due to complex nature of IMC presence and formation (as almost all the IMC formed in joint have much higher Young's Modulus than conventional solder materials). Also bulk solder sample have higher creep rate due to presence of more micro defect as compared to miniature solder joints.

Evolution of plastic work with time and temperature were plotted from Figure 5-29 to Figure 5-32. To better visualize these plots, the time-temperature profile (Figure 5-28) used in simulation is also added again.

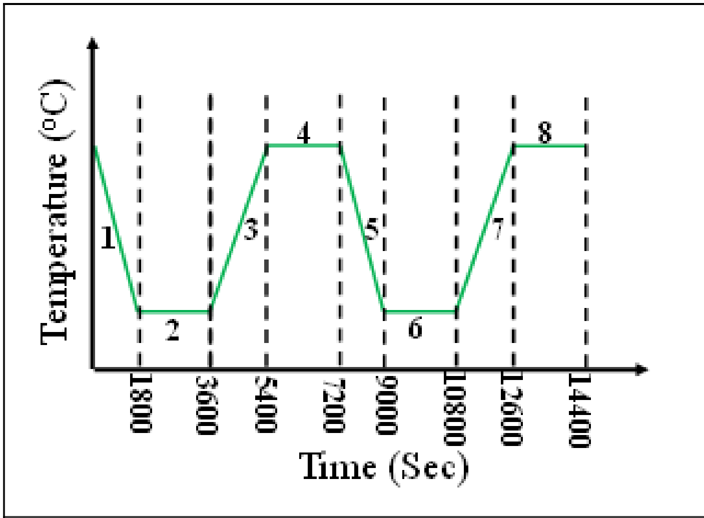


Figure 5-28: Temperature Profile

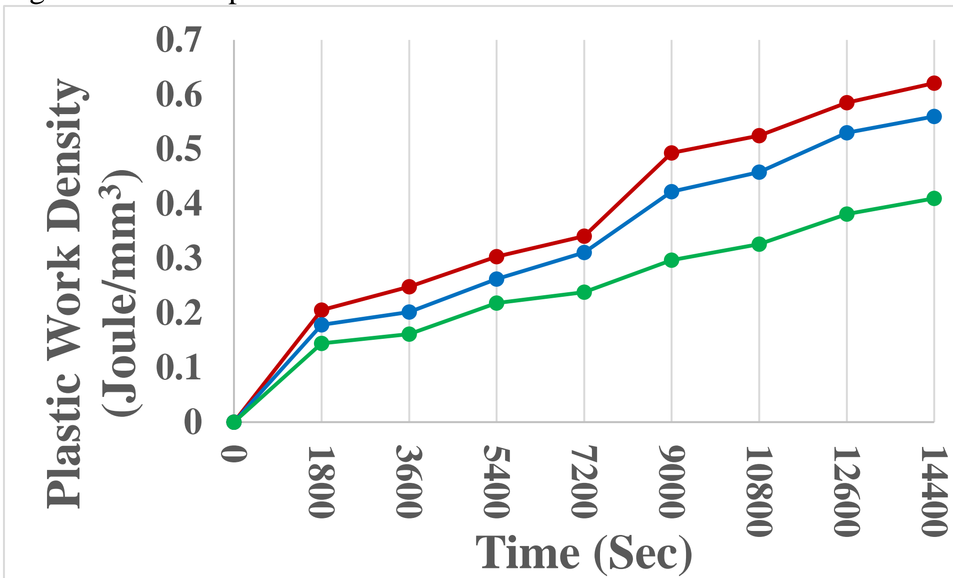


Figure 5-29: Plastic work density at different steps of thermal cycle for CABGA 256 (SAC105)

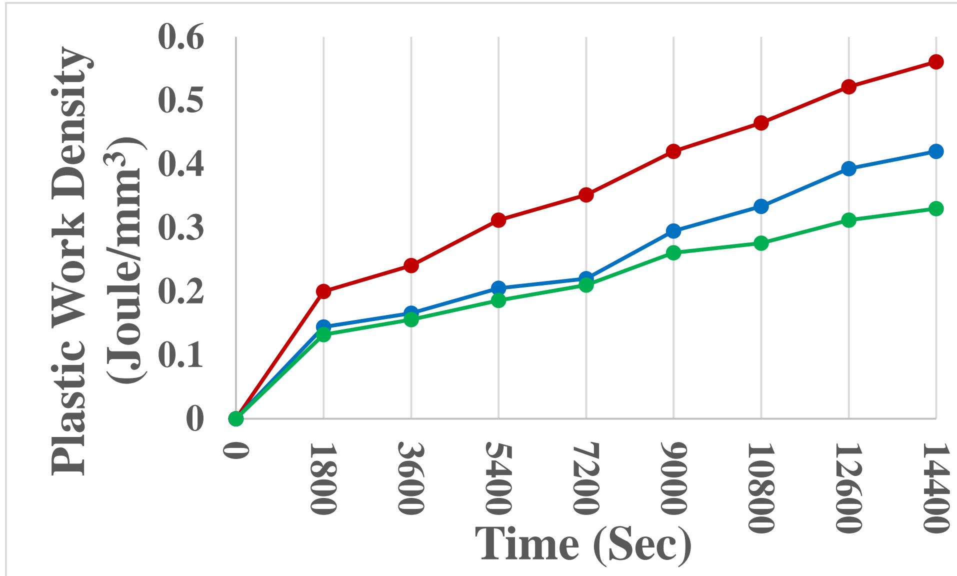


Figure 5-30: Plastic work density at different steps of thermal cycle for CABGA 144 (SAC105)

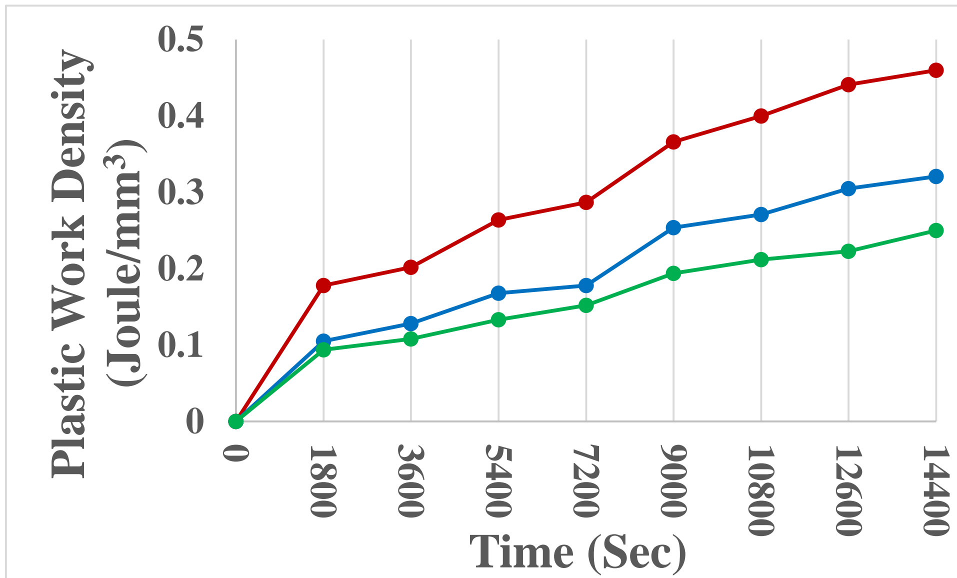


Figure 5-31: Plastic work density at different steps of thermal cycle for CABGA 144 (SAC305)

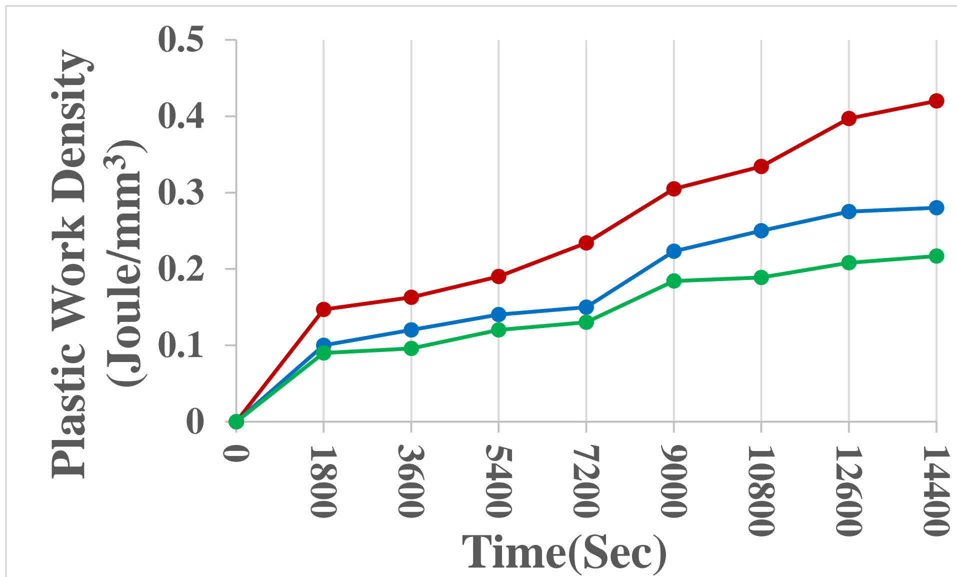


Figure 5-32: Plastic work density at different steps of thermal cycle for PBGA 256 (SAC305)

### 5.7 Conclusions

Using two different packages with two different solder alloys, effect of mean temperature of temperature cycling on package reliability was investigated. Thermal cycling condition having higher mean temperature is shown to have adverse effect on package reliability. Effect of different level of Ag content in SnAgCu alloys on fatigue life reliability also investigated. Package having higher number of solder balls i.e larger geometry shown to be more reliable.  Simulation results well supported our experimental findings.

# Chapter 6

# Determining the Effect of Aging on Thermal Cycling Reliability of Sn-Ag-Cu Interconnects Using Digital Image Correlation

## 6.1 Overview

High reliability electronics may be subjected to thermo-mechanical fatigue loads under harsh environmental conditions, which finally gives rise to solder joint failure. So to ensure safety, physical damage state and remaining useful life of electronic modules must be quantified prior to any future redeployment. Previous studies demonstrated the effect of aging and the effect of aging on thermal cycling reliability through material property evolution but evolution of strain as a function of aging and number of thermal cycling is yet to be studied. Additionally, industry needs a more realistic and quicker approach to quantify damage. Prior studies have revealed that lead-free material properties degrade with prolonged exposure to high temperature storage or thermal fatigue environment which in turn influences the stress-strain behavior of solder ball. Effects include the degradation in the yield strength and the ultimate tensile strength of the materials. In operational environment, it is of utmost necessity to assess the damage state and the remaining useful life of components to avoid any unexpected situation or accidents. From this aspect, evolution of shear strain range with number of thermal cycling undergone can be used as a strong prognostic tool. The degree of how much shear strain varies between aged and non-aged thermal cycled samples is worth investigating, as well. Mostly optical methods are employed to study strain field, mainly Moiré and Digital Image Correlation (DIC), but DIC is much easier, quicker and cheaper than Moiré, as it needs less surface preparation. It is a

novel effort to implement a measurement technique like Digital Image Correlation as compared to existing state of the art techniques like microstructural investigation, crack growth measurement or finite element simulation etc. to derive strain data and thereby investigate the effect of aging under different thermal cycling condition on solder joint reliability.

### 6.2 Test Vehicle

In this study, two different leadfree assemblies BGA 144 and BGA-256 with two different SAC alloys namely SAC105 and SAC305 have been used. The packages are full-array configuration and the ball diameter for the 144 I/O and 256 I/O is 0.3 and 0.32 mm respectively. Package attributes are shown in Table 6-1. The printed circuit board was a double-sided FR4-06 material. The printed circuit board pads were solder mask defined (SMD) with immersion silver finish. Figure 6-1 shows the packages. All test vehicles were subjected to thermal cycling environments ranging from TC1: -50°C to 50°C, TC2: 0°C to 100°C and TC3: 50°C to 150°C. The test board is a JEDEC form-factor test board with corner holes. Each test package has four daisy chain patterns corresponding to the four quadrants. Board assemblies were assembled at in-house surface mount facility of CAVE3. The reflow profile used for assembly is shown in Figure 6-3.

Table 6-1: Package attributes

| | Board A | Board B | Board C | Board D |
|---|---|---|---|---|
| Solder | Sn3Ag0.5Cu | Sn3Ag0.5Cu | Sn1Ag0.5Cu | Sn1Ag0.5Cu |
| Body Size (mm) | 17 mm | 13mm | 17 mm | 13mm |
| Package Type | PBGA | CABGA | CABGA | CABGA |
| I/O Count | 256 | 144 | 256 | 144 |
| I/O Pitch (mm) | 1 | 1 | 1 | 1 |

| Ball Diameter (mm) | 0.32 | 0.3 | 0.32 | 0.3 |
|---|---|---|---|---|
| Matrix | 16 x 16 | 12 x 12 | 16 x 16 | 12 x 12 |
| Pad (board) | NSMD | NSMD | NSMD | NSMD |
| Pad (package) | SMD | SMD | SMD | SMD |
| Board Finish | ImSn | ImSn | ImSn | ImSn |

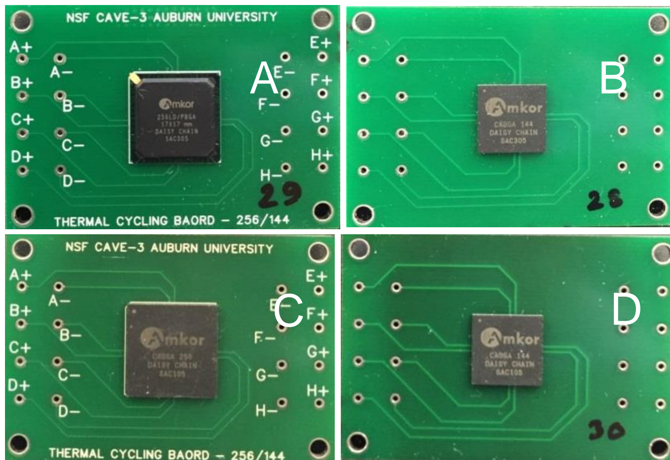


Figure 6-1: Test assembly

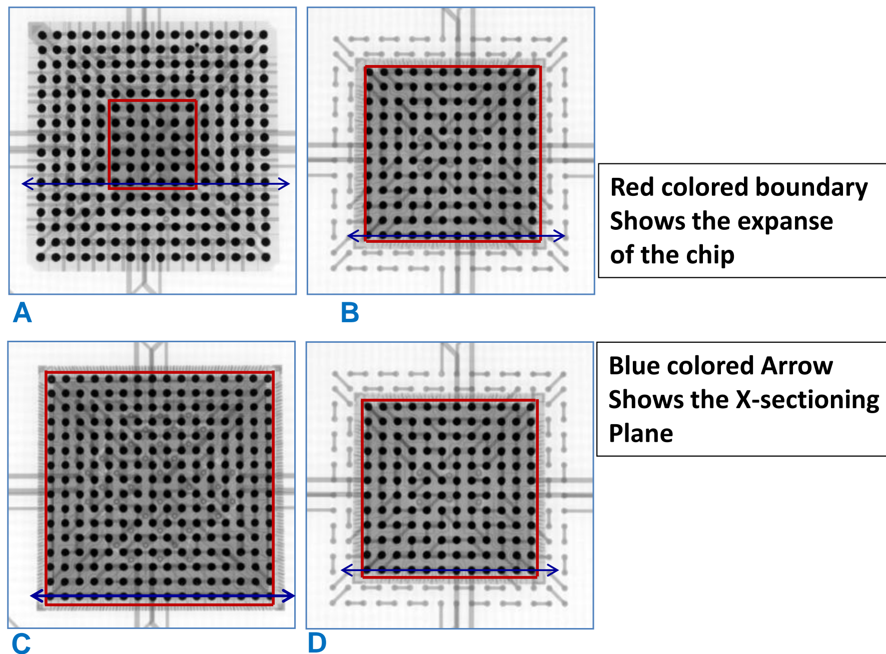


Figure 6-2: X-Ray Image of Packages

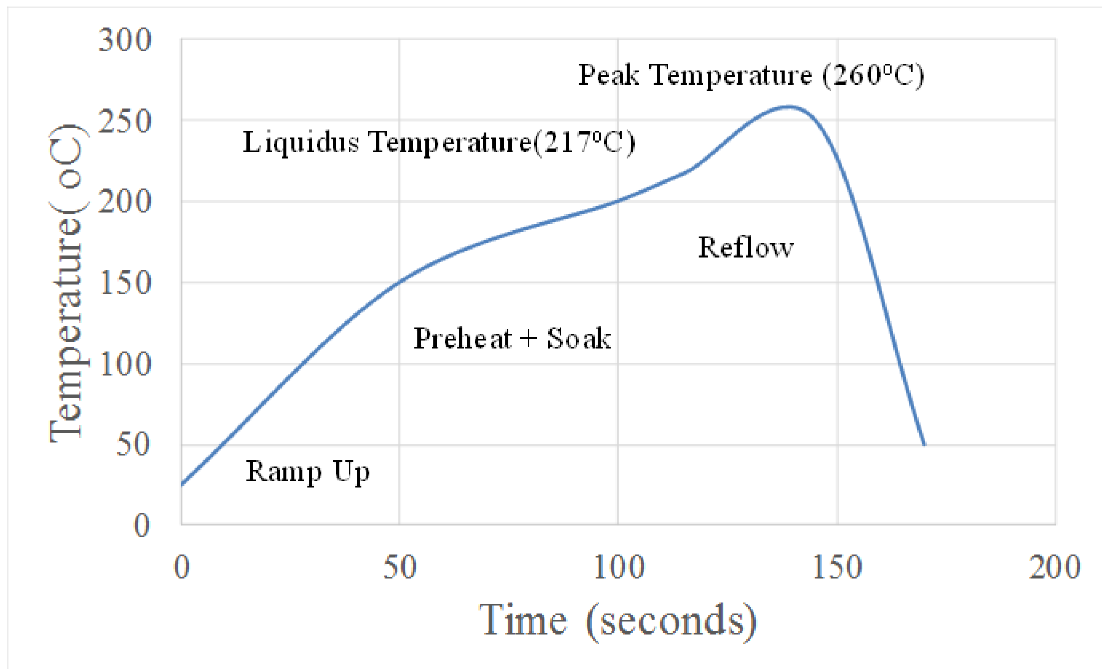


Figure 6-3: SAC Reflow profile

### 6.3 Experimental Procedure

All the packages (pristine and thermally cycled) were sectioned and polished by very fine polishing paper until the half section of the first row of balls under die shadow showed up. Then the polished surface was black painted and then given a very thin layer of gold sputtering to facilitate DIC. Then these speckled samples with their past history of aging and cycling, were then subjected to 1 more complete thermal cycle in an environmental chamber to facilitate DIC. A Nikon ED camera with reverse stack lens was used to get magnified image of desired solder ball (the bottom-left solder joint surrounded by red lines in Figure 6-2) at different stage of thermal cycling. Board assemblies A, B, C and D were subjected to cycling at -50°C to 50°C, 0°C to 100°C and 50°C to 150°C . A separate set of same test samples was subjected to isothermal aging under 125°C for 20 days first and then again subjected to three different thermal cycling conditions as 50-150°C, 0-100°C and -50-50°C. So we have 24 different cases and for each case we have 5 different samples, in

total 120 samples. It took on an average 15-20 minutes to ramp from lowest to highest temperature with a ramp rate from 5 to 6.5 ºC/min. and stabilize and dwell time was 15 minutes. For the in-plane (2D) DIC measurement, the speckled cross-sectioned surface (Figure 6-5) of the solder joints was projected onto the camera through the glass window. The sample surface was magnified by 50mm reverse stack lens mounted over 200mm primary lens. Image resolution is 1920X1080 pixels. 1 mm actual physical length is represented by 390 pixels in magnified image rendering 1 pixel approximately equal to 0.00256mm.

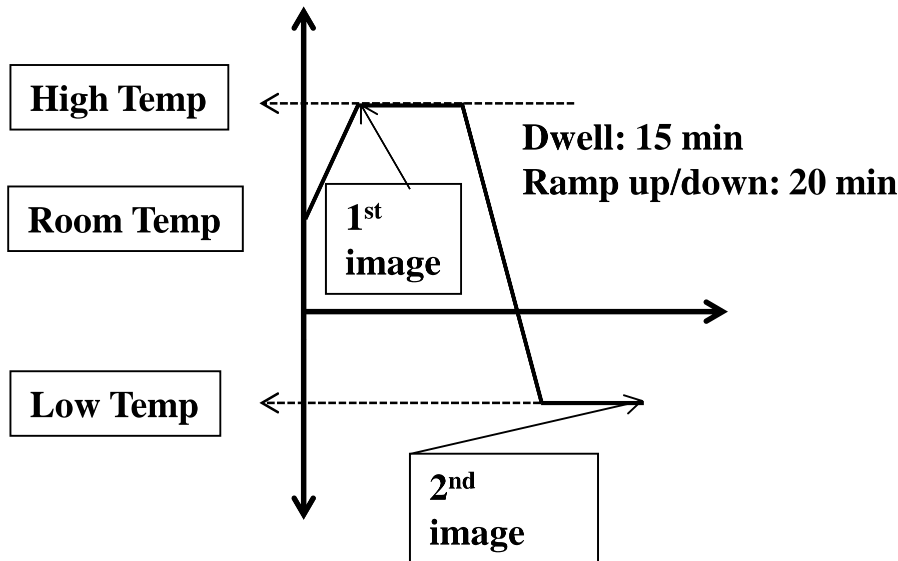


Figure 6-4: Stages of Image Acquisition in cycling

In this experiment images were taken at stage 1 and 2 as shown in Figure 6-4. Then DIC was done using image 1 as a reference and image 2 as deformed image. DIC analysis was done by VIC 2D software.

### 6.4 Experimental Results

To calculate shear strain we took average of all the pixels situated on the lines denoted by upper and lower layer (Figure 6-5) to investigate where the maximum shear strain occurs.

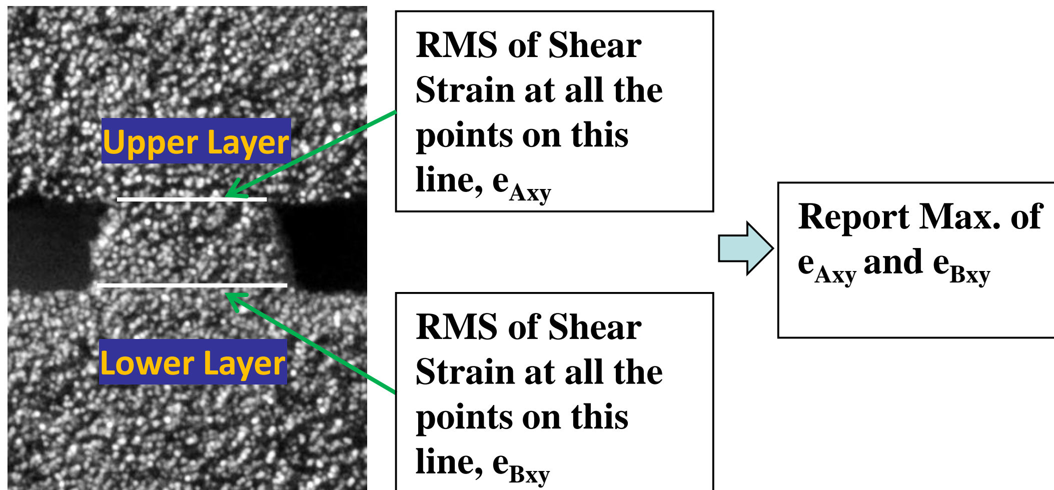


Figure 6-5: Location where shear strain are measured

Only the maximum shear strain value was reported. The following figures show contour plots showing shear strain experienced by a solder ball under die shadow region. It is evident from these contour plots that shear strain is the maximum either at the interface of solder joint and substrate or at the interface of solder joint and PCB.

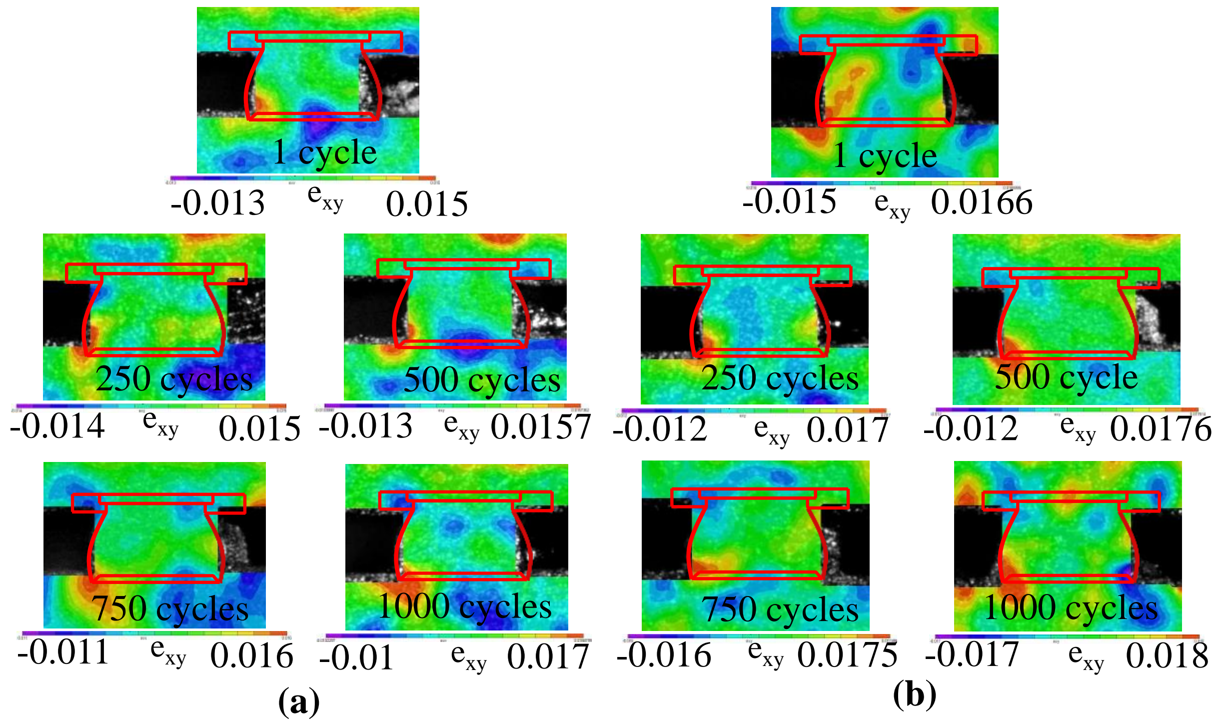


Figure 6-6: Shear strain contour of CABGA 256 (SAC 105) at different cycle's count of 50-150°C (a) without aging (b) with aging

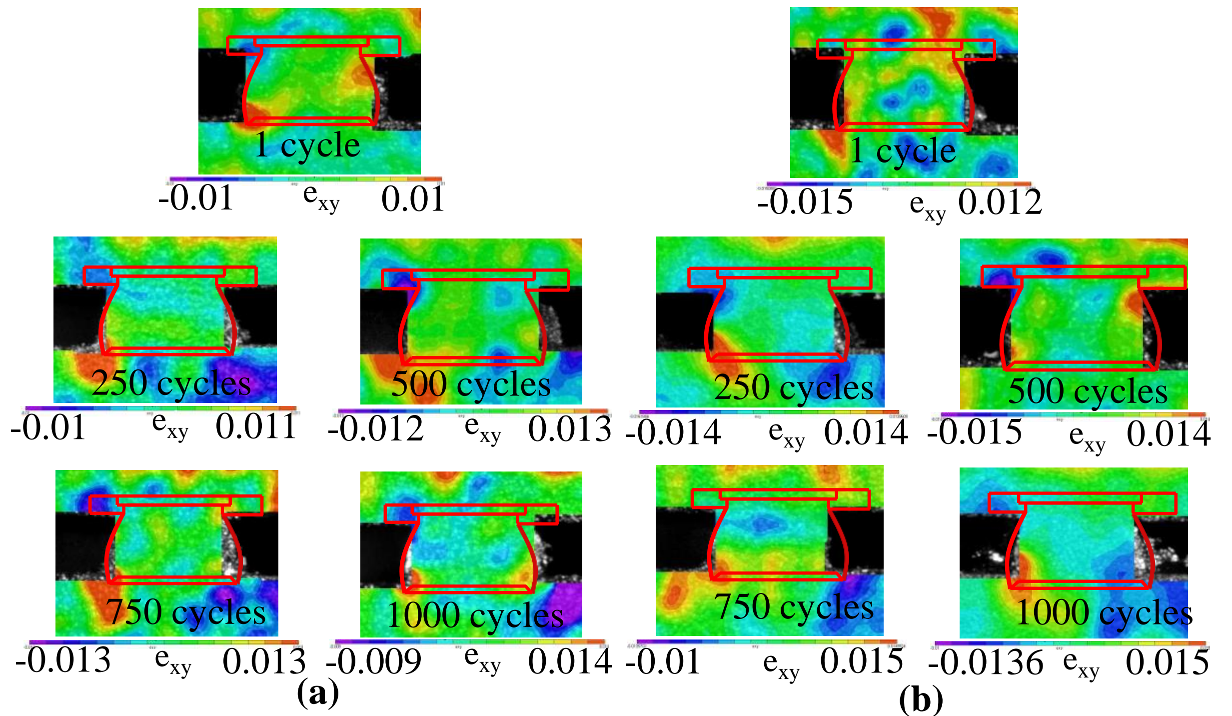


Figure 6-7: Shear strain contour of CABGA 256 (SAC 105) at different cycle's count of 0-100°C (a) without aging (b) with aging

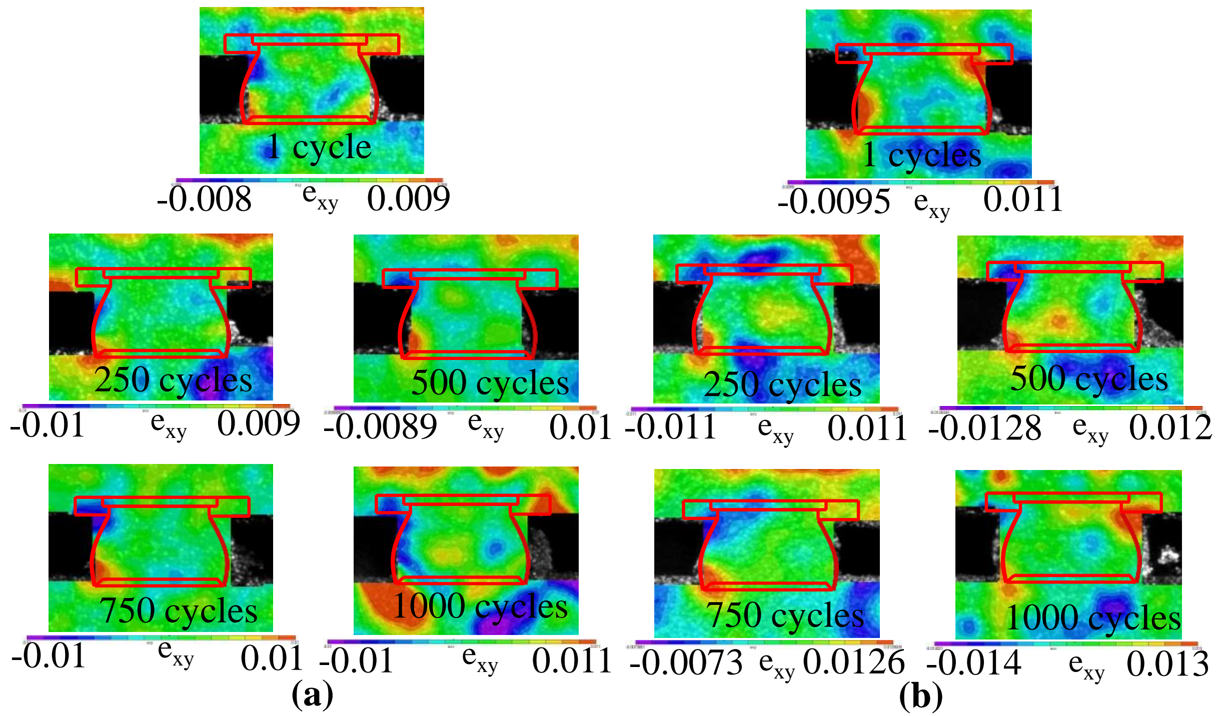


Figure 6-8: Shear strain contour of CABGA 256 (SAC 105) at different cycle's count of -50-50ºC (a) without aging (b) with aging

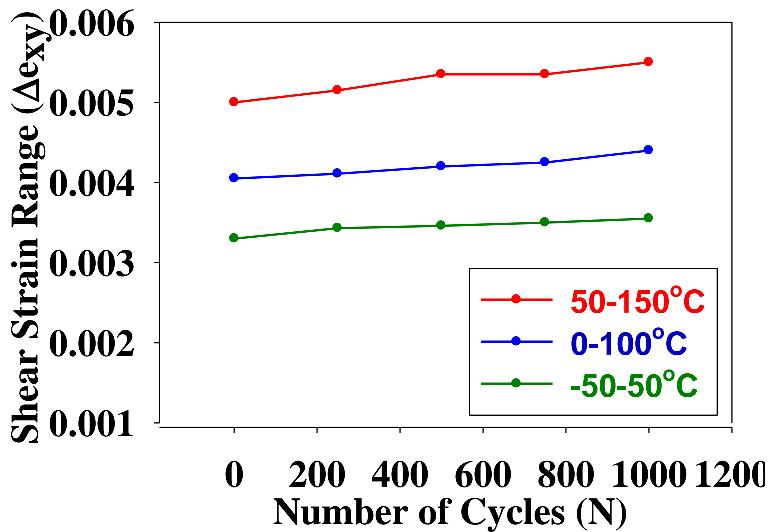


Figure 6-9: Effect of mean temperature and shear strain range evolution with number of cycles for CABGA 256 (SAC 105)

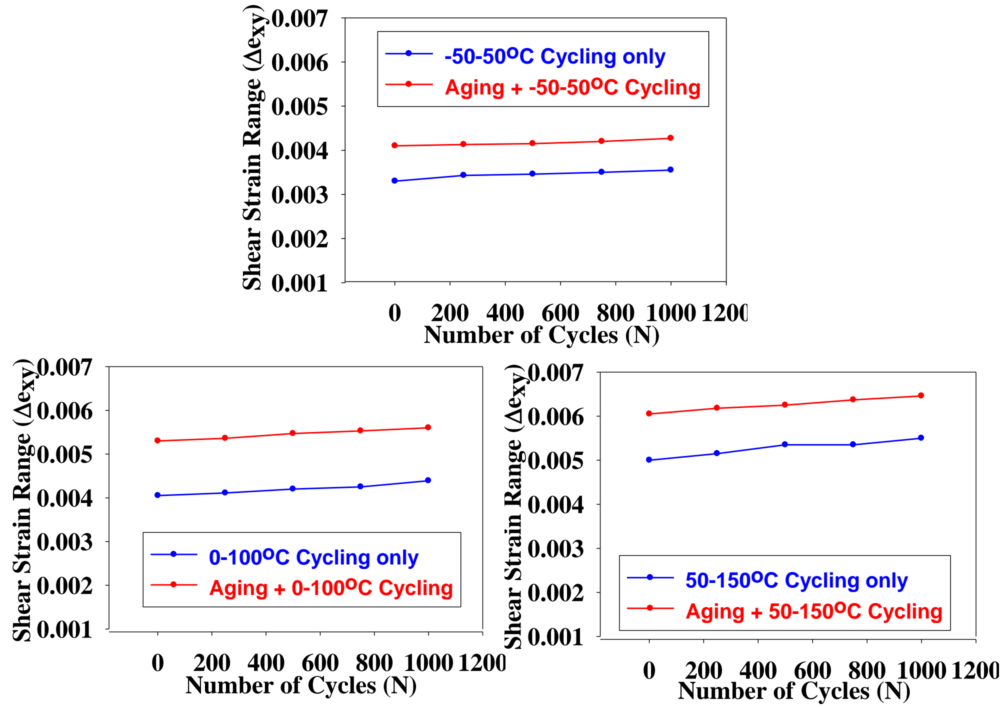


Figure 6-10: Effect of prior aging on shear strain range for CABGA 256 (SAC 105)

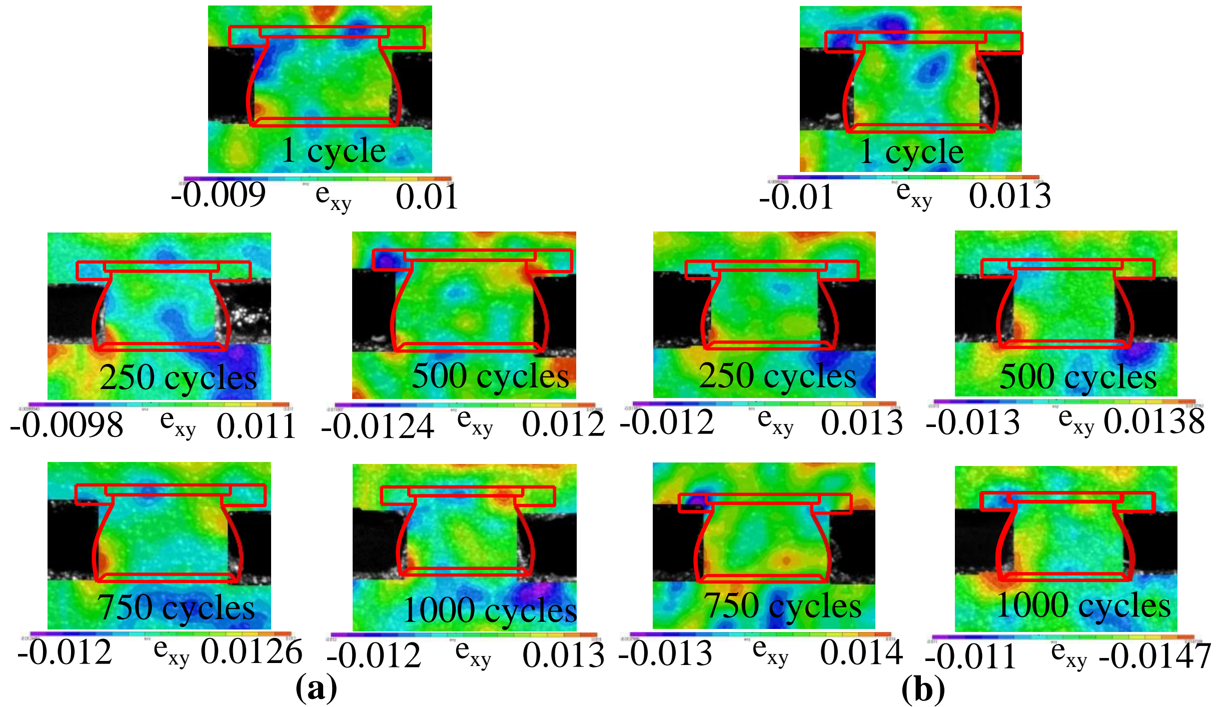


Figure 6-11: Shear strain contour of CABGA 144 (SAC 105) at different cycle's count of 50-150°C (a) without aging (b) with aging

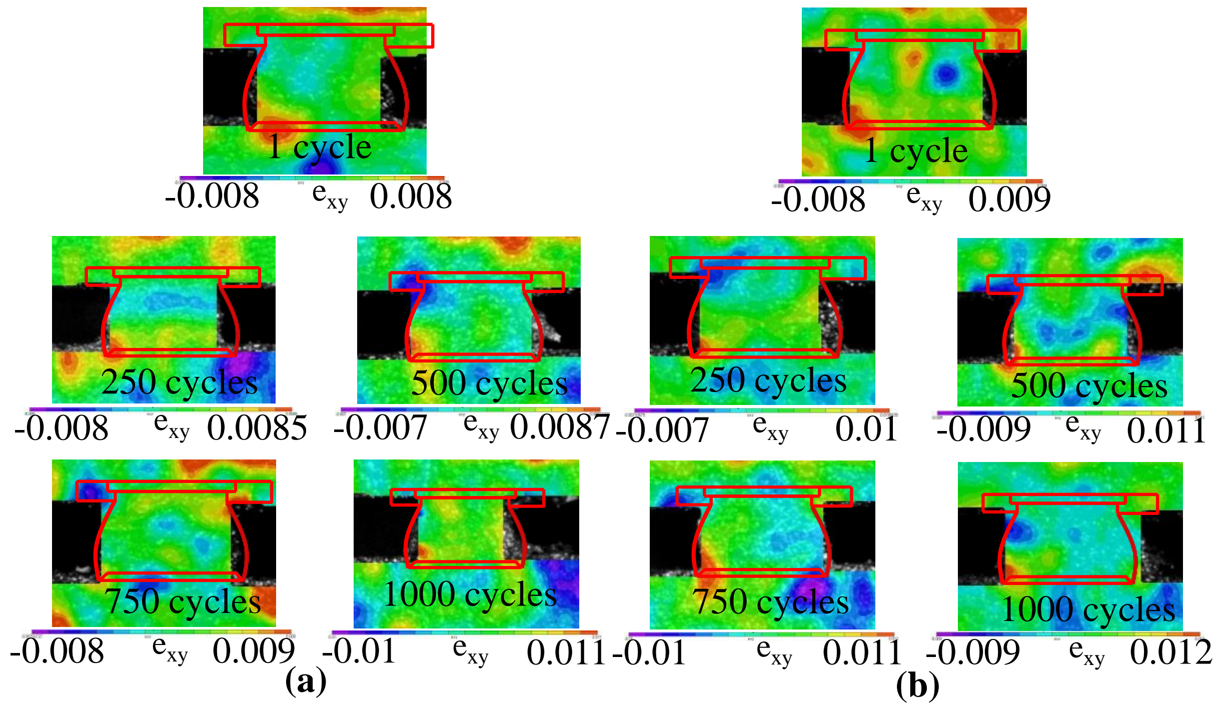


Figure 6-12: Shear strain contour of CABGA 144 (SAC 105) at different cycle's count of 0-100°C (a) without aging (b) with aging

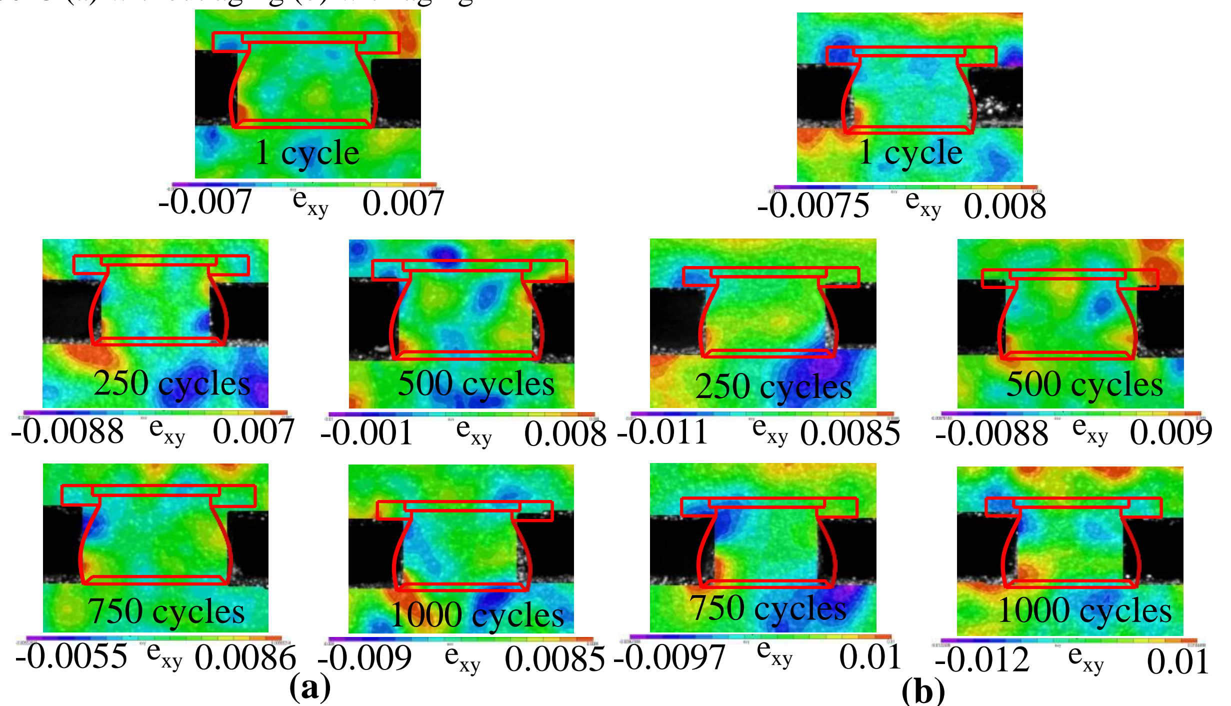


Figure 6-13: Shear strain contour of CABGA 144 (SAC 105) at different cycle's count of -50-50°C (a) without aging (b) with aging

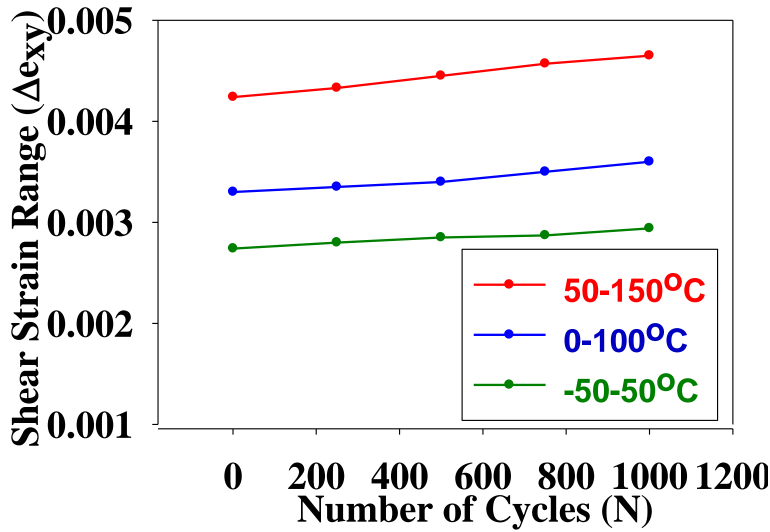


Figure 6-14: Effect of mean temperature and shear strain range evolution with number of cycles for CABGA 144 (SAC 105)

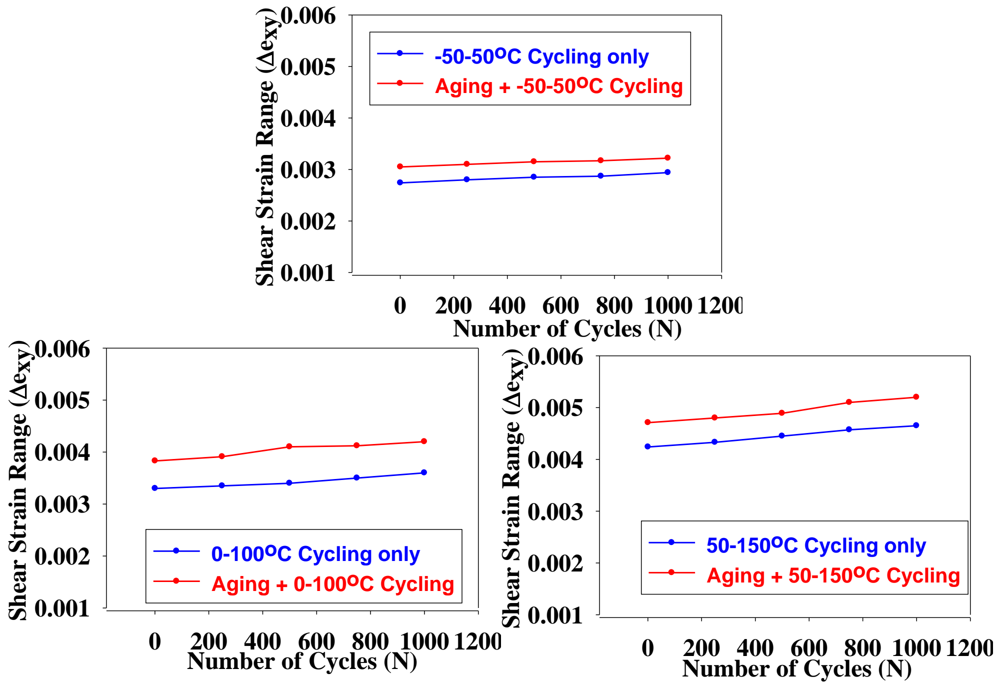


Figure 6-15: Effect of prior aging on shear strain range for CABGA 144 (SAC 105)

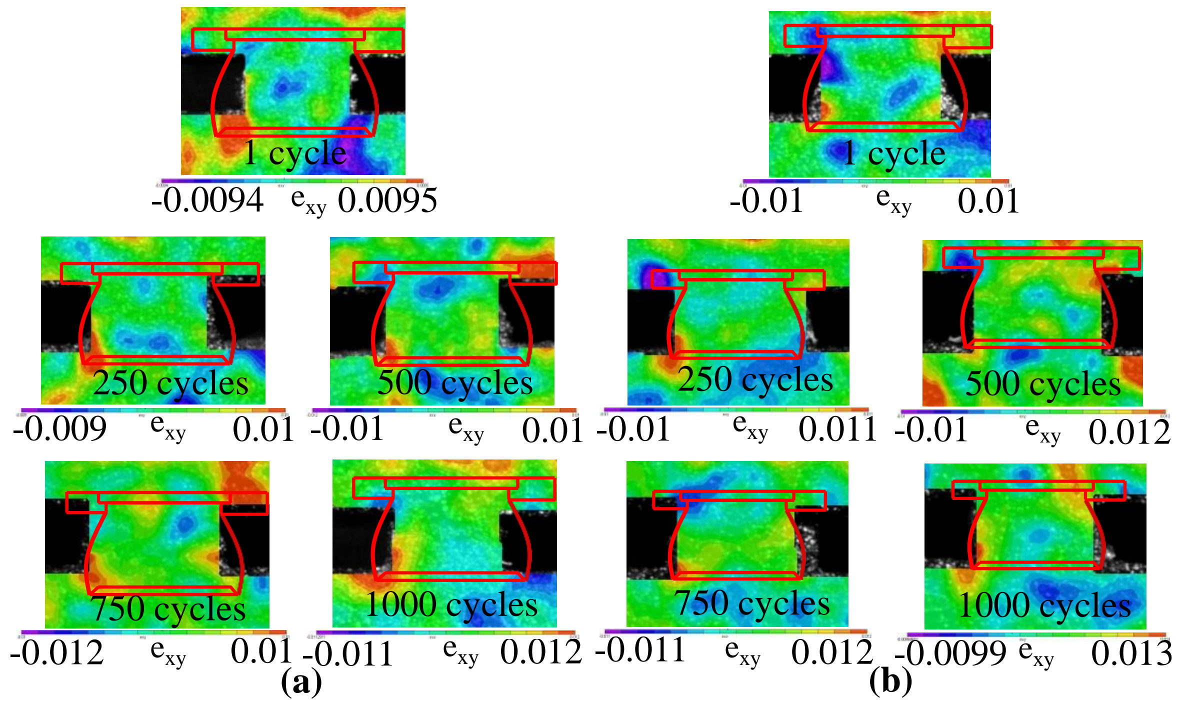


Figure 6-16: Shear strain contour of CABGA 144 (SAC 305) at different cycle's count of 50-150ºC (a) without aging (b) with aging

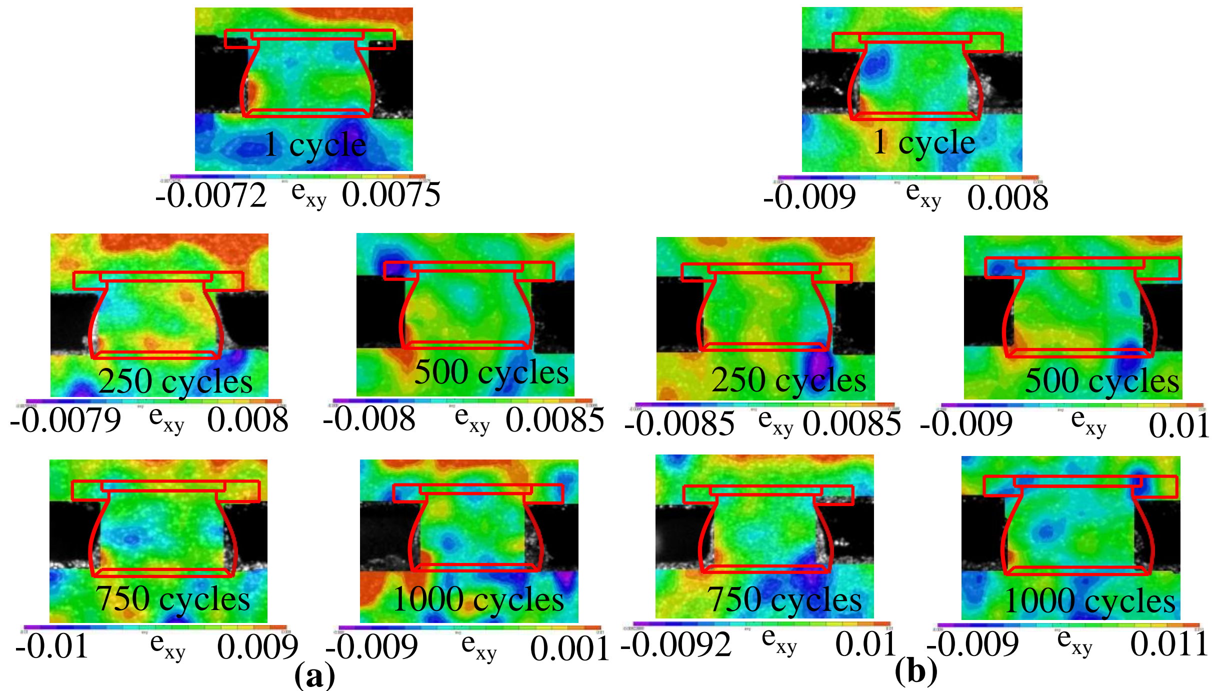


Figure 6-17: Shear strain contour of CABGA 144 (SAC 305) at different cycle's count of 0-100ºC (a) without aging (b) with aging

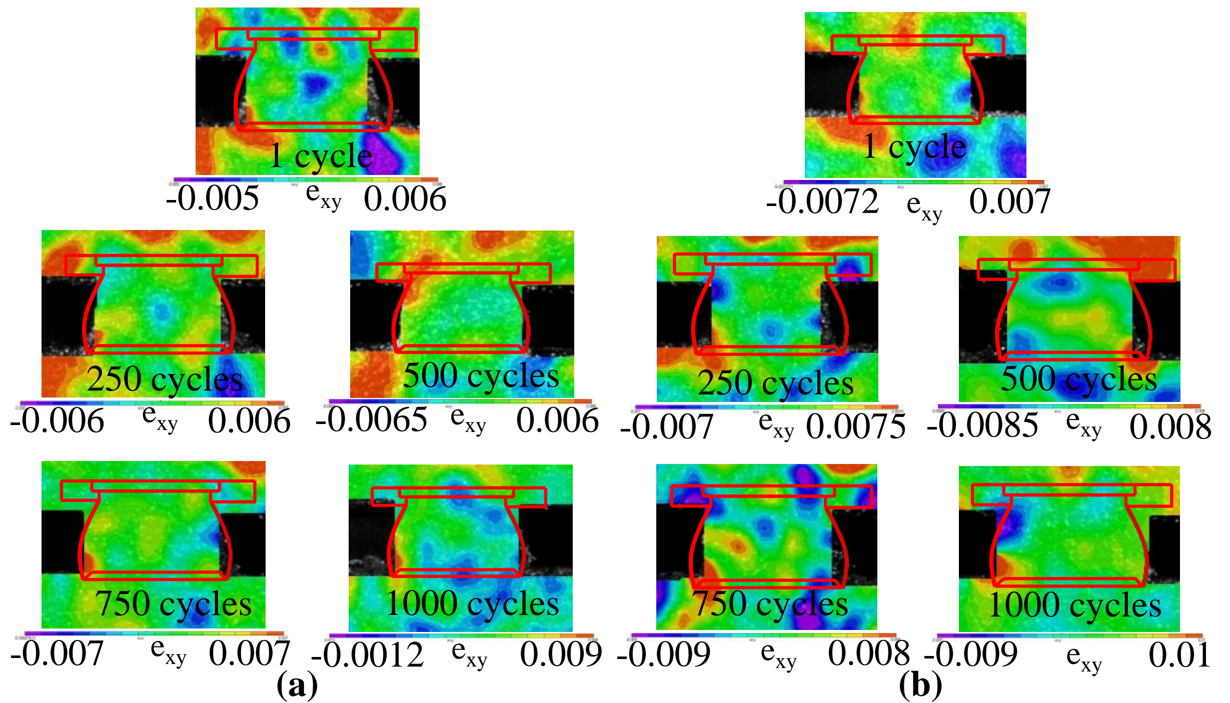


Figure 6-18: Shear strain contour of CABGA 144 (SAC 305) at different cycle's count of -50-50ºC (a) without aging (b) with aging

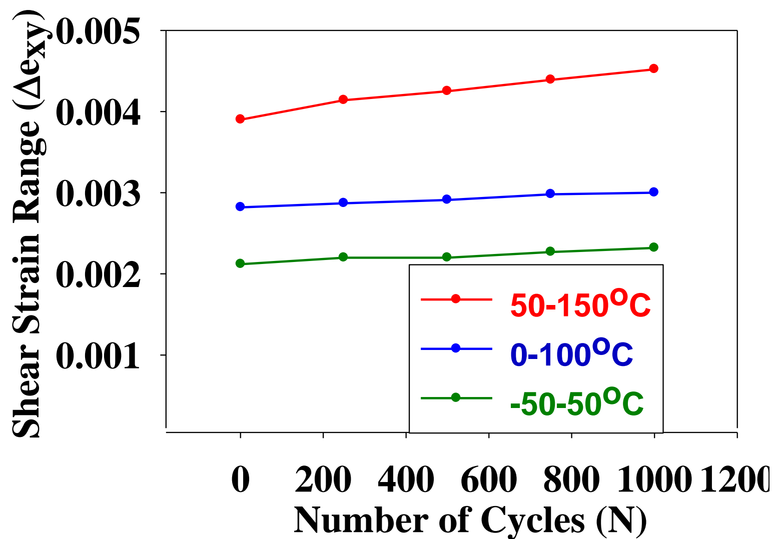


Figure 6-19: Effect of mean temperature and shear strain range evolution with number of cycles for CABGA 144 (SAC 305)

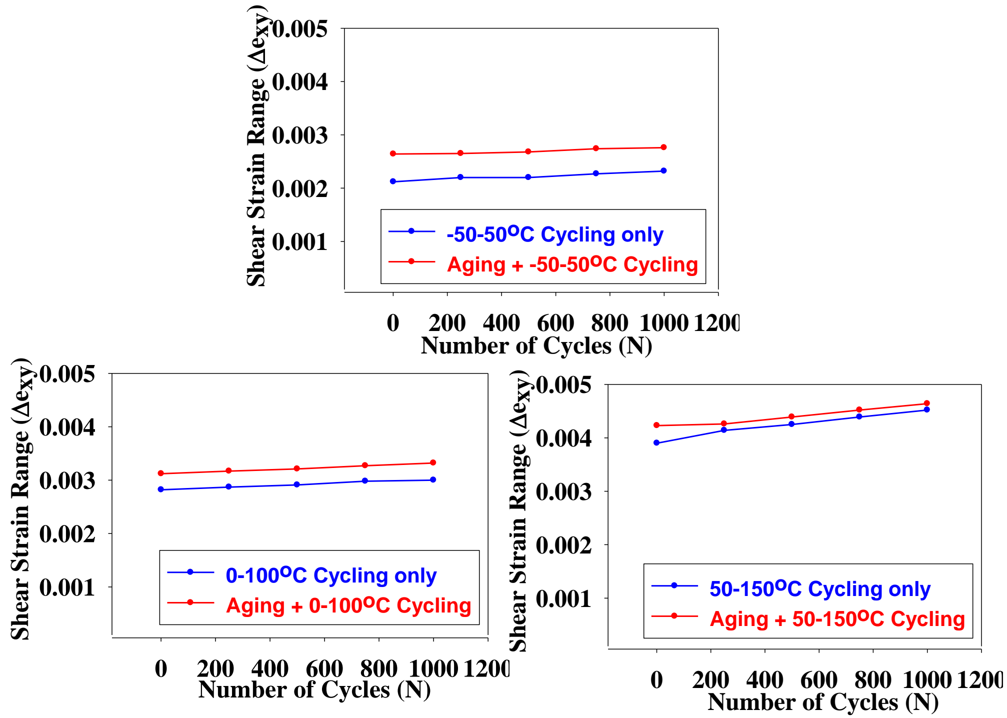


Figure 6-20: Effect of prior aging on shear strain range for CABGA 144 (SAC 305)

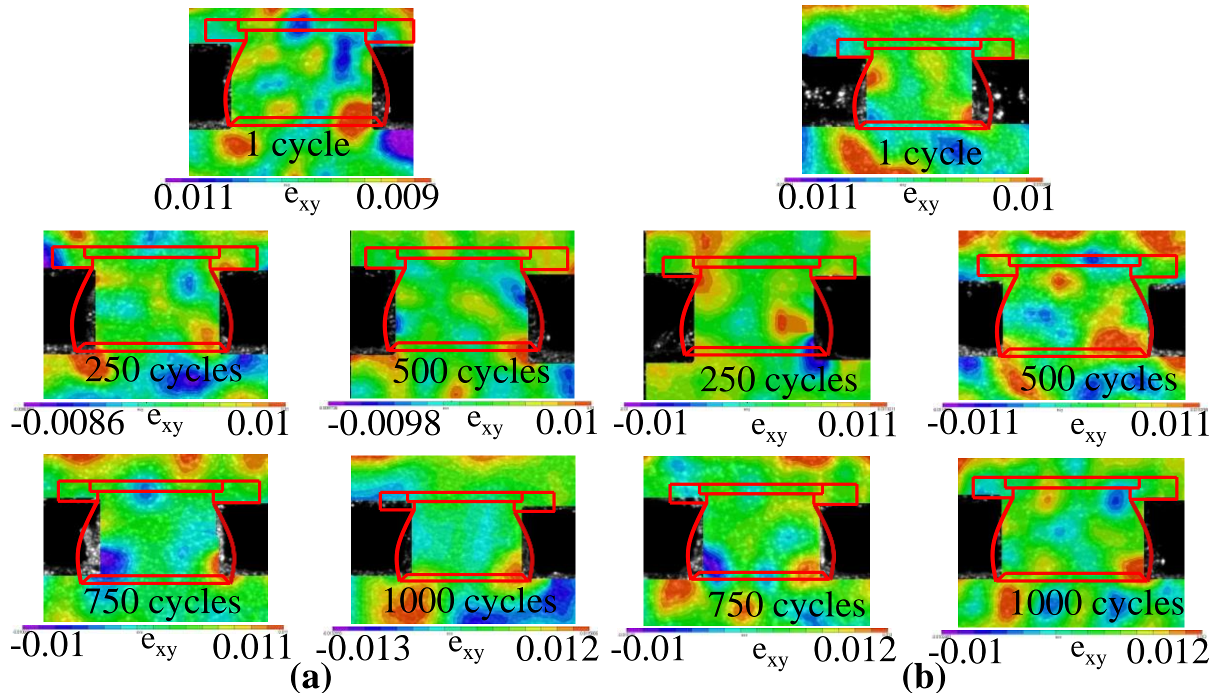


Figure 6-21: Shear strain contour of PBGA 256 (SAC 305) at different cycle's count of 50-150$^{o}$C (a) without aging (b) with aging

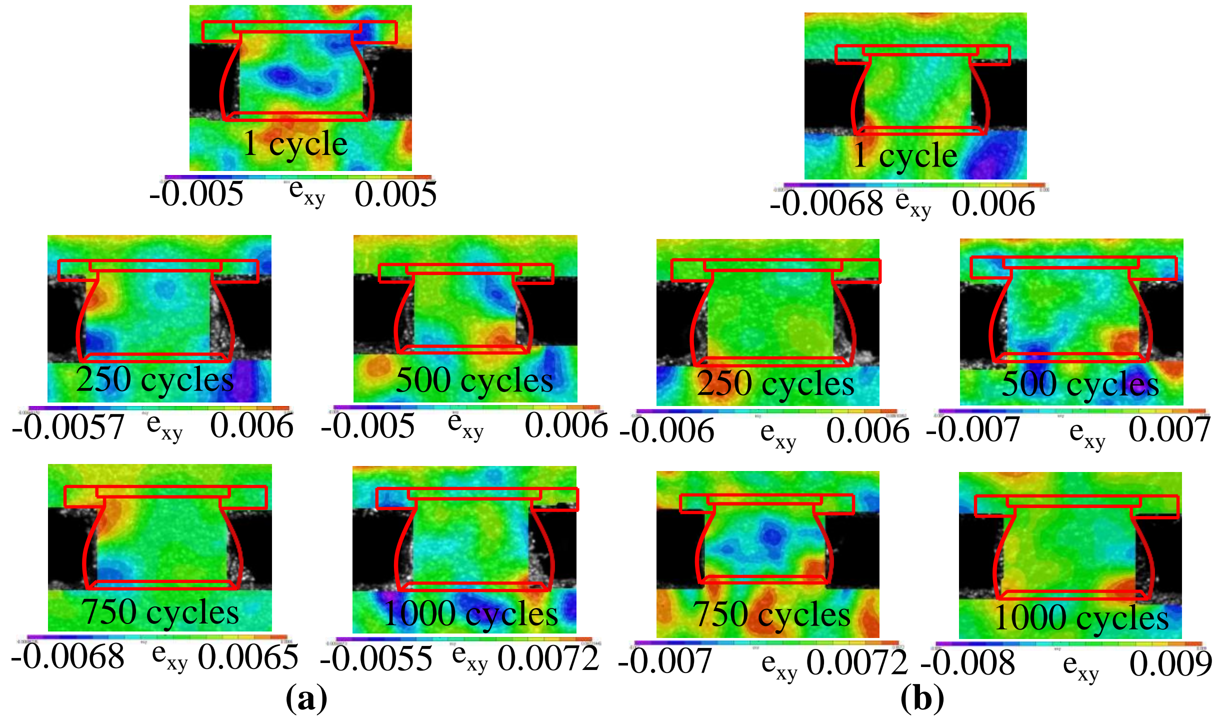


Figure 6-22: Shear strain contour of PBGA 256 (SAC 305) at different cycle's count of 0-100°C (a) without aging (b) with aging

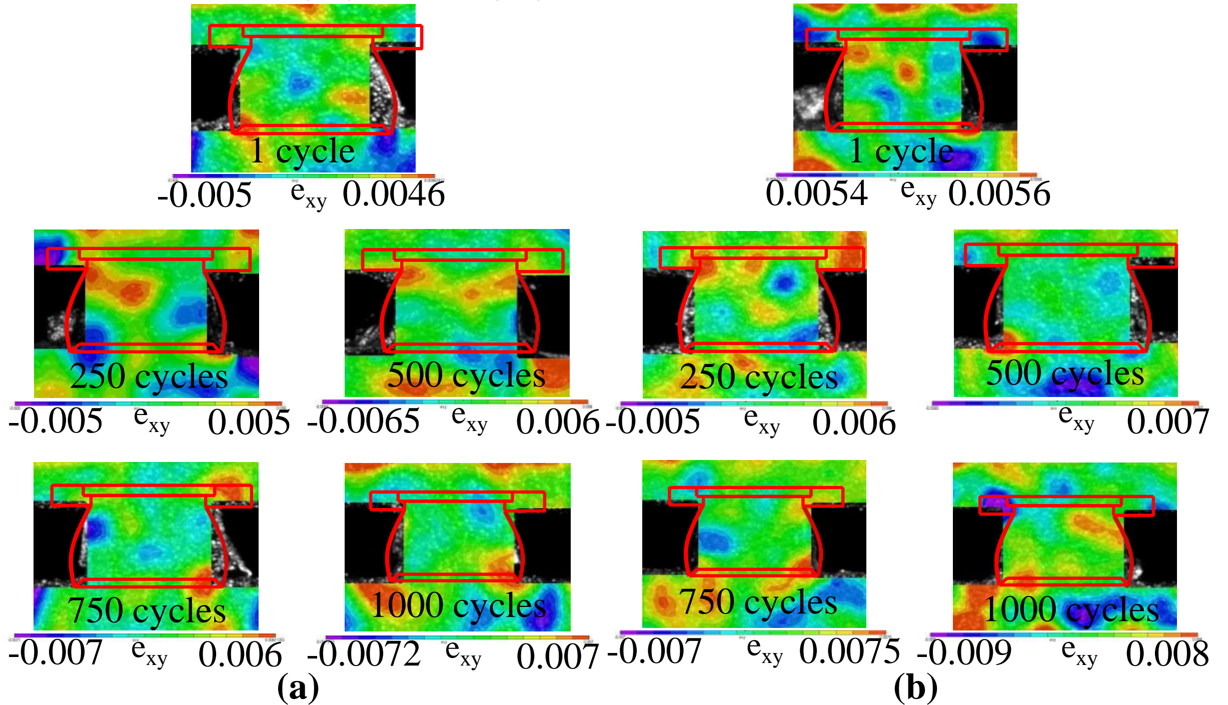


Figure 6-23: Shear strain contour of PBGA 256 (SAC 305) at different cycle's count of -50-50°C (a) without aging (b) with aging

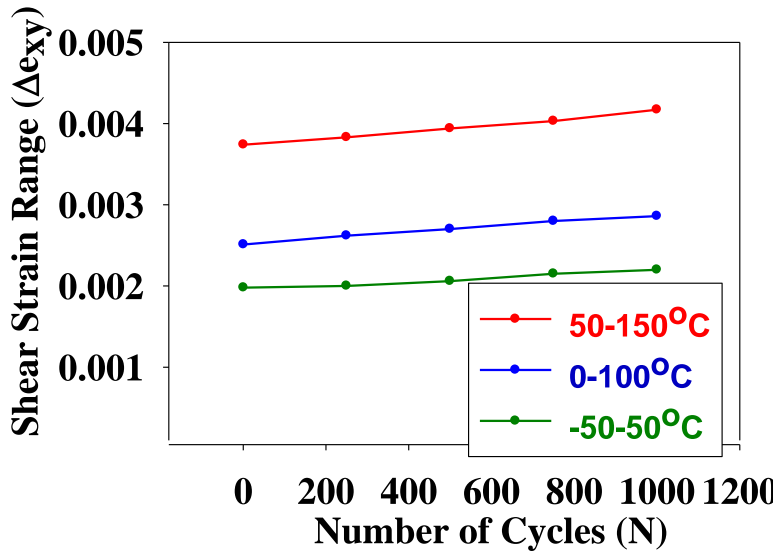


Figure 6-24: Effect of mean temperature and shear strain range evolution with number of cycles for PBGA 256 (SAC 305)

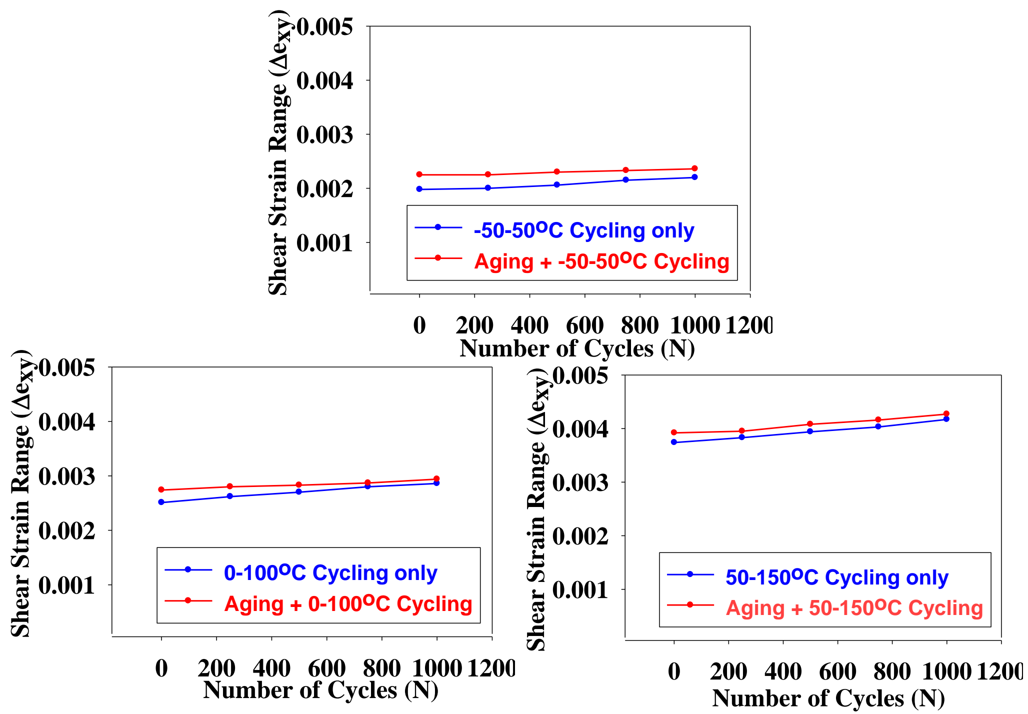


Figure 6-25: Effect of prior aging on shear strain range for PBGA 256 (SAC 305)

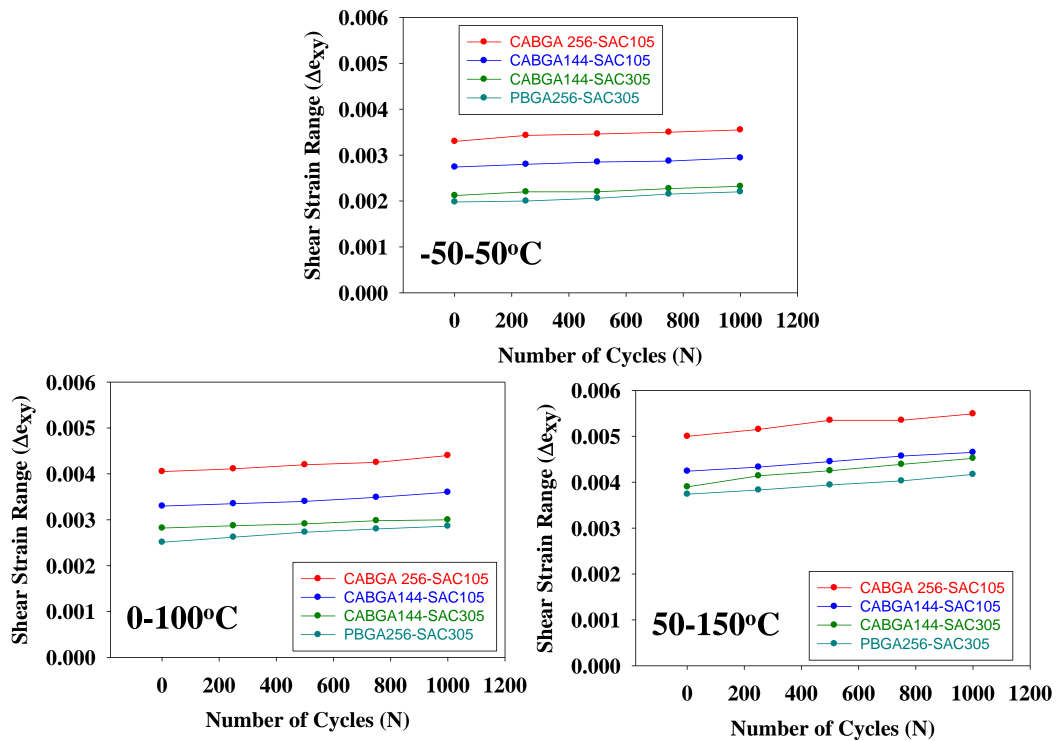


Figure 6-26: Effect of solder alloy composition and package geometry on shear strain range (without prior aging)

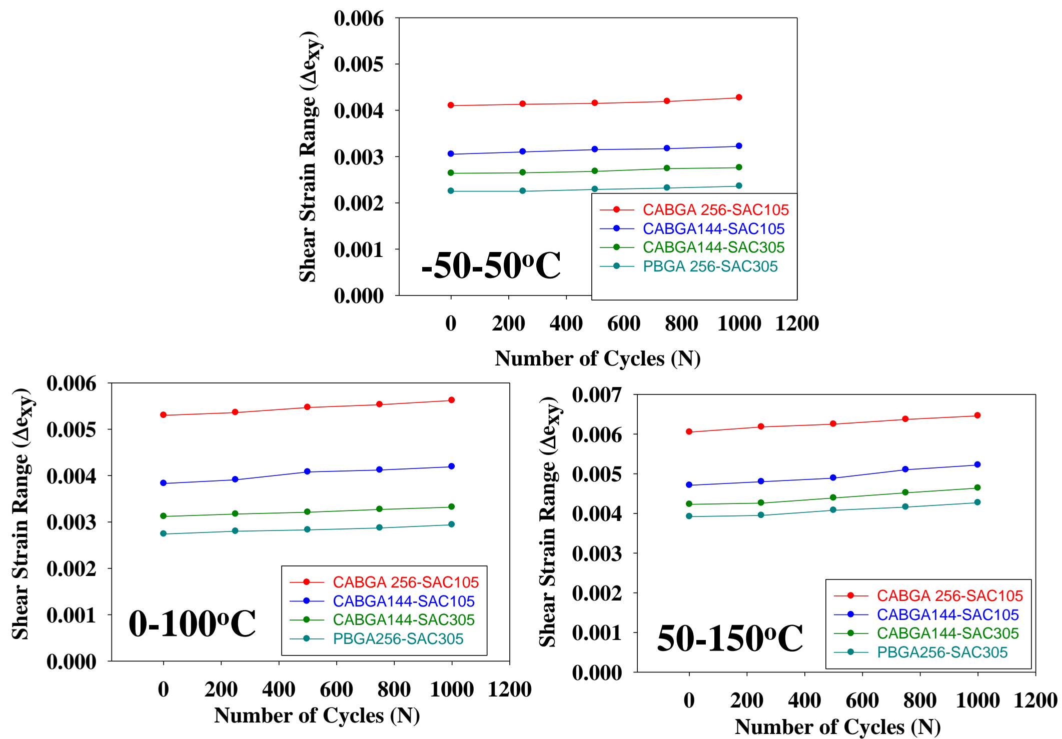


Figure 6-27: Effect of solder alloy composition and package geometry on shear strain range (with prior aging)

## 6.5 Discussion

Figure 6-9, Figure 6-10, Figure 6-14, Figure 6-15, Figure 6-19, Figure 6-20, Figure 6-24 and Figure 6-25 reveal several facts, firstly shear strain range is increasing with mean temperature of thermal profiles and secondly prior aging adversely affecting fatigue reliability, as in all the above mentioned figure samples having prior aging show higher shear strain range as compared to those not aged initially. This can be explained by degrading effect of aging has on mechanical properties. Previous researches also support this finding. Pang et al. [124] found intermetallic layer growth, and shear strength degradation in SAC single ball joints being aged at elevated temperature. Ma and Suhling [65] found up to 40% degradation in tensile strength after 2 months of aging even at room temperature. Iso-thermal aging decreases thermal cycling reliability, as iso-thermal aging affects by coarsening of IMCs and depletion of IMCs. Both this coarsening and depletion process happening in microstructural level make solder joint weaker, less thermal fatigue resistant and more prone to crack propagation. As more is the coarsening, the bigger will be the grain structure, consequently the less will be number of grain. As a result, resistance to dislocation movement drops with less number of grains. Another interesting finding is the evolution of shear strain range with number of cycles. All the plots show that shear strain range shows increasing trend (although not at a noticeable amount) with number of thermal cycles. This can be explained by the age softening effect resulting from phase coarsening. Lall [111] showed that IMC size grows with increasing number of thermal cycles. Pang [124] reported significant phase coarsening in IMCs subjected to shear fatigue in case of lead free alloy. Pao et al. [126] reported how shear strain range increases with number of cycles where he plotted shear stress and strain response of SAC 405 joint in the

form of a hysteresis loop using strain gauge while the sample being thermally cycled. To better visualize how shear strain influenced by package geometry and also solder alloy composition, shear stain range values obtained from contour plots were listed in following tables.

Table 6-2: Shear Strain range value for CABGA 256 (SAC 105)

| | Without aging | | | With aging | | |
|---|---|---|---|---|---|---|
| | 50-150$^{o}$C | 0-100$^{o}$C | -50-50$^{o}$C | 50-150$^{o}$C | 0-100$^{o}$C | -50-50$^{o}$C |
| 1 | 5.0000e-3 | 4.0500e-3 | 3.3000e-3 | 6.0500e-3 | 5.3000e-3 | 4.1000e-3 |
| 250 | 5.1500e-3 | 4.1100e-3 | 3.4300e-3 | 6.1800e-3 | 5.3600e-3 | 4.1300e-3 |
| 500 | 5.3500e-3 | 4.2000e-3 | 3.4600e-3 | 6.2500e-3 | 5.4700e-3 | 4.1500e-3 |
| 750 | 5.3500e-3 | 4.2500e-3 | 3.5000e-3 | 6.3700e-3 | 5.5300e-3 | 4.1900e-3 |
| 1000 | 5.4900e-3 | 4.4000e-3 | 3.5500e-3 | 6.4600e-3 | 5.6200e-3 | 4.2700e-3 |

Table 6-3: Shear Strain range value for CABGA 144 (SAC 105)

| | Without aging | | | With aging | | |
|---|---|---|---|---|---|---|
| | 50-150$^{o}$C | 0-100$^{o}$C | -50-50$^{o}$C | 50-150$^{o}$C | 0-100$^{o}$C | -50-50$^{o}$C |
| 1 | 4.2400e-3 | 3.3000e-3 | 2.7400e-3 | 4.7100e-3 | 3.8300e-3 | 3.0500e-3 |
| 250 | 4.3300e-3 | 3.3500e-3 | 2.8000e-3 | 4.8000e-3 | 3.9100e-3 | 3.1000e-3 |
| 500 | 4.4500e-3 | 3.4000e-3 | 2.8500e-3 | 4.8900e-3 | 4.0800e-3 | 3.1500e-3 |
| 750 | 4.5700e-3 | 3.4900e-3 | 2.8700e-3 | 5.1000e-3 | 4.1200e-3 | 3.1700e-3 |
| 1000 | 4.6500e-3 | 3.6000e-3 | 2.9400e-3 | 5.2200e-3 | 4.1900e-3 | 3.2200e-3 |

Table 6-4: Shear Strain range value for CABGA 144 (SAC 305)

| | Without aging | | | With aging | | |
|---|---|---|---|---|---|---|
| | 50-150$^{o}$C | 0-100$^{o}$C | -50-50$^{o}$C | 50-150$^{o}$C | 0-100$^{o}$C | -50-50$^{o}$C |
| 1 | 3.9000e-3 | 2.8200e-3 | 2.1200e-3 | 4.2300e-3 | 3.1200e-3 | 2.6400e-3 |
| 250 | 4.1400e-3 | 2.8700e-3 | 2.2000e-3 | 4.2600e-3 | 3.1700e-3 | 2.6500e-3 |
| 500 | 4.2500e-3 | 2.9100e-3 | 2.2000e-3 | 4.3900e-3 | 3.2100e-3 | 2.6800e-3 |
| 750 | 4.3900e-3 | 2.9800e-3 | 2.2700e-3 | 4.5200e-3 | 3.2700e-3 | 2.7400e-3 |

| 1000 | 4.5200e-3 | 3.0000e-3 | 2.3200e-3 | 4.6400e-3 | 3.3200e-3 | 2.7600e-3 |
|---|---|---|---|---|---|---|

Table 6-5: Shear Strain range value for PBGA 256 (SAC 305)

| | Without aging | | | With aging | | |
|---|---|---|---|---|---|---|
| | 50-150°C | 0-100°C | -50-50°C | 50-150°C | 0-100°C | -50-50°C |
| 1 | 3.7400e-3 | 2.5100e-3 | 1.9800e-3 | 3.9200e-3 | 2.7400e-3 | 2.2500e-3 |
| 250 | 3.8300e-3 | 2.6200e-3 | 2.0000e-3 | 3.9500e-3 | 2.8000e-3 | 2.2500e-3 |
| 500 | 3.9400e-3 | 2.7300e-3 | 2.0600e-3 | 4.0800e-3 | 2.8300e-3 | 2.2900e-3 |
| 750 | 4.0300e-3 | 2.8000e-3 | 2.1500e-3 | 4.1600e-3 | 2.8700e-3 | 2.3200e-3 |
| 1000 | 4.1700e-3 | 2.8600e-3 | 2.2000e-3 | 4.2700e-3 | 2.9400e-3 | 2.3600e-3 |

By comparing Table 6-3 and Table 6-4, we see that solder joint made by SAC 105 shows higher level of shear strain range than those made by SAC 305 i.e. SAC105 is more ductile than SAC305, which supports the notion that SAC105 is more vulnerable in thermal fatigue than its counterpart SAC305. Terashima et al.[33] found that increasing Ag content increases the fatigue resistance of SAC solder due to presence and more abundance of an IMC named as $Ag_3Sn$, which inhibit coarsening of alloys, thereby makes it more fatigue resistant. Furthermore, Sn grain structure cannot grow much due to higher presence of Ag, so there will be less chance of stress buildup at the grain boundaries during temperature cycling. Another interesting finding from this experiment is shear strain dependency on package geometry. Figure 6-26, and Figure 6-27 show how package geometry can have an effect on shear strain response. Shear strain shows decreasing tendency with decreasing die or chip size. This is a valid consequence as the larger the die size the more the die shadow solder ball will undergo shear strain according to DNP formula (Distance from neutral point). In case of SAC 305, PBGA 256 has smaller die size than CABGA 144 and in case of SAC 105, PBGA 256 has larger die size than CABGA 144 as revealed by Figure 6-2.

### 6.6 Finite Element Validation

From previous researches it is quite obvious that both iso-thermal aging and thermal cycling have almost similar effect on microstructure or in other words material property evolution, but at different scale. Therefore, researchers tried to find thermal cycle equivalent to isothermal aging in terms microstructural damage undergone. Lall et. al. proposed a damage mapping model to find number of thermal cycles needed to reach a particular damage caused by known hours of aging or vise-versa based upon phase growth and IMC damage proxies. Here similar technique was followed to check the validity of results i.e. shear strain evolution with number of thermal cycles through finite element simulation. From Section 3.4.1, the damage mapping equation for PBGA 256 (SAC 305) correlating damage parameter with aging hours under 125$^{o}$C is as follows,

$$S_n = 0.0035t^{0.65} \qquad \text{Eq. 6.1}$$

Where, $S_n$ is normalized phase growth parameter and t is aging hour.

Again from Sec 4.4, the damage mapping equation for PBGA 256 (SAC 305) correlating damage parameter with number of cycles under 50-150$^{o}$C is as follows,

$$S_n = 0.00032N^{0.96} \qquad \text{Eq. 6.2}$$

Where, $S_n$ is normalized phase growth parameter and N is number of cycles.

Equating the above two damage mapping relations we can get

$$N = 12t^{0.68} \qquad \text{Eq. 6.3}$$

Using this relation any known period of isothermal aging can be converted to equivalent number of thermal cycling. Using this relation and the Table 6.6 thermal cycling effect can be simulated.

Table 6-6: Anand's constant for SAC 305 under aging condition of 125°C [128]

| Parameters | Unit | 0 days aging | 60 days aging | 120 days aging |
|---|---|---|---|---|
| $s_0$ | MPa | 21 | 6 | 5.9 |
| Q/R | 1/K | 9320 | 9320 | 9320 |
| A | $Sec^{-1}$ | 3501 | 4095 | 4105 |
| $\xi$ | | 4 | 4 | 4 |
| M | | 0.25 | 0.18 | 0.18 |
| $h_0$ | MPa | 180000 | 89682 | 80825 |
| $\hat{s}$ | MPa | 30.2 | 22.3 | 22 |
| n | | 0.01 | 0.0011 | 0.001 |
| a | | 1.78 | 2.04 | 2.05 |

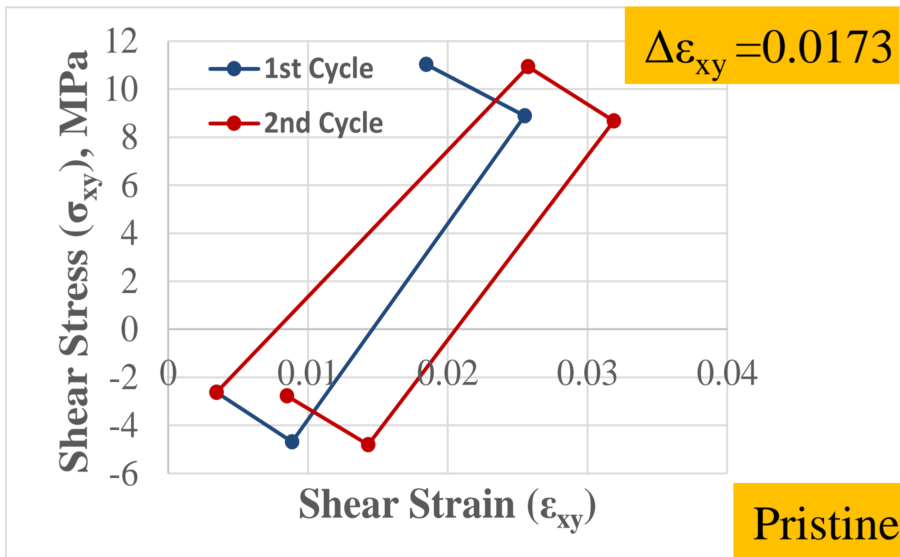


Figure 6-28: Shear stress-strain hysteresis loop of PBGA 256 (SAC305) for pristine condition

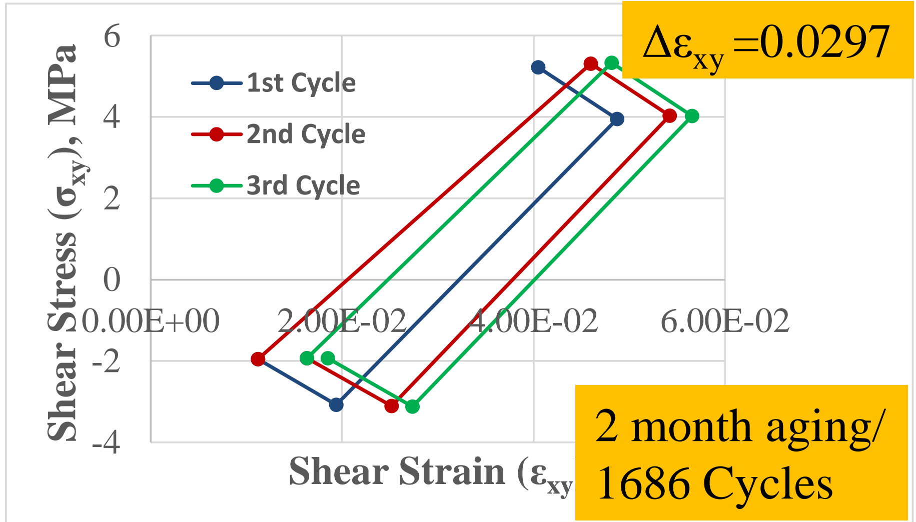


Figure 6-29: Shear stress-strain hysteresis loop of PBGA 256 (SAC305) after 2 months aging or after 1700 cycles in 50-150$^{o}$ C.

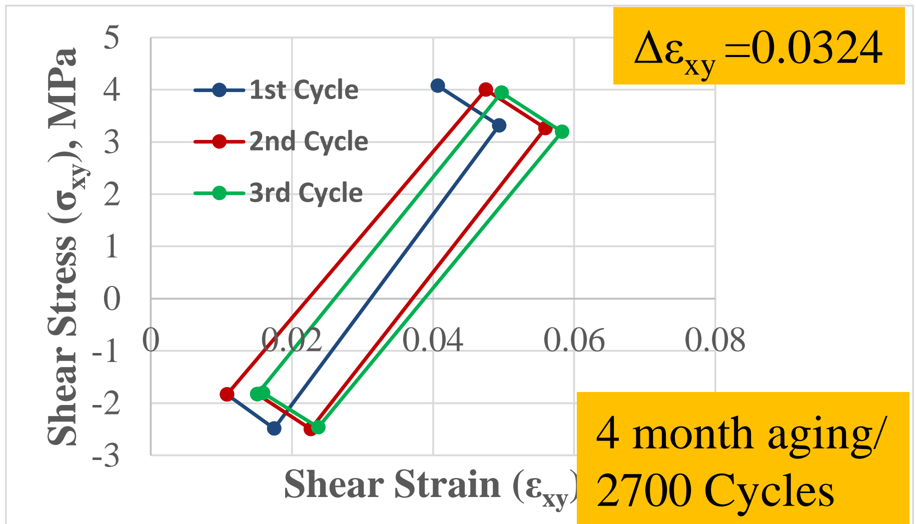


Figure 6-30: Shear stress-strain hysteresis loop of PBGA 256 (SAC305) after 4 months aging or after 2700 cycles in 50-150$^{o}$ C.

The above three figures show the shear stress-strain hysteresis plot for three different aging conditions. These three aging conditions are equivalent to 0, 1700 and 2700 cycles respectively under 50-150$^{o}$C condition. Some of the simulations was done for three cycles to check the stability of the loop, but there was no significant difference between 2$^{nd}$ and

3rd loop. Using these hysteresis loop shear strain range was calculated and results were tabulated as below;

Table 7-7: Shear strain range values from simulation

| Aging duration (days) | Number of cycles | Shear strain range ($\Delta e_{xy}$) |
|---|---|---|
| 0 | 0 | 0.0173 |
| 60 | 1700 | 0.0297 |
| 120 | 2700 | 0.0324 |

This table clearly shows the validity of our results as it shows that strain range is increasing with number of cycles. Also the hysteresis loop plots revealed that the yield shear stress is decreasing with number of cycles which is a clear implication of age softening.

### 6.8 Conclusion

The evolution of shear strain with number of thermal cycles for different mean temperature thermal profiles was examined using Digital Image Correlation. The same technique was used for investigating the effect of aging on thermal cycling reliability. Shear strain ranges increases with higher level of mean temperature of thermal cycling range, and also very slowly with number of cycle count. Iso-thermal aging is shown to have detrimental effect on thermal cycling reliability.

# Chapter 7

# Life Prediction Model and Remaining Useful Life Prognostication

## 7.1 Overview

Ensuring fatigue reliability of solder joints is one of the most crucial factors industries have been concerned with for long, and this concern is getting more and more critical and engaging with fast paced miniaturization with tons of functionalities. Added to these is the transition from Sn-Pb to lead free alloy system. To accommodate these added functionalities BGAs are evolving in geometry and layout profile with tighter pitch, which gave rise to heating problem. Change in alloy system required higher reflow temperature, posing greater threat to reliability. Microstructural growth kinetics for lead free alloy also is totally different from Sn-Pb system. Considering all these factors researchers tried to come up with bunch of fatigue life models, some of them are strain based, some are energy based and so on. But none of them is universal in its applicability. In this chapter we discussed some of very popular fatigue models like Coffin-Manson Model and Darveaux Model, derived the constants pertinent to a specific model, and compare them with existing research, and then use them to verify our results. Additionally, a new approach of fatigue model was proposed taking microstructural growth parameter into account. For all these we took SAC 305 alloy as a test case.

## 7.2 Coffin-Manson Model

This model was proposed for low cycle fatigue (not more than $10^4$). All kinds of thermal fatigue problems fall into this category. Initially used for ductile materials like steel and

Aluminum alloys for aircraft, but later also was used for brittle materials. This model can be written as

$$\frac{\Delta e_{xy}}{2} = \varepsilon'_f \left(2N_f\right)^c \qquad \text{Eq. 7.1}$$

Where $\Delta e_{xy}$ is plastic shear strain range ($\Delta e_{xy}/2$ is strain amplitude), $N_f$ is number of cycles to failure ($2N_f$ is number of strain reversals), $\varepsilon'_f$ is an empirical constant, known as fatigue ductility coefficient, defined by strain intercept at 2N=1, and c is fatigue ductility exponent (-0.5>c>-0.7 for most materials, for many materials -0.6 as typical).

### 7.2.1 Damage Mapping Using Coffin-Manson Relation

In this section a damage mapping model was developed in an effort to establish relation between damage accrual rate and shear strain range. This kind of relation can be explained by physics of failure. With continuous thermally induced load like isothermal aging and thermal cycling solder alloy undergoes softening. Plastic deformation takes place through slip of dislocation or dislocation gliding. Therefore, anything which makes this gliding difficult finally results in less ductility. Coarser grains offer less grain boundary area, thereby make dislocation sliding easier and make metal more ductile. This phenomenon can also be better visualized by Hall-Petch relation;

$$\sigma_y = \sigma_0 + K_y d^{-0.5} \qquad \text{Eq. 7.2}$$

Where $\sigma_y$ is the yield strength, $\sigma_0$ is the resistance of lattice to dislocation motion, d the average grain diameter and $K_y$ is strengthening coefficient. In this thesis almost a similar kind of relation has been established to see how damage accrual rate (dS/dN i.e. the rate average phase diameter or IMC thickness increases with number of thermal cycles undergone) is related to shear strain range.

Before going to derive the damage mapping relation, the Coffin-Manson model was implemented first using the characteristic life data and shear strain range data at pristine condition obtained experimentally (listed in the following table).

Table 7-1: Life and shear strain for CABGA 144 (SAC305) and PBGA 256 (SAC305)

| | CABGA 144 (SAC 305) | | PBGA 256 (SAC 305) | |
|---|---|---|---|---|
| | $N_f$ | $\Delta e_{xy}$ | $N_f$ | $\Delta e_{xy}$ |
| 50-150ºC | 3135 | 0.0039 | 3475 | 0.00374 |
| 0-100ºC | 5726 | 0.00282 | 6202 | 0.0025 |
| -50-50ºC | 8775 | 0.00212 | 9691 | 0.00198 |

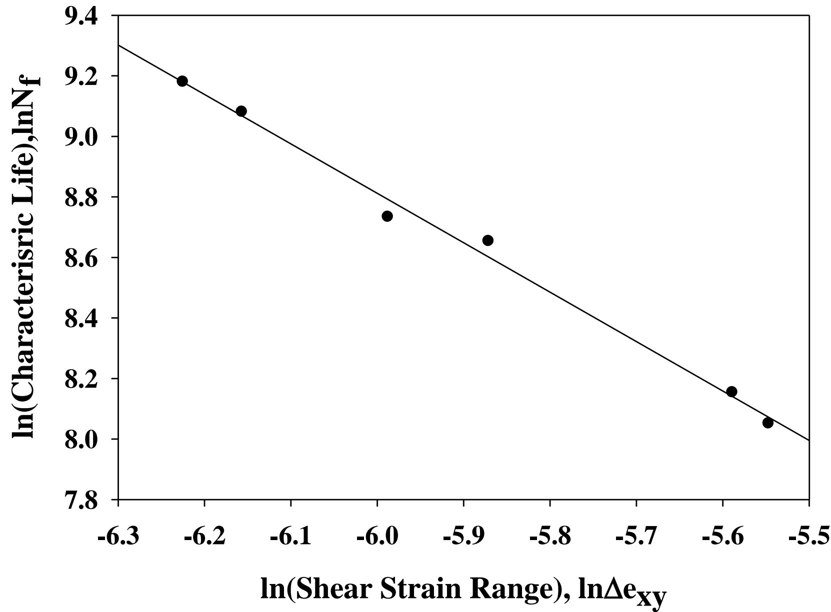


Figure 7-1: Characteristic Life (Nf) vs. Shear Strain Range ($\Delta e_{xy}$)

From the above fit, two constants of Coffin-Manson relation were determined, which when compared with existing research findings showed close correspondence, as shown in the following table.

Table 7-2: Coffin-Manson constant value

| | Fatigue ductility coefficient ($\varepsilon_f'$) | Fatigue ductility Exponent (c) |
|---|---|---|
| From fit | 0.42 | -0.61 |
| Mi et. al. [127] | 0.325 | -0.57 |

In mathematical form;

$$N_f = 0.372 \Delta e_{xy}^{-1.63} \qquad \text{Eq. 7.3}$$

Now the Coffin-Manson formula assumes that shear strain range does not change after hysteresis loop being stabilized after first few number of cycles, but experiment showed that it is changing with number of thermal cycles. As shear strain range changes, fatigue life also should change according to Coffin-Manson rule, but fatigue life is single valued entity which should not change under a particular condition for a particular material. Now to accommodate the experimental findings and fatigue life property of materials in a single model, a new model was proposed here correlating Remaining Useful Life (RUL) and shear strain range as shown in following figure;

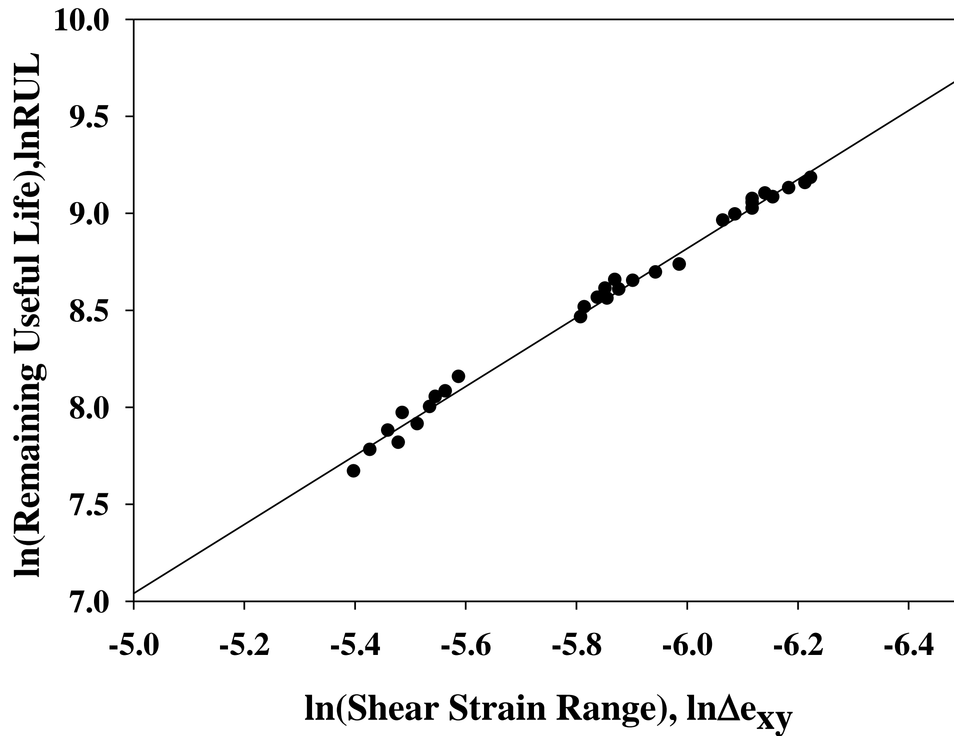


Figure 7-2: Remaining Useful Life vs. Shear Strain Range plot

Mathematically this plot can be expressed as;

$$RUL = 0.157\Delta e_{xy}^{-1.78} \quad \text{Eq. 7.4}$$

Also we know;

$$RUL + N_c = N_f \quad \text{Eq. 7.5}$$

Now life prediction model based on microstructural damage accrual rate (see section 4.4.1 and section 4.4.2 )

$$N_f = 3500\left(\frac{d\ln S_n}{d\ln N}\right)^{-0.89} \quad \text{Eq. 7.6}$$

$$N_f = 3232.46\left(\frac{\mathrm{dln}Y_n}{\mathrm{dln}N}\right)^{-0.875} \quad \text{Eq. 7.7}$$

Eq. 7.6 is based on phase growth and Eq. 7.7 is on IMC growth damage proxy. Now using Eq. 7.4 to Eq. 7.7 following damage mapping relations can be obtained which can accommodate shear strain range evolution with number of thermal cycles.

$$0.157\Delta e_{xy}^{-1.78} + N_c = 3500\left(\frac{\mathrm{dln}S_n}{\mathrm{dln}N}\right)^{-0.89} \quad \text{Eq. 7.8}$$

$$0.157\Delta e_{xy}^{-1.78} + N_c = 3232.46\left(\frac{\mathrm{dln}Y_n}{\mathrm{dln}N}\right)^{-0.875} \quad \text{Eq. 7.9}$$

The following table shows the model result and comparison with experimental values.

Table 7-3: Results from damage mapping model based on phase growth damage proxy

| | | Characteristic Life ($N_f$) | Life Consumed | Remaining Useful Life (RUL) | Shear Strain Range ($\Delta e_{xy}$) | $dlnS_n/dlnN$ (Model) (Eq.7.8) | $dlnS_n/dlnN$ (exp) | Error |
|---|---|---|---|---|---|---|---|---|
| CABGA 144 SAC305 | 50-150ºC | 3135 | 1 | 3134 | 0.0039 | 1.17 | 0.984 | 19.21 |
| | | | 250 | 2885 | 0.00414 | 1.20 | | 21.85 |
| | | | 500 | 2635 | 0.00425 | 1.14 | | 16.31 |
| | | | 750 | 2385 | 0.00439 | 1.10 | | 12.07 |
| | | | 1000 | 2135 | 0.00452 | 1.06 | | 7.31 |
| | 0-100ºC | 5726 | 1 | 5725 | 0.00282 | 0.61 | 0.6 | 1.48 |
| | | | 250 | 5476 | 0.00287 | 0.60 | | 0.23 |
| | | | 500 | 5226 | 0.00291 | 0.58 | | 2.68 |
| | | | 750 | 4976 | 0.00298 | 0.58 | | 3.41 |
| | | | 1000 | 4726 | 0.003 | 0.56 | | 7.00 |
| | -50-50ºC | 8775 | 1 | 8774 | 0.00212 | 0.34 | 0.31 | 10.30 |
| | | | 250 | 8525 | 0.0022 | 0.36 | | 15.02 |
| | | | 500 | 8275 | 0.0022 | 0.35 | | 11.37 |
| | | | 750 | 8025 | 0.00227 | 0.35 | | 14.39 |
| | | | 1000 | 7775 | 0.00232 | 0.36 | | 15.19 |
| PBGA 256 SAC305 | 50-150ºC | 3475 | 1 | 3475 | 0.00374 | 1.08 | 0.956 | 11.11 |
| | | | 250 | 3225 | 0.00383 | 1.04 | | 6.92 |
| | | | 500 | 2975 | 0.00394 | 1.00 | | 3.61 |
| | | | 750 | 2725 | 0.00403 | 0.96 | | 0.67 |
| | | | 1000 | 2475 | 0.00417 | 0.94 | | 3.12 |

| | | | | | | | | |
|---|---|---|---|---|---|---|---|---|
| | 0-100ºC | 6202 | 1 | 6202 | 0.00251 | 0.48 | 0.55 | 12.52 |
| | | | 250 | 5952 | 0.00262 | 0.50 | | 8.78 |
| | | | 500 | 5702 | 0.00273 | 0.52 | | 5.68 |
| | | | 750 | 5452 | 0.0028 | 0.52 | | 5.62 |
| | | | 1000 | 5202 | 0.00286 | 0.51 | | 6.41 |
| | -50-50ºC | 9691 | 1 | 9691 | 0.00198 | 0.30 | 0.284 | 4.86 |
| | | | 250 | 9441 | 0.002 | 0.30 | | 4.06 |
| | | | 500 | 9191 | 0.00206 | 0.30 | | 7.18 |
| | | | 750 | 8941 | 0.00215 | 0.32 | | 12.88 |
| | | | 1000 | 8691 | 0.0022 | 0.32 | | 14.28 |

Table 7-4: Results from damage mapping model based on IMC growth damage proxy

| | | Characteristic Life ($N_f$) | Life Consumed | Remaining Useful Life (RUL) | Shear Strain Range ($\Delta e_{xy}$) | $dlnY_n/dlnN$ (Model) (Eq.7.9) | $dlnY_n/dlnN$ (exp) | Error |
|---|---|---|---|---|---|---|---|---|
| CABGA 144 SAC305 | 50-150ºC | 3135 | 1 | 3134 | 0.0039 | 1.07 | | 18.85 |
| | | | 250 | 2885 | 0.00414 | 1.09 | | 21.50 |
| | | | 500 | 2635 | 0.00425 | 1.04 | | 15.94 |
| | | | 750 | 2385 | 0.00439 | 1.01 | 0.9 | 11.69 |
| | | | 1000 | 2135 | 0.00452 | 0.96 | | 6.93 |
| | 0-100ºC | 5726 | 1 | 5725 | 0.00282 | 0.55 | | 5.16 |
| | | | 250 | 5476 | 0.00287 | 0.54 | | 3.38 |
| | | | 500 | 5226 | 0.00291 | 0.53 | | 0.82 |
| | | | 750 | 4976 | 0.00298 | 0.53 | 0.526 | 0.06 |
| | | | 1000 | 4726 | 0.003 | 0.51 | | 3.67 |
| | -50-50ºC | 8775 | 1 | 8774 | 0.00212 | 0.31 | | 10.58 |
| | | | 250 | 8525 | 0.0022 | 0.32 | | 15.33 |
| | | | 500 | 8275 | 0.0022 | 0.31 | | 11.65 |
| | | | 750 | 8025 | 0.00227 | 0.32 | 0.28 | 14.69 |
| | | | 1000 | 7775 | 0.00232 | 0.32 | | 15.51 |
| PBGA 256 SAC305 | 50-150ºC | 3475 | 1 | 3475 | 0.00374 | 0.98 | | 11.25 |
| | | | 250 | 3225 | 0.00383 | 0.95 | | 7.03 |
| | | | 500 | 2975 | 0.00394 | 0.92 | | 3.69 |
| | | | 750 | 2725 | 0.00403 | 0.88 | 0.883 | 0.62 |
| | | | 1000 | 2475 | 0.00417 | 0.86 | | 3.08 |
| | 0-100ºC | 6202 | 1 | 6202 | 0.00251 | 0.44 | | 13.90 |
| | | | 250 | 5952 | 0.00262 | 0.46 | | 10.20 |
| | | | 500 | 5702 | 0.00273 | 0.47 | | 7.13 |
| | | | 750 | 5452 | 0.0028 | 0.47 | 0.507 | 7.07 |
| | | | 1000 | 5202 | 0.00286 | 0.47 | | 7.86 |
| | -50-50ºC | 9691 | 1 | 9691 | 0.00198 | 0.27 | | 3.63 |
| | | | 250 | 9441 | 0.002 | 0.27 | | 2.84 |
| | | | 500 | 9191 | 0.00206 | 0.28 | | 5.94 |
| | | | 750 | 8941 | 0.00215 | 0.29 | 0.26 | 11.61 |
| | | | 1000 | 8691 | 0.0022 | 0.29 | | 12.99 |

The above table shows clearly the validity of the model where shear strain evolution is correlated with damage evolution through remaining useful life. This model worked good

as a modification to Coffin-Manson formula which does not allow change in shear strain range with thermal cycles undergone.

### 7.3 Darveaux Energy Based Model

Darveaux [129] life prediction model is one of the most popular in microelectronics industry, which can be expressed mathematically as follows;

$$N_i = k_1 \Delta W^{k_2}$$
$$\frac{da}{dN} = k_3 \Delta W^{k_4} \qquad \text{Eq. 7.10}$$

Where $N_i$ is the cycle to crack initiation (normally taken as 10% of Characteristic life $N_f$), $\Delta W$ is plastic energy density per cycle (volume weighted average of critical elements at the neck region of solder joint is taken), a is the diameter of joint at the neck region or the region through which crack propagates, and $k_1$, $k_2$, $k_3$ and $k_4$ are crack growth constants. Here we used characteristic life data and plastic work density under each thermal cycling profile obtained through Non-Linear Finite Element Model to derive $k_1$, $k_2$, $k_3$ and $k_4$ values and compared them with existing published results.

Table 7-5: Characteristic life and Plastic work under different thermal conditions.

| | Temperature | $N_f$ | $N_i$ (10% of $N_f$) | $\Delta W$ (MPa) |
|---|---|---|---|---|
| CABGA 144 (SAC 305) | 50-150°C | 3135 | 313.5 | 0.202 |
| | 0-100°C | 5726 | 572.6 | 0.142 |
| | -50-50°C | 8775 | 877.5 | 0.093 |
| PBGA 256 (SAC 305) | 50-150°C | 3475 | 347.5 | 0.192 |
| | 0-100°C | 6202 | 620.2 | 0.132 |
| | -50-50°C | 9691 | 969.1 | 0.086 |

In calculating ΔW, we took volume average of highly strained elements to overcome mesh sensitivity. Following simplification of Eq. 7.11 is used to calculate crack growth rate.

$$\frac{da}{dN} = \frac{a}{N_f - N_i} \qquad \text{Eq. 7.11}$$

From the above equation it is evident that we took crack growth rate as constant throughout the crack propagation process.

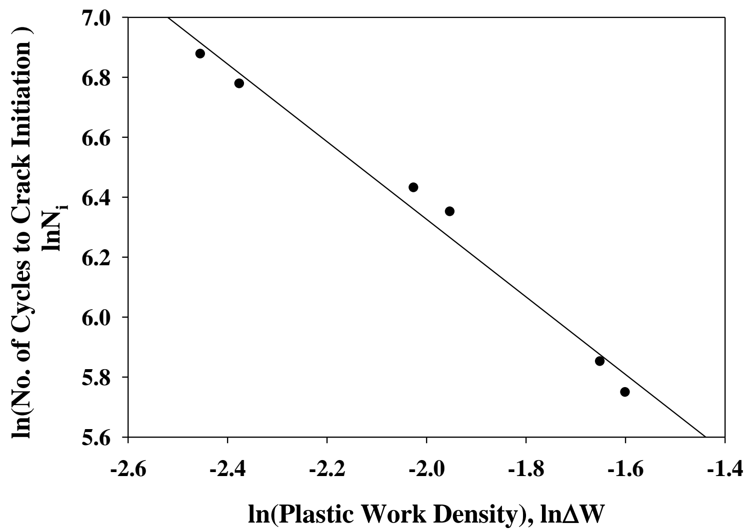


Figure 7-3: $N_i$ (Cycles to crack initiation) vs. Plastic Work Density (ΔW)

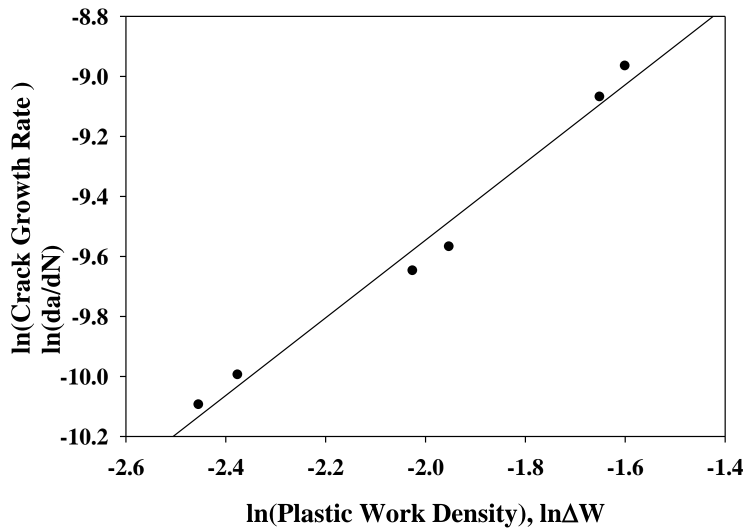


Figure 7-4: Crack Growth Rate (da/dN) vs. Plastic Work Density (ΔW)

Following table shows the k values obtained through above data fit.

| $k_1$ (Cycle/MPa$^{k2}$) | $k_2$ | $k_3$ (mm/cycle-MPa$^{k4}$) | $k_4$ |
|---|---|---|---|
| 42 | -1.3 | 0.00095 | 1.3 |

### 7.4 Life Model based on Microstructural Growth Rate

There is a direct correlation between strain energy, microstructural evolution and crack propagation. Normally grain coarsening takes place near high angle grain boundaries as diffusion is much faster along high angle grain boundaries. As grain coarsening continues, at a particular point both intermetallic and Sn phase become large, making it difficult to rotate or slide to accommodate strain, which finally results into grain boundary crack. Also grain coarsening itself gives rise to High Angle Grain Boundaries (HAGB) which prevents persistent slip bands (PSB) to pass through easily. This effect helps increase dislocation pile-ups, stress concentration and finally crack initiation [130]. In this section a new approach to life prediction model was presented using phase coarsening rate a driving

parameter to failure instead of crack growth rate used in Darveaux's Energy based Model. The pathway to this model alongside with Energy Based Model is depicted in the following figure;

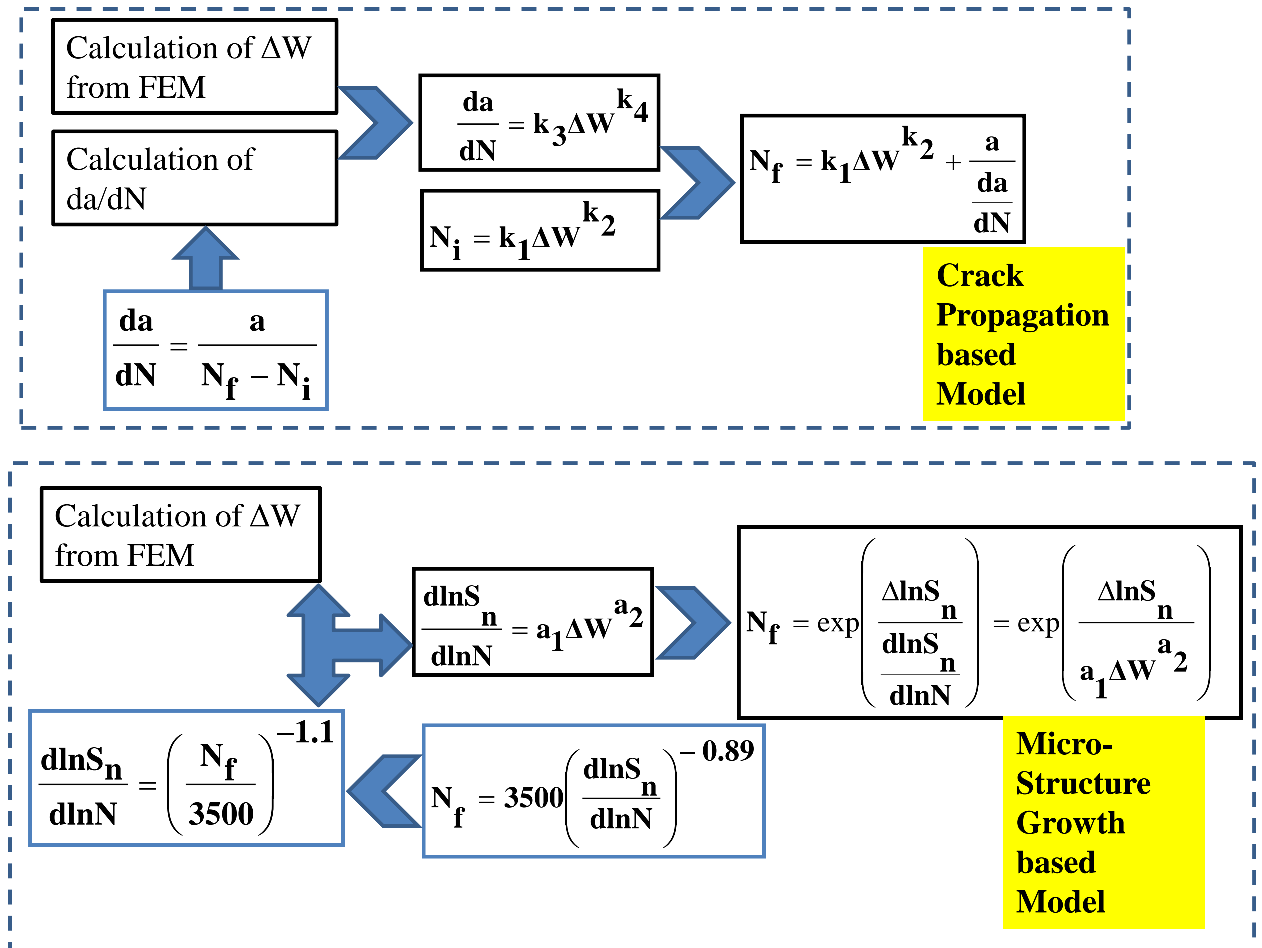


Figure 7-5: Phase growth based life model

Where $S_n$ is normalized phase growth parameter at any particular time. The following figure shows the data fit between plastic work density and Phase growth rate.

Table 7-6: Required values for data fit

| | Nf | $dlnS_n/dlnN$ | ΔW |
|---|---|---|---|
| PBGA 256 (SAC 305) | 3475 | 0.96 | 0.192 |
| | 6202 | 0.55 | 0.133 |
| | 9691 | 0.284 | 0.086 |
| CABGA 144 (SAC 305) | 3135 | 0.98 | 0.202 |
| | 5726 | 0.6 | 0.142 |
| | 8775 | 0.31 | 0.093 |

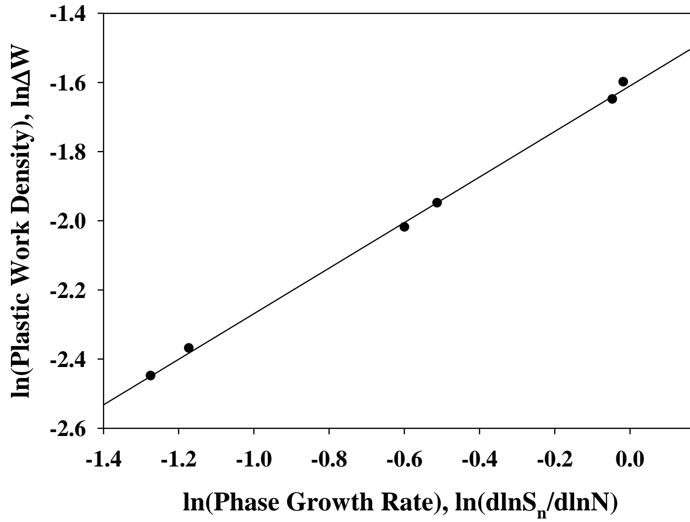


Figure 7-6: Plastic Work Density vs. Phase growth rate

The above data fit can be mathematically expressed as

$$\frac{dlnS_n}{dlnN} = 11\Delta W^{1.5} \quad \text{Eq. 7.12}$$

Table 7-7: Results from life model based on Phase growth

| | $N_f$ | $N_f$ (Model) | Error |
|---|---|---|---|
| PBGA 256 | 3475 | 3958.32 | 13.91 |
| | 6202 | 7268.4 | 17.19 |
| | 9691 | 8676.32 | 10.47 |
| CABGA144 | 3135 | 2465.68 | 21.35 |
| | 5726 | 5726.87 | 0.02 |
| | 8775 | 6689.69 | 23.76 |

Similar model can be developed based on IMC growth as shown in the following flow chart,

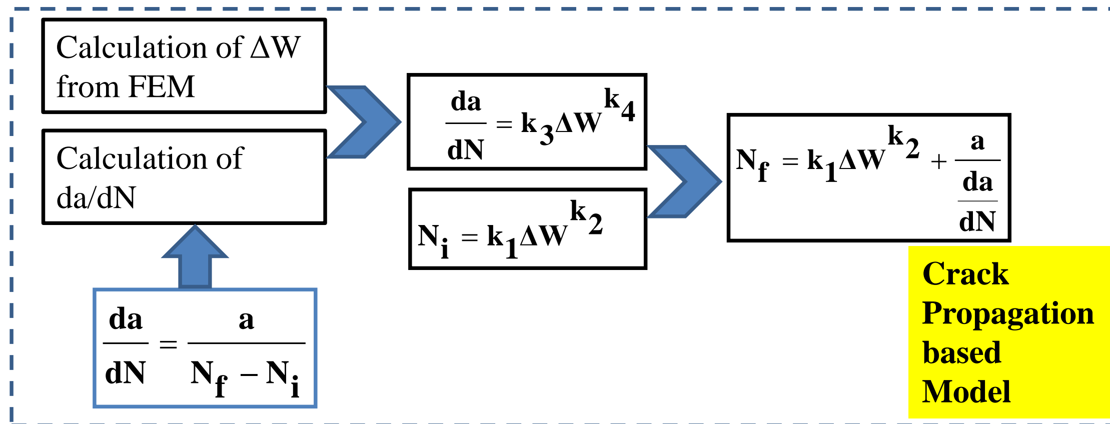


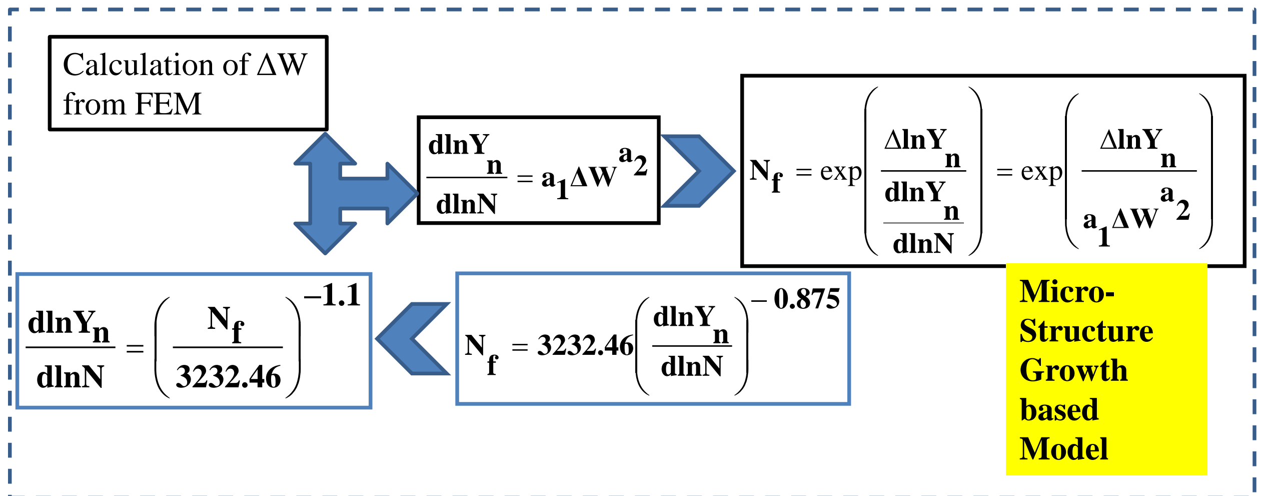


Figure 7-7: IMC growth based life model

Table 7-8: Required values for data fit

| | Nf | $dlnY_n/dlnN$ | ΔW |
|---|---|---|---|
| PBGA 256 (SAC 305) | 3475 | 0.88 | 0.192 |
| | 6202 | 0.51 | 0.133 |
| | 9691 | 0.26 | 0.086 |
| CABGA 144 (SAC 305) | 3135 | 0.9 | 0.202 |
| | 5726 | 0.526 | 0.142 |
| | 8775 | 0.28 | 0.093 |

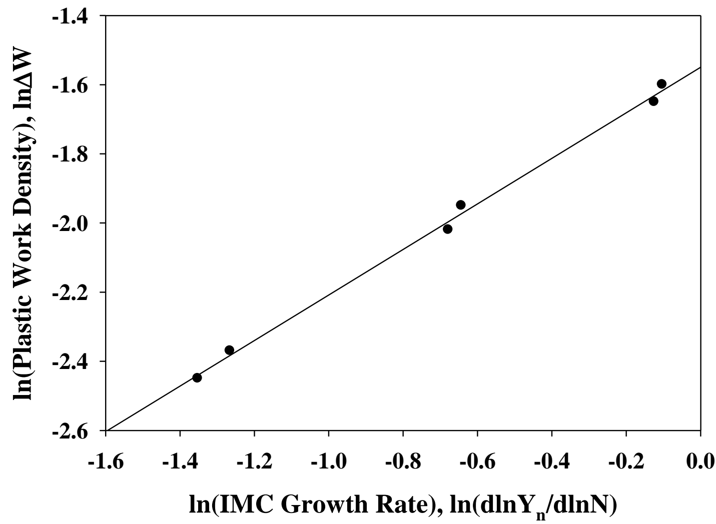


Figure 7-8: Plastic Work Density vs. IMC growth rate

The above data fit can be mathematically expressed as

$$\frac{d\ln Y_n}{d\ln N} = 10 \Delta W^{1.5}$$

Eq. 7.13

Table 7-9: Results from life model based on IMC growth

| | $N_f$ | $N_f$ (Model) | Error |
|---|---|---|---|
| PBGA 256 | 3475 | 4301.14 | 23.77 |
| | 6202 | 8120.56 | 30.93 |
| | 9691 | 9866.78 | 1.81 |
| CABGA144 | 3135 | 2591.58 | 17.33 |
| | 5726 | 4100.01 | 28.40 |
| | 8775 | 6622.71 | 24.53 |

### 7.5 Remaining Life Prognostics

Based upon life prediction models developed in Chapter 4 can be used to predict remaining useful life. Revisiting Eq. 7.5, Eq. 7.6 and Eq. 7.7

$$RUL + N_c = N_f \qquad \text{Eq. 7.5}$$

$$N_f = 3500\left(\frac{d\ln S_n}{d\ln N}\right)^{-0.89} \qquad \text{Eq. 7.6}$$

$$N_f = 3232.46\left(\frac{d\ln Y_n}{d\ln N}\right)^{-0.875} \qquad \text{Eq. 7.7}$$

Now combining the Eq. 7.6 and Eq. 7.7 with Eq. 7.5 following remaining useful life prognostic model can be developed,

$$RUL + N_c = 3500\left(\frac{d\ln S_n}{d\ln N}\right)^{-0.89} \qquad \text{Eq. 7.14}$$

$$RUL + N_c = 3232.46\left(\frac{d\ln Y_n}{d\ln N}\right)^{-0.875} \qquad \text{Eq. 7.15}$$

Table 7-10: Results from RUL prognostic Model based on Phase Growth

| PBGA 256 (SAC 305) | | | | | |
|---|---|---|---|---|---|
| Nf | dlnS/dlnN | Nc | RUL | RUL (Model) | Error |
| | | 1 | 3474 | 3642.01 | 4.84 |
| | | 250 | 3225 | 3393.01 | 5.21 |
| 3475 | 0.956 | 500 | 2975 | 3143.01 | 5.65 |
| | | 750 | 2725 | 2893.01 | 6.17 |
| | | 1000 | 2475 | 2643.01 | 6.79 |
| | | | | | |
| | | 1 | 6201 | 5957.61 | 3.92 |
| | | 250 | 5952 | 5708.61 | 4.09 |
| 6202 | 0.55 | 500 | 5702 | 5458.61 | 4.27 |
| | | 750 | 5452 | 5208.61 | 4.46 |
| | | 1000 | 5202 | 4958.61 | 4.68 |
| | | | | | |
| | | 1 | 9690 | 10729.37 | 10.73 |
| | | 250 | 9441 | 10480.37 | 11.01 |
| 9691 | 0.284 | 500 | 9191 | 10230.37 | 11.31 |
| | | 750 | 8941 | 9980.37 | 11.62 |
| | | 1000 | 8691 | 9730.37 | 11.96 |

Table 7-11: Results from RUL prognostic Model based on Phase Growth

| CABGA 144 (SAC 305) | | | | | |
|---|---|---|---|---|---|
| Nf | dlnS/dlnN | Nc | RUL | RUL (Model) | Error |
| 3135 | 0.984 | 1 | 3134 | 3549.61 | 13.26 |
| | | 250 | 2885 | 3300.61 | 14.41 |
| | | 500 | 2635 | 3050.61 | 15.77 |
| | | 750 | 2385 | 2800.61 | 17.43 |
| | | 1000 | 2135 | 2550.61 | 19.47 |
| | | | | | |
| 5726 | 0.6 | 1 | 5725 | 5513.59 | 3.69 |
| | | 250 | 5476 | 5264.59 | 3.86 |
| | | 500 | 5226 | 5014.59 | 4.05 |
| | | 750 | 4976 | 4764.59 | 4.25 |
| | | 1000 | 4726 | 4514.59 | 4.47 |
| | | | | | |
| 8775 | 0.31 | 1 | 8774 | 9924.59 | 13.11 |
| | | 250 | 8525 | 9675.59 | 13.50 |
| | | 500 | 8275 | 9425.59 | 13.90 |
| | | 750 | 8025 | 9175.59 | 14.34 |
| | | 1000 | 7775 | 8925.59 | 14.80 |

Table 7-12: Results from RUL prognostic Model based on IMC Growth

| PBGA 256 (SAC 305) | | | | | |
|---|---|---|---|---|---|
| Nf | dlnY/dlnN | Nc | RUL | RUL (Model) | Error |
| 3475 | 0.88 | 1 | 3474 | 3604.34 | 3.75 |
| | | 250 | 3225 | 3355.34 | 4.04 |
| | | 500 | 2975 | 3105.34 | 4.38 |
| | | 750 | 2725 | 2855.34 | 4.78 |
| | | 1000 | 2475 | 2605.34 | 5.27 |
| | | | | | |
| 6202 | 0.51 | 1 | 6201 | 5850.63 | 5.65 |
| | | 250 | 5952 | 5601.63 | 5.89 |
| | | 500 | 5702 | 5351.63 | 6.14 |
| | | 750 | 5452 | 5101.63 | 6.43 |
| | | 1000 | 5202 | 4851.63 | 6.74 |
| | | | | | |
| 9691 | 0.26 | 1 | 9690 | 10547.47 | 8.85 |
| | | 250 | 9441 | 10298.47 | 9.08 |
| | | 500 | 9191 | 10048.47 | 9.33 |
| | | 750 | 8941 | 9798.47 | 9.59 |
| | | 1000 | 8691 | 9548.47 | 9.87 |

Table 7-13: Results from RUL prognostic Model based on IMC Growth

| CABGA 144 (SAC 305) | | | | | |
|---|---|---|---|---|---|
| Nf | dlnY/dlnN | Nc | RUL | RUL (Model) | Error |
| 3475 | 0.9 | 1 | 3474 | 3535.72 | 12.82 |
| | | 250 | 3225 | 3286.72 | 13.92 |
| | | 500 | 2975 | 3036.72 | 15.25 |
| | | 750 | 2725 | 2786.72 | 16.84 |
| | | 1000 | 2475 | 2536.72 | 18.82 |
| | | | | | |
| 6202 | 0.526 | 1 | 6201 | 5672.98 | 0.91 |
| | | 250 | 5952 | 5423.98 | 0.95 |
| | | 500 | 5702 | 5173.98 | 1.00 |
| | | 750 | 5452 | 4923.98 | 1.05 |
| | | 1000 | 5202 | 4673.98 | 1.10 |
| | | | | | |
| 9691 | 0.28 | 1 | 9690 | 9778.03 | 11.44 |
| | | 250 | 9441 | 9529.03 | 11.78 |
| | | 500 | 9191 | 9279.03 | 12.13 |
| | | 750 | 8941 | 9029.03 | 12.51 |
| | | 1000 | 8691 | 8779.03 | 12.91 |

The above tables show how well the RUL prognostication works, obvious from low margin of error.

## 7.5 Conclusion

Different life prediction models like Coffin-Mansion model and Darveaux's Energy based Model were implemented with experimental data obtained through microstructural investigation, Digital Image Correlation, Accelerated Life Testing and Finite Element Modeling, showed good correspondence with experimental findings. Also a modification in Coffin Mansion formula was presented to accommodate shear strain evolution with number of thermal cycles. A new prognostication model was shown using life prediction model based upon two damage proxies namely phase growth and IMC growth. Finally a new model, based on microstructural growth was proposed.

# Chapter 8

# Summary

The total outcome of this work can be summarized into three distinct areas;

## 8.1 Damage Mapping Model

A novel time-temperature damage mapping model was proposed. Two distinctly different packages in terms of geometry and I/O count were tested under three different isothermal aging conditions. Relations between damage state and aging duration were derived by fitting experimental data for two different damage proxies. Then a unified damage mapping model was derived using Arrhenius type model which can accommodate geometric difference and other features and can be used to probe time-temperature combination to reach a particular damage state. Validity of this model was tested by comparing with experimental data and margin of error was found to be well below tolerable limit.

## 8.2 Life Prediction Model

A unified life prediction model was proposed which incorporates microstructural damage accrual rate for the first time. Conventional life prediction models are based on either on plastic work or strain. Model based on plastic work parameter are fully simulation based. For the strain based model, scientists or engineers have to depend on either simulation or bulk solder specimen. There are very little scope to implement these techniques on real time solder joint. Keeping these in mind and also considering the fact of damage accumulation rate being a potential and established damage indicator, a novel approach of life model was developed which incorporates microstructural change factor. Three different test conditions having same temperature difference but different mean temperatures were used on three different package geometries. Damage mapping relations

were derived by fitting experimental data using Arrhenius type model. A separate set of packages were put under similar conditions until failure to extract characteristics life using Weibull distribution. This life data then was correlated with damage state information from all packages tested to develop a unified life prediction model. Validity of this model was checked by comparing model and experimental outcomes. The uniqueness of this model is its ability to accommodate the real time microstructural information from solder joint.

## 8.3 Real time Investigation of Damage

A full field optical method was implemented to investigate mechanical property evolution of solder joint in real time setup i.e. while solder joint being thermally cycled unlike state of the art microstructural investigation. Shear strain was calculated and found to be increasing with number of cycle count. Also effect of aging on thermal fatigue reliability was investigated and the result found to be with good agreement with previous findings. Another notable finding of this work was the continuous change of shear strain range as contrary to popular belief that it does not change after some number of cycles. But in this work, it showed continuous, although slow change with number of thermal cycles undergone, which is also validated by microstructural investigation results from previous section. A final damage mapping model was developed which can correlate shear strain range and damage accrual rate. This model can be very useful in estimating damage accrual rate for a particular temperature profile by performing Digital Image Correlation which is much easier and simple technique than microstructural investigation.

## 8.4 Future Work

It would be interesting to see the effect of dwell period, temperature ramp rate and humidity on reliability, as previous researches proved their effect on fatigue reliability. Also thermal load frequency and effect of both maximum and minimum temperature of thermal cycling

range can be evaluated. Relative importance of these above mentioned factor on package reliability can be assessed by using statistical technique and then can be included to develop higher order life prediction model. Another very important factor is solder alloy composition and Sn grain orientation. Due to highly anisotropic nature of Sn, its grain orientation always play a vital role in IMC formation. To make the proposed life prediction model more encompassing, Electron Migration effect also can be included, because in operational environment thermal load is almost always coupled with power load. Also in final damage mapping model, fatigue ductility exponent was assumed constant. Although this assumption in this work did not push error beyond tolerable limit, but it is worth investigating to see how much this exponent is changing with number of cycles.

# Reference

1. J. C. Suhling. (2009). Mechanics of Electronic Packaging, (Mech 6310 notes). Auburn University.

2. N. J. Rao and G. A. Rao. (1999 Jun.). A Course on Introduction to Electronic Packaging. Centre of Electron. Design & Technology. Indian Institute of Science, Bangalore,India.[Online]. Available: http://ieeexplore.ieee.org/document/776289.

3. G. E. Moore. (1965 Apr.), Cramming More Components onto Integrated Circuits. *Electronics*, [Online] Vol. *38(8)*, pp. 114-117, Available: http://web.eng.fiu.edu/npala/eee6397ex/gordon_moore_1965_article.pdf.

4. R. R. Tummala. (1999) Electronic Packaging Research and Education: A Model for the 21st Century. *John Hopkins Apl Technical Digest*, Volume *20*, Number 1, page: 111-121. Available: www.jhuapl.edu/techdigest/TD/td2001/Tummula.pdf .

5. M. G. Bevan, and B. M. Romenesko. (1999 Jan.). Modern Electronic Packaging Technology. [Online] *John Hopkins APL Technical Digest*, Vol. *20(1).* Available:https://www.researchgate.net/publication/228693666_Modern_electronic_packaging_technology.

6. H. Zhou, "Reliability of Lead-Free Electronic Package Interconnections Under Harsh Environment," Ph.D. dissertation, Dept. Mech. Eng., Auburn Univ., Auburn, Al, 2014.

7. Fairchild Semiconductor. (2004 Oct.). Surface Mounting Technology Assembly Guidelines for Fairchild's Microcouplers. ON Semiconductor, CA. [Online].Available:https://www.fairchildsemi.com/application-notes/AN/AN-3011.pdf.

8. A. R. Syed. (1996 May). Thermal Fatigue Reliability Enhancement of Plastic Ball Grid Array (PBGA) Packages, Presented at ECTC, pp.1211-1216, Orlando, Fl. [Online] Available:http://ieeexplore.ieee.org/document/550889.

9. H. L. Pang, L. H. Xu, X. Q. Shi, W. Zhou, and S. L. Ngoh. (2004 Oct.). Intermetallic Growth Studies on Sn-Ag-Cu Lead-free Solder. *Journal of Electronic Materials*, Vol.*33(10)*,pp.1219-1226.[Online]. Available: http://link.springer.com/article/10.1007/s11664-004-0125-7.

10. F. Sun, P. Hochstenbach, W. D. Van Driel, and G. Q. Zhang. (2008 Aug.). Fracture Morphology and Mechanism of IMC in Low-Ag SAC Solder/UBM (Ni(P)-Au) for WLCSP. *Microelectronics Reliability* [Online], Vol. *48*, pp. 1167-1170. Available:www.sciencedirect.com/science/article/pii/S0026271408001789.

11. I. Anderson, and J. Harringa. (2004 Jun.). Elevated Temperature Aging of Solder Joints Based on Sn-Ag-Cu: Effects on Joint Microstructure and Shear Strength. *Journal of Electronic Materials*, [Online] Vol. *33*, pp. 1485-1496, 2004. Available: link.springer.com/article/10.1007/s11664-004-0090-1.

12. M. Abtew and G. Selvaduray. (2000 Jun.). Lead-free Solders in Microelectronics. Materials Science and Engineering: R: Reports, [Online]. Vol. 27. Available: www.sciencedirect.com/science/article/pii/S0927796X00000103.

13. C. A. Handwerker, “NCMS lead-free solder project: a summary of results, conclusions and recommendations”. *IPC.IPC Work ’99: An International Summit on Lead-Free Electronics Assemblies; Proceeding*, 1999; Minneapolis, MN.

14. T. Sawamura and T. Igarashi. (2005 June ). Difference Between Various Sn/Ag/Cu Solder Compositions. Almit Ltd. [Online]. Available: http://www.almit.com/dloads/Agents/SAC Alloy Comparison.pdf.

15. B. Sandy and R. C. Lasky. (2011). Choosing a Low Cost Alternative to SAC Alloys for PCB Assembly. SMTAI 2011, Fort Worth, TX. [Online]. Available: http://www.techni-tool.com/site/ARTICLE_LIBRARY/Indium- Choosing a Low-Cost Alternative to Sac Alloys for PCB Assembly.pdf.

16. K. Nimmo. (2004). Alloy Selection. Lead-Free Soldering in Electronics: Science, Technology and Environmental Impact, K. Suganuma, Ed. Marcel Dekker, pp. 61-83.

17. C. M. Miller, I. E. Anderson, and J. F. Smith. (1994 Jul.). A Viable Tin-Lead Solder Substitute: Sn-Ag-Cu. *Journal of Electronic Materials*. Vol. *23*, pp. 595-602. Available: http://link.springer.com/article/10.1007/BF02653344.

18. M. E. Loomans, and M. E. Fine. (2000 Apr.). Tin-silver-copper eutectic temperature and composition. Metallurgical and Materials Transactions A, Vol. 31A, pp. 1155-1162. Available: http://link.springer.com/article/10.1007/s11661-000-0111-5.

19. K. W. Moon, W. J. Boettinger, U. R. Kattner, F. S, Biancaniello, and C. A. Handwerker. (2000 Oct.) Experimental and Thermodynamic Assessment of Sn-

Ag-Cu Solder Alloys. *Journal of Electronic Materials*, Vol. *29*, pp. 1122-1136. Available: http://link.springer.com/article/10.1007/s11664-000-0003-x.

20. S. A. Nelson. (Jan. 2011). Crystallization in Ternary Systems. Tulane University.[Online].Available:http://www.tulane.edu/*sanelson/geol212/ternaryphdiag.htm.

21. U. R. Kattner. (2000). Phase diagrams & Computational Thermodynamics. NIST.[Online]Available:http://www.metallurgy.nist.gov/phase/solder/solder.html.

22. H. Ma and J. C. Suhling. ( 2009 Mar.). A review of mechanical properties of lead-free solders for electronic packaging. *Journal of Material Science*. Vol. *44*, pp:1141–58.[Online]. Available: http://link.springer.com/article/10.1007/s10853-008-3125-9.

23. D. A. Shnawah, M. F. M. Sabri, I. A. Badruddin. (2012 Jan.). A review on thermal cycling and drop impact reliability of SAC solder joint in portable electronic products. *Microelectronics Reliability*. Vol. *52 (1),* pp. 90-99. [Online].Available:http://www.sciencedirect.com/science/article/pii/S0026271411003581.

24. M. Tarr. Electronics Materials-Stress caused by thermal mismatch. IDC Technologies.[Online].Available:http://www.ami.ac.uk/courses/topics/0162_sctm/index.html.

25. M. Basit, M. Motalab, J. Roberts, J. C. Suhling, P. Lall, “The Effects of Silver Content and Solidification Profile on the Anand Constitutive Model for SAC Lead Free Solders”, *ITHERM*, Orlando, FL, 2014.

26. Creep and Constitutive Models for Near-Eutectic SnPb. NIST. Available: www.metallurgy.nist.gov/solder/clech/Sn-Pb_Creep.html.

27. F. Garofalo. (1966). Fundamentals of Creep and Creep-Rupture in Metals, 2 Ed., Macmillan.

28. M. Kassner, and M. T. Perez-Prado. (2004). Fundamentals of Creep in Metals and Alloys, Elsevier Science.

29. Structure of Metals. University of Illinois Urbana-Champaign [Online]. Available: http://matse1.matse.illinois.edu/metals/prin.html.

30. Tapany Udomphol. (2007 May). Dislocation Theory. Suranaree university of Technology.[Online].Available:http://eng.sut.ac.th/metal/images/stories/pdf/05_ Dislocation_theory.pdf.

31. M. L. Weaver. (2011 Mar.). Jogs, Kinks, and Dislocation Intersections. (Module 16) University of Alabama. [Online]. Available: http://bama.ua.edu/~mweaver/courses/MechBeh/Day16.pdf.

32. R. W. Hertzberg. (1996). Deformation and Fracture Mechanics of Engineering Materials, 4 Ed., John Wiley & Sons, Inc.

33. DoITPoMS. Dislocation Glide. University of Cambridge. [Online]. Available: http://www.doitpoms.ac.uk/tlplib/dislocations/dislocation_glide.php.

34. P. G. Caceres. Fatigue: Failure under fluctuating/cycling stress. [Online]. Available: academic.uprm.edu/pcaceres/Courses/MatEng?MSE2-2.pdf.

35. G. Totten. (2008 May). Fatigue crack propagation. Advanced Materials and Processes.[Online].Available:http://www.asminternational.org/emails/enews/amp_pdfs/amp16605p039.pdf.

36. P. G. Caceres. Fatigue: Failure under fluctuating/cycling stress. [Online]. Available: http://academic.uprm.edu/pcaceres/Courses/MatEng3045/EME8-4.pdf.

37. Fatigue Crack Initiation. NDT Resource Center. [Online]. Available: https://www.nde-ed.org/EducationResources/CommunityCollege/Materials/Mechanical/Fatigue.htm.

38. M. A. Miner, (1954) “Cumulative Damage in Fatigue,” *Journal of Applied Mechanics*, Vol. *12(3)*, pp. 159-164.

39. T. J. Kilinski, J. R. Lesniak, and B. I. Sandor. (1991). Modern Approaches to Fatigue Life Prediction of SMT Solder Joints," Solder Joint Reliability Theory and Applications, J. H. Lau, Ed., Chapter 13, pp: 384-405, Van Nostrand Reinhold. [Online]. Available: http://link.springer.com/book/10.1007/978-1-4615-3910-0.

40. M. Pecht. (2009 May). Prognostics and Health Management of Electronics. [Online].Available://onlinelibrary.wiley.com/doi/10.1002/9780470061626.shm118/full.

41. CAVE3, Prognostic Helth Management for Electronics. Auburn University. [Online]. Available: http://cave.auburn.edu/rsrch-thrusts/prognostic-health-management-for-electronics.html.

42. Mohammad Hossain Shirangi. Reliability in Electronic Packaging. Cuvillier Verlag Gottingen. [Online]. Available: https://cuvillier.de/uploads/preview/public_file/1519/9783869554334.pdf.

43. A. R. Syed. (1996 May). Thermal Fatigue Reliability Enhancement of Plastic Ball Grid Array (PBGA) Packages. IEEE-ECTC, pp.1211-1216, Orlando, FL. [Online].Available:http://ieeexplore.ieee.org/xpl/mostRecentIssue.jsp?punumber =3763.

44. R. Ghafarrian. (2001 Jun.). Effect of Thermal Cycling Ramp Rate on CSP Assembly Reliability. 51st IEEE-ECTC, pp.1232- 37. [Online] Available: http://ieeexplore.ieee.org/document/927974.

45. E. Bradely and K. Banerji. (1996 May). Effect of PCB Finish on the Reliability and Wettability of Ball Grid Array Packages. IEEE Transaction on Component Packaging and Manufacturing *Technology* Part B-Advanced Packaging, Vol.19, pp.320-330. [Online]. Available: http://ieeexplore.ieee.org/document/496035.

46. J. C. Suhling, R. W. Johnson, J. L. Evans, N. Islam, J. Liuand S. Gale. (2002). Reliability of Small BGAs in the Automotive Environment. Proceedings-SPIE. [Online]. Available: http://www.eng.auburn.edu/apl/files/Small_BGAs.pdf.

47. A. Mawer, N. Vo, Z. Johnzon, W. Lindsay. (June 1999). Board-Level Characterization of 1.0 and 1.27 mm Pitch PBGA for Automotive Under-Hood

Applications. 49th IEEE-ECTC , Sandiego, Ca, pp. 118-124. [Online]. Available: http://ieeexplore.ieee.org/document/776159.

48. Y. A. Elkaday, R. W. Knight, J. C. Suhling. ( 2004 Jun.). Thermal Performance of Underfilled BGA's. ITHERM. pp. 624-634. [Online]. Available: http://ieeexplore.ieee.org/document/1319234.

49. J. Pyland, R. Pucha and S. Sitaram. (2000 Dec.). Does Underfilling Enhance BGA Reliability? Proceedings of the Electronics Packaging Technology Conference, [Online]. Available: ieeexplore.ieee.org/document/906380.

50. K. N. Chiang, Y. T. Lin, H. C. Cheng. (2000 Feb.). On Enhancing Eutectic Solder Joint Reliability Using a Second-Reflow-Process Approach. *IEEE Transactions on Advanced Packaging*, Vol 23 (1), pp. 9-14. [Online]. Available: http://ieeexplore.ieee.org/document/826755.

51. H. K. Charles and G. V. Clatterbaugh. (1990 Jun.). Solder Joint Reliability — Design Implications from Finite Element Modeling and Experimental Testing. *Journal of Electronic Packaging,* Volume *112 (2).* [Online]. Available: http://electronicpackaging.asmedigitalcollection.asme.org/article.aspx?articleid= 1404366.

52. M. A. Matin, W. P. Vellinga and M. G. D. Geers. (2007 Feb.). Thermomechanical fatigue damage evolution in SAC solder joints. *Mater Science and Engineering: A*, Vol. *445–446*, pp.73–85. [Online]. Available: http://www.sciencedirect.com/science/article/pii/S092150930602003X.

53. T. T. Mattila, M. Mueller, M. Paulasto-Krockel, K-J Wolter. (2010 Sep.). Failure mechanism of solder interconnections under thermal cycling conditions. IEEE-ESTC, [Online]. Available: http://ieeexplore.ieee.org/document/5642843.

54. T. Mattila, "Reliability of high-density lead-free solder interconnections under thermal cycling and mechanical shock loading," PhD dissertation, Helsinki University of Technology, Finland, 2005.

55. D. R. Frear, L. N. Ramanathan, J-W. Jang, N. L. Owens. (2008 May). Emerging reliability challenges in electronic packaging. IEEE IRPS, pp. 450–4. [Online]. Available: http://ieeexplore.ieee.org/document/4558927.

56. S. Terashima, Y. Kariya, T. Hosoi and M. Tanaka. (2003 Sep.). Effect of silver content on thermal fatigue life of Sn–xAg–0.5Cu flip-chip interconnects. Journal of Electronic Materials, Vol. *32 (12),* pp. 1527–33. [Online]. Available: http://link.springer.com/article/10.1007/s11664-003-0125-z.

57. S. Terashima, K. Takahama, M. Nozaki and M. Tanaka. (June 2005). Recrystallization of Sn grains due to thermal strain in Sn–1.2Ag–0.5Cu–0.05Ni solder. *Materials Transactions*, Vol. *45 (4),* pp. 1383-1390. [Online]. Available: https://www.jstage.jst.go.jp/article/matertrans/45/4/45_4_1383/_article.

58.S. Terashima, Y. Kariya and M. Tanaka. (2005 Jun.). Improvement on thermal fatigue properties of Sn–1.2Ag–0.5Cu flip chip interconnects by Nickel addition. *Materials Transactions*, Vol *45 (3),* pp. 676-680. [Online]. Available: https://www.jstage.jst.go.jp/article/matertrans/45/3/45_3_673/_article.

59. S. Terashima and M. Tanaka. (2005 Jun.). Thermal fatigue properties of Sn–1.2Ag–0.5Cu–xNi flip-chip interconnects. *Materials Transactions*, Vol *45 (3),* pp. 681-688.[Online].Available: https://www.jstage.jst.go.jp/article/matertrans/45/3/45_3_681/_article.

60. S. Terashima and M. Tanaka. (2013 Dec.). Effect of fine dispersoids and anisotropic nature of b- Sn on thermal fatigue properties of flip chips connected by Sn–xAg–0.5Cu (x: 1, 3 and 4 mass%) lead free solders. *Science and Technology of Welding and Joining*, Vol. *14,* pp. 468–475. [Online]. Available: http://www.tandfonline.com/doi/abs/10.1179/136217109X437169.

61. Y. Kariya, T. Hosoi, S. Terashima, M. Tanaka and M. Otsuka. (2003 Aug.) Effect of silver content on the shear fatigue properties of Sn–Ag–Cu flip-chip interconnect. *Journal of Electronic Materials*, Vol. *33 (4),* pp. 321-328. [Online]. Available: http://link.springer.com/article/10.1007/s11664-004-0138-2.

62. M. Berthou, P. Retailleau, H. Frémont, A. Guédon-Gracia and C. Jéphos-Davennel. (2009 Nov.). Microstructure evolution observation for SAC solder joint: Comparison between thermal cycling and thermal storage. *Microelectronics Reliability*, Volume *49 (9-11),* pp. 1267–1272. [Online]. Available: http://www.sciencedirect.com/science/article/pii/S0026271409002509.

63. L. Xu and J. H. L. Pang. (2006 Jun.). Intermetallic growth studies on SAC/ENIG and SAC/Cu-OSP lead-free solder joints. 10th IEEE-ITHERM. [Online]. Available: http://ieeexplore.ieee.org/document/1645472.

64. B. Arfaei, S. M. Shirazi, S. Joshi, M. Anselm, P. Borgesen, E. Cotts, J. Wilcox, and R. Coyle. (2013 May). Reliability and Failure Mechanism of Solder Joints in Thermal Cycling Tests. 63rd IEEE-ECTC. [Online]. Available: http://ieeexplore.ieee.org/document/6575693.

65. H. Ma, J. C. Suhling. (March 2009). A review of mechanical properties of lead-free solders for electronic packaging. *Journal of Material Science*. Vol. *44,* pp.1141–58.[Online]. Available: http://link.springer.com/article/10.1007/s10853-008-3125-9.

66. T-K. Lee, H. Ma, K-C Liu and J. Xue. (Sep. 2010). Impact of Isothermal Aging on Long-Term Reliability of Fine-Pitch Ball Grid Array Packages with Sn-Ag-Cu: Interconnects: Surface Finish Effects. *Journal of Electronic Materials*, Vol. *39 (12),* [Online]. Available: http://link.springer.com/article/10.1007/s11664-010-1352-8.

67. D. Li, C. Liu and P. P. Conway. (2005 Mar.). Microstructure and Shear Strength Evolution of Sn-Ag-Cu Solder Bumps During Aging at Different Temperatures. *Journal of Electronic Materials*, Vol. *35 (3),* pp. 388-398. [Online]. Available: http://link.springer.com/article/10.1007/BF02690524.

68. D. Li, C. Liu and P. P. Conway. (2005 Jan.). Characteristics of Intermetallics and Micromechanical Properties during Thermal Ageing of Sn-Ag-Cu Flip-Chip Solder Interconnects. *Materials Science and Engineering: A*, Vol. *391 (2),* [Online].Available:

http://www.sciencedirect.com/science/article/pii/S092150930401250X.

69. T-C. Chiu, K. Zeng, R. Stierman, D. Edwards and K. Ano. (2004 Jun.). Effect of Thermal Aging on Board Level Drop Reliability for Pb-Free BGA Packages. 54th ECTC. [Online]. Available: http://ieeexplore.ieee.org/document/1320275.

70. A. PIETRIKOVÁ, and J. ĎURIŠIN. (2010). Microstructure of solder joints and isothermal aging. *Acta Electrotechnica et Informatica*, Vol. *10 (3),* pp. 43–46. [Online]. Available: http://www.aei.tuke.sk/pdf/2010-03/09_Pietrikova.pdf.

71. T-K. Lee, H. Ma, K-C. Liu and J. Xue. (2010 Dec.). Impact of Isothermal Aging on Long-Term Reliability of Fine-Pitch Ball Grid Array Packages with Sn-Ag-Cu:Solder Interconnects: Surface Finish Effects. *Journal of Electronic Materials*, Vol. *39 (12),* pp. 2564-2573. [Online]. Available: http://link.springer.com/article/10.1007/s11664-010-1352-8.

72. R. Darveaux, J. Heckman and A. Mawer. (1998). Effect of test board design on the 2nd level reliability of a fine pitch BGA package. Proc. SMI. pp. 105-111. [Online].Available:http://electronicpackaging.asmedigitalcollection.asme.org/article.aspx?articleid=1406571.

73. R. Darveaux, J. Heckman, A. Syed and A. Mawer. (2000 Jul.). Solder joint fatigue life of fine pitch BGAs- impact of design and material choices. *Microelectronics Reliability*, Vol. *40 (7),* pp. 1117-1127. [Online]. Available: http://www.sciencedirect.com/science/article/pii/S002627140000038X.

74. A. Syed. (2001). Reliability of Lead-free Solder Connections for Area-Array Packages. IPC SMEMA council APEX. [Online]. Available:

http://www.jovysys.com/jovysystems/images/stories/pdf/Reliability_of_Lead-Free_Solder_Connections_Whitepaper.pdf.

75. R. Ghaffarian. (2000 Mar.). Accelerated Thermal Cycling and Failure Mechanisms For BGA and CSP Assemblies. *Journal of Electronic Packaging*, Vol.*122(4),*[Online].Available:http://electronicpackaging.asmedigitalcollection.asme.org/article.aspx?articleid=1406042.

76. H. Yang, P. Deane, P. Magill and K. L. Murty. (1996 May). Creep Deformation of 96.5Sn-3.5Ag Solder Joints in a Flip-Chip Package. 46$^{th}$ IEEE-ECTC. pp. 1136-1142. [Online]. Available: http://ieeexplore.ieee.org/document/550880.

77. R. W. Hertzberg. (1996). Deformation and Fracture Mechanics of Engineering Materials, 4 Ed., John Wiley & Sons, Inc.

78. W. K. Jones, Y. Liu, M. A. Zampino, G. Gonzalez and M. Shah. (1997). A Study on Mechanical Properties of Eutectic and Solid Solution Pb-Sn-Ag Solders from 200 °C to 150° C. Design and Reliability of Solders and Solder Interconnections, R. K. Mahidhara, D. R. Frear, S. M. L. Sastry, K. L. Murty, P. K. Liaw and W. Winterbottom, eds., The Minerals, Metals & Materials Society, pp. 85-96.

79. H. Nose, S. Masao, Y. Tsukada and H. Nishimura. (Mar. 2003). Temperature and Strain Rate Effects on Tensile Strength and Inelastic Constitutive Relationship of Sn-Pb Solders. *Journal of Electronic Packaging*, Vol. 125 (1), pp. 59-66. [Online].Available:http://electronicpackaging.asmedigitalcollection.asme.org/article.aspx?articleid=1406834.

80. J. H. L. Pang, B. S. Xiong and F. X. Che. (2004 May). Modeling Stress Strain Curves For Lead-Free 95.5Sn-3.8Ag-0.7Cu Solder. EuroSime, pp. 449-453. [Online].Available: http://ieeexplore.ieee.org/document/1304077.

81. X. Q. Shi, Z. P. Wang, Q. J. Yang and H. L. J. Pang. (2002 Dec.). Creep Behavior and Deformation Mechanism Map of Sn-Pb Eutectic Solder Alloy. *Journal of Engineering Materials and Technology*, Vol. 125 (1), pp. 81-88. [Online].Available:http://materialstechnology.asmedigitalcollection.asme.org/article.aspx?articleid=1426892.

82. L. Anand. (1982 Jan.). Constitutive Equations for the Rate-Dependent Deformation of Metals at Elevated Temperatures. *Journal of Engineering Materials and Technology*, Vol. *104 (1),* pp. 12-17. [Online].Available: http://materialstechnology.asmedigitalcollection.asme.org/article.aspx?articleid=1423043.

83. S. B. Brown, K. H. Kim and L. Anand. (1989). An Internal Variable Constitutive Model for Hot Working of Metals. *International Journal of Plasticity*, Vol. 5, pp. 95-130. [Online]. Available: http://www.sciencedirect.com/science/article/pii/0749641989900259.

84. B. Rodgers, B. Flood, J. Punch and F. Waldron. (2006 Apr.). Experimental Determination and Finite Element Model Validation of the Anand Viscoplasticity Model Constants for SnAgCu. EuroSimE, pp. 490-496. [Online].Available: http://ieeexplore.ieee.org/document/1502854.

85. M. Amagai, M. Watanabe, M. Omiya, K. Kishimoto and T. Shibuya. (2002 Jun.). Mechanical Characterization of Sn-Ag-Based Lead-Free Solders. *Microelectronics Reliability*, Vol. *42 (6),* pp. 951-966. [Online].Available: http://www.sciencedirect.com/science/article/pii/S0026271402000173.

86. J. Chang, L. Wang, J. Dirk and X. Xie. (2006 Mar.). Finite Element Modeling Predicts the Effect of Voids on Thermal Shock Reliability and Thermal Resistance of Power Devices. *Welding Journal*, pp. 63-70. [Online].Available: http://img2.aws.org/wj/supplement/03-2006-CHANG-s.pdf.

87. X. Chen, G. Chen and M. Sakane. (2005 Mar.). Prediction of Stress-Strain Relationship with an Improved Anand Constitutive Model for Lead-Free Solder Sn-3.5Ag. IEEE-ECTC, Vol. 28, Issue 1, pp. 111-116. [Online].Available: http://ieeexplore.ieee.org/document/1402620.

88. D. Chan, X. Nie, D. Bhate, G. Subbarayan and I Dutta. (2009 Jul.). High Strain Rate Behavior of Sn3.8Ag0.7Cu Solder Alloys and Its Influence on the Fracture Location Within Solder Joints. ASME InterPACK, pp. 989-995. [Online].Available:http://proceedings.asmedigitalcollection.asme.org/proceeding.aspx?articleid=1632526.

89. W.W. Lee, L. T. Nguyen and G. S. Selvaduray. (2000 Feb.). Solder Joint Fatigue Models: Review and Applicability to Chip Scale Packages. *Microelectronics Reliability*, Vol. 40(2), pp. 231-244. [Online].Available: http://www.sciencedirect.com/science/article/pii/S002627149900061X.

90. S. Park, R. Dhakal, L. Lehman and E. Cotts. (2007 Jan.). Measurement of deformations in SnAgCu solder interconnects under in situ thermal loading. *Acta Materialia,* Vol. *55,* pp. 3253–60. [Online]. Available: http://ws.binghamton.edu/park/publications/2007-4.pdf.

91. T. T. Nguyen, D. Yu and S. B. Park. (2011 Jun.). Characterizing the Mechanical Properties of Actual SAC105, SAC305, and SAC405 Solder Joints by Digital Image Correlation. *Journal of Electronic Materials*, Vol. 40(6), pp. 1409-1415. [Online].Available: http://link.springer.com/article/10.1007/s11664-011-1534-z.

92. Y. Sun, J. H. L. Pang, X. Shi and J. W. R. Tew. (2006 Jun.). Thermal Deformation Measurement by Digital Image Correlation Method. 10$^{th}$ IEEE-ITHERM. [Online].Available: http://ieeexplore.ieee.org/document/1645444.

93. J. Zhang, M. Li, C. Y. Xiong, J. Fang and S. Yi. (2005). Thermal Deformation Analysis of BGA Package by Digital Image Correlation Technique. *Microelectronics International*, Vol. 22(1), pp. 42. [Online].Available: http://www.emeraldinsight.com/doi/full/10.1108/13565360510575530.

94. R. D. Pendse and P. Zhou. (2002 Feb.). Methodology for predicting solder joint reliability in semiconductor packages. *Microelectronics Reliability*, Vol. *42 (2)*, pp. 301–305. [Online]. Available: http://www.sciencedirect.com/science/article/pii/S0026271401001305.

95. R. Drees and N. Young. (2004 Aug.). Role of BIST in Support System Maintenance and Availability. *IEEE Aerospace and Electronic Systems*

*Magazine,* Vol. *19 (8),* pp. 3-7. [Online].Available: http://ieeexplore.ieee.org/document/1346885.

96. D. Allen. (2003 Sep.). Probabilities Associated with a Built-in-Test System, Focus on False Alarms. IEEE Systems Readiness Technology Conference, pp. 643-645.

97. R. X. Gao and A. Suryavanshi. (2003 Jan.). BIT for Intelligent System Design and Condition Monitoring. IEEE Transactions on Instrumentation and Measurement, Vol. 51, Issue: 5, pp. 1061-1067. [Online].Available: http://ieeexplore.ieee.org/document/1174042.

98. D. Rosenthal and B. Wadell. (2002 Aug.). Predicting and Eliminating Built-in Test False Alarms. *IEEE Transactions on Reliability*, Vol. *39 (4),* pp. 500-505. [Online].Available: http://ieeexplore.ieee.org/document/58728.

99. I. E. Anderson and J. L. Harringa. (2004 Dec.). Elevated Temperature Aging of Solder Joints Based on Sn-Ag-Cu: Effects on Joint Microstructure and Shear Strength. *Journal of Electronic Materials*, Vol. *33 (12),* pp. 1485-1496. [Online]. Available: http://link.springer.com/article/10.1007/s11664-004-0090-1.

100. P. Lall, N. Islam, K. Rahim, J. C. Suhling and S. Gale, “Leading Indicators-of-Failure for Prognosis of Electronic and MEMS Packaging”, 54th *ECTC*, Las Vegas, Nevada, 2004.

101. P. Lall, N. Islam, P. Choudhary and J. C. Suhling, “Prognostication and Health Monitoring of Leaded and Lead Free Electronic and MEMS Packages in Harsh Environments”, 55th *ECTC*, pp. 1-9, Orlando, FL, 2005.

102. P. Lall, N. Islam, K. Rahim, J. C. Suhling and S. Gale. (2006 Sep.). Prognostics and Health Management of Electronic Packaging. *IEEE Transactions on Components and Packaging Technologies, Vol. 29, No. 3*, pp. 666-677.

103. P. Lall, M. Hande, C. Bhat, J. C. Suhling, and J. Lee, "Prognostics Health Monitoring (PHM) for Prior-Damage Assessment in Electronics Equipment under Thermo-Mechanical Loads", 57th *ECTC*, Reno, Nevada, pp. 1097-1111, M, 2007.

104. P. Lall, C. Bhat, M. Hande, V. More, R. Vaidya, R. Pandher, J. C. Suhling, and K. Goebel, "Interrogation of System State for Damage Assessment in Lead-free Electronics Subjected to Thermo-Mechanical Loads", 58th *ECTC*, Orlando, Florida, pp. 918-929, May 27-30, 2008.

105. P. Lall, V. More, R. Vaidya and K. Goebel, "Prognostication of Latent Damage and Residual Life in Leadfree Electronics Subjected to Multiple Thermal-Environments", 59th *ECTC*, pp. 1381-1392, San Diego, California USA, 2009.

106. P. Lall, V. More, R. Vaidya and K. Goebel, "Assessment of Residual Damage in Lead-free Electronics Subjected to Multiple Thermal Environments of Thermal Aging and Thermal Cycling", 60th *ECTC*, pp. 206-218, Las Vegas, Nevada, USA, 2010.

107. P. Lall, V. More, R. Vaidya and K. Goebel, "PHM-Based Residual Life Computation of Electronics Subjected to a Combination of Multiple Cyclic-Thermal Environments", *ITHERM* 2010, Las Vegas, NV, 2010.

108. P. Lall, M. Harsha, K. Kumar, K. Goebel, J. Jones and J. C. Suhling, "Interrogation of Accrued Damage and Remaining Life in Field-Deployed

Electronics Subjected to Multiple Thermal Environments of Thermal Aging and Thermal Cycling", 61st *ECTC*, pp.775- 789, 2011.

109. P. Lall, M. Harsha, J. C. Suhling and K. Goebel, "Sustained Damage and Remaining Useful Life Assessment in Leadfree Electronics Subjected to Sequential Multiple Thermal Environments", 62nd *ECTC*, pp.1695-1708,2012.

110. P. Lall, K. Mirza, M. Harsha, J. C. Suhling and K. Goebel, "Damage Pre-Cursor Based Assessment of Impact of High Temperature Storage on Reliability of Leadfree Electronics", 63rd *ECTC*, pp. 817-826, San Diego, California, 2013.

111. P. Lall, M. Harsha, J. C. Suhling and K. Goebel, "Damage Pre-cursors based Prognostication of Accrued Damage and Assessment of Operational Readiness of Leadfree Electronics", *InterPACK*, Burlingame, CA, USA, 2013.

112. P. Lall, K. Mirza, M. Harsha, J. C. Suhling and K. Goebel, "Study on the Effect of Mean Temperature of Thermal Cycle on the SnAgCu Solder Joint Reliability", 64th *ECTC*, Orlando, Florida USA, 2014.

113. M. I. A. Lourakis. (2005 Feb.). A brief Description of the Levenberg-Marquardt algorithm implemented by Levmar. Foundation of Research & Technology – Hellas (Forth), Greece, pp. 1- 6.

114. K. Madsen, H. B. Nielsen and O. Tingleff. (2004). *Methods for Non- Linear Least Squares Problems* (2nd ed.). [Online]. Available: http://www.imm.dtu.dk/courses/02611/nllsq.pdf.

115. A. Saxena, J. Celaya, B. Saha, S. Saha and K. Goebel. (2009 Mar.). Evaluating Algorithm Performance Metrics Tailored for Prognostics. IEEE

Aerospace Conference, pp. 1-14. [Online]. Available: http://ieeexplore.ieee.org/document/4839666.

116. X. Guan, Y. Liu, R. Jha, A. Saxena, J. Celaya and K. Goebel. (2011). Comparison of Two Probabilistic Fatigue Damage Assessment approaches Using Prognostics Performance Metrics. *International Journal of Prognostics and Health Management,* PHM Seciety, Vol *2,* pp. 1-11. [Online]. Available: https://www.phmsociety.org/sites/phmsociety.org/files/GUAN_IJPHM_final.pdf

117. D. Ahlburg. (1992). A Commentary on Error Measures: Error Measures and Choice of a Forecast Method. *International Journal of Forecasting*, Vol 8, pp. 99-111.

118. B. Pan, K. Qian, H. Xie, and A. Asundi. (2009 Apr.). Two dimensional digital image correlation for in-plane displacement and strain measurement: a review. *Measurement Science and Technology*, Vol. *20, (06).* [Online]. Available: http://iopscience.iop.org/article/10.1088/0957-0233/20/6/062001/meta.

119. D. Lecompte, A. Smits, S. Bossuyt, H. Sol, J. Vantomme, D. V. Hemelrijck, and A. M. Habraken. (2006). Quality assessment of speckle patterns for digital image correlation. *Opt. Lasers Eng*, Vol. *44 (11),* pp. 1132–1145. [Online]. Available: http://www.sciencedirect.com/science/article/pii/S0143816605001727

120. B. Pan, H. Xie, Z. Wang, K. Qian, and Z. Wang. (2008). Study of subset size selection in digital image correlation for speckle patterns. *Optics Express,* Vol. *16 (10),* pp. 7037–7048. [Online]. Available: https://www.osapublishing.org/oe/abstract.cfm?uri=oe-16-10-7037.

121. B. Pan, Z. Lu, and H. Xie. (2010). Mean intensity gradient: an effective global parameter for quality assessment of the speckle patterns used in digital image correlation. *Optics and Lasers Engineering*, Vol. *48(4),* pp. 469–477. [Online]. Available: http://www.sciencedirect.com/science/article/pii/S0143816609002139

122. B. Pan, H. Xie, and Z. Wang. (2010). Equivalence of digital image correlation criteria for pattern matching. *Applied Optics*, Vol. *49,* Issue 28, pp. 5501-5509. [Online]. Available: https://www.osapublishing.org/ao/abstract.cfm?uri=ao-49-28-5501.

123. D. A. Shnawah, M. F. M. Sabri, I. A. Badruddin. (2012 Jan.) A review on thermal cycling and drop impact reliability of SAC solder joint in portable electronic products. *Microelectronics Reliability*. Vol. *52 (1),* pp. 90-99. [Online].Available:http://www.sciencedirect.com/science/article/pii/S0026271411003581.

124. J. H. L. Pang, T. H. Low, B. S. Xiong, X Luhua and C. C. Neo. (2004 Sep.). Thermal cycling aging effects on Sn-Ag-Cu solder joint microstructure, IMC and strength. *Thin Solid Films,* Vol. *462–463,* pp. 370-375. [Online].Available: http://www.sciencedirect.com/science/article/pii/S0040609004006418.

125. Y. Pao, S. Badgley, R. Govila, E. Jih. (1994 Jan.). Thermomechanical and Fatigue Behavior of High Temperature Lead and Lead Free Solder Joints. Fatigue of Electronic Materials, STP23916S, S. Schroeder and M. Mitchell, Ed., ASTM International, pp. 60-81. [Online].Available: https://doi.org/10.1520/STP23916S.

126. J. Mi, Y-F Li, Y-J. Yang, W. Peng, H-Z. Huang. (2014 Jul.). Thermal Cycling Life prediction of Sn-3.0 Ag-0.5 Cu Solder Joint using Type I Censored Data. *The*

*Scientific World Journal*, Vol. *2014,* Article ID 807693. [Online].Available: https://www.hindawi.com/journals/tswj/2014/807693/abs.

127. M. Motalab, Z. Cai, J. C. Suhling, J. Zhang, J. L. Evans, M. Bozach and P. Lall. (2012). Improved Prediction of Lead Free Solder Joint Reliability that Include Aging Effectc. 62nd IEEE-ECTC, San Diego,CA. [Online].Available: http://ieeexplore.ieee.org/document/6248879.

128. R. Darveaux. (2000 May). Effect of simulation methodology on solder joint crack growth correlation. 50th IEEE-ECTC. [Online].Available: http://ieeexplore.ieee.org/document/853299.

129. M. D. Sangid, H. J. Maier and H. Sehitoglu. (2011 May). The role of grain boundaries on fatigue crack initiation – An energy approach. *International Journal of Plasticity*, Vol 27 (5), pp. 801-821. [Online].Available: http://www.sciencedirect.com/science/article/pii/S074964191000135X.